Electron and optical spectroscopy of 2D semiconductors and defects in the electron microscope

Noémie Bonnet

université PARIS-SACLAY

Electron and optical spectroscopy of 2D semiconductors and defects in the electron microscope

Spectroscopie optique et électronique de semiconducteurs 2D et de défauts dans le microscope électronique

Thèse de doctorat de l'université Paris-Saclay

École doctorale n° 572 : ondes et matière (EDOM)
Spécialité de doctorat : Physique
Graduate School : Physique, Référent : Faculté des sciences d'Orsay

Thèse préparée dans l'unité de recherche LPS Laboratoire de Physique des Solides (Université Paris-Saclay, CNRS), sous la direction de Luiz TIZEI, directeur de recherche et la co-direction de Mathieu KOCIAK, directeur de recherche.

Thèse soutenue à Paris-Saclay, le 17 janvier 2022, par

Noémie BONNET

Composition du jury

Maria TCHERNYCHEVA Diretrice de Recherche, Centre de Nanosciences et Nanotechnologies (UMR 9001), Université Paris-Saclay, France	Présidente
Arnaud ARBOUET Directeur de recherche, Centre d'Élaboration de Matériaux et d'Etudes Structurales (UPR 8011), France	Rapporteur & Examinateur
Robert MARTIN Professeur des Universités, University of Strathclyde Glasgow, United-Kingdom	Rapporteur & Examinateur
Stéphane BERCIAUD Professeur des Universités, Institut de Physique et Chimie des Matériaux de Strasbourg (UMR 7504), Université de Strasbourg, France	Examinateur
Rachel OLIVER Professeur des Universités, University of Cambridge, United-Kingdom	Examinatrice
Luiz TIZEI Directeur de recherche, Laboratoire de Physique des Solides (UMR 8502), Université Paris-Saclay, France	Directeur de thèse

THESE DE DOCTORAT
NNT : 2022UPASP006

Acknowledgements

Je souhaite en premier lieu remercier mes directeurs de thèse, Luiz et Mathieu, qui ont été des modèles, aussi bien scientifiquement que sur le plan personnel. Ils ont été présents durant toute ma thèse, aussi bien dans les moments difficiles que pour les bons moments.
Luiz, pour avoir partagé avec moi des bières, des manips cool (pas en même temps) et surtout des leçons de vie: toujours enlever la vis avant toute chose (si vous ne connaissez pas l'histoire, demandez-lui !).
Mathieu, pour toujours savoir comment me dire les choses (comme ça je n'avais pas trop peur de poser des questions bêtes), et ses nombreuses, très nombreuses, très très nombreuses blagues.
Votre présence et vos conseils m'ont permis de mener à bien ce travail pendant trois ans, dans des conditions pas évidente, particulièrement à cause du covid.

Je remercie également mon comité de thèse, Maria Tchernycheva, Arnaud Arbouet, Robert Martin, Stéphane Berciaud et Rachel Oliver, pour avoir accepté de relire et évaluer mon travail.

Je souhaite ensuite remercier ma famille, et en particulier ma maman, qui m'a toujours soutenue et a toujours cru en moi, et avec qui je peux avoir des conversations pendant des heures (on parle autant l'une que l'autre).

Je remercie aussi mes colocs (Hervé et Zoé), qui en plus de m'avoir supportée au quotidien m'ont soutenue quand j'en avais besoin.
Je remercie également mes amis préférés (Anissa, Christelle, Laure, Vince, Mag, Foriane, Mathilde, Antoine, Margaux et Marine), qui sont toujous là pour moi (et c'est réciproque!), en particulier pour aller manger des sushis et boire des bières.

Je remercie aussi mes amis du badminton, grâce à qui j'ai pu acquérir quelques muscles, et boire pas mal de bières (pour fêter quand on gagne, et oublier quand on perd !). C'était vraiment génial d'avoir une équipe aussi soudée dans un club avec des gens aussi géniaux (et je sais de quoi je parle parce que j'ai joué dans plein d'autres clubs, le CAOBAD est le mieux !).
En particulier je remercie Manu et Hélène, parce qu'ils savent exactement quand est-ce qu'il faut m'engueuler ou m'encourager pour que je gagne (et aussi merci infiniment de m'avoir prêté votre voiture pendant les vacances !!), ainsi que Hugo et Anaïs, qui m'ont bien supporté lors des trajets en voiture!

Je remecie également mes collègues du groupe STEM, qui ont été comme une seconde famille (avec qui j'ai passé plus de temps que ma première famille!). Vraiment, je me suis sentie comme à la maison, avec les discussions plus ou moins perchées et un grand nombre de fous rires.
Ainsi que l'administration du labo, qui a toujours été super efficace pour résoudre les soucis (et commander les meubles pour la salle thésard !)

Je remercie également K.V. Pham, le responsable de la L2 physique. La L2 a été une année particulièrement difficile pour moi, et il a su me faire reprendre confiance. Sans son aide, je ne pense pas que j'aurais réussi à continuer les études à la fac.

Je remercie enfin Anissa, pour m'avoir aidée à écrire ces remerciements, qui a été une tâche bien plus coûteuse que la rédaction de ma thèse.

Résumé

La compréhension des interactions lumière-matière est essentielle au développement de nouveaux dispositifs opto-électroniques à l'échelle nanométrique. Ces interactions sont souvent régies par la physique des excitons, qui n'est pas encore bien comprise à l'échelle de ces quasi-particules. Les mesures à haute résolution spatiale de l'absorption et de l'émission de lumière sont cruciales pour comprendre la physique des excitons à l'échelle nanométrique, ce qui est particulièrement difficile en raison de la limite fondamentale de la diffraction optique. De nombreuses techniques purement optiques ont été développées au cours de ces dernières décennies pour surpasser cette limite, et sont appelées microscopie à super-résolution (MSR). Elles permettent de réaliser des mesures optiques en dessous de la limite de la diffraction pour différents types d'échantillons, en particulier pour des nano-objets.

Il existe deux grandes catégories de MSR optiques: les techniques de champ proche et de champ lointain. La spectroscopie Raman stimulée (tip-enhanced Raman spectroscopy, TERS) est un exemple de MSR en champ proche. Cette technique est basée sur le confinement de la lumière dans l'espace nanométrique entre une pointe métallique et l'échantillon pour mesurer l'émission en champ proche à haute résolution spatiale. Les mesures stimulées par la pointe peuvent souvent être couplées à la mesure de la topographie de l'échantillon en microscopie à force atomique (AFM) [1]. Le principal inconvénient de ce type de méthode est la forte interaction entre la pointe et l'échantillon, dont l'environnement diélectrique est fortement modifié [2].

Un autre exemple de MSR est la microscopie à déplétion par émission stimulée (stimulated emission depletion microscopy, STED) [3], qui est une technique de champ lointain. Elle utilise deux lasers, l'un pour exciter la fluorescence, et l'autre, en forme d'anneau, pour désexciter les émetteurs de manière non radiative. Ainsi, la fluorescence provient précisément du centre de l'anneau, qui peut être une zone de taille nanométrique. Cette technique très puissante est largement utilisée en biologie, où les molécules fluorescentes peuvent être choisies spécifiquement pour correspondre aux longueurs d'onde du montage, mais elle dépend largement de la connaissance des particules émettrices de lumière utilisées.

Dans cette thèse, j'ai utilisé une approche différente en champ lointain qui permet des résolutions bien en dessous de la limite de diffraction et une excitation non sélective des échantillons: la cathodoluminescence (CL) avec des électrons rapides dans un microscope électronique en transmission à balayage (STEM) [4]. J'ai principalement étudié deux sortes de nano-objets. Les centres colorés azote-lacune (nitrogen-vacancy, NV) dans des nanodiamants, qui ont été excités à la fois par le faisceau d'électrons rapides et par divers lasers afin de comprendre la photophysique de ces défauts. Les autres objets que j'ai étudiés étaient des monocouches de dichalcogénures de métaux de transition (TMD) encapsulées dans du nitrure de bore hexagonal (h-BN), en utilisant à la fois la CL (émission), la spectroscopie de perte d'énergie des électrons (electron energy-loss spectroscopy, EELS, correspondant à l'absorption) et la µ-diffraction (mesure de diffraction avec un faisceau d'électron, permettant de cartographier la déformation locale).

Centres azote-lacune dans les nanodiamants

Les centres NV des nanodiamants fluorescents (FND) sont les sources de photons uniques à l'état solide les plus brillantes et les plus stables [5], ce qui les rend particulièrement adaptés pour étudier l'optique quantique [6] ou la détection à l'échelle nanométrique [7]. Malgré les efforts considérables déployés pour comprendre la photophysique des centres NV, certaines questions demeurent, comme la raison pour laquelle on ne voit qu'un seul état de charge des centres NV en CL [8]. En effet, les centres NV peuvent exister dans deux états de charge luminescents: neutre (NV^0) et chargé négativement (NV^-). Ils ont chacuns des caractéristiques différentes, de leurs lignes d'émission (575 nm pour NV^0 et 637 nm pour NV^-), à leur structure énergétique qui permet des applications très différentes.

Dans cette thèse, j'ai étudié la photophysique des centres NV avec une excitation à la fois par le faisceau d'électrons rapides (CL) et par la lumière laser (photoluminescence, PL) afin de comprendre la conversion d'état de charge. J'ai construit une installation d'injection laser afin de permettre l'illumination des centres NV avec plusieurs longueurs d'onde dans le STEM, tel que représenté sur la Fig. 1. Comme la plupart des applications reposent sur l'utilisation des centres NV^-, j'ai tenté de pomper optiquement les centres NV avec une lumière laser de 1064 nm pour obtenir un signal de cathodoluminescence NV^- [9]. Ce fut malheureusement un échec, probablement à cause de l'échauffement local de l'échantillon. Cela m'a conduit à effectuer des expériences de CL en température dans le STEM, puisque les centres NV dans les diamants sont également des nanothermomètres largement utilisés. Les résultats ont ensuite été comparés à ceux du chauffage de l'échantillon avec le laser infra-rouge [10].

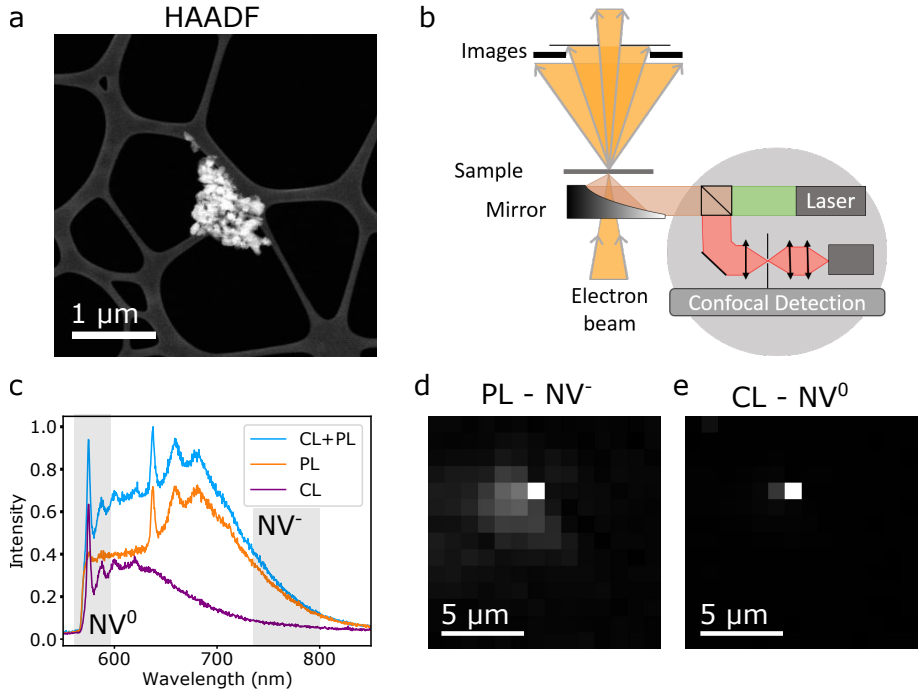

Figure 1: Micro-PL et CL combinées in-situ sur un agrégat de nanodiamants: **(a)** image de champ sombre (HAADF) montrant un agrégat d'environ 1 µm sur une grille TEM. **(b)** Schéma du montage: le faisceau d'électrons est transmis à travers l'échantillon, ce qui permet d'imager, et la lumière de CL est collectée par un miroir parabolique. Les lasers sont amenés à l'échantillon avec le même miroir. La lumière collectée est ensuite dispersée dans un spectromètre optique. **(c)** Spectres typiques de CL (violet), PL (orange), CL et PL combinées (bleu), provenance l'aggrégat en (a). Les plages d'intégration pour NV^0 (570-590 nm) et NV^- (750-800 nm) sont indiquées en gris, ce qui produit respectivement les cartes **(d)** et **(e)**. Les mesures ont été effectuées à 150 K.

Le couplage de l'injection de lumière avec le microscope STEM ouvre de nombreuses possibilités puisque la PL est un outil de caractérisation largement utilisé, qui peut désormais être utilisé en parallèle de la microscopie à haute résolution en STEM [11, 12]. Ce type d'expérience est particulièrement adapté aux échantillons fragiles puisqu'un laser de faible puissance produit moins de dégâts qu'un faisceau d'électrons focalisé, et aux échantillons qui n'émettent pas de lumière en CL, comme les monocouches de TMD ou de h-BN.

Monocouches de métaux de transition dichalcogénures encapsulées dans du nitrure de bore hexagonal

Les TMD sont récemment apparus comme l'un des principaux éléments constitutifs des hétérostructures de Van der Waals avec le h-BN et le graphène. Les monocouches de TMD sont des semi-conducteurs directs, ce qui en fait de bons émetteurs de lumière [13]. La plupart des applications possibles nécessitent une compréhension et un contrôle suffisants de l'émission et de l'absorption de lumière à l'échelle nanométrique de ces monocouches. La caractérisation de l'émission de lumière est souvent effectuée par des expériences de PL, qui ont été réalisées au cours de ces dix dernières années pour les monocouches de TMD, mais la CL de ces systèmes n'a été détectée pour la première fois qu'en 2017 [14]. La caractérisation de l'émission de lumière par CL présente l'avantage d'une meilleure résolution spatiale que la PL et peut être directement couplée à l'imagerie haute résolution. La difficulté à mesurer la CL à partir d'une monocouche vient principalement de la faible densité de porteurs de charge excités par le faisceau d'électrons, qui est insuffisante pour fournir une CL mesurable. Pour augmenter la densité des porteurs de charge, la monocouche de TMD a été encapsulée dans un matériau isolant: le h-BN.

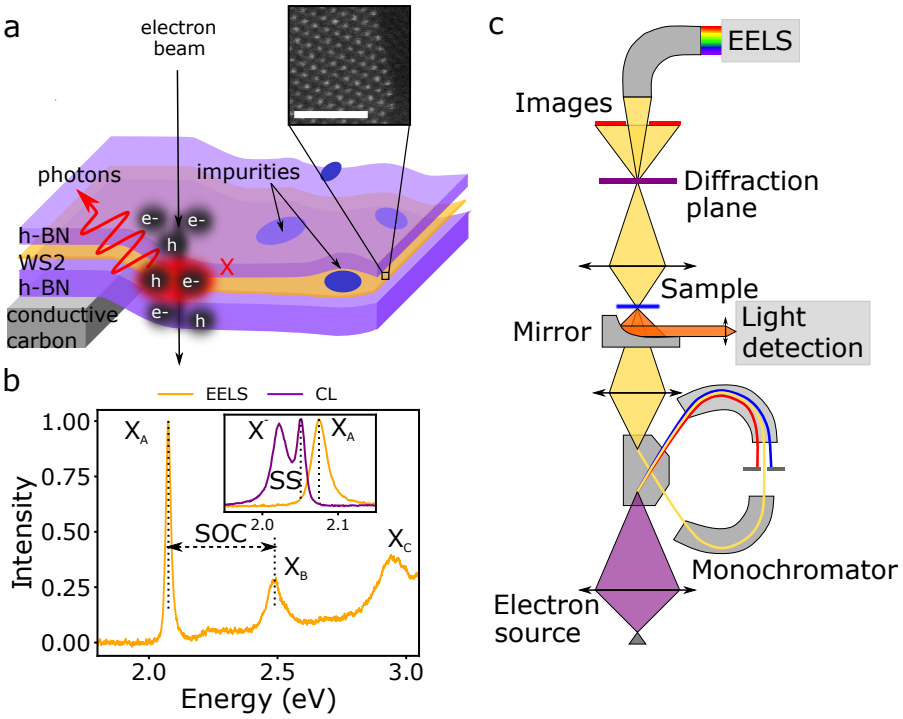

Figure 2: CL et EELS d'une monocouche de TMD: (a) schéma de la monocouche (WS_2, orange) encapsulée dans du h-BN (violet). L'émission de X_A est représentée en rouge. L'encart montre une image HAADF résolue atomiquement de la monocouche encapsulée (barre d'échelle de 2 nm). **(b)** Spectre EELS typique (courbe orange) avec les pics associés à différentes transitions excitoniques (X_A, X_B, X_C) indiqués. L'émission typique de CL est montrée sur l'encart (courbe violette), où X_A et X^- sont visibles. La différence d'énergie entre l'absoprtion (EELS) et l'émission (CL) est le décalage de Stokes (SS). **(c)** Schéma du STEM utilisé pour l'expréience. Le monochromateur permet d'effectuer des mesures d'absorption EELS à haute résolution en énergie. La CL émise est collectée par un miroir parabolique (NA=0.5) et dirigée vers un spectromètre optique. Sur le même montage, des clichés de diffraction et des images à haute résolution peuvent être mesurées avec différents angles de collection, en parallèle des mesures spectroscopiques. Les mesures ont été effectuées à 150 K.

L'encapsulation permet l'imagerie à résolution atomique de la monocouche encapsulée, comme le montre la figure 2. En plus de l'imagerie à haute résolution spatiale, les microscopes STEM permettent de mesurer d'autres signaux dans la même expérience, comme la CL, l'EELS et la µ-diffraction. Cela a permis d'observer les variations spatiales de l'émission CL de l'exciton A (X_A), de l'exciton A chargé (trion: X^-), et des excitons localisés de plus faible énergie (L) [15], comme le montre la figure 3. La combinaison des mesures de CL et d'EELS sur un même phénomène est un outil puissant [16, 17], et a été réalisée ici pour caractériser le X_A dans les monocouches WS_2.

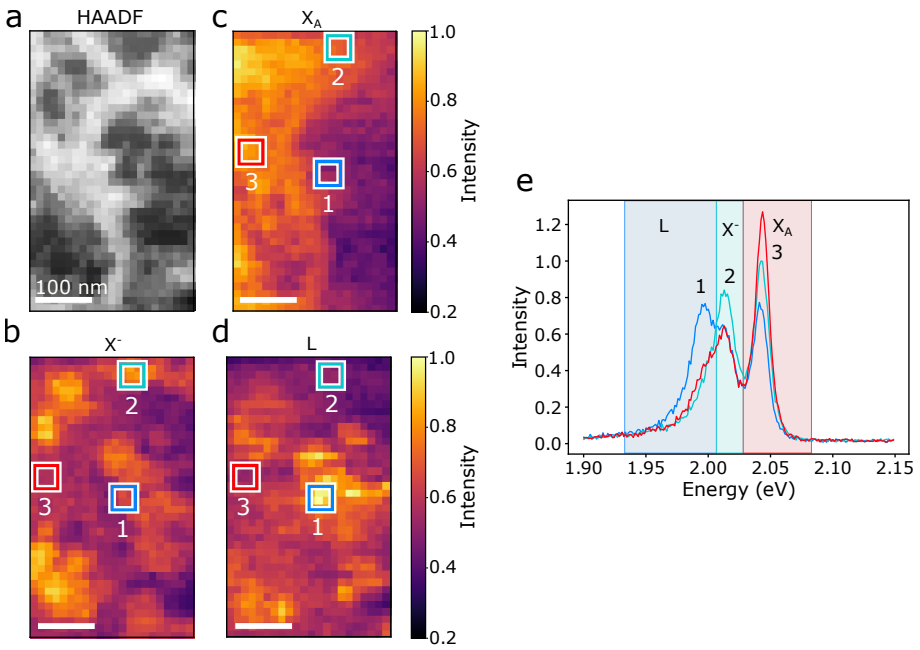

Figure 3: CL provenant d'une monocouche de TMD encaspulée résolue spatialement et spectralement: (a) image HAADF de la zone, **(b)** carte d'intensité filtrée en énergie des pics de X^-, **(c)** X_A, **(d)** et L (basse énergie), **(e)** spectres extraits des positions 1 à 3. Les zones surlignées correspondent aux filtres d'énergie des spectres (c, b et d). Les spectres sont normalisés.

La microscopie S(T)EM permet de de connecter plusieurs signaux provenant de zones nanométriques [18], ce qui permet d'obtenir des informations sur les phénomènes physiques se produisant à ces échelles de longueur. Les variations spatiales de X_A et X^- dans les monocouches de TMD ont été reliées à des changements chimiques à la surface des monocouches de TMD, entraînant des des changements dans le rapport d'intensité d'émission entre X_A et X^-. Ces mesures ont été combinées avec des mesures EELS de perte d'énergie des électrons de coeur, qui cartographient les éléments chimiques de l'échantillon, et la µ-diffraction, pour cartographier la déformation locale. Les variations de X^- ont montré une corrélation avec des résidus riches en carbone provenant du processus de fabrication de l'échantillon.

Des expériences préliminaires combinant CL, EELS et µ-diffraction, ont été réalisées pour caractériser les émetteurs à basse énergie (L) et l'origine de leur localisation [15, 19]. Une telle combinaison d'expériences dans la même installation ouvre la possibilité d'étudier de nombreux autres systèmes émetteurs de lumière et de comprendre l'origine de la variation à l'échelle nanométrique de leur émission. Ces expériences peuvent être poussées encore plus loin pour la caractérisation de l'émission de sources de photons uniques (single photon emitters, SPE), en utilisant les techniques précédentes et en les couplant avec l'interférométrie d'intensité lumineuse, comme l'expérience de Hanbury-Brown et Twiss [20, 21].

Dans cette thèse j'ai étudié en détail ces deux systèmes, les centres NV dans les nanodiamants et les monocouches TMD.

Contents

Chapter 1

Introduction

Contents

Understanding the interactions between light and matter is essential to develop new nanoscale opto-electronic devices. These interactions are often governed by exciton physics that is still not well understood at the scale of these quasi-particles. High spatial resolution measurements of the light absorption and emission is therefore crucial for understanding the exciton physics at the nanoscale, which is particularly challenging due to the optical diffraction fundamental limit. Many purely optical techniques have been developed in the past decades to overcome this limit, which are called super-resolution microscopy (SRM). They enable the sub-diffraction optical measurements of various samples, including nano-objects.

There are two main categories of optical SRM: the near-field and the far-field techniques. The tip-enhanced Raman spectroscopy (TERS) is an example of near-field SRM. It uses the light confinement in the nanometric space between a metallic probe and the sample to measure emission at high spatial resolution. Tip-enhanced measurements can often be coupled to topography through atomic force microscopy (AFM) measurements [1]. The major drawback of this type of method is the high interaction between the tip an the sample, which dielectric environment is highly modified [2].

Another example of SRM is the stimulated emission depletion microscopy (STED) [3], which is a far-field technique. It uses two lasers, one to excite the fluorescence, and the other, in a doughnut shape, to de-excite non-radiatively the emitters. This way, the fluorescence precisely comes from the center of the doughnut, which can be a nanometer-sized area. This very powerful technique is widely used in biology, where the fluorescent molecules can be specifically chosen to match the wavelengths of the setup, but this technique largely relies on the knowledge of the light-emitting particles used. A table summarizing the capabilities of various SRM techniques is in table 1.1.

Technique combination	Emission	Absorption	Subwavelength optics	Topography	Chemical mapping	Structural mapping (Raman)	Structural mapping	Atomic scale imaging	Cryogenic temperature (all techniques)	Encapsulated layers	References
µPL + Raman	●					●			●	●	van der Zande 2013
TEPL + AFM + Raman/TERS	●		●	●		●			●		Darlington 2020, Jariwala 2018
µPL + Nano-Auger	●				●						Bao 2015
µPL +reflectance difference/ transmission	●	●							●	●	Jo 2021
µPL + STEM + EELS/EDS	●				●		●	●		●	Hayee 2020
TEPL + STEM + EELS/EDS	●		●		●		●	●			Kastl 2017
CL + EELS + STEM	●	●	●		●		●	●	●	●	This work

Table 1.1: Summary of the capabilities of various SRM techniques applied to the study of excitons physics in TMDs. The techniques used in this thesis are highlighted in pink.

In this thesis, I used a different far-field approach that enables resolutions far below the diffraction limit and non-selective excitation of samples: cathodoluminescence (CL) with fast electrons in a scanning transmission electron microscope (STEM) [4]. I mainly studied two sorts of nano-objects. The nitrogen-vacancy (NV) color centers in nanodiamonds, which were excited both by the fast electron beam

and various lasers, to understand the defects photophysics. The other objects studied were transition metal dichalcogenides (TMDs) monolayers encapsulated in h-BN, using combined CL (emission), electron energy-loss spectroscopy (EELS, absorption) and μ-diffraction (strain mapping).

1.1 Nitrogen-Vacancy centers in nanodiamonds

NV centers in fluorescent nanodiamonds (FNDs) are the brightest and most stable solid-state single photon sources [5], which makes them particularly suited for the study of quantum optics [6], or for nanoscale sensing [7]. Even with the extensive efforts made to understand the photophysics of NV centers, some questions still remain, such as the reason why in CL only one charge state of NV is seen [8]. Indeed, NV centers can exist in two luminescent charge-states: neutral (NV^0) and negatively-charged (NV^-). They both have different characteristics, from their emission lines (575 nm for NV^0 and 637 nm for NV^-), to their energy structure that allow for very different applications.

Here, I studied the photophysics of NV centers with excitation both from the fast electron beam (CL) and from laser light (photoluminescence, PL) to understand the charge-state conversion. I built a PL excitation setup in order to enable the illumination of NV centers with multiple laser wavelengths inside the electron microscope, such as represented in Fig. 1.1. Since most of the applications rely on the use of NV^-, I attempted to optically pump the NV centers with 1064 nm laser light to get NV^- cathodoluminescence signal [9]. It was unfortunately unsuccessful, probably due to sample heating. This lead me to perform temperature-controlled CL experiments in the STEM, since NV centers in nanodiamonds are also widely used nanothermometers. The results were then compared to that of sample heating with the IR laser [10].

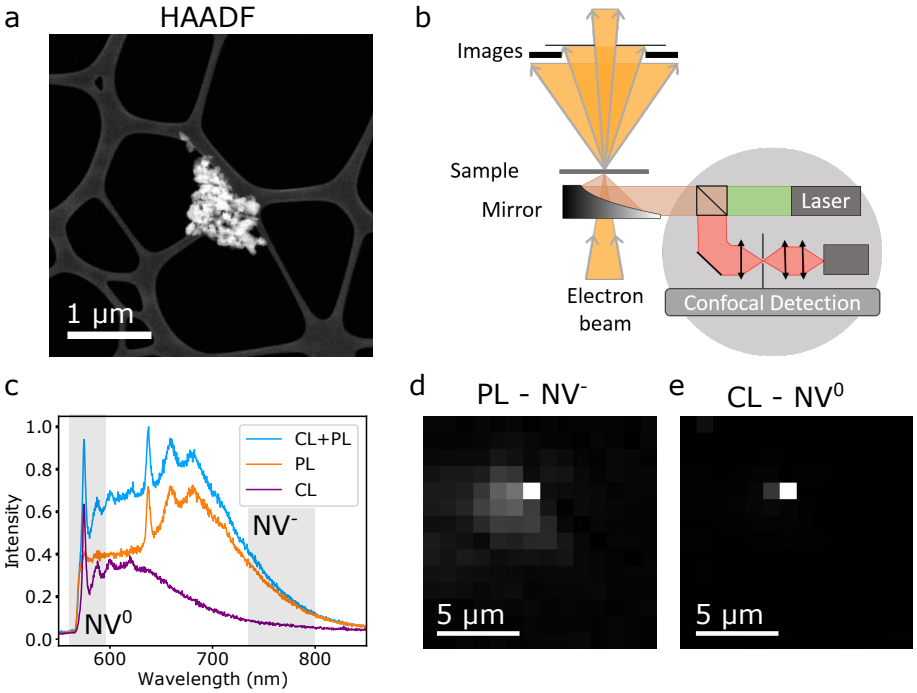

Figure 1.1: Combined in-situ micro-PL and CL on an aggregate of FNDs: **(a)** high angle annular dark field image (HAADF) showing an aggregate of size about 1 µm on a TEM grid. **(b)** Scheme of the setup: the electron beam is transmitted across the sample, allowing for imaging, and the CL light is collected by a parabolic mirror. The lasers are brought to the sample using the same mirror. The light detected is then dispersed in an optical spectrometer. **(c)** Typical spectra for CL (purple), PL (orange), CL and PL combined (blue) from aggregate (a). The integration ranges for NV^0 (570-590 nm) and NV^- (750-800 nm) are highlighted in grey, leading respectively to **(d)** and **(e)** raster scans. At the 1 µm step size of these scans, the CL map displays mainly one bright pixel, in agreement with the 1 µm-sized aggregates considered and with nanometer scale of the electron beam, while PL raster scan (d) shows a spot extended over about 3 µm, corresponding to the laser beam spot shape. The measurements were performed with the sample kept at 150 K using a liquid nitrogen cooled sample holder.

The light-injection coupling with the STEM microscope opens many possibilities since PL is a widely used characterization tool, that can now be measured in parallel with the high spatial resolution of STEM microscopes [11, 12]. These experiments are particularly adapted to fragile samples since a low power laser induces less damages than a focused electron beam, and to samples that do not emit light in CL, such as bare TMD or h-BN monolayers.

1.2 Transition metal dichalcogenides monolayers encapsulated in h-BN

TMDs have recently emerged as one of the main building blocks for van der Waals heterostructures, together with h-BN and graphene. TMD monolayers are direct bandgap semiconductors, which makes them bright light emitters [13]. Many promising device applications require sufficient understanding and control of the nanoscale light emission and absorption of TMD monolayers. Light emission characterization is often done with PL experiments, which have been done for the past ten years for TMD monolayers, but the CL of such systems was detected for the first time only in 2017 [14]. Light emission characterization with CL has the advantage of

higher spatial resolution than PL and it can be directly coupled with high-resolution imaging. The challenge of measuring CL from a monolayer comes primarily from the low density of charge-carriers excited by the electron beam, which is insufficient to provide measurable CL. To increase the charge-carriers density, the TMD monolayer was encapsulated in an insulating material: h-BN.

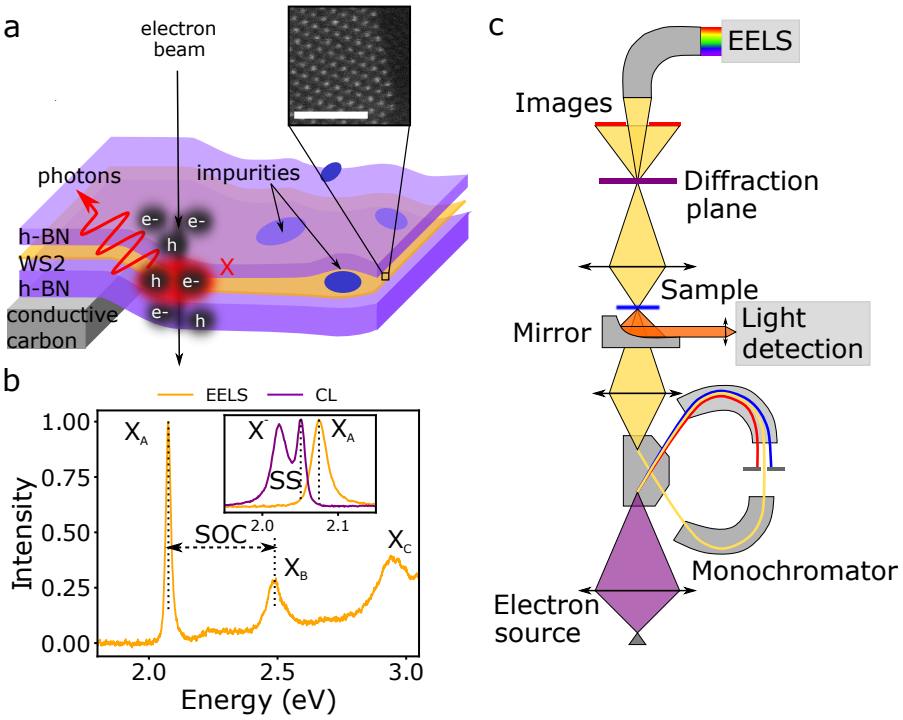

Figure 1.2: CL and EELS of a TMD monolayer: (a) Scheme of the TMD (WS_2) monolayer (orange) encapsulated in h-BN (purple), with the X_A emission in red. The inset shows an atomically-resolved HAADF image of an edge in the encapsulated TMD monolayer (scale bar is 2 nm). **(b)** Typical EELS spectrum (orange curve) with the peak labels associated to different excitonic transitions excitons (X_A, X_B, X_C). A typical CL emission is shown on the inset (purple curve), where both X_A and X^- are visible. The energy difference between the absorption (EELS) and emission (CL) of X_A is the Stokes shift (SS), and that between X_A and X_B in the spin-orbit coupling (SOC). **(c)** Scheme of the STEM microscope used for the experiment. The monochromator allows for high energy resolution low-loss EELS absorption measurements. The light emitted from the sample upon electron excitation (CL) is collected by a parabolic mirror (NA= 0.5) and directed to an optical spectrometer. On the same setup diffraction patterns and images at different collection angles can also be measured in parallel to spectroscopic information. The measurements were performed with the sample kept at 150 K using a liquid nitrogen cooled sample holder.

The encapsulation still enables the atomically-resolved imaging of the embedded monolayer, such as shown in Fig. 1.2. Additionally to achieving high-spatial resolution imaging, STEM microscopes allow for the measurement of other signals in the same experiment, such as CL, EELS and μ-diffraction (diffraction measurement with a convergent electron beam). This enabled the observation of spatial variations of the CL emission of the A exciton (X_A), the charged A exciton (trion: X^-), and the lower energy localized excitons (L), [15] such as displayed in Fig. 1.3. The correlation between CL and EELS measurements of the same phenomenon is a powerful tool [16, 17], and has been performed here to characterize the X_A in WS_2 monolayers.

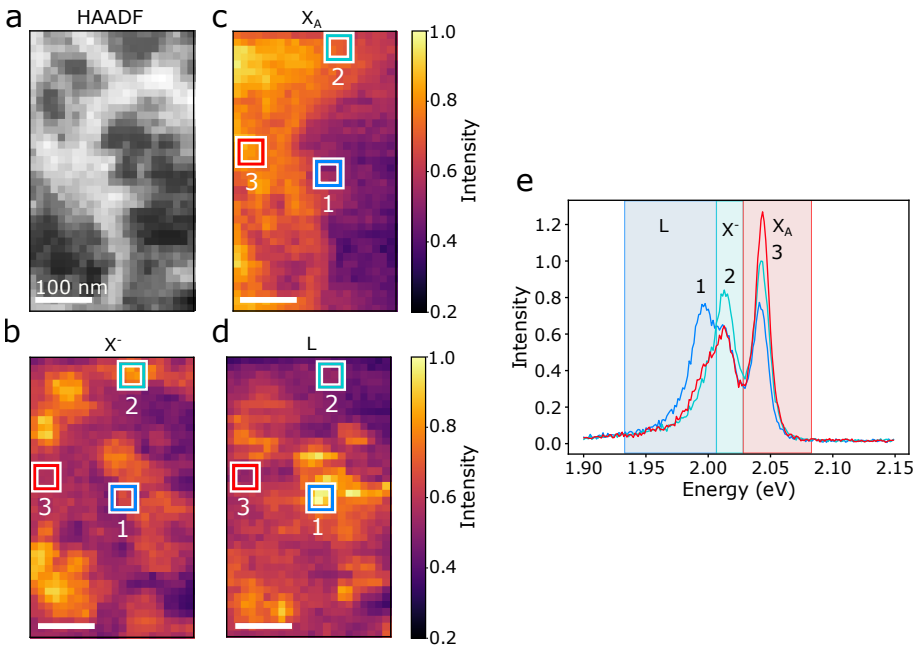

Figure 1.3: Spatially and spectrally resolved CL from a TMD encapsulated monolayer: (a) HAADF image of the area, **(b)** energy-filtered intensity map of the X^- peak, **(c)** of the X_A peak, **(d)** of the L (lower energy) peak, **(e)** spectra extracted from positions 1 to 3. The shaded areas correspond to the energy filters of the (b,c,d) intensity maps. The spectra are normalized.

S(T)EM microscopes have the capability of connecting several signals from small-sized area [18], which can give insights on the physical phenomena occurring at these length scales. The spatial variations of X_A and X^- in the TMD monolayers were linked to chemical changes at the surface of the TMD monolayers, leading to changes in the X_A to X^- emission intensity ratio. The measurements were combined with core-loss EELS measurement that map the chemical elements on the sample and μ-diffraction, to map the local strain. The X^- variations showed a correlation with carbon-rich residues from the sample transfer process.

Preliminary experiments combining CL, EELS and μ-diffraction, have been performed to characterize L emitters and the origin of their localization [15, 19]. Such combination of experiments in the same setup opens the possibility to study many other light-emitting systems and understand the origin of the nanoscale variation of their emission. These experiments can be pushed even further for the single photon emission (SPE) characterization, by coupling them with light-intensity interferometry, such as Hanbury-Brown and Twiss experiment [20, 21].

In the following chapters, I will explore these two systems, the NV centers in nanodiamonds and TMD monolayers, in detail.

Chapter 2

Elements of theory, electron microscopy and spectroscopy

Contents

Matter can be excited in many ways that lead to de-excitation by luminescence, including the optical excitation with photons and the excitation with electrons, that occur through electromagnetic interactions with a sample. These two types of interactions are fundamentally different. In particular, the photons create a direct excitation in the eV range, whereas for the electron excitation, in the energy range of a few tens to a few hundreds of keV, the light emission mediated by bulk plasmon (collective oscillation of free electrons) decay to produce luminescence [22].

When the electron beam crosses a sample, several types of interactions can occur. The interaction between the electrons and the sample leads to various interactions which can be classified in two groups [23]:

1. the elastic scattering, corresponding to the interaction between the incoming electrons and the nuclei of the sample, that leads to contrast in imaging,

2. the inelastic scattering, corresponding to the interaction between the incoming electrons and the electrons of the sample, that can be used for electron spectroscopy, in particular electron energy-loss spectroscopy (EELS).

Once excited, the sample can de-excite through many paths, such as Auger recombination or photon emission. In this work, we are particularly interested in the photon emission of energy in the UV-visible-IR range, which is called photoluminescence (PL) when the sample has been excited by photons, and cathodoluminescence (CL), when the sample has been excited with electrons.

The light-emission of materials can be studied in far-field microscopy, such as in confocal PL microscopy or CL electron microscopy. The advantage of electron microscopy, on top of having sub-wavelength spatial resolution for optical measurements, is the possibility of measuring other spectroscopy signals in the same experiment, such as EELS, or structural signals such as µ-diffraction. Additionally, the scanning transmission electron microscopes (STEM), which use a picometer-sized focused electron beam probe, enable the atomically-resolved imaging, and nanometer sized spectroscopy.

The chapter is organized as follows: first, I present the electron beam and sample interaction, in absorption (EELS) and emission (CL) in section 2.1, which I compare to the all-optical processes in section 2.2, which are absorption of photons and PL. Then, I describe the spectral changes with temperature in section 2.4. Then, I present the STEM microscopes used in this work in section 2.6, with the imaging principle. Finally, I describe the numerical tools, in particular those used for diffraction data processing, in sections 2.7.

2.1 Elastic and inelastic electron scattering

In this section, I describe the elastic and inelastic interactions between the electron beam and the sample. As mentioned in introduction, the elastic scattering comes from the collision between the incoming electron beam and the nuclei of the specimen, with negligible energy exchanges. The inelastic interaction comes from the energy exchanges between the incoming electron beam and the electrons in the sample, possibly leading to large energy losses. The samples need to be thin enough to be electron transparent, and typically have to be thinner than the mean free path of electrons in the material (which is about 50 to 150 nm at 100 keV, depending on

the material). If the sample thickness is large, multiple scattering effects have to be taken into account.

2.1.1 Elastic interaction: image contrast

The elastic scattering is characterized by the means free path and the elastic cross section (σ). The electrons can be scattered at high angle θ by the Coulomb potential of the atoms' nuclei. In elastic scattering, the total kinetic energy and momentum are conserved. At small scattering angles, the energy transfer between the incoming electron beam and the sample is negligible [23].

The differential elastic cross section is defined by the ratio $d\sigma/d\Omega$ where $d\sigma$ is the area from which the incoming parallel electron beam arrive, and $d\Omega$ is the solid angle in which the electrons are scattered. For an incident plane wave scattered into a spherical wave, the elastic differential cross section can be written [23]:

$$\frac{d\sigma(\theta)}{d\Omega} = \frac{\lambda_e^4 Z^2}{64\pi a_0^2 (sin^2(\frac{\theta}{2}) + \frac{\theta_0^2}{2})^2} \propto Z^2 \tag{2.1}$$

Where λ_e is the wavelength of the electron, Z the atomic number of the atom, a_0 the hydrogen bohr radius.

Therefore, the cross section increases with Z, giving rise to a measurable contrast when scanning the beam on a sample and collecting the resulting cross sections for each pixel of the scan.

2.1.2 Inelastic interaction: electron energy-loss spectroscopy (EELS)

The EELS measures the energy of the electrons from the transmitted direct beam. The electron beam is collected with low angle and dispersed in a magnetic prism, which sorts the electrons by kinetic energy [23].

The various inelastic interactions leading to the EELS spectrum are represented in Fig. 2.1.

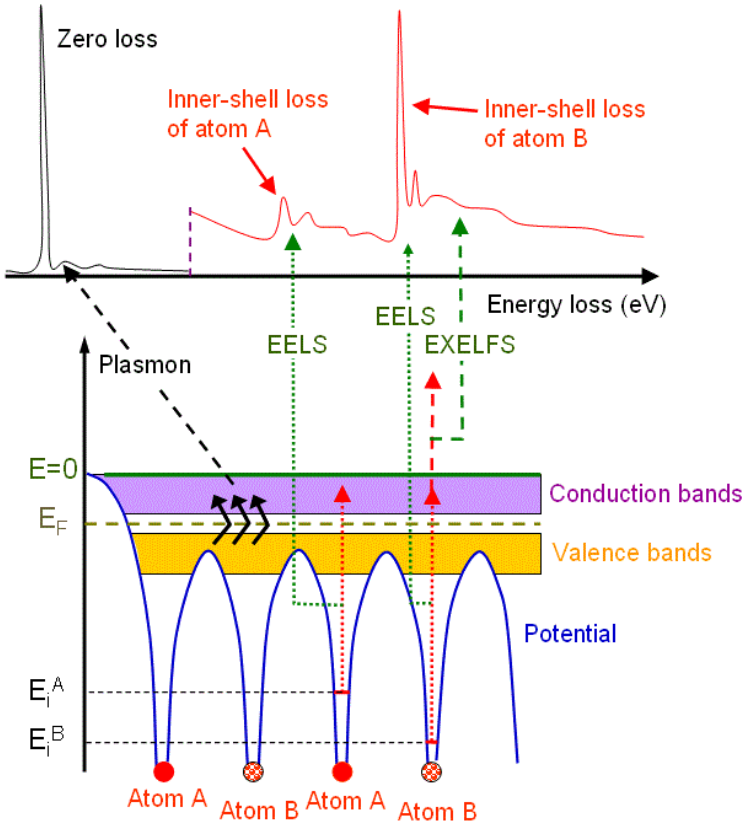

Figure 2.1: Scheme of the EELS principle: the top figure represents an EELS spectrum, where the zero-loss peak, plasmons, and two core-loss spectral features (from atoms A and B) are seen. At the bottom, the band diagram of a seminconducting material is sketched, showing the energy level origin of each EELS spectral feature: the deep electrons excitation give rise to inner-shell edges on the EELS spectrum, whereas the excitation from the valence and conduction band create low-loss spectral features such as plasmons. Reproduced from [24]. (EXELFS: extended energy-loss fine structure)

Most electrons do not exchange energy with the sample. They are contained in the zero loss peak (ZLP) of the EELS spectrum, located at 0 eV. A decreasing tail expands from the ZLP towards the higher energies. Specific spectral features from the sample interaction can be seen. Two energy ranges are distinguished: 0-50 eV is the low-loss range, and >50 eV, the core-loss range. They are described in the two following subsections.

EELS low-loss:

In the low-loss range, the incoming electron beam interacts with the valence electrons of the specimen. Spectral features originating from inter and intra band absorption can be seen.

The most common quasi-particles at play are excitons, plasmons and phonons. They all have resonances in the energy range corresponding to the UV-visible-IR. The excitons are electron-hole pairs bound by Coulomb interaction. Their energy is linked to that of the bandgap of a semiconductor [25]. The plasmons are collective oscillations of electrons in the conduction band. Their energy is linked to the plasma frequency that depends on the number of valence electron per atom [24]. The phonons are crystal lattice oscillations. They have energy in the IR part of the optical spectrum [26].

EELS core-loss for chemical analysis:

The core-loss energy range of the EELS spectrum displays features from the deep core electrons of the sample. Inner-shell ground state levels are typically hundreds to a few thousands of eV below the Fermi energy. They are characterized by the ionization threshold energy, that is characteristic of the chemical elements. The ionization edges are labeled with K, L, M, N and O corresponding to the main quantum numbers n=1-5:

$$E_n = -\frac{R(Z-\sigma_n)^2}{n^2} \tag{2.2}$$

where R=13.6 eV (ionization energy of the hydrogen atom), E_n is the energy position of the ionization edge, and $(Z-\sigma_n)$ is the effective atomic number.

The fine structure located at 0-30 eV after the ionization edge gives information about the valence, hybridization, or site symmetry of the atoms. This fine structure is called energy-loss near edge structure (ELNES). From the unoccupied density of states (DOS) beyond the Fermi energy, and extended energy-loss fine structure (EXELFS) can be seen. It corresponds to weak oscillations of the tail of an edge. The oscillations come from the interference between the outgoing spherical wave of electrons and the backscattered waves at the next neighboring atoms [23].

From the edge intensity (in an energy window Δ), the number of atoms N_a of a chemical element can be estimated with:

$$N_a(\alpha,\Delta) = n_0.\sigma_a(\alpha,\Delta).c_a\frac{N_A}{A_a}.x.exp^{-\frac{x}{x_k(\alpha)}} \tag{2.3}$$

where α is the scattering angle, the number of atoms of element a per unit area is $n_a = c_a N_A x/A_a$, $\sigma(\alpha,\Delta)$ is the partial cross section, $x=\rho t$ is the mass thickness, and $x_k(\alpha)$, the contrast thickness.

The relative number of atoms in a unit area might be less difficult to estimate (ratio method):

$$\frac{n_A}{n_B} = \frac{N_A}{N_B}\frac{\sigma_B(\alpha,\Delta)}{\sigma_A(\alpha,\Delta)} \tag{2.4}$$

where σ_i is the partial cross section of chemical element i.

EELS spectra give information about the excitation process. Once excited, the sample can relax in various ways, such as Auger recombination, X-ray emission, CL etc. In the following, I describe the CL emission principle.

2.1.3 Cathodoluminescence

After exchanging energy with the incoming electron beam, the sample is in an excited state. The mechanism for CL emission has some differences with that of PL, which is described in section 2.2. First, the excitation of the sample comes mainly from the decay of a bulk plasmon, which is of the order of few tens of eV, whereas the lasers used in PL are of a few eV. Second, the electron beam is a non-monochromatic excitation. Here, I discuss the CL excitation mechanism, and the spatial resolution of CL is presented in section 2.1.4. The CL excitation mechanism is described in more

details in [4, 22].

The CL process as a function of time is schematized in Fig. 2.2.

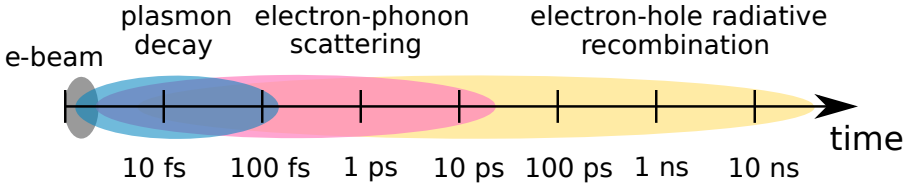

Figure 2.2: Scheme of the time-scale succession of events leading to CL: the electron beam excitation (e-beam, grey) is considered instantaneous. The plasmon decay (blue) occurs typically in the fs time-scale, followed by the electron-phonon scattering (pink), which occurs in the ps time-scale. Finally, the electron-hole recombination occurs typically in the ns time-scale.

First, the electron beam exchanges energy with the sample by exciting electrons in the conduction band of the material. When the excitation energy is high, a bulk plasmon can be created (at least 3 times energy of the the bandgap; in diamond the bulk plasmon is at 30 eV, with E_g=5.5 eV). The bulk plasmon decays into hot electron and hole pairs, in a time scale of typically 1 to 100 fs (Fig. 2.2). They migrate in the sample and start decaying by thermal dissipation (electron-phonon scattering). The radiative recombination occurs when the hot electron and hole pairs have decayed to respectively the bottom of the conduction band and the top of the valence band. The electron and hole pairs that have decayed can bind by Coulomb interaction to form excitons, and the recombination of the exciton produces photons.

For example, in STEM, the inelastic interaction leads to typically 0 or 1 e-h pair above the diamond energy bandgap. Since the CL emission stems from a bulk plasmon excitation, they can decay into several electron-hole pairs, which can excite several excitons or defects. This process creates a photon bunching in the light-intensity statistics, explained in more details in section 2.2.6.

2.1.4 Spatial resolution in EELS and CL

In EELS, the spatial resolution is limited by a number of factors, including (i) the probe size, (ii) the Coulomb field generated by the incident electron beam, and (iii) the spatial extension of the excitation in the sample [27]. The probe size (i), with the use of aberration-corrected electron microscopes, is now smaller than the Angström [28]. The delocalization of the Coulomb field generated by the incident fast electron beam (ii) can be roughly estimated by the Coulomb adiabatic parameter $v/\hbar\omega$, where v is the electron speed, which is typically $0.5c$, and ω corresponds to the energy of the transition measured. For example, for a 2 eV transition excited with a 100 keV electron beam, this gives a 40 nm spatial resolution. Then the nature of the excitation inside the sample itself can have a spatial extension, for example, a core-loss transition, corresponding to a large energy transfer, is localized at the atoms [29]. Smaller energy transfer, such as conduction- and valence-band excitations, including phonons, plasmons or excitons, can have a spatial extension up to hundreds of nm. Contrast in the loss signal can still be seen at the interface between different materials, down to 10 nm in TMD lateral heterostructures [30]

In CL for seminconductors, the spatial resolution is limited by the charge-carrier diffusion and the presence of recombining traps. The CL spatial resolution generally

depends on the probe size, the probe broadening through propagation, the excitation peak and the charge-carrier diffusion. For thin samples in STEM, the charge-carrier diffusion is dominant [4]. The best spatial resolution reported is of the order of 4 nm in quantum wells of AlN/GaN [31]. For TMDs (see chapters 5 and 6) this depends on the presence of efficient charge-carrier recombination centers.

Fig. 2.3 displays an example of comparison between the spatial resolution in EELS and in CL.

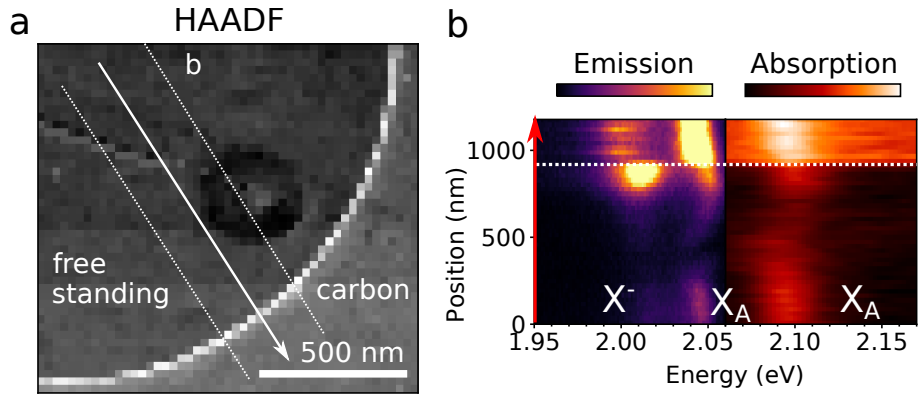

Figure 2.3: Illustration of the spatial resolution difference between EELS and CL: (a) ADF image of the area, with the arrow showing the position of the spectral profile extraction, **(b)** spectral profiles extracted from the CL (left) and EELS (right) data.

On top of the crack, along the energy profiles, the CL is seen to be quenched. This decrease in CL intensity is seen few tens of nm away from the crack. In EELS, no decrease of intensity is seen, even on top of the crack, the signal is measured.

2.2 Light-matter interaction

In this section, I describe the specificity of light-matter interaction in the case of photon excitation, instead of electrons. The PL emission occurs in the UV-visible-IR range. The mechanism leading to it might differ for various materials. In this section, I describe the PL absorption and emission of a semiconductor, which occurs typically at an interband transition. The principle of the absorption and emission described here is also valid, to some extent, for light-emitting point defects.

2.2.1 Absorption

Here, I describe the absorption of a photon, which has negligible momentum ($\omega/c = k$). In the band diagram, this corresponds to a vertical transition.

The interband absorption in semiconductors typically leads to PL emission. The electrons are excited from the filled valence band to an empty conduction band state by absorption of a photon. The absorption process is sketched in Fig. 2.4.

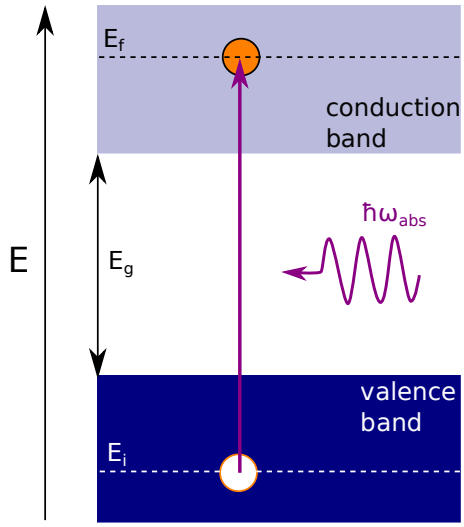

Figure 2.4: Scheme of the absorption process: the band structure of a semiconductor with gap energy E_g is represented. An incoming photon of energy $\hbar\omega_{abs} > E_g$ excites an electron from the filled valence band to an empty state in the conduction band.

The energy conservation can be written: $E_f = E_i + \hbar\omega_{abs}$, with $\hbar\omega_{abs} > E_g$. For a direct bandgap semiconductor, the absorption coefficient α corresponds to the quantum mechanical transition rate $W_{i\to f}$ from the Fermi's golden rule [25]:

$$W_{i\to f} = \frac{2\pi}{\hbar}|M|^2 g(\hbar\omega) \tag{2.5}$$

where M is the matrix element and $g(\hbar\omega)$ is the density of states. Transition of the electron wavefunction from ψ_i to ψ_f the matrix element is defined by:

$$M = \langle f|H'|i\rangle = \int \psi_f^*(\overrightarrow{r})H'(\overrightarrow{r})\psi_i(\overrightarrow{r})d^3\overrightarrow{r} \tag{2.6}$$

where H' is the perturbation operator associated with the light wave.

$$H' = -\overrightarrow{p_e}.\overrightarrow{E}_{photon} \tag{2.7}$$

where $\overrightarrow{p_e}$ is the dipole moment of the electron ($\overrightarrow{p_e} = e.\overrightarrow{r}$), and E_{photon} is the perturbing field.

The process described above is valid for a direct bandgap semiconductor. For indirect bandgap semiconductor, the momentum conservation involves the absorption or emission of phonons. This leads to heating, which is often unwanted, and direct bandgap semiconductors are preferred.

Once excited, the material can relax by many paths including the emission of photons (PL), which is described in the next section.

2.2.2 Photoluminescence

Photoluminescence is the re-emission of light after absorbing a photon of higher energy. It comes from the annihilation of an electron-hole pair by emission of a photon. The process is determined by the spontaneous emission A Einstein coefficient.

A scheme of the interband emission of a semiconductor in is Fig. 2.5.

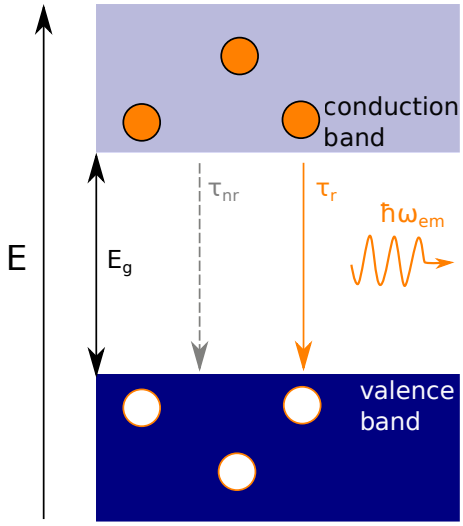

Figure 2.5: Scheme of the PL emission process: the band structure of a semiconductor with gap energy E_g is represented. The electrons occupying states in the conduction band relax by annihilation with holes in the valence band. This process leads to photon emission with characteristic time τ_r. The electrons can also relax by non-radiative means, such as Auger recombination or defect trapping, with characteristic time τ_{nr}.

The excited material can de-excite through various path, which are noted *r* for radiative, and *nr* for non-radiative. The non-radiative decay paths can be scattering with phonons. They are typically faster than the electron-hole recombination, and occur in the ps time-scale. A time-scale of the processes involved is sketched in Fig. 2.6.

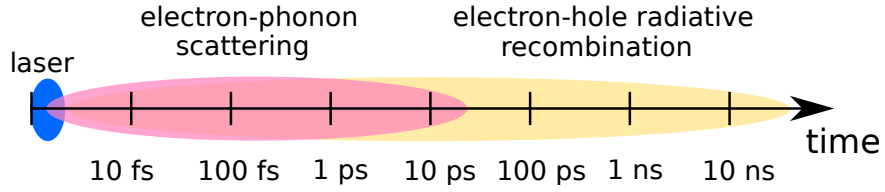

Figure 2.6: Scheme of the time-scale succession of events leading to PL: the laser excitation (blue) is considered instantaneous. The electron-phonon scattering (pink) occurs typically in the ps time-scale. Then, the electron-hole recombination occurs in the ns time-scale.

The shape of the emission spectrum is affected by the thermal distribution of electrons and hole within their bands. The spontaneous emission rate between two levels corresponds to the Einstein A coefficient:

$$\left(\frac{dN}{dt}\right)_{rad} = -A.N \tag{2.8}$$

where N is the excited state population at time t. The radiative decay time is linked to the A coefficient by $\tau_r = A^{-1}$. The absorption B coefficient is proportional to the A (spontaneous emission) coefficient. This implies that a good emitter is also a good absorbing material.

The absorption and emission spectra differ even if A and B are proportional due to the population factors. The luminescence intensity $I(h\nu)$, from Fermi's golden rule is given by:

$$I(h\nu) \propto |M|^2 g(h\nu) \times l \tag{2.9}$$

where ν is the frequency, M, the matrix element, $g(h\nu)$, the DOS of the transition and l is the level occupancy factor (the probability that the relevant upper level is occupied and the lower level is empty).

Light emitted between the electron and hole states that are thermally occupied and are in a narrow energy range. It contrasts with the absorption spectrum, where the photon can be absorbed to any state within the excited state band.

The excited state can also relax through non radiative processes, such as heat dissipation or trapping. This modifies the radiative decay rate η_r:

$$\eta_r = \frac{AN}{N\left(\frac{1}{\tau_r} + \frac{1}{\tau_{nr}}\right)} = \frac{1}{1 + \frac{\tau_r}{\tau_{nr}}} \tag{2.10}$$

For a direct bandgap semiconductor, the transition probability is high, and the radiative lifetime is typically of few to tens of ns. The momentum of photons being negligible compared to that of the electron, the electron and hole that recombine must have the same $\overrightarrow{k}$ (corresponding to a vertical transition).

For an indirect bandgap semiconductor, the maximum of the valence band and the minimum of the conduction band are not at the same position in the first Brillouin zone (FBZ), meaning that a phonon must be implied for momentum conservation. This being a 2^{nd} order process, the transition probability is low and the indirect bandgap semiconductors are poor emitters.

2.2.3 Stokes shift

The term Stokes shift comes from molecular physics, and it refers to the energy difference between the maximum of absorption of a molecule and the maximum of emission (PL) of the same molecule. In that case, instead of having valence and conduction band, the energy levels are discrete, and called HOMO (highest occupied molecular orbital) and LUMO (lowest unoccupied molecular orbital), as sketched in Fig. 2.7.

If there were only the HOMO and LUMO levels, both absorption (promotion of an electron from HOMO to LUMO) and emission (de-excitation from LUMO to HOMO) would be at the exact same energy, thus no Stokes shift would be seen. This is the case for a particular peak, called zero phonon line (ZPL). For the energy difference between absorption and emission, one has to consider the phonon levels of the molecular orbitals.

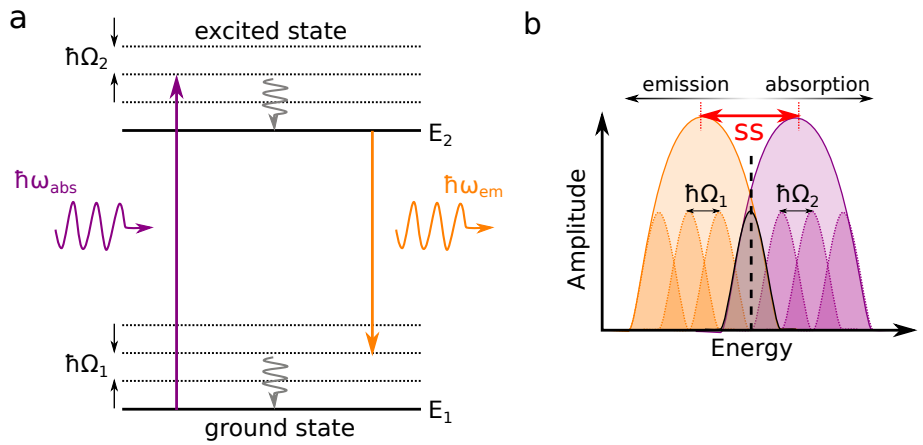

Figure 2.7: Scheme of the excitation and de-excitation process in optics for a two-level molecular system: (a) energy-level scheme of the process. A photon is of energy $\hbar\omega_{abs} > (E_2 - E_1)$ is absorbed. **(b)** emission (orange) and absorption (purple) spectra produced, with the subcomponents of the spectra plotted. The maximum of each curve is separated by the Stokes shift (SS) highlighted with a double red arrow. The zero phonon line (ZPL) is highlighted in grey.

This scheme is valid for isolated atoms, molecules or point-defects in solids.

In the case of materials, with energy bands instead of discrete levels, the origin of the Stokes shift is not as straightforward. The splitting between the absorption and emission bands can originate from various phenomena, including doping, strain etc.

2.2.4 Purcell effect

The Purcell effect corresponds to the weak coupling between an emitter and a cavity. It causes a change in the photonic density of states (PhDOS). The PhDOS measures how efficiently an oscillator transfers energy to its environment.

The Purcell factor F can be described by:

$$F = \frac{4}{4\pi^2}\left(\frac{\lambda}{n}\right)^2 \cdot \left(\frac{Q}{\Omega_{cav}}\right) \tag{2.11}$$

where λ is the wavelength of the light, n, the refractive index of the material at that wavelength, Q, the quality factor of the cavity, and Ω_{cav}, the volume in which the light is confined.

The transition rate enhancement factor γ is: $\gamma = \rho(r,\omega)/\rho_0(r,\omega)$, where ρ_0 is the PhDOS for the free structure, and $\rho(r,\omega)$ is that inside the cavity.

The transition rate enhancement induces a lifetime broadening [32]. From the relation $\Delta E \Delta t \gtrsim \hbar$, which is linked to the lifetime τ with $\Delta t = \tau$, the lifetime broadening $\Delta\omega_{lifetime}$ can be written:

$$\frac{1}{\tau} = \Delta\omega_{lifetime} \tag{2.12}$$

The transition rate $\frac{1}{\tau}$ is linked to the energy linewidth ΔE by:

$$\Delta\omega_{lifetime} = \frac{\Delta E}{\hbar} \tag{2.13}$$

The intrinsic lineshape function is a lorentizan centered on the energy of the transition and with linewidth $\Delta\omega$:

$$g_\omega(\omega) = \frac{\Delta\omega}{2\pi} \frac{1}{(\omega - \omega_0)^2 + \left(\frac{\Delta\omega}{2}\right)^2} \tag{2.14}$$

The lifetime broadening in solids comes from the presence of non-radiative transitions (e.g. the emission of phonons instead of photons):

$$\frac{dN}{dt} = -AN - \frac{N}{\tau_{nr}} = -(A + \frac{1}{\tau})N \tag{2.15}$$

The new expression for radiative lifetime is: $\frac{1}{\tau} = A + \frac{1}{\tau_{nr}}$, where τ is shorter than previously.

The environmental broadening is also to take into account, and it corresponds to the local environment in which the excitons find themselves. This shifts the energy of the transition, and for an ensemble of emitters at various positions, it results in a broadened emission peak.

The coupling with phonon leads to peaks from phonon replicas, which also broaden the PL spctra (cf Franck-Condon). The Huang-Rhys S factor is a way of characterizing the coupling between the electrons and phonons for a defect. It indicates the average phonons emitted during an electronic transition. $S = \frac{\Delta}{2\hbar\omega}$ [33], where Δ is the stokes shift, and $\hbar\omega$ is the mean phonon energy.

2.2.5 Photoluminescence excitation (PLE)

The PLE measurements probe the joint density of states of a particular excited state - ground state transition. This gives information about the excitation and de-excitation paths that lead to PL of a particular transition.

The process is the following: a laser is scanned in energy on a sample, and for each wavelength, the intensity emitted is recorded at a particular energy. Examples of PLE measurements are shown in chapter 4, where the experiment is used to understand the charge transfer in nitrogen-vacancy centers in nanodiamonds.

2.2.6 Light-intensity interferometry

The photon emission statistics of a light source can give information about the nature of that source. In particular, light intensity interferometry is often used to probe single photon emitters, which have a particular signature explained in the following.

The light statistics can be probed by measuring the second order correlation function, also referred to as the autocorrelation function. Its expression is :

$$g^{(2)}(\tau) = \frac{\langle I_1(t) I_2(t+\tau) \rangle}{\langle I_1(t) \rangle \langle I_2(t) \rangle} \tag{2.16}$$

Where I_1 is the intensity measured in the detector 1, and I_2 in detector 2 (the scheme of the setup is displayed in Fig. 2.9). τ is the delay between two detected photons, when the first photon was detected at time t.

The profile of $g^{(2)}(\tau)$ differs for various types of photon sources:

- Coherent light (e.g. monochromatic laser) for a coherent state $|\alpha\rangle$ such as $a|\alpha\rangle = \alpha|\alpha\rangle$, where $g^{(2)}(\tau) = 1$, which is independent of τ.
- Thermal light (e.g. Doppler widening of gas molecules in motion), in this case $g^{(2)}(\tau) = 1 + |g^{(1)}(\tau)|^2 \geq 1$ At $\tau = 0$, it can be shown that $g^{(2)}(0) = 2$ and decreases at higher delay. This behavior is called photon bunching.
- Single photon sources: they are better described in terms of photon number n_1 and n_2, detected in detector 1 and 2 respectively, since they emit one photon at a time:

$$g^{(2)}(\tau) = \frac{\langle n_1(t) n_2(t+\tau)\rangle_t}{\langle n_1(t)\rangle_t \langle n_2(t)\rangle_t} \tag{2.17}$$

The autocorrelation function can then be defined by the probability of detecting photons at times t and τ as:

$$g^{(2)}(\tau) = \frac{P(t|t+\tau)}{P(t)^2} = \frac{P(t+\tau|t)}{P(t)^2} \tag{2.18}$$

where P are the probabilities of detecting photons at time t and t + τ.

The $g^{(2)}(\tau)$ expression becomes:

$$g^{(2)}(\tau) = 1 - e^{-(r+\Gamma).\tau} \leq 1 \tag{2.19}$$

where r is the pumping rate, and Γ is the radiative recombination rate. It can be shown that at $\tau = 0$, the $g^{(2)}(0) = 0$ which is a specificity of single photon sources This behavior is known as anti-bunching.

Examples of $g^{(2)}(\tau)$ for the various source types are displayed in Fig. 2.8.

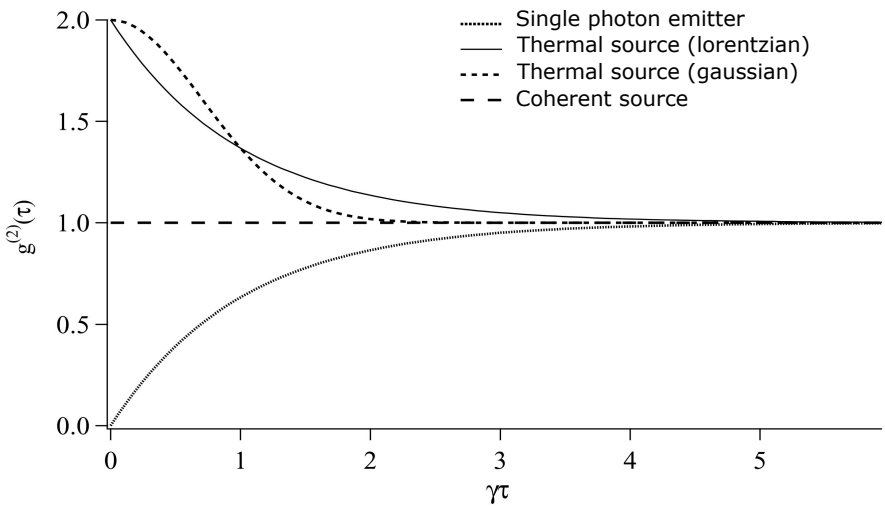

Figure 2.8: Intensity autocorrelation function ($g^{(2)}(\tau)$): represented for several types of sources, single photon emitters (dotted line), Lorentzian thermal source (continuous line), Gaussian thermal source (dashed line), and coherent source (horizontal dashed line). Reproduced from [34].

The photon sources cited above are the usual light sources cited. Cathodoluminescence follows a different emission process. Indeed, as described in section 2.1, the CL emission is mediated by a bulk plasmon, which can excite several defects into emitting light at the same time. This leads to a $g^{(2)}(\tau = 0)$>1, corresponding to photon bunching, that can be expressed as [22]:

$$g^{(2)}(\tau) = \frac{I_0}{I}\frac{\lambda_e}{Le^{-L/\lambda_e}}\left(1-\frac{1}{N}\right)e^{-\tau/\tau_e} + \left(1-\frac{1}{N}e^{-\tau/\tau_e}\right) \tag{2.20}$$

where L is thickness of the sample, N, the number of emitters, λ_e, the mean free path of the bulk plasmon, τ_e, the lifetime of the quantum emitters and $I_0 = e/\tau_e$, the normalization factor corresponding to typically one incoming electron per lifetime. From this expression, one can see that the lifetime τ_e can be recovered by exponential fitting.

The autocorrelation function is often measured with a Hanbury-Brown and Twiss (HBT) setup, sketched in Fig. 2.9.

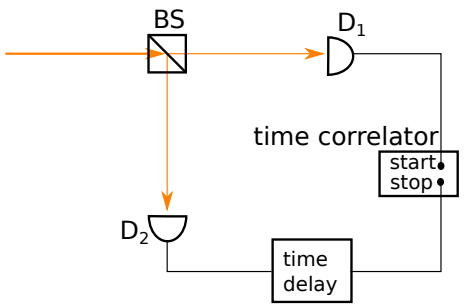

Figure 2.9: Scheme of the HBT setup used for the $g^{(2)}(\tau)$ measurement: the light arrives at a 50/50 beamsplitter (BS) that divides the beam in two paths, leading to the two detectors (D_1, D_2). The time correlator treats the start and stop signals triggered by the detection of a photon in the detectors. The time delay is a long cable that allows for measuring $g^{(2)}(\tau)$ at negative times.

The HBT setup principle is the following: two detectors are put on two detection arms separated by a beamsplitter. When a photon is detected in D_1, it sends a start, and the next photon detected in D_2 sends a stop. An histogram of the delay between the start and stop values, τ, is then build point by point. The negative part of the autocorrelation function is measured by introducing an electronic time delay by using a long (here, 23 m) cable, that introduces a delay (here, 120 ns).

2.2.7 Non-radiative relaxation

Sections 2.1.3 and 2.2.2 have detailed the radiative decay processes for PL and CL emission. Other types of light emission, not relevant for this thesis, exist, such as phosphorescence (from inter-system crossing with forbidden optical transition, which makes them long-lived and emit light for times up to several hours), or electroluminescence (EL), which excitation consists of electrically injecting electrons and holes into the light emitting material, which can then recombine radiatively.

On top of radiative decay paths, which lead to photon emission, non-radiative paths exist. The most common non-radiative recombination for excitons are (i) Auger recombination (exciton-exciton annihilation without photon emission), (ii) phonon emission, and (iii) trapping in defects [35, 36]. These processes are not detailed since they are of low interest in the frame of this thesis. They might lead to changes in radiative lifetime of emitters, but can directly be added as τ_{nr} (nr for non-radiative) in the equations.

2.3 Comparison electron spectroscopy-optics

2.3.1 EELS

The electromagnetic response of a material is often described by the dielectric function $\epsilon(\omega) = \epsilon_1(\omega) + i\epsilon_2(\omega)$. The dielectric function is linked to the complex refractive index $\tilde{n}(\omega) = n(\omega) + i\kappa(\omega)$ by $\tilde{n}^2(\omega) = \epsilon(\omega)$. In optics, $\epsilon(\omega)$ can be extracted from differential reflectance.

For atomically thin materials, the EELS is directly proportional to the imaginary part ϵ_2 of the dielectric function.

2.3.2 Optical absorption

The optical absorption can be measured by measuring the light transmitted across a thin sample from a white light source. Part of the light is also reflected at the interface between the media. In optics, the absorption A gives information about:

$$A = 1 - R - T \tag{2.21}$$

Where R is the reflectance [25]:

$$R = \left|\frac{\tilde{n}-1}{\tilde{n}+1}\right|^2 = \frac{(n-1)^2+\kappa^2}{(n+1)^2+\kappa^2} \tag{2.22}$$

and the transmittance T is:

$$T = (1 - R)^2 . e^{-\alpha \ell} \tag{2.23}$$

where α is the absorption coefficient $\alpha = \frac{4\pi\kappa}{\lambda}$.

The formalism described above is valid for macroscopic systems, and fails for $\lambda \geq t$ where t is the thickness of the sample. In nano-optics, we use both the electromagnetism and quantum optics formalism to tackle this issue (such as in section 2.2). Here, to estimate the number of photons emitted for a single photon excitation, we arbitrarily estimate that the photon absorption is of the order of 1 %, which is a usual value for absoprtion of nanoscale materials [37]. A precise value can be obtained by directly using the absorption spectrum of the nanoscale material.

2.3.3 Estimation of the number of photons emitted from a single excitation

Here, as an example, I use the parameters of nanodiamonds of about 50 nm (similar to the ones used in Chap. 3 and 4).

From a photon excitation:

The PL absorption process has been described in 2.2.2. Here I detail the steps of the process and estimate the probability of each step. The final result is then the product of all steps probabilities.

(i) absorption (estimation of 1% absorption):

$$P_{abs} \approx 0.01 \tag{2.24}$$

(ii) charge diffusion (negligible) [22]:

$$P_{diff} \approx 1 \tag{2.25}$$

(iii) radiative recombination:

$$P_{rad} = e^{-t/\tau} \tag{2.26}$$

if we look at the typical number of emitted photons, during the lifetime ($\Delta t = \tau$), $P_{rad} \approx 0.63$.

Which gives:

$$P_{abs} \times P_{diff} \times P_{rad} \approx 6.3.10^{-3} \text{ photons} \tag{2.27}$$

From an electron excitation:

The CL emission process has been described in 2.1.3. From reference [22], we calculate the probability of emitting a photon from a single electron excitation, in nanodiamonds.

(i) creation of n bulk plasmons:

$$P_{el}^{n} = \frac{1}{n!}\left(\frac{L}{\lambda_e}\right)^{n}.e^{-L/\lambda_e} \tag{2.28}$$

The parameter L/λ_e is the ratio of the thickness crossed by the electron to its mean free path for plasmon excitation. It can be estimated from EELS data [22], and for nanodiamonds, is about 1.8. We can now estimate the probability P_{el}^{n} of creating n=1, 2 and 3 plasmons:

$$\begin{aligned} P_{el}^{1} &= 0.2975 \\ P_{el}^{2} &= 0.2678 \\ P_{el}^{3} &= 0.1607 \end{aligned} \tag{2.29}$$

The probability of forming n plasmons falls below 0.1 % for n>8, and tends to 0 for $n \to \infty$.

(ii) decay of the plasmon into e-h pairs (I use the plasmon energy for diamond $E_{plasmon} \approx 30$ eV, and the badgap energy of the diamond, which is about 5.5 eV):

$$P_{e-h} \approx \frac{E_{plasmon}}{E_g} \approx 6 \text{ e-h pairs/plasmon} \tag{2.30}$$

(iii) charge diffusion (negligible) [22]:

$$P_{diff} \approx 1 \tag{2.31}$$

(iv) radiative recombination:

$$P_{rad} = e^{-t/\tau} \tag{2.32}$$

if we look at the typical number of emitted photons, during the lifetime ($t = \tau$), $P_{rad} \approx 0.63$.

Which gives:

$$\sum_{n=1}^{\infty} P_{el}^{n} \times n.P_{e-h} \times P_{diff} \times P_{rad} \approx 6.7 \text{ photons} \tag{2.33}$$

2.3.4 Overall comparison

A comparison between the signals measured in CL and EELS, and that measured in differential reflectance and ouf-of-resonance PL for an h-BN encapsulated 2D semiconductor (WS_2 monolayer) is shown in Fig. 2.10.

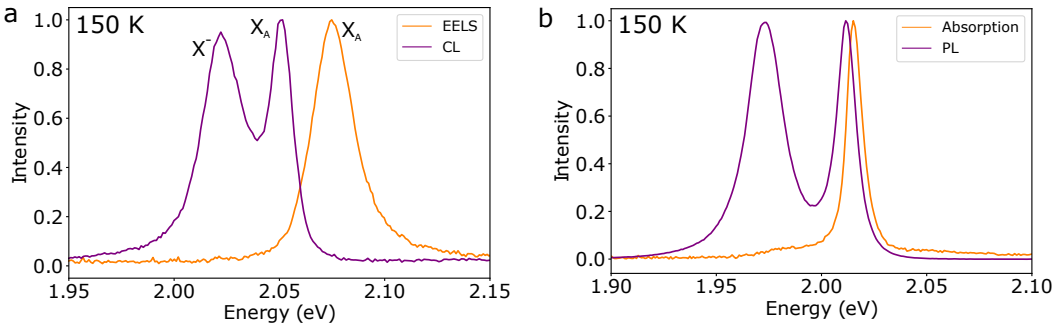

Figure 2.10: Comparison between spectra: (a) from electron excitation **(b)** from pure optical excitation. The measurements are done on encapsulated WS_2 monolayers at 150 K, performed on two different samples. The optical measurements curves (PL and absorption) were reproduced from [38] with permission.

As displayed in the figure, the spectra are similar for PL and CL, and for differential reflectance and EELS low-loss. The measurements were performed on different h-BN encapsulated WS_2 monolayers at 150 K, which explains the energy shift between the two measurements. The EELS energy position has precison of about 1 %, which can participate to the large Stokes shift in the CL and EELS figure.

2.4 Spectral changes with temperature

Light emission variations linked to the temperature change are investigated in chapter 4 and 5. In this section, I describe the general spectral changes expected for light emitters at different temperatures.

Examples of varying parameters with temperature are illustrated in Fig. 2.11.

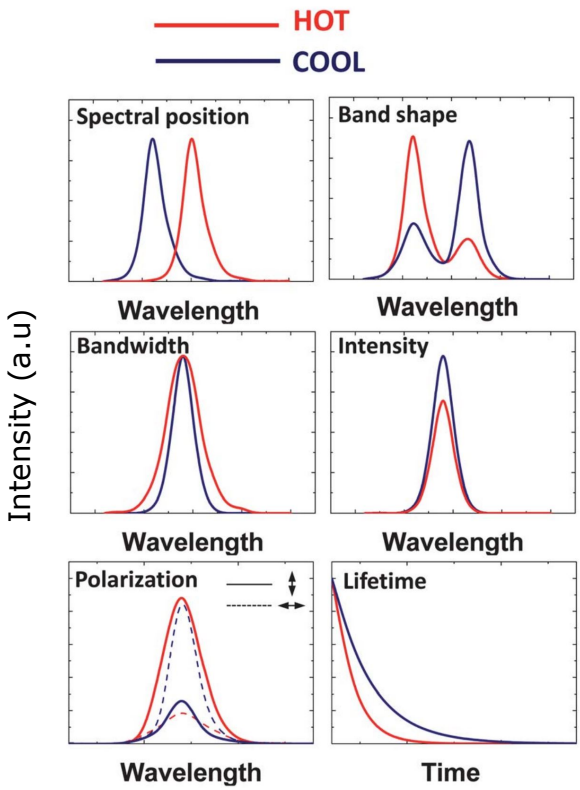

Figure 2.11: Representation of the effect of temperature on light emission for a normal semiconductor or a molecule: higher temperature (red) and lower temperature (blue) are shown. Reproduced from [39].

In particular, the lifetime τ dependence with temperature is:

$$\tau = \frac{1}{P_r + P_{nr}} = \frac{1}{\tau_0^{-1} + k \exp\left(-\frac{\Delta E}{k_B T}\right)} \tag{2.34}$$

where P_r is the probability of de-excitation by emitting light, and P_{nr} is the probability of de-excitation without light emission. ΔE is the energy difference between the emitting level and the excited state.

The lifetime shortening with temperature is linked to the intrinsic linewidth widening, since the linewidth is $\Delta\omega_{lifetime} = \frac{1}{\tau}$. It expands the lorentzian peak function $g_\omega(\omega)$:

$$g_\omega(\omega) = \frac{\Delta\omega}{2\pi} \frac{1}{(\omega - \omega_0)^2 + \left(\frac{\Delta\omega}{2}\right)^2} \tag{2.35}$$

This leads to the intensity lowering (due to creating of non radiative decay channels, such as scattering with phonons) [40]:

$$I \propto gAE \exp\left(-\frac{E}{k_B T}\right) \tag{2.36}$$

where g is degeneracy of states, A the spontaneous emission rate, and E the energy of the level.

2.5 Diffraction measurements

The diffraction measurements can give information about the strain in a sample. The deformation of the lattice deforms the diffraction pattern, which can be measured. The link between lattice deformation with the diffraction spots displacements is detailed in this section, as well as the numerical data processing with the pyxem [41] python library, and the specificity of the measurements performed on different microscopes.

In a crystal lattice, the conditions for constructive interference are given by the Bragg condition:

$$2.d_{hkl}.\sin(\theta_B) = \lambda \tag{2.37}$$

where d_{hkl} is the inter plane distance, θ_B the diffraction semi-angle, and λ is the wavelength of the electrons.

The measurement of θ_B in the diffraction plane allows to recover the interplanar distance, which give information about the lattice atoms displacement.

2.5.1 Displacement and rotation matrices

The decomposition described here is the same (right-handed polar decomposition) performed by the pyxem software that I used, presented in the next section.

Deformation gradient:

The deformation gradient matrix F is the derivative of each component of the deformed vector $\vec{a} = x\vec{i} + y\vec{j}$ (in the orthonormal basis $(0,\vec{i},\vec{j})$), with respect to each component of the reference vector $\vec{A} = X\vec{i} + Y\vec{j}$:

$$F_{mn} = \frac{\partial a_m}{\partial A_n} \tag{2.38}$$

Where m and n are the indexes of the directions in space. For a 2×2 matrix, corresponding to the 2D case, the deformation matrix is:

$$F = \begin{pmatrix} \frac{\partial a_x}{\partial A_x} & \frac{\partial a_x}{\partial A_y} \\ \frac{\partial a_y}{\partial A_x} & \frac{\partial a_y}{\partial A_y} \end{pmatrix} \tag{2.39}$$

The displacement vector $\vec{u}$ is defined by the difference $\vec{u} = \vec{a} - \vec{A}$. Its derivative then is the displacement gradient tensor:

$$\begin{aligned} F &= \frac{\partial}{\partial \vec{A}}(\vec{A} + \vec{u}) \\ &= \frac{\partial}{\partial \vec{A}}\vec{A} + \frac{\partial}{\partial \vec{A}}\vec{u} \\ &= \mathbb{1} + \frac{\partial \vec{u}}{\partial \vec{A}} \end{aligned} \tag{2.40}$$

$$F = \begin{pmatrix} \frac{\partial(x-X)}{\partial X} & \frac{\partial(x-Y)}{\partial Y} \\ \frac{\partial(y-X)}{\partial X} & \frac{\partial(y-Y)}{\partial Y} \end{pmatrix} \tag{2.41}$$

Polar decomposition:

From the displacement gradient tensor, one can retrieve the deformation matrix and the rotation matrix. The process to seperate both contributions is called polar decomposition, and can be performed two ways: by considering first a deformation then a rotation: $F = V.R$ (left-handed decomposition) or the opposite, first a rotation then a deformation $F = R.U$ (right-handed decomposition), where U and V are the deformation matrices, and R the rotation matrix.

Rotation matrix:

The rotation matrix R is defined by:

$$R = \begin{pmatrix} \cos\theta & -\sin\theta \\ \sin\theta & \cos\theta \end{pmatrix} \tag{2.42}$$

From the R matrix, the angle θ is extracted.

Right-handed polar decomposition:

The deformation matrix is symmetric $U^T = U$. The decomposition can be performed in the following way:

$$\begin{aligned} F^T.F &= (R.U)^T.(R.U) \\ &= U^T.R^T.R.U \\ &= U^T.U \\ &= U.U \end{aligned} \tag{2.43}$$

Then the square root of the matrix has to be taken to retrieve U. The rotation matrix can then be found by performing $F.U^{-1} = (R.U).U^{-1} = R$.

Strain tensor:

Two types of strain exist, the "normal" strain ϵ, that accounts for elongations and contractions, and the shear strain γ. They are respectively defined by:

$$\begin{aligned} \epsilon_{ii} &= \frac{\partial u_{ii}}{\partial A_{ii}} \\ \gamma_{ij} &= \frac{\partial u_i}{\partial A_j} + \frac{\partial u_j}{\partial A_i} \end{aligned} \tag{2.44}$$

The normal strain is on the diagonal components, whereas the shear strain is the off-diagonal component. The strain tensor is symmetrical, for a 2×2 matrix there is only one shear strain component $\gamma_{xy} = \gamma_{yx} = \gamma$.

The 2D strain tensor is:

$$\epsilon = \begin{pmatrix} \epsilon_{xx} & \gamma/2 \\ \gamma/2 & \epsilon_{yy} \end{pmatrix} \tag{2.45}$$

The Pyxem library [41] uses a different strain tensor, since the shear strain components in 2.45 are redundant:

$$\epsilon_{pyxem} = \begin{pmatrix} E_{11} & E_{22} \\ E_{12} & \theta \end{pmatrix} \tag{2.46}$$

Where 1 and 2 correspond to the two orthogonal in-plane directions (here $x = 1$ and $y = 2$). This way, all the information from the deformation and rotation are compacted into one single matrix for in-plane measurements. The data processing of diffraction images are described in the next section.

2.5.2 Data processing with the Pyxem package

The pyxem package has been used to process all the µ-diffraction data of chapter 5 and 6. It allows for the retrieval of the strain components from a 4D image dataset containing a diffraction pattern in each pixel of the area scanned [41]. The steps in processing are detailed in the following.

The first step is the alignment of the center of the beam, which is done with pyxem with a cross correlation method (between the position of the beam of the first pixels and that in the others). This process is illustrated in Fig. 2.12a,b. It is composed of two steps: the cross-correlation within the radii, which aligns the direct beam for each diffraction picture, and then the alignment of the beam center to the origin coordinates of the image.

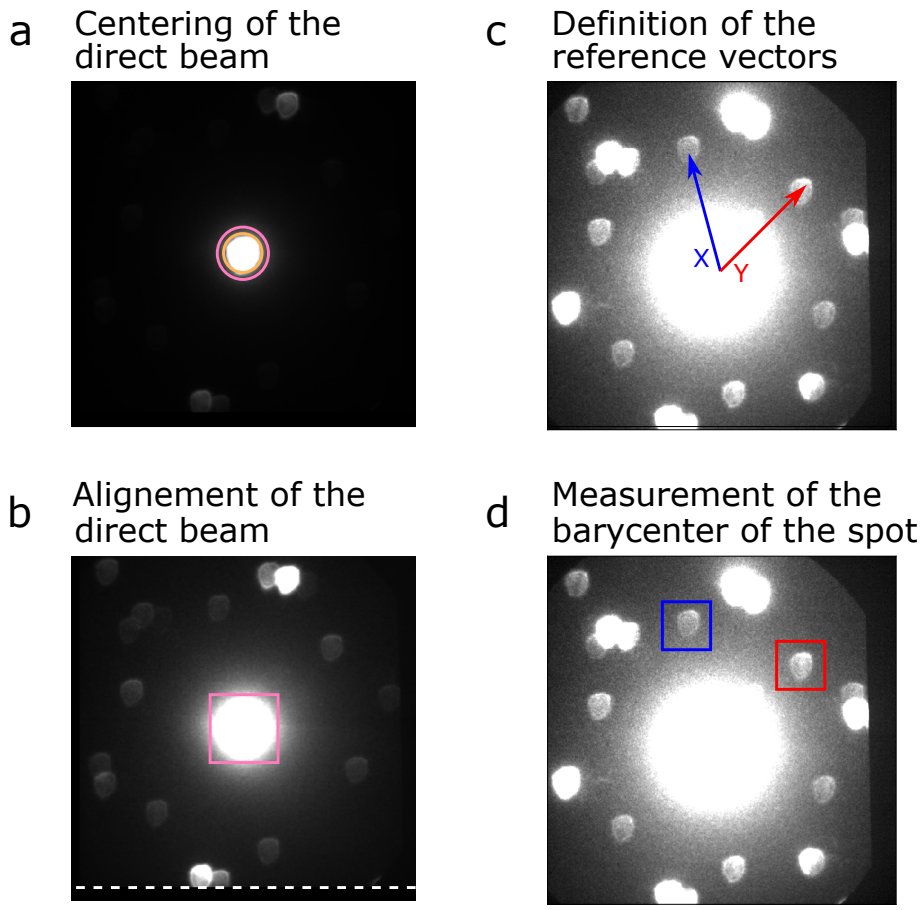

Figure 2.12: Illustration of the diffraction data treatment: (a) the center beam is aligned using a cross-correlation method selected by the circles (orange and pink), **(b)** then centered to the image origin using the pink square area. **(c)** The reference vectors X and Y (in blue and red) are defined, and **(d)** the barycenter of the square areas (blue and red) are measured. From the extracted values of the deformed vectors x and y, the strain tensor is recovered. The saturation of the images is varied for visibility.

The reference vectors $\vec{X}$ and $\vec{Y}$ are calculated vectors with the reciprocal space length and orientation for unstrained WS_2. The right-handed polar decomposition described in the previous section is then used to separate the deformation U and rotation R matrices. The results obtained are put in the ϵ_{pyxem} matrix (which actually is a BaseSignal hyperspy object), containing the two in-plane strain parameters, the shear strain and the rotation angle.

The principal limit of this method is the determination of the deformed vectors $\vec{x}$ and $\vec{y}$ using the barycenter of the diffraction spots. Here, since the measurement is done in µ-diffraction with a convergent electron beam (CBED), the spots are large (tens of pixels). The change in illumination (that can arise from the orientation or thickness change of the substrate) can displace the barycenter, thus artificially changing $\vec{x}$ and $\vec{y}$.

2.5.3 Alignment of the microscope (experimental tricks)

The diffraction experiments have been performed in the ChromaTEM and the UltraSTEM, which are presented in section 2.6. The convergence angle used were between few µrad and 5 mrad in both cases, leading to beam spot sizes of few

nanometers to a hundred nanometer. As illustrated in Fig. 2.13, the smaller convergence angle leads to the smaller spots in diffraction. As explained in the previous section, smaller spots are preferred since the illumination is less subject to artificial changes.

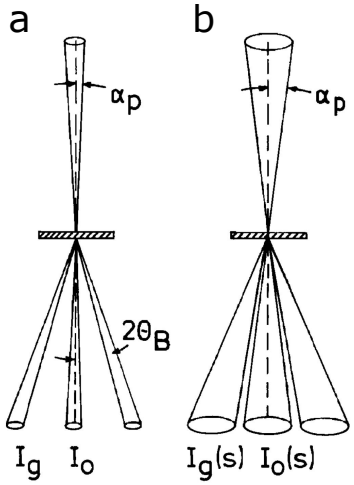

Figure 2.13: Diffraction with a convergent beam: (a) small angle convergent beam, **(b)** higher angle convergent beam. The smaller the convergence angle, the smaller diffraction spot size.

For the experiments performed in ChromaTEM, the diffraction images were acquired on the Ronchigram camera (dwell time of 50 ms), whereas in the UltraSTEM, they were acquired with the EELS camera (dwell time 50 ms). In ChromaTEM, two conditions have been used: first, the beam size was set to few nanometers to measure strain maps with spatial resolution, and later on, with a beam size larger than 100 nm. The latter was used to have a better precision in reciprocal lattice parameter, and no spatially resolved maps were measured in these condition. The UltraSTEM experiments were performed with a nanometer-sized electron beam. The different types of diffraction patterns obtained are illustrated in Fig. 2.14.

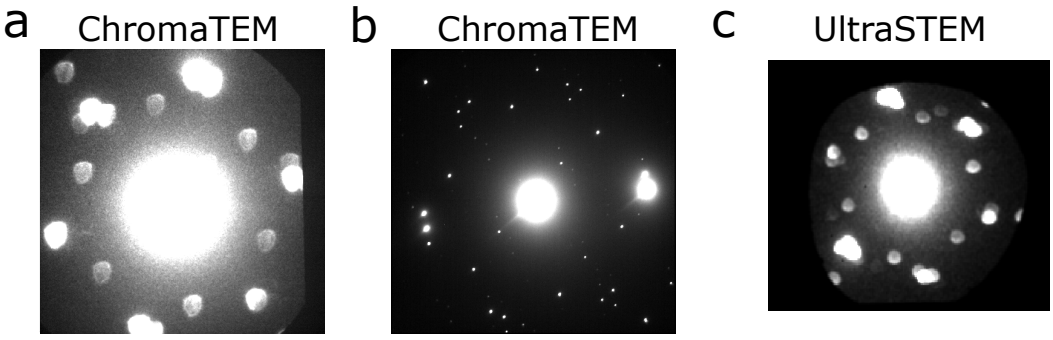

Figure 2.14: Types of diffraction patterns: (a) first measurements in ChromaTEM (beam size: few nm), **(b)** later measurements on ChromaTEM (beam size: a hundred nm), **(c)** measurements in the UltraSTEM (beam size: few nm).

As displayed in Fig. 2.14, the diffraction pattern spots in µ-diffration have an extension, which can be of the order of hundreds of pixels. Since the algorithm measures the barycenter of the diffraction spots, its position can vary if there is a change in illumination inside the spot. This way, artifacts can appear, and look like the strain is changing, whereas only the illumination of the spot has changed.

A way of precisely identifying the center is by using patterned probes. They can be created by using patterned apertures [42], or phase plates. The pattern can be used to project a dark spot or shape in the center of the beam, which creates a dark spot in the diffraction patterns spot centers, making them easier to identify.

The illumination change of the diffraction spots, in our case, come mainly from the presence of the substrate, which contains h-BN and contaminants. This creates an inhomogeneous background, which can potentially be numerically separated from the actual diffraction signal of the monolayer. This has not been tried in our data yet.

2.5.4 Geometrical phase analysis, with high resolution STEM images

GPA is used in chapter 5 to compare to our µ-diffraction measurements. It is an image processing method for the analysis of strain in crystal lattices using HR (S)TEM images.

In this section, the geometrical phase analysis (GPA) principle is described shortly, the full information can be found in [43]. The algorithm used here is implemented in Digital Micrograph (Gatan).

From the high-resolution (S)TEM image, the reciprocal space image is constructed, and then filtered on a lattice reflection to determine the local displacement of atomic columns. The strain is determined with respect to a reference area in the image.

The operating principle is the following:

1. The Fourier transform of the image is performed,
2. The mask is applied to two lattice reflections, such as illustrated in Fig. 2.15,
3. The phase part inside these marks is used to extract an image of the real-space phase for each reflection,
4. The strain and phase maps are computed using the phase images.

In particular, the software I use has the following outputs:

- a* and b*, which are the lengths of reciprocal lattice vector corresponding to the two reflections selected by the apertures,
- the strain components: ϵ_{xx}, ϵ_{yy}, ϵ_{xy}, and the rotation angle θ,
- the phase components ϕ_a and ϕ_b.

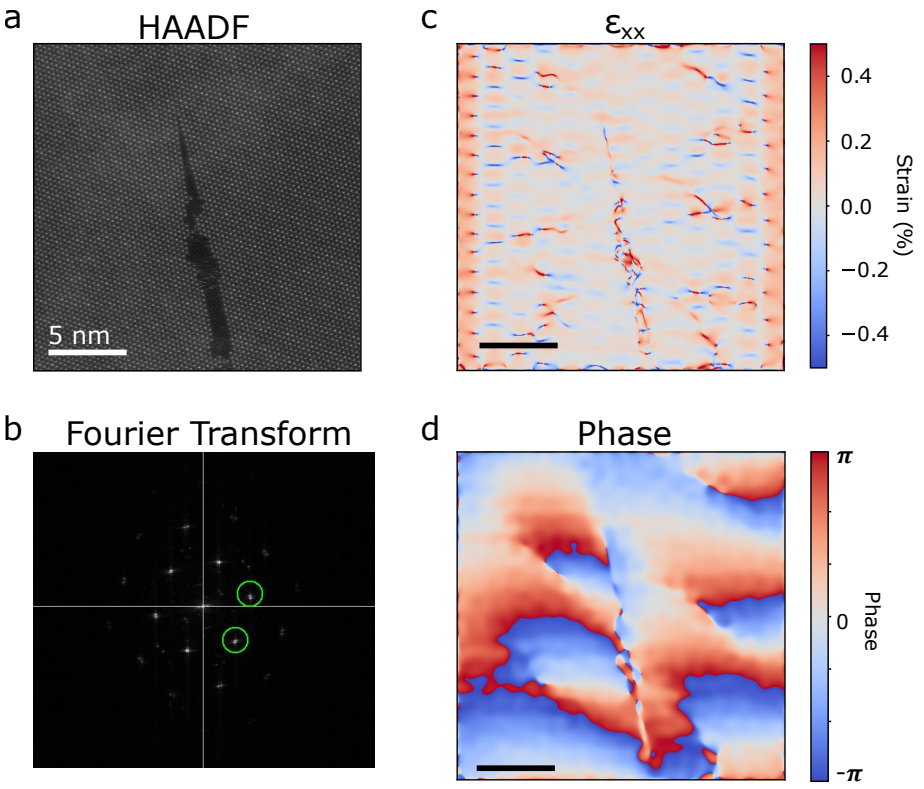

Figure 2.15: Example of GPA: (a) Atomically-resolved HAADF image of a WS_2 monolayer encapsulated in h-BN. The bright atoms are tungsten atoms, **(b)** Fourier transform of the image in (a), **(c)** ϵ_{xx} component of strain extracted with GPA, **(d)** phase component extracted from GPA.

GPA is a powerful tool but it requires atomically-resolved images, which limit the field of view to few tens of nanometers.

2.6 Scanning transmission electron microscopy (STEM)

As presented in introduction, STEM microscopes benefit both from the high-resolution of fast electrons and the possibility of performing various types of spectroscopy.

In this section, I present the structure of the STEM microscopes used in this thesis. There are two main types of STEM microscopes: the aberration corrected microscopes, such as the Nion UltraSTEM 200 and the Nion Hermes 200 (ChromaTEM), and the uncorrected microscopes, such as the VGHB501 (VG cold). The two main imaging modes, annular dark-field (ADF) and bright-field (BF), are introduced, and finally, the principle of aberration is presented at the end of the section.

2.6.1 Structure of a STEM

A scheme of the STEM microscope is displayed in Fig. 2.16. The electrons are typically accelerated to energies of few tens to a few hundreds of keV, which enable the transmission of the beam through the sample. The wavelength of the electrons are 3.7 pm at 100 keV, and about 4.9 pm at 60 keV, which are the two voltages used in this work. More information about (S)TEM microscopes can be found in [23].

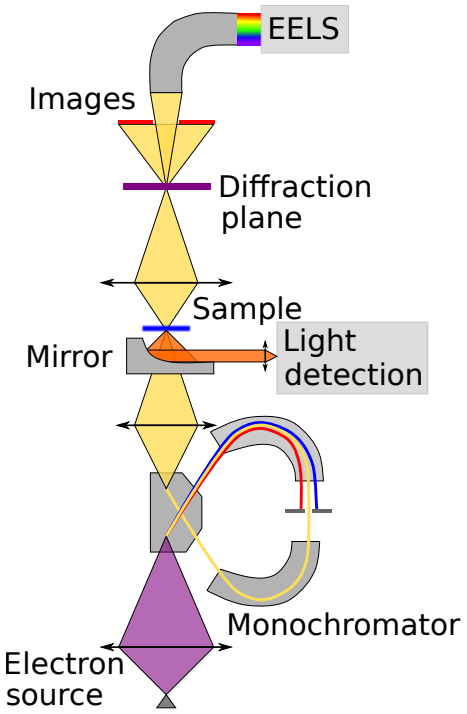

Figure 2.16: Scheme of a STEM microscope equipped with a monochromator and a parabolic mirror: the monochromator is used to energy-filter the primary beam, thus leading to higher spectral resolution in EELS, and the parabolic mirror collects the CL light emitted by the sample.

Parts of the microscope include:

- The electron source, called the gun, is a tip from which the electrons are extracted. In our case, the electron source is a cold field emission gun (FEG),

- The electrons optics and apertures, which shape the electron beam in the column of the microscopes, including:
  - the condenser lenses, for the demagnification of the probe,
  - the aberration corrector, which is optional and allows for atomically-resolved imaging,
  - the objective lens, for the formation of the probe on the sample,
  - the scanning coils, that allow the focused beam to move on the sample to create the images and multi-dimensional datacubes,
  - the projector lenses or system, for the coupling between the transmitted beam and the detectors at the end of the column,

- The sample holders, whose mechanical stability is crucial for high resolution imaging of samples,

- The EELS spectrometer, which includes a magnetic prism (deflection of the electrons depending on their speed - which depends on the kinetic energy lost during inelastic interaction with the sample) with Lorentz force $\overrightarrow{F} = \overrightarrow{v} \times \overrightarrow{B}$. The EELS spectrometer has to be aberration corrected to improve the spectral resolution. The quadrupoles after the magnetic prism modulate the energy dispersion.

- The detectors, such as the bright-field (BF) and annular dark-field (ADF) for imaging, and the CL and EELS cameras, that record the CL and EELS spectra,

- The vacuum, even if it is not directly a constituent of the microscopes, it is crucial to obtain good data and low contamination.

At the voltages used in this work (60 to 100 keV), the electrons mean free path is about 50 to 150 nm, depending on the material. This means that for measuring the transmitted electron beam, such as what is done in (S)TEM, the samples need to be of this thickness, or thinner. This makes the (S)TEM microscopes particularly fitted for the study of nanomaterials and 2D materials, which are, by definition, with small dimensions. Moreover, for the spectroscopies performed in STEM, in particular in EELS, the multiple inelastic scattering is to be avoided, to prevent undesirable effects.

The most simple STEM microscope used in this work is the VG cold. It contains only two condensers and an objective lens as the electron optics. Generally, only one of the two condenser lenses is used, and the second condenser is added when a higher current is required.

Modified VGHB501 (VG cold):

Operating voltage (here)	60 kV
Aberration correction	none
Electron monochromator	none
Sample temperature	150 K
CL setup	3 mm mirror (NA $\approx$ 0.6)
Column vacuum	10^{-8} mbar
Typical convergence angle	15 mrad
Typical collection angle	3-15 mrad
Energy resolution	375 meV
Software	(Gatan) Digital Micrograph

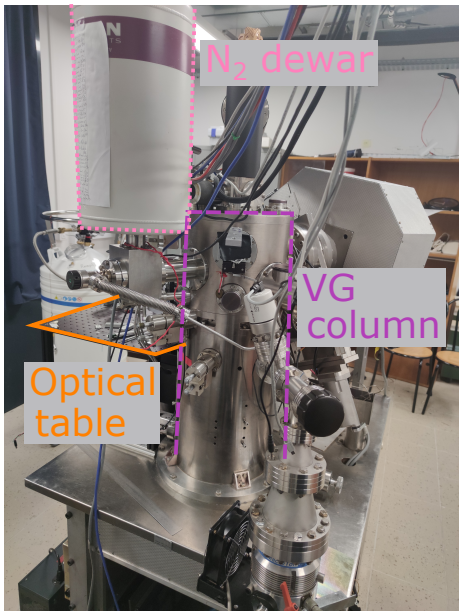

Figure 2.17: VG cold: picture of the microscope, with the column (purple), the liquid nitrogen dewar (pink) and the optical table (orange).

The two other microscopes used are aberration corrected. The aberration correction principle is described in section 2.6.3.

Nion UltraSTEM 200:

Operating voltage (here)	100 kV
Aberration correction	order 3
Electron monochromator	none
Sample temperature	300 K
CL setup	none
Column vacuum	10^{-8} mbar
Typical convergence angle	1-30 mrad
Typical collection angle	10-50 mrad
Energy resolution	300 meV
Software	(Gatan) Digital Micrograph

The UltraSTEM has a C3/C5 Nion corrector, The HAADF detector is at 80-240 mrad of the optical axis.

The EELS detector is a Medipix, which is a direct detector [44]. The core-loss typical exposure time is 50 ms.

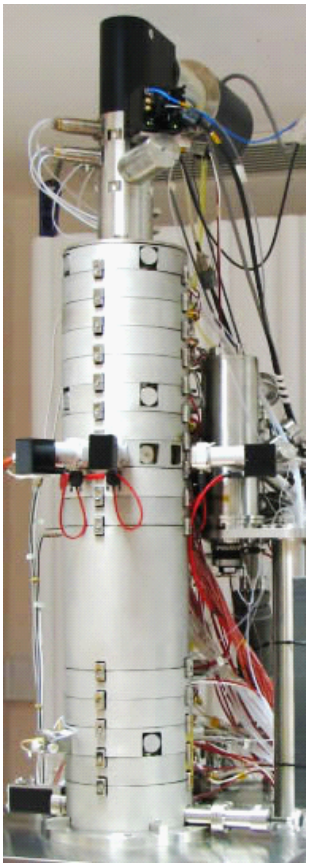

Figure 2.18: UltraSTEM: picture of the column of the UltraSTEM, the various sections of the column contain electron optics, such as the aberration corrector, which are absent in the VG cold.

Modified Nion Hermes 200 (ChromaTEM):

Operating voltage (here)	60 and 100 kV
Aberration correction	order 5
Electron monochromator	yes
Sample temperature	150 to 300 K
CL setup	2 mm mirror (NA $\approx$ 0.5)
Column vacuum	typically 1×10^{-9} Torr
Typical convergence angle	1-30 mrad
Typical collection angle	10-50 mrad
Energy resolution	20-30 meV
Software	NionSwift

The EELS typical exposure time is 300 ms, and for CL, 300 ms.

The ChromaTEM is an aberration-corrected STEM microscope with unique capabilities, thanks to its monochromator, that allows for probing low-loss EELS with high-resolution (down to 5 meV), and its CL mirror, which can collect the CL light with high efficiency. The two combined measurements enable probing the energy absorption and light emission of the same phenomenon, such as shown in chapter 5 and 6 with the exciton in TMD monolayers.

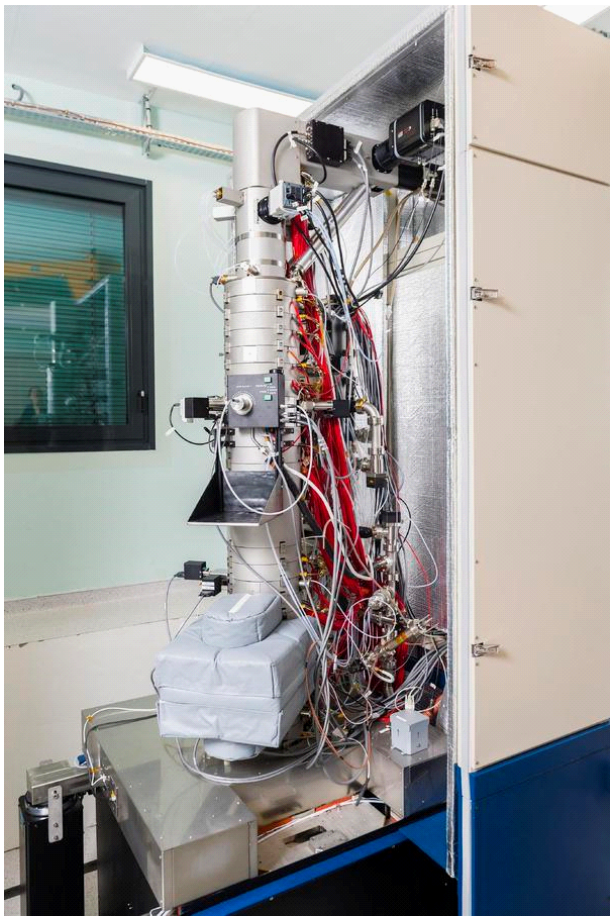

Figure 2.19: ChromaTEM: picture of the ChromaTEM, the monochromator is inside the grey fabric box.

Monochromator:

To access the low energy phenomena with high spectral resolution, one can use an electron monochromator. The principle is to narrow the primary electron beam in energy, so that the ZLP is narrower, and low-energy features become accessible [28].

The principle used by Nion for electron monochromation is to use three magnetic sectors to the EELS prism, with a slit in the center, allowing for the selection of a thin energy-selected slice of the primary electron beam [45, 46]. This requires extremely stable electron optics. This type of electron monochromation allows for reaching the energy range for vibrational spectroscopy (100 meV range) [26] and keep a high spatial resolution. Other types of monochromators exists and are described in the reference [24].

The ultimate spectral resolution of the ChromaTEM is around 5 meV [47], but in our measurements, instabilities in the microscope prevented to reach such small values for the EELS measurements.

CL detection setup:

The CL system used in both VG cold and ChromaTEM is the Mönch system from Attolight [4]. A parabolic mirror pierced of a hole is used for light collection, and the usual CL measurements are done with an optical fiber bundle with cores of 200 µm. The use of a fiber bundle rather than a monomode fiber increases the light collection while conserving the spectral resolution. The optical fiber bundle is inserted directly in the CL system in the microscope, which is separated from the vacuum by a silica window, and sends the light to an optical spectrometer. The parabolic mirror is placed at the end of an arm that can be positioned in the 3 X,Y and Z space directions and in angle (if necessary) thanks to screws.

Different spectrometers were used for the light measurements:
- in the VG cold: Princeton Instruments spectrometer model Acton Advanced SP2300A equipped with a ProEM 1600^2 CCD camera. 3 gratings, blazed at 300, 500 and 1000 nm, and the camera detection efficiency is maximum around 500 nm. The grating used in this thesis is the one blazed at 500 nanometers. It has a groove density of 150 lines/mm, which, in our conditions, leads to a spectral resolution of 5 meV or 1 nm.
- in the ChromaTEM, with the gratings blazed at 300 and 500 nm, the spectral resolution for the grating used is similar to that of the VG cold,
- in the all-optical setup, Acton SpectraPro 2150i, with a groove density of 300 lines/mm, blazed at 500 nm. It leads to a spectral resolution of about 10 meV or 2 nm.

2.6.2 Imaging in STEM

The convergent electron beam is scanned across the sample. At each beam position, the detectors record an intensity proportional to the number of electron they measure. Point by point, the images are built with these intensities, corresponding to the area scanned.

The shape of the active area of the detectors is either a disk, as in bright-field imaging, or annular, such as in annular dark-field imaging (Fig. 2.20). Collection of the transmitted electrons with detectors cover different areas around the optical

axis. The detectors are made of 1 pixel, and are made up of a scintillator and a photomultiplier.

In STEM, the spatial resolution is limited by the probe size.

Probe size:

The limitation of the probe size is mainly due to three factors [48]:

- the aberration of the lenses. The electron optics are not stigmatic: the image of a point object is not exactly point.
- the diffraction of the electrons: Rayleigh criterion $d_d = 0.611\frac{\lambda_e}{\alpha}$, where d_d is the smallest probe size, and for λ_e=3.7 pm (100 keV), and 30 mrad, d_d=75 pm.
- the source size: $d = \sqrt{d_a^2 + d_s^2}$ where d_a is the probe size taking into account the effects of aberrations, and d_s is the source size, which is linked to the probe current I with $I = \frac{B\pi^2 d_s^2 \alpha^2}{4}$, where B is the brightness of the source.

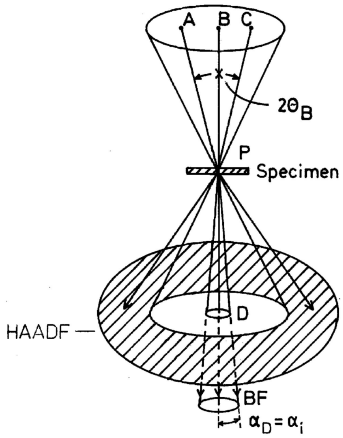

Figure 2.20: STEM imaging modes: scheme of the electron beam crossing the sample. The high-angle annular dark-field (HAADF) detector measures the electrons deflected at high angle, whereas the bright-field (BF) measures the electrons from the transmitted direct beam and electrons deflected at low angle.

Bright-field (BF):

The name bright-field comes from the image contrast obtained with this imaging mode: if the beam is in vacuum, with no sample to interact with, the image will appear bright, since all the beam is detected. The detector is a disk located on the optical axis. The contrast in this type of image is phase contrast.

Dark-field (DF, or ADF):

The name dark-field comes from the image contrast obtained with this imaging mode: if the beam is in vacuum, with no sample to interact with, the image will appear dark, since no electrons are detected. It is often called ADF, for annular dark-field, or HAADF, for high-angle ADF (for collection angles superior to 30 mrad). The contrast is proportional to the atomic number of the atoms (eq. 2.47).

The intensity comes from the detected electrons, which have been scattered elastically by the nuclei of the samples' atoms. In this case, the intensity detected is proportional to the square of the atomic number of the atom. The HAADF intensity also depends on the sample thickness (projected atomic number).

The elastic scattering comes from the Coulomb interaction of the electrons with the nuclei of atoms. It is characterized by the Rutherford scattering [23]:

$$\frac{d\sigma(\theta)}{d\Omega} = \frac{\lambda_e^4 Z^2}{64\pi a_0^2 (sin^2(\frac{\theta}{2}) + \frac{\theta_0^2}{2})^2} \propto Z^2 \tag{2.47}$$

Note that the scattering cross section, which is related to the number of electrons scattered at a specific angle, is proportional to the square of the atomic number. For this reason, high-angle scattering images, such as HAADF, are often referred to as Z-contrast imaging.

Examples of BF and HAADF images are shown in Fig. 2.21.

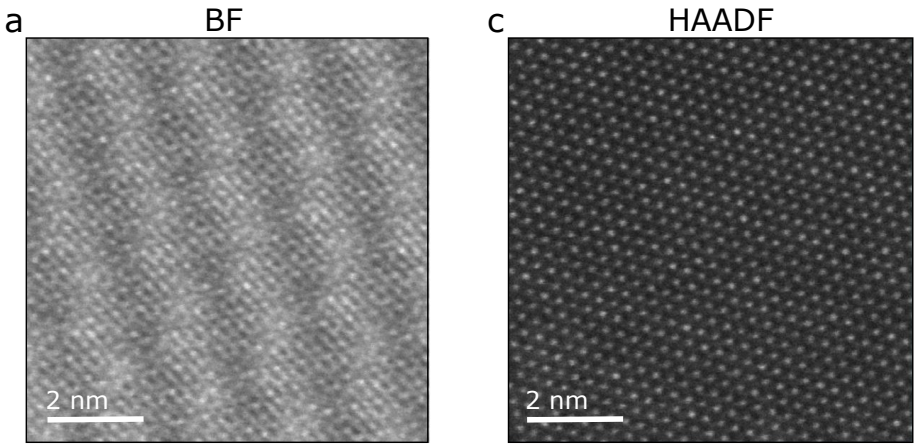

Figure 2.21: Atomically-resolved images of the h-BN/WS_2/h-BN heterostructure presented in chapter 5: (a) Bright-field (BF) image. The fringes of about 2 nm come from moiré patterns. **(b)** High-angle annular dark-field (HAADF). The bright dots are the tungsten atoms.

In (S)TEM, the diffraction limit being very small (e.g. at 100 keV, the wavelength of electrons is about 3 pm), the first limitations are the aberrations. These aberrations have various origins that are detailed in the next part. In scanning mode, with the focused electron beam, the aberrations limit the probe size. They can be corrected to get closer to the diffraction limit.

2.6.3 Aberration correction

The aberrations correspond to an image deformed from the initial object through the optics. The aberration of the lenses induce a phase change χ of the electron wavefront that distorts it [49].

There are two families of aberrations, the chromatic aberrations and the geometrical aberrations:

Chromatic aberration:

The chromatic aberration (C_C) comes from the fact that the magnetic field act on an electron depending on its speed (i.e. its kinetic energy). The name chromatic comes from the analogy with optics, where the lenses are dispersive and each wavelength is not focused at the same position, blurring the image. The use of a cold FEG reduces the effects of the chromatic aberrations. C_c can be further reduced by using a monochromator [45].

Geometrical aberrations:

The aberrations are classified with orders corresponding to the expression of the expansion of the phase change $\chi(\theta)$. The principal aberration encountered are the defocus and spherical aberrations (1-fold), the astigmatism (2-fold) and the coma (3-fold). Their order can be found in the expression of the phase change $\chi(\theta)$ expression [49], for the geometric aberrations with cylindrical symmetry and the chromatic aberrations:

$$\chi(\theta) = \frac{\theta^2}{2}\Delta f + \frac{\theta^2}{2}\frac{\Delta E}{E_0}C_c + \frac{\theta^4}{4}C_s + o(\theta^6, \theta \to 0) \tag{2.48}$$

where θ is the angle between the optical axis and the propagating electrons, Δf, the defocus, C_s, the spherical aberration, ΔE, the energy spread of the source, E_0, the energy of the electron beam, and C_c, the chromatic aberration). Reducing α (and by extension θ) decreases the aberration function. Δf and C_s can be compensated by aberration corrector.

2.6.4 Hyperspectral images acquisition

As mentioned before, the images in STEM are formed by scanning the convergent beam across the sample and recording the intensity of BF and HAADF detectors. Other types of signals can be measured for each beam position, such as EELS or CL spectra, or diffraction patterns. The dataset thus formed are multidimensional:

- images, which are 2D datasets,
- spectrum images (EELS, CL), which are 3D datasets (2 dimensions for the space, corresponding to the images, and at each position, the third dimension contains the spectra),
- diffraction datasets, which are 4D datasets (2 dimensions for the space, corresponding to the images, and at each position, a diffraction image is recorded). For this type of datasets, one has to take into account the size of the measured data, which are heavy and can be difficult to process without a dedicated computer.

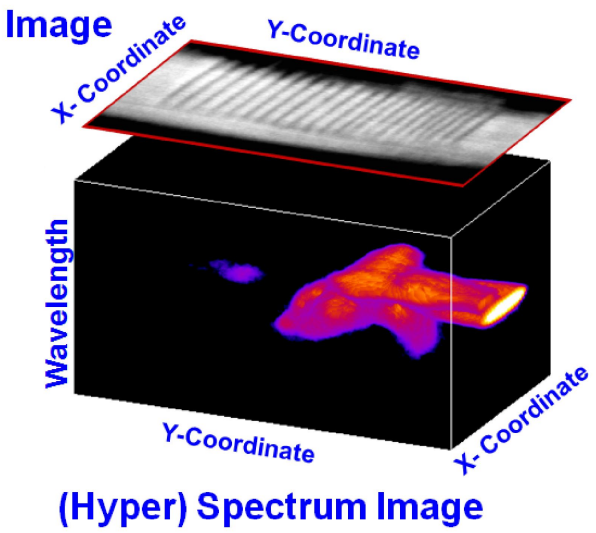

Figure 2.22: Representation of an hyperspectral image (3D dataset): the space coordinates are labeled X and Y. The HAADF image (on top), displays contrast from a GaN/AlN nanowire containing quantum wells. The bottom cube corresponds to the hyperspectral CL image acquired at the same position as the image. The X and Y coordinates correspond to the space coordinates, and the vertical axis is the wavelength of the CL emission measured. Reproduced from [31].

2.7 Numerical methods

In this section, I rapidly introduce the tools used for the data treatment of 3D datacubes (the treatment for 4D datacubes, referred to as µ-diffraction, is detailed in section 2.5), with first the typical decomposition process refereed to as principal component analysis (PCA), and then the specific blind source separation (BSS) algorithm used. The model fitting is detailed for the case of EELS, CL and PL measurements. The multi-dimensional data have been processed with HyperSpy [50].

2.7.1 Decomposition and principal component analysis

The principal component analysis (PCA) corresponds to a reduction of the dimension of the data in a large dataset, with minimization of information loss. It uses the principle that noises should have a low variance value and the signal should have a large variance value [48]. This is a widely used technique for denoising, and for rapid interpretation of a large dataset.

The principle is the following:

(i) the dataset is first rescaled by a reduction to compatible scales, so that each variable contributes equally to the analysis,

(ii) the covariance matrix is then calculated to identify the correlations present in the dataset,

(iii) the eigenvectors and eigenvalues of the covariance matrix are then computed to identify the principal components. The new uncorrelated variables produced are constructed as linear combinations of the initial variables, so that the majority of the information is contained in the first variables. The first component contains most of

the information, and has the largest variance.

(iv) the number of components kept in the final dataset is chosen. Usually, a graphical representation of the components is used to identify which have the highest values (called the principal components) and the ones with the low variance values are removed (this can be done manually by choosing an integer number of components that are to be kept). Since the low variance components are supposed to contain mainly noise, this process corresponds to denoising the data (an example is shown in reference [48]),

(v) the change of basis, corresponding to the representation of the new dataset along the principal components, can then be performed.

Overall, PCA is performed through matrix products, which are highly efficient in computers contrary to curve fit, explained shortly in section 2.7.3. The specific algorithms used in this thesis is detailed below. The advantage of using them rather than simple PCA is that the uncorrelated components obtained are additive, which makes them more physically meaningful.

2.7.2 Blind source separation (BSS) with independent component analysis (ICA)

The blind source separation (BSS) technique consists of the separation of a mixed signal into individual components. The algorithm used here is the independent component analysis (ICA) implemented in HyperSpy [50]. In the ICA algorithm, the individual components are additive, and treated as non-Gaussian and statistically independent. This type of additive algorithm produces more physically consistent spectra. More details can be found on the hyperspy web page [50].

2.7.3 Model fitting

Two manners of fitting the data were used. The first one is adapted for precisely fitting single spectra, and uses the scipy library optimizer. The second one is used for 3D hyperspectral datasets (EELS and CL) and is the bounded multifit tool from hyperspy. The latter is limited when there are large spectral variations across the dataset, or when areas are with too low intensity.

The fitting of a dataset by a curve is generally done by minimizing the difference between the curve and the points composing the dataset. To do so, a first guess is usually required. A first estimation of the difference is made, and the curve is modified. The new difference is calculated. If the difference decreases, the algorithm continues in that direction. If not, it goes to the opposite direction. When a minimum in the difference is found, the algorithm stops. This iterative process is very resource-consuming, and requires a pre-knowledge of the type of function adapted for fitting the dataset, whereas PCA and BSS do not make any assumptions on the types of curves, and are much more efficient.

Moreover, curve fitting requires quite high signal to noise ratio, which can be difficult to obtain for each pixels in a measurement. In general, some pixels remain poorly fitted, even for high quality data. The difficulty to fit these pixel also creates longer computational times, since many function parameters have to be tried, until reaching a maximum of iterations meaning that the fit failed. For this reasons, in my

thesis, BSS was often used to have an rapid look at the datasets (the BSS algorithm is less than 1 second, whereas curve fittings can take up to tens of minutes).

Calibration:

Before data treatment, all datasets are calibrated: for CL, the spectra are calibrated using a mercury spectral lamp, and for EELS, the dispersion is calibrated by measuring the drift tube dispersion, and then centering the zero-loss peak to 0 eV using the hyperspy align1d tool. The precision of this method is limited to about 1%, which is about 20 meV at 2 eV.

2.8 Summary

In this chapter, I have described the tools for understanding the results obtained in this thesis. In particular, I have described the electron beam and sample interaction, as well as the light and sample interaction, and have compared them.

The temperature dependence of light emission spectra were introduced to understand the temperature-controlled CL data in chapter 3 and 4.

The µ-diffraction with convergent electron beam processing and limits have been presented. They were used to estimate the strain and lattice deformation in chapters 5 and 6.

I have presented the STEM microscopes used in this work, as well as the data acquisition principle.

Finally, the data was processed using the hyperspy and pyxem python libraries, and are detailled in the last section.

Chapter 3

Instrumental developments

Contents

Photoluminescence (PL) microscopy is a widely used technique that enables the optical characterization of a large range of systems, such as point defects [51] or 2D materials [17]. It is spatially limited by the optical diffraction, which prevents the characterization of nano-objects except if they are highly diluted. Many purely optical techniques have been developed to overcome this limit, and are called super-resolution microscopies.

There are two main categories of super-resolution microscopy: the near-field and the far-field techniques. The tip-enhanced Raman spectroscopy (TERS) is an example of near-field super-resolution microscopy [52]. It uses the light confinement in the nanometric space between a metallic probe and the sample to measure the sample emission at high spatial resolution. The major drawback of this type of method is the interaction between the tip and the sample, which dielectric environment is modified. Another example, this time of a far-field technique, is the stimulated emission depletion microscopy (STED) [3]. It uses two lasers, one to selectively excite the fluorescence, and the other to de-excite fluorescent particles in a doughnut shape. This way, the area where the fluorescence comes from is of the order of a few nanometers. This very powerful technique is widely used in biology, where the fluorescent molecules have to be specifically chosen to emit light at specific wavelength of excitation, and be quenched at another. Yet, this technique largely relies on the prior knowledge of the light-emitting particles used [53].

Therefore, the far-field techniques are either diffraction-limited and/or specific to a particular dye, or light-emitting center. A way to beat both these limits is the use of cathodoluminescence (CL), which is the light emission triggered by excitation with electrons (see chapter 2). It has a spatial resolution limited by charge-carrier diffusion, which is of the order of a few nanometers. The electron beam is a non-resonant source of excitation, similar to out-of-resonance PL [4]. Nevertheless, for

some samples, the CL and PL light emission differ, and some specimens do not emit detectable CL light. For this reason, PL is still an attractive tool for characterization.

To combine the advantages of PL and the high-resolution achieved with electron microscopy, we have merged them in a STEM microscope. This is done by injecting laser light inside the STEM microscope through the CL collection mirror. Even if CL and PL often give similar information, this is not the case for nitrogen-vacancy (NV) centers, which have a different spectral signature when excited in CL or in PL (see chapter 4). PL spectroscopy of NV centers have been used in this chapter for characterizing the spatial extension of the laser beam.

However, the light injection has led to sample heating, which can alter the PL response of the sample. This heating can also be used for in-situ sample cleaning. I have further investigated the sample heating by comparing the spectral evolution with temperature-controlled CL experiments. In this case, temperature is controlled by means of a micro electro mechanical system (MEMS) on a cryo sample holder.

In this chapter, I therefore present the instrumental developments for µ-PL implemented inside a STEM microscope and temperature-dependent CL experiments in a STEM. Indeed, even if coupled µ-PL and atomically-resolved imaging in TEM have been performed [54], they are done in two separate setups, therefore the areas probed may differ. In SEM, µ-PL has been done for some time, in particular for pump-probe experiments [8]. For this type of setup, only the superposition between the electron and the laser beams is required. Thus, the spatial resolution obtained can be sub optimal.

The setups I have developed are implemented on two microscopes: a modified STEM VGHB501 (VG cold), and a modified Nion Hermes 200 (ChromaTEM), which is an aberration-corrected electron microscope. Both STEMs are equipped with an Attolight Mönch system for CL, which is used both for light collection and light injection.

The chapter is organized as follows: in section 3.1, the first setups made for the VG cold are presented, the mechanical hyperspectral acquisition is described at the end of the first section. Then, section 3.2 shows the multi-laser setup that has been used for the optical pumping of NV centers presented in chapter 4. Section 3.3 introduces the compact PL setup that has been made for the ChromaTEM. Then, section 3.4 presents the micro electro-mechanical system (MEMS) used to perform the temperature-controlled CL measurements. Finally, the control experiments that have been built in parallel in a full-optical setup.

Lasers used:
- IR 1064 nm laser: CrystalLaser IRLC-100-1064-S (output maximum power 100 mW), referred to as IR laser,
- He-Ne 633 nm laser: Thorlabs HNL020LB (output maximum power 2 mW), referred to as alignment laser,
- He-Ne 543 nm laser: Melles Griot 05-LGP-173 (output maximum power 5 mW), referred to as green laser,
- green diode 532 nm: Thorlabs CPS532 (output maximum power 4.5 mW), referred to as green laser diode,
- UV diode 405 nm: Thorlabs CPS405 (output maximum power 4.5 mW), referred to as UV laser diode.

3.1 Light detection and injection in the electron microscope

The first instrumental step is to get both the CL and PL in the same setup, which means to add the light injection in the STEM, and separate it from the light collection. The setup already in place contains an Attolight parabolic mirror made of aluminum and pierced with a hole to let the electrons through. The mirror is placed in the center of the electron microscope objective lens pole pieces, below the sample. The CL setup is described in details in chapter 2. To perform the separate light injection and detection, two distinct optical paths are required. One for the incoming laser, and the other one for the emitted signal detection, such as illustrated in Fig. 3.1. This is impossible with the bundle fiber, so I have built a free-space optical setup. In this thesis, I refer to as free-space the optical setups where the laser beams are either in air or in vacuum, as opposed to laser beams traveling through optical fibers.

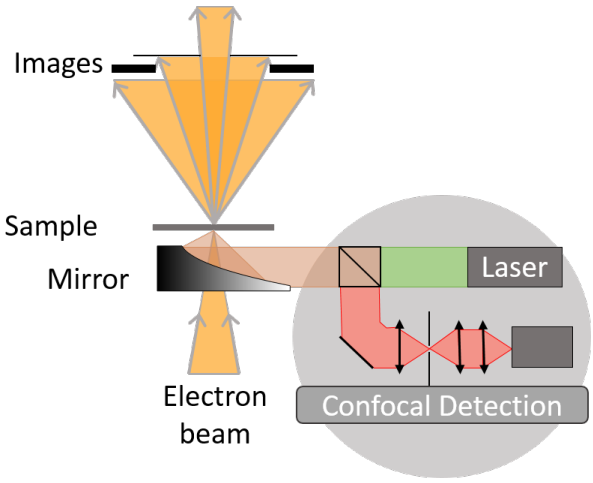

Figure 3.1: Scheme of the setup: the convergent electron beam interaction with the sample produces CL light, that is collected by the parabolic mirror. On the optical table (grey circle), the detection (red) is separated from the injection (green) with a dichroic mirror. The laser is directed to the sample by using the parabolic mirror.

The setup reproduces what is usually done for all-optical setups: the laser source is brought to the sample thanks to a dichroic mirror that separates the incoming laser and the signal. The fiber bundle is still used for light collection after the dichroic mirror, but is moved away from the vacuum window of the usual CL setup. The optical fiber is kept because of the small size of the optical table, that prevents having the spectrometer directly on the setup. This way, the alignments are also more simple since the optical fiber can be displaced easily.

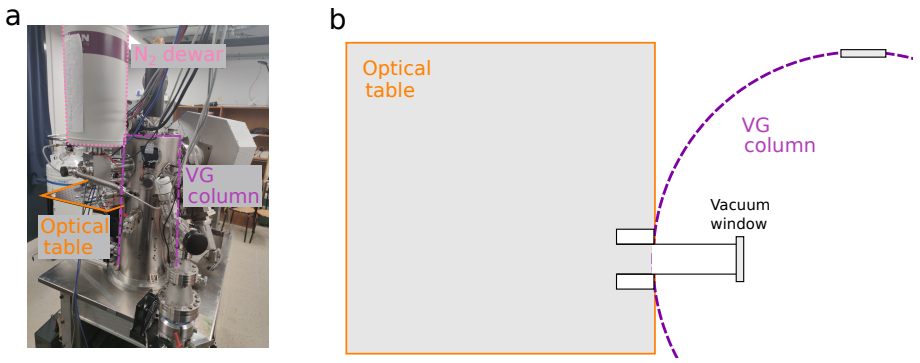

Figure 3.2: Optical setup configuration in the VG cold: (a) photograph of the microscope, with the optical table (orange), electron microscope column (purple) and liquid nitrogen dewar (pink). **(b)** Scheme of the configuration (top view). The optical table is represented in orange, and VG column chamber in purple dashed line.

The optical setup has been put next to the VG STEM microscope on a 45×45 cm black aluminum optical table at first, which has later been upgraded to a 120×45 cm optical table to enable the multi-laser excitation. Parasitic light is present in the VG room, even if it is designed specifically for optics. Therefore, one needs to make sure that they are covered for the measurements: the optical setup can be in a black box, or the parasitic light can be blocked with optical black sheets and optical tape. Several irises are used in the setup, ideally one per portion (between each mirror). This ensures to keep the alignment of the laser beams, which can be realigned easily by centering them on the irises holes.

3.1.1 Light injection in the VG STEM microscope

Most samples used for these experiments are made up of FNDs containing NV centers, which are detailed in chapter 4. The alignment process of the setup is described in details below. Here, we just note that the NV centers are very bright light emitters, and that they emit red light both in CL and PL, with characteristic spectral lineshapes. One important feature is that the signal excited by the electron beam and by the green laser is different, which allows for their distinction.

For alignments, other samples have been made up of larger diamonds, of the order of 1 µm, that contain many different color centers. For this reason, some images with CL light have different colors, from blue and green to red.

Basic alignment:

The first alignment step requires: an optical table, a laser source (here the red alignment laser at 633 nm), mirrors, a beamsplitter, a camera. The setup has to be implemented on a microscope equipped with a CL mirror.

The first step of every laser beam alignment in the VG setup is the centering of the parabolic mirror by optimizing the CL signal on the spectrometer. Once the mirror in position, one can start aligning the other elements. An illustration of what the illumination of the CL mirror should look like through the vacuum window is shown in Fig. 3.3 (it should be looked at with a camera, not directly the eye).

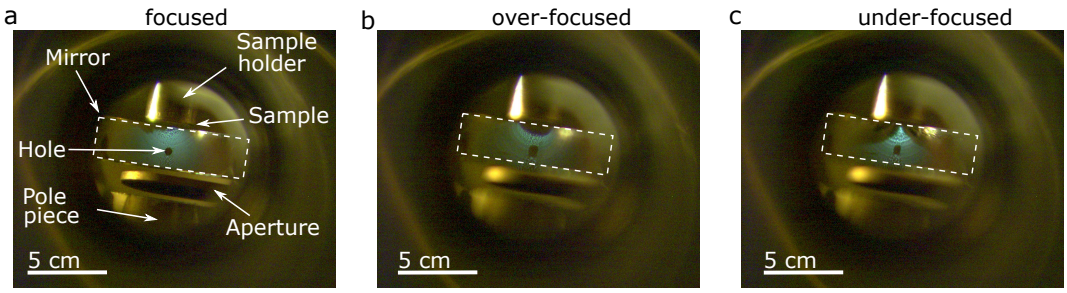

Figure 3.3: Positioning of the parabolic mirror: the CL emission is green, and the electron microscope chamber is illuminated with a LED yellow lamp. Photograph of the mirror **(a)** aligned, **(b)** over-focused (too close to the sample) and **(c)** under-focused (with the mirror being too far from the sample). The parabolic mirror position is highlighted in the white dashed rectangle.

The picture is taken at the end of the tube supporting the CL mirror so that the mirror appears in projection, as a rectangle (delimited by the dashed white line) with a hole.

After drawing the light path on the optical table as a guide and placing the optics roughly in position, one has to use a target to ensure that the laser beam is parallel to the optical table (horizontal) and parallel to the drawn optical path. The precise alignment of the optics on the table and the correct centering of the parabolic mirror are crucial for free-space PL excitation of the sample.

The laser beam and CL beam are then superimposed, such as represented in Fig. 3.4. First, a camera is placed facing the microscope window, after the beamsplitter that brings the laser to the sample. The approximate superposition of the CL and laser beams is estimated by changing the focus of the camera objective (Fig. 3.4). The laser beam and CL superposition is further described in the following paragraph.

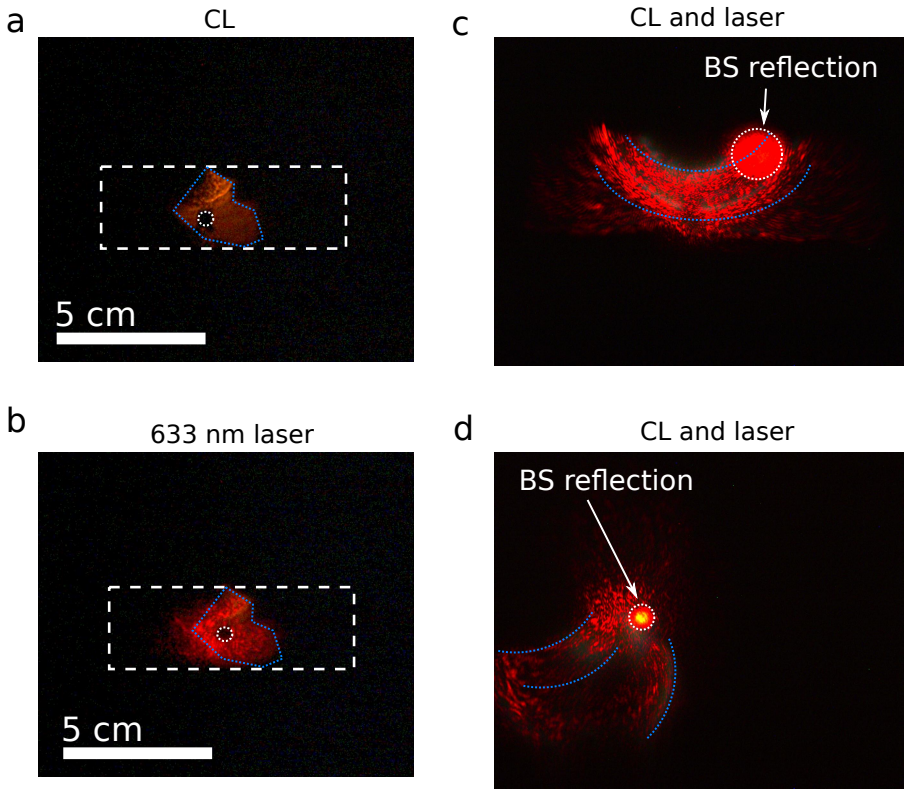

Figure 3.4: Superposition of the CL signal and the 633 nm laser beam: (a) photograph of the parabolic mirror with only CL light. The illumination is sub optimal due to a tilt in angle of the mirror that was corrected later on. **(b)** 633 nm laser pattern on the mirror, being superimposed to the CL pattern. The mirror position and its hole are represented in the white dashed lines. **(c,d)** two examples of images at different focus of the Thorlabs camera to evaluate the correct superposition between the CL (green) and the 633 nm laser (red). The shapes of the two beams (CL and laser) are highlighted in blue dotted lines. A laser beam reflection from the beamsplitter (BS) is marked with white dotted circles, and does not matter for the experiment.

The illumination shape of light on the mirror has to be the same for both CL (Fig. 3.4a) and the laser beam (Fig. 3.4b). A way to check their correct superposition, in other words if the two beams form a unique line, is to look at both beams at two positions along this line. To do that, the focus of the camera is changed, which leads to the shapes in Fig. 3.4c,d. The contrast might not be sufficient on the figures printed on paper, it is better to visualize the figure on a screen. The green halo is the CL (which can be difficult to distinguish), and the red pattern is the 633 nm laser beam. The beam shapes are highlighted with the blue dotted lines for more visibility.

When it is perfectly aligned, the parabolic mirror defocuses a point source at its focal point to a parallel beam. The beam is then circular, with a diameter slightly superior to 5 mm, which is wider than the laser beam. Still, a correct superposition of the two beams is possible.

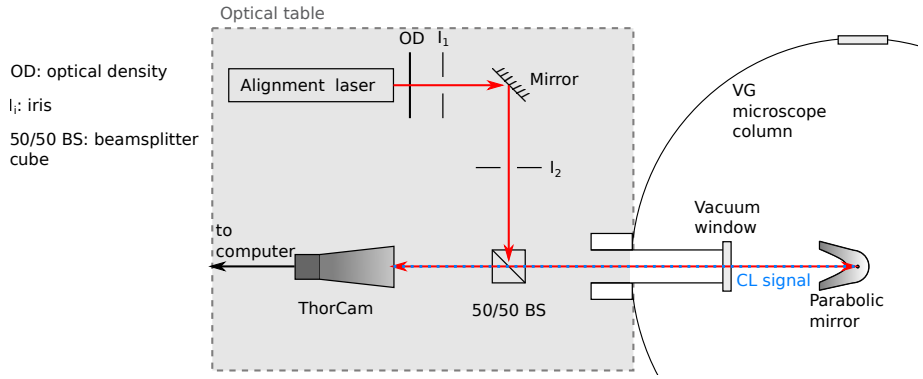

Figure 3.5: Alignment setup in VG: the alignment laser used is a He-Ne 633 nm red laser. The correct superposition of the CL and laser is controlled with a ThorLabs camera, with an objective that allows for the imaging of the mirror. A 50/50 beamsplitter is used to allow for the superposition of both signals.

The alignment described previously can be used to bring a laser beam to the sample in an approximate manner. This can be useful, for example, if one wants to use laser heating to clean samples in situ. It does not require the sample to emit light in PL. Nanodiamonds can be placed on one part of the sample to perform the alignment with the CL beam. I then have modified the setup to use a 543 nm laser beam, which can excite PL in NV centers.

PL alignment:

This setup uses the ThorLabs camera only for the very first alignment steps, as described in the previous paragraph. The beamsplitter is also replaced by a dichroic mirror, that does not decrease the incoming laser power. Otherwise, the setup material used is the same as previously. The ThorLabs camera can be changed to an optical fiber coupled to the optical spectrometer for experiments. The optical fiber is precisely positioned outside of the microscope, after the dichroic mirror, in the detection path. The optical fiber's position can be optimized by moving it while enhancing the CL signal detected by the spectrometer.

The spectrometer signal can now be used as a target: the PL intensity can be increased by moving the mirrors on the optics table. When the PL signal is maximized, the CL and PL beams are well superimposed.

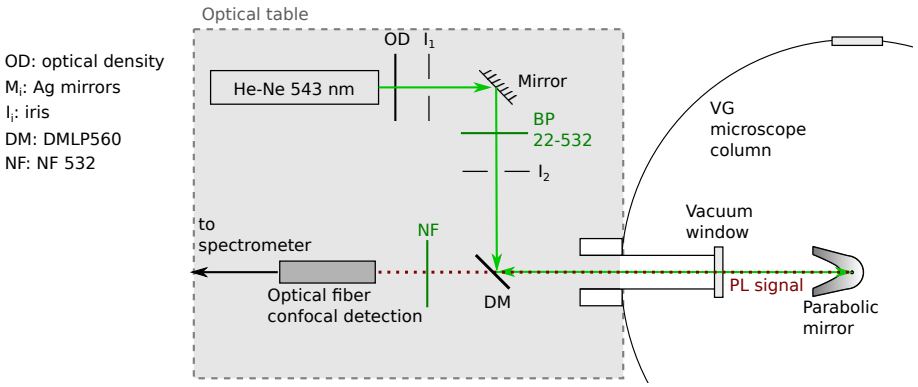

Figure 3.6: PL setup in the VG: the He-Ne 543 nm laser is used as the PL excitation. It is brought to the sample with a dichroic mirror at 560 nm that reflects the green and lets the lower energy signal (PL and CL) through. The alignment process is the same as before, except that here the PL signal from the sample can be optimized with the spectrometer intensity. The bandpass filter (BP) is used to remove the undesired laser lines in the excitation path. The notch filter (NF) is placed in the detection path to remover the excitation laser peak.

The correct superposition of the electron beam and laser beam can then be tested with the mechanical hyperspectral image acquisition, which is described in the next section.

3.1.2 Mechanical hyperspectral acquisition and spatial resolution

The mechanical hyperspectral image acquisition consists of the measurement of an optical signal (PL, CL or the CL and PL combination) at several positions on the sample as shown in Fig. 3.7. Usually, in STEM, the electron beam is moved to scan the sample. At each position of the beam, the spectral signals are measured. On the contrary, here, both the electron beam and the laser beam are fixed at the same position. The sample is moved to perform the raster scan. This process allows for the electron and laser beams to be superimposed in the same way at all times without any further alignment, whereas if we moved the electron beam with the scanning coils and the laser beams, the alignment would be difficult to maintain.

The main spatial limitation comes from the reproducibility of the sample holder motion, which which is limited to about 1 µm in the VG cold. The estimation of 1 µm has been made in the following way: a displacement step size is chosen, and a one line raster scan is performed. At each position, an image is acquired. The precise position of the sample holder is then recovered by cross-correlating the images.

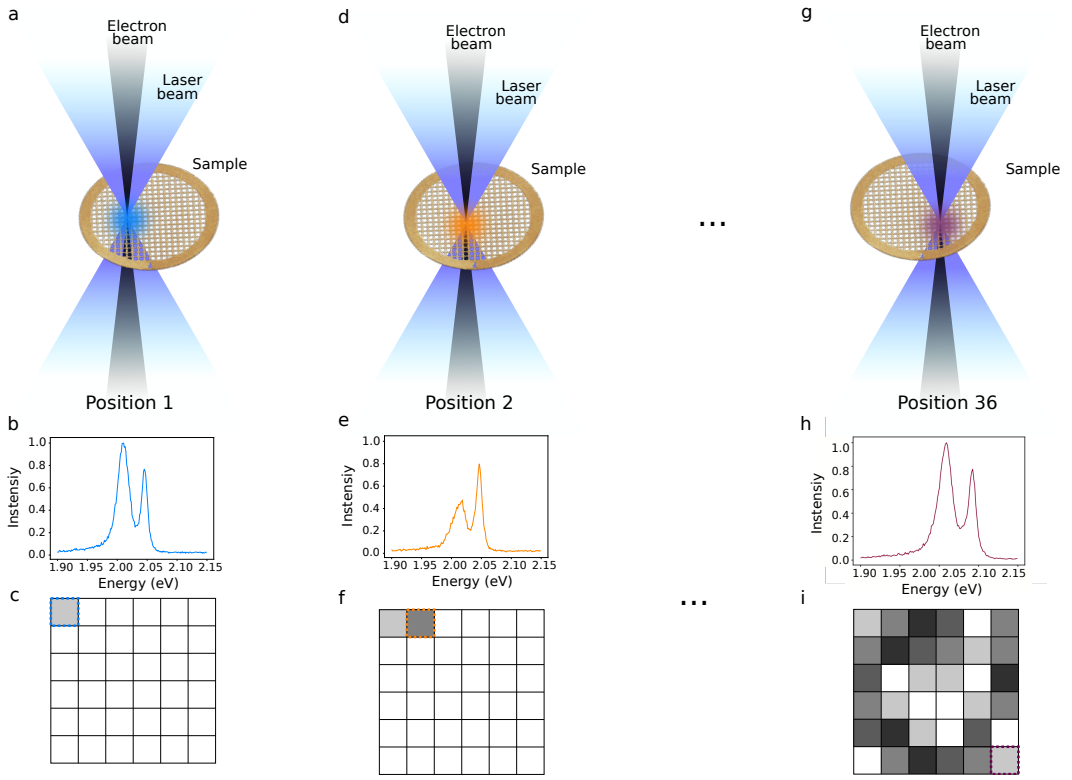

Figure 3.7: Scheme of the mechanical hyperspectral image acquisition process: (a,d,g) scheme of the sample (TEM grid) being moved with the laser beam (blue) and electron beam (black) being superimposed. The convergence of both beam is exaggerated for visibility. **(b,e,h)** spectra illustrating that the CL and/or PL signals are changing when the sample moves. **(c,f,i)** intensity map being built from the spectra intensity at each position, until forming a full spectrum-image.

The first step to perform this measurement is to find a FND aggregate of right size (between one to few µm). Two examples are shown in Fig. 3.8 and Fig. 3.9. The laser and electron beams can be selectively used to excite the sample, leading to PL, CL or combined PL and CL signal acquisition. This is exemplified in Fig. 3.8. Alternatively, both the electron and laser beams can be used at the same time, and the contribution from CL and PL can be spectrally separated later on, such as shown in Fig. 3.9. The latter method is less reliable since the spectrum excited in CL slightly overlaps that of the PL, making it difficult to fully separate the contributions.

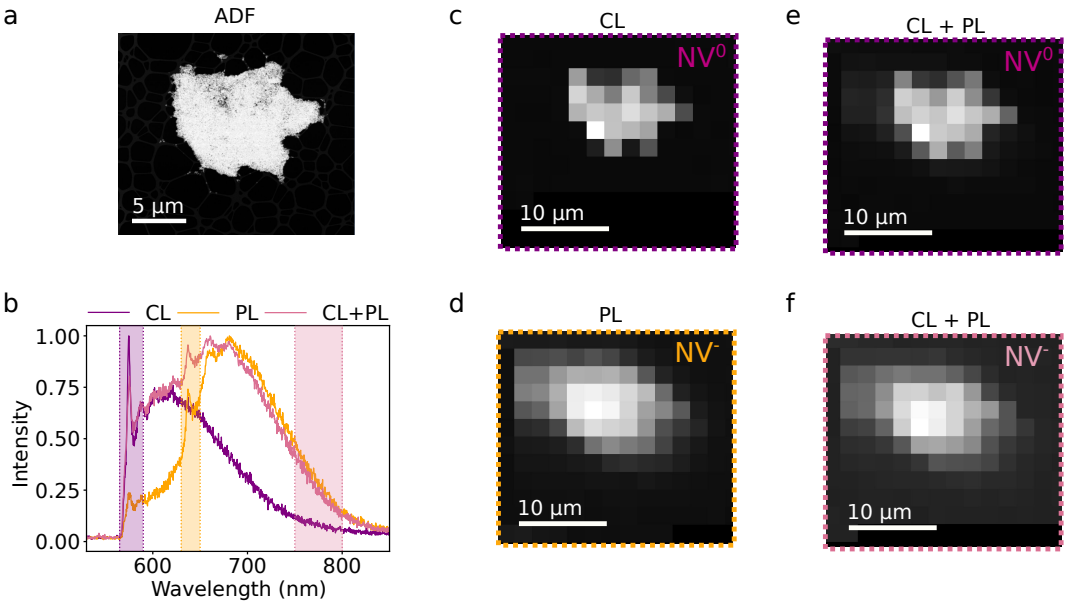

Figure 3.8: Mechanical hyperspectral acquisition, separate measurements of CL, PL and CL+PL: (a) HAADF image of the FND aggregate, **(b)** spectra extracted from CL (purple), PL (orange) and combined CL and PL (pink), corresponding respectively to the raster scans **(c)** CL **(d)** PL **(e)** and **(f)** combined CL and PL filtered at two different energies (570-590 nm for (e) and 750-800 for (f)).

In PL only, it makes sense to filter the image on the ZPL of NV^-, since no background from other emission is present. When both CL and PL are triggered, the phonon sideband of NV^0 increases greatly the signal at the NV^- ZPL energy. In these conditions, the filtering at the low energy tail of NV^- is preferred.

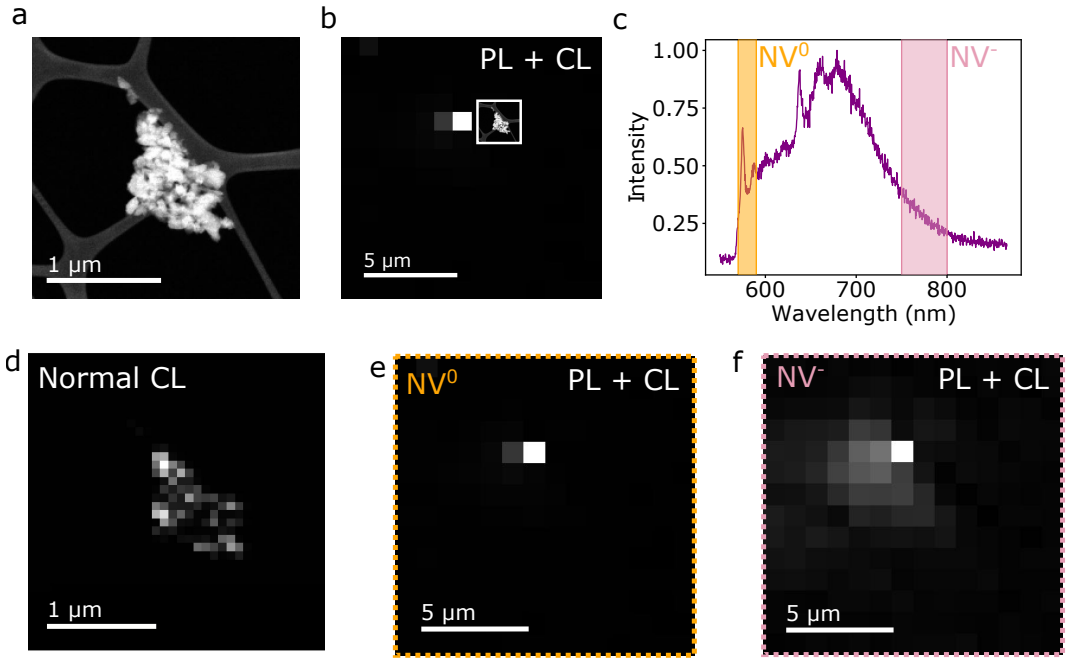

Figure 3.9: Mechanical hyperspectral acquisition, simultaneous measurement of PL and CL: (a) HAADF image of the FND aggregate with a size of the order of 1 µm, **(b)** mechanical hyperspectral image, with the ADF of the FND aggregate in inset to compare with the pixel size. **(c)** Spectrum extracted from the mechanical hyperspectral acquisition, where both the electron beam and the 543 nm laser were superimposed. **(d)** Usual spectrum image measured, where the electron beam is moved to scan the sample, with high spatial resolution, **(e)** energy filtered (570-590 nm) and **(f)** (750-800 nm) raster scan. The size of the pixel is 1 µm, which corresponds to the reproducibility of the sample motion.

Fig. 3.9 shows a measurement of the laser beam size and shape. The FND aggregate has been chosen to match the size of the sample holder step size limit, which is about 1 µm. The CL spot is then one single pixel, and the PL spot displays directly the shape of the laser beam. With these measurements, we have reached a spatial size of the green laser beam of the sample of 2.8 µm (FWHM of the Gaussian fitting of NV^- intensity on the hyperspectral map) inside the electron microscope. The theoretical limit should be of the order of 452 nm with the 543 nm laser and a numerical aperture of 0.6.

This value is much below the displacement reproducibility of the sample holder. To characterize a reduction of the size of the laser spot to increase the PL resolution, one would have to use a more precise sample stage.

3.2 Multi-laser experiments in the VG microscope

To perform the actual optical pumping which uses both an IR laser (1064 nm) and a green PL excitation (here at 543 nm), I have built a more complex optical setup next to the VG microscope. This setup has up to three lasers (1064, 543 and 405 nm). The simultaneous use of the IR and green lasers is crucial to reproduce the ex-situ pumping experiments inside the VG electron microscope.

The IR laser cannot be aligned in the manner presented in section 3.1.1 with the spectrometer, since it does not excite any luminescence in FNDs. The technique used

is similar to that of the alignment of the 633 nm He-Ne laser, and then optimized by looking at the image of the sample. The IR laser heats the sample locally. When the laser power is increased, it changes the contrast on the sample: at the indicated area, the carbon membrane becomes darker. This effect is probably due to the heating of the membrane, and is irreversible. It can be used for in-situ sample cleaning.

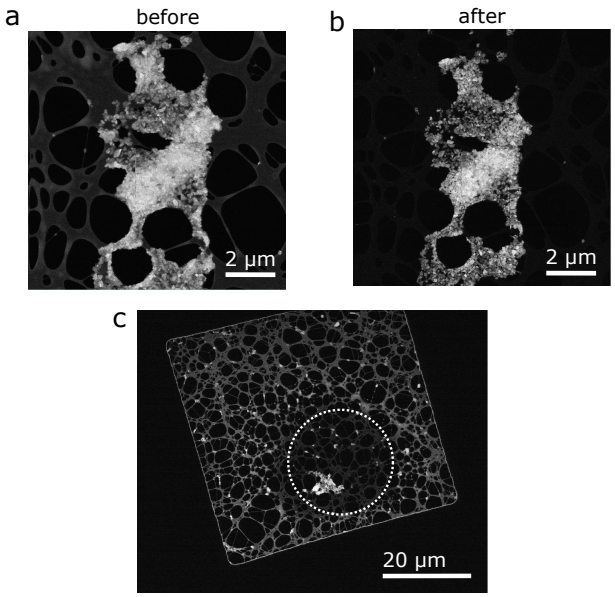

Figure 3.10: Influence of the 1064 nm laser on samples: (a) HAADF of a large FND aggregate before high power IR illumination. The carbon membrane supporting the diamonds are visible. **(b)** Same aggregate after high power IR illumination, the carbon membrane is less visible than in (a). **(c)** HAADF image of a hole of the TEM copper grid, with the carbon supporting membrane. The position of the IR laser beam is highlighted by the dotted circle. The size of the beam is actually smaller, since the darkened area shows the position were the membrane was heated sufficiently to remove the residue.

The optical setup with the two lasers is represented in Fig. 3.11, which has been used for the optical pumping experiments in chapter 4. The actual size of the laser beam could be measured in a scattering experiment, where the intensity of the laser beam is directly measured in hyperspectral imaging. Unfortunately, the spectrometer and detector used are not optimized for IR detection.

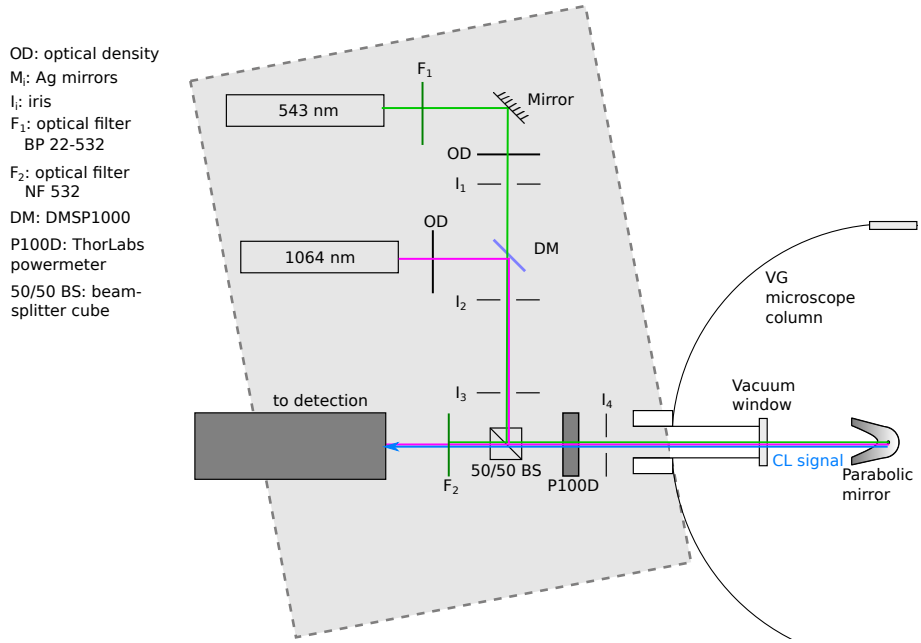

Figure 3.11: Scheme of the multi laser excitation for optical pumping in the VG: two lasers are brought in free space to the sample, a 543 nm He-Ne green laser, for the PL control experiment, and the 1064 nm solid state laser, for the optical pumping. They are superimposed by means of dichroic mirrors and aligned with a set of 4 irises.

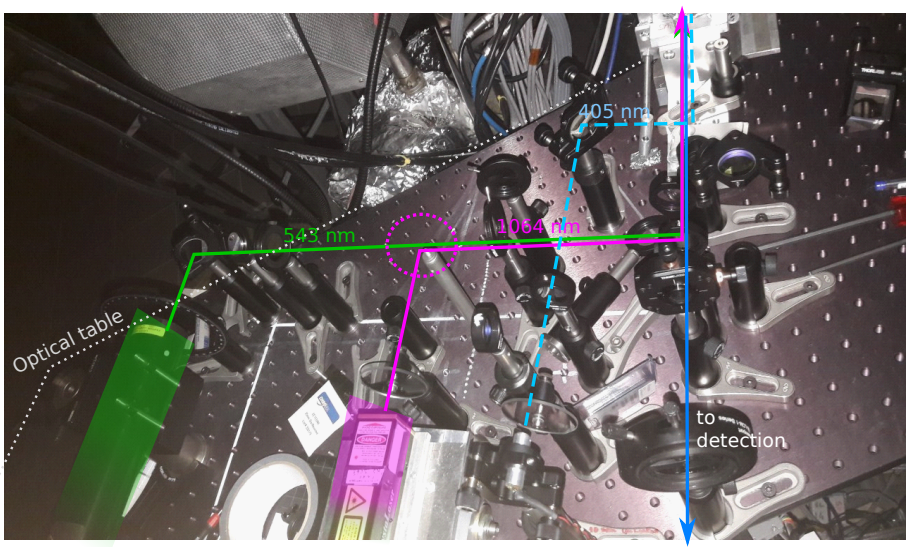

Figure 3.12: Picture of the actual setup: the optical table is delimited by the grey dashed line, and the laser paths are highlighted with colored arrows: in green the 543 nm He-Ne laser, in pink, the 1064 nm solid state laser (the circle indicates the position of the dichroic mirror that was not in place at the time of the photo), the blue dashed line, for the 405 nm laser diode, and in the continuous blue arrow, directed towards detection, the CL light emission path.

3.3 Photoluminescence setup in the ChromaTEM

There is not enough space in the ChromaTEM microscope box to place an optical table. Therefore a more compact system has to be used. The CL system from Attolight is compatible with ThorLabs cubes of 6 cm, which are the principal components of the compact PL setup, as shown in Fig. 3.13, 3.14 and 3.15. The compact PL system's alignment is independent of that of the electrons, which means that it

can be added during an experiment and aligned completely separately.

The main difference with the previous optical setup is that the laser sources are not on a table next to the microscope, but on a separate optical table. The lasers are brought to the system by means of optical fibers. The optical fiber used for light injection is a broadband monomode (core diameter 3 µm, operating wavelengths 400 to 680 nm - reference S405-XP) fiber coupled with the laser beam with collimators aligned at 532 nm. The monomode fiber acts as a spatial filter and the output beam is of high quality. For this reason, this type of fiber is important if one wants spatial resolution. The drawback is the laser beam power lost in the coupling, due to the fiber core small size. If high laser power is required, a large core fiber would be preferred.

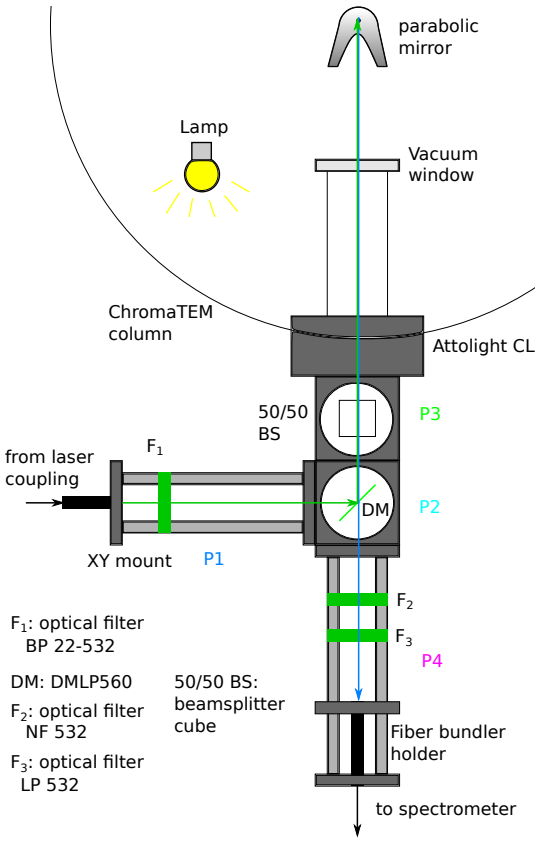

Figure 3.13: Scheme of the compact PL setup for ChromaTEM: the compact PL setup is made of four parts, P1 (laser coupling), P2 (dichroic mirror), P3 (beamsplitter for alignment, optional) and P4 (coupling to detection). These parts are attached to the microscope by the Attolight cathodoluminescence setup that is compatible with ThorLabs cubes. The 50/50 beamsplitter is used for superposition of the injected laser beam and the CL emission, and is directed to the top, where the ThorCam is attached (see Fig. 3.15).

The four parts composing the compact PL system are:

- P1: the first part is used for light injection. It is composed of a 3 cm cage, with the fiber being attached at one end with an XY mount. This mount allows for centering the laser beam in the optical system. The cages have an adapter that allows for attachment to the 6 cm cubes at the other end.
  Filters can be added to this part to ensure the laser line is the only light present. An optical density filter can also be added in the cages, nevertheless, both color filters and optical density can be put directly on the separate optical table with

the laser.

- P2: the second part has the dichroic mirror, which is the crucial part for PL detection. It enables the separation between the excitation and luminescence beams. The alignment of this section is the most important, it has to be precisely at 45°or else some cavity modes can modify the signal. For this reason, a home-made 3D-printed holder has been fabricated. The dichroic mirror can be aligned in angle in the optical axis direction. The other rotation axes can be oriented by the ThorLabs cube itself.

- P3: the third part has a beamsplitter directed to the top, where the ThorLabs camera is attached to the microscope. A power meter can also be put instead of the camera to measure the laser intensity fluctuations in real time.
  This beamsplitter part is optional and can be removed, since it decreases the laser power and light intensity in the detection.

- P4: the fourth and last part is the detection arm. It is made of a 3 cm cage system adapted on the 6 cm cubes. It has room for optics such as lenses (to increase the collection angle) or optical filters. The end of the optical fiber bundle is put on two optical mounts. Once the parabolic mirror is well centered and does not have any angle in the out of optical-axis direction, the detection is directly in the adequate position since all parts are attached together (if necessary, it can be optimized with a XY mount).

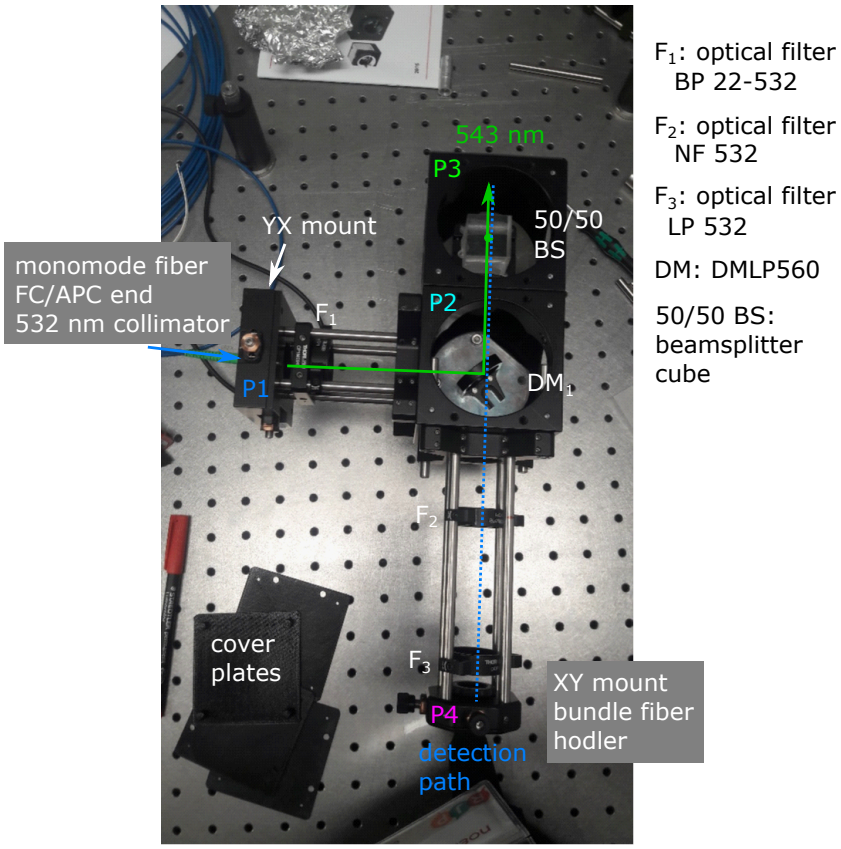

Figure 3.14: Compact PL setup: top view of the compact PL setup made for the ChromaTEM. The different components, P1, P2, P3 and P4 are labelled. The setup has to be attached to the microscope at the end of the green arrow. Cover plates have been 3D printed to ensure the limitation of parasitic light and the low weight of the setup.

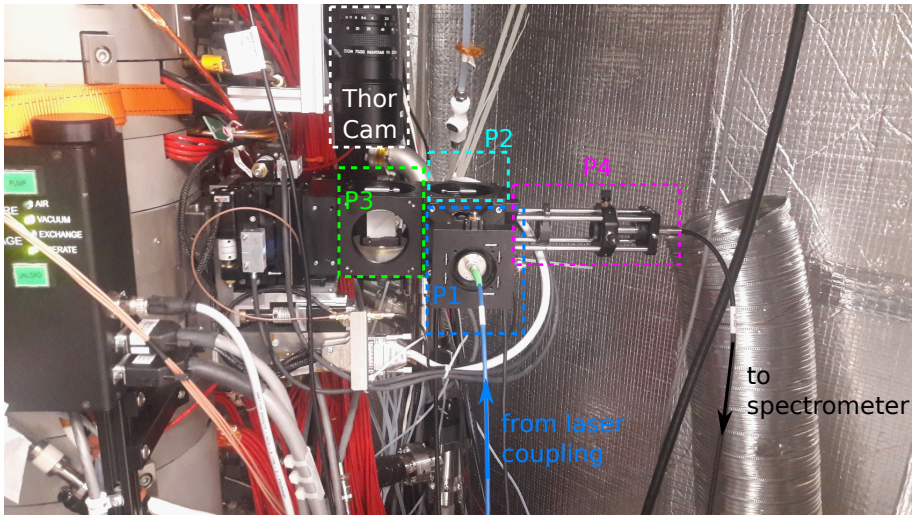

Figure 3.15: PL setup installed on the ChromaTEM: the four parts, P1, P2, P3 and P4 are highlighted. The ThorCam is attached directly on the microscope in a vertical position, corresponding to that of the 50/50 beamsplitter. The blue optical fiber is coupled at the other end to the excitation laser. The black optical fiber bundle is coupled to the optical spectrometer.

3.4 Temperature-controlled cathodoluminescence with micro electro mechanical system (MEMS)

NV centers in nanodiamonds are widely used as sensors, for nanoscale magnetic field [7] or temperature measurements [55, 56]. The latter can use the spectral changes of NV centers emission to probe the FND local environment. The measurements I have performed on temperature-controlled CL are shown in chapter 4.

In this section, the setup used for such an experiment is presented. To the best of our knowledge, the temperature-controlled CL-compatible cryo sample holder is the first one to combine all these capabilities in a STEM. It combines the cryo holder technology for imaging stability, and the local heating of the MEMS. The cryo sample holder is compatible with the modified Nion Hermes 200 (ChromaTEM), which has a 6 mm gap between the two sides of the electron objective lens pole pieces. This space is crucial for the STEM-CL experiments since it allows for the positioning of the 2 mm CL mirror and the single tilt cryo sample holder.

3.4.1 Device structure

The sample holder has been designed and constructed by HennyZ. It has a cooling system linked to a liquid nitrogen tank with a conductive braid that allows for cooling the samples down to 110 K. It enables mechanical stability for high resolution imaging. Indeed, the temperature outside the rod of the holder, close to the tip, is maintained at room temperature to avoid thermal drift of the sample due to exchange with the electron microscope column. The sample holder also has 6 electronic tracks that can be controlled outside of the microscope for sample heating and biasing through a MEMS system, which are described below.

With this setup, the temperature can be controlled from about 110 K to 1000 K. The sample holder is first cooled down with liquid nitrogen and the temperature is controlled by locally heating the MEMS.

The samples have to be specifically designed to work with this setup. The MEMS systems are made of Si chips with an Si_3N_4 membranes which support the micro circuits (made of Pt, with a Ta sticking layer). The MEMS are attached with carbon tape or vacuum-compatible Ag glue on alumina (Al_2O_3) plates and contacted with Al-Si wirebonds. The alumina plates contain 6 electrodes that fit the electric tracks of the holder, such as displayed in Fig. 3.16. The four central tracks are used for heating, whereas the two exterior ones are for biasing.

The electrical pins that are usually used to contact MEMS' electrodes could not be implemented on the holder due to the lack of space with the presence of the CL mirror, therefore HennyZ proposed a specific design where the MEMS are connected with the holder electric tracks through wirebond. The wirebonds need to be of a small height, due to the small size available inside the pole piece of the microscope.

The Si chip has a central hole, where only a thin Si_3N_4 membrane supports the micro circuit. This thin membrane hole enables STEM measurements since the electrons can be transmitted through the 200 nm Si_3N_4 membrane. The membrane itself can be pierced with holes using focused ion beam (FIB) to enable EELS measurements. The samples can be placed on the membrane by drop cast of liquids, such as what was done to deposit the FNDs, or by transfer and attachment of a crystal in a

FIB.

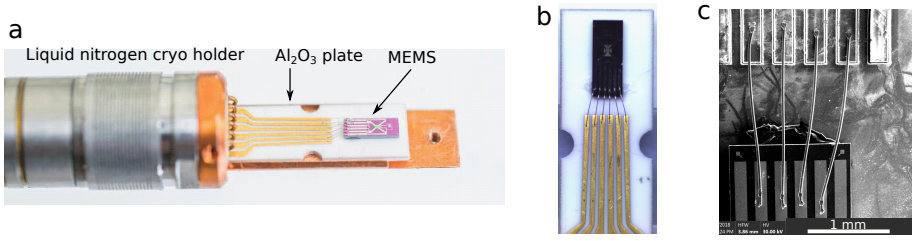

Figure 3.16: MEMS and HennyZ sample holder: (a) picture of the MEMS system (white plate with metal contacts and Si chip) on the sample holder tip, from © Cyril FRESILLON/LPS/CNRS Photothèque, **(b)** top view of the MEMS system, in white the alumina plate with TiAu contacts, bound by Pt wires to the MEMS engraved on the Si chip, **(c)** SEM image of the Pt contacts between the alumina plate and the Si chip, with the four contacts required for heating.

The MEMS and sample holder electronics (for thermal stabilization and sample heating) are controlled by a Raspberry Pi computer. The software used is called modular microscope instrument (MMI). It controls two main features: the dual heater, that controls the temperature of the outside rod of the holder close to the tip (which is in contact with the microscope column) for the stabilization of the sample holder for HR imaging, and the sample heater, which is the temperature regulation of the sample.

3.4.2 Heating

The sample on the MEMS is heated by injecting a current that heats locally the device through Joule's effect. The temperature is homogeneous across the membrane. The MEMS temperature is measured with the resistance R_T of the micro circuit by means of 4 points contacts. The temperature-dependent resistance R_T is related to the temperature T by :

$$R_T = R_0[1 + AT + BT^2], \tag{3.1}$$

where R_0 is the resistance measured at 0 °C, and the coefficient A and B are determined by a calibration and change for each MEMS batch produced. For the single tilt holder MEMS, the calibration coefficients are A = 3.908 $°C^{-1}$, and B = - 5.774 $°C^{-2}$. These values are measured for a MEMS having R_{300K} = 73 Ω (such as the MEMS labeled as D2). The other MEMS used, B33, has a R_{300K} = 93 Ω, so that the calibration coefficients are slightly imprecise. Imprecision on the temperature measurement can arise from the calibration of the MEMS, and the aging of the electrodes through multiple thermal cycles.

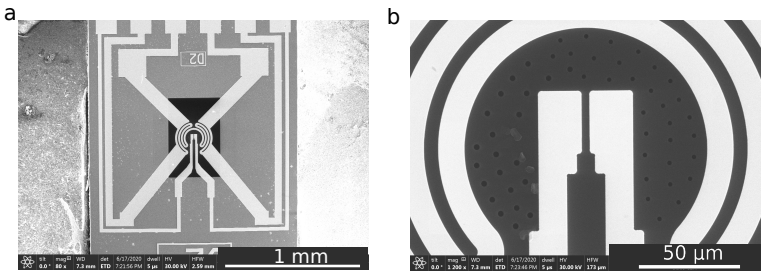

Figure 3.17: SEM images of the circuit on the MEMS: (a) image of the MEMS, in black the SiN membrane is visible, with the metal contacts going from the top tracks to the center of the SiN membrane with curls,**(b)** closer view of the heated part of the MEMS, with the SiN membrane pierced with holes made in FIB.

To understand if these measurements give the correct order of magnitude for the temperature, I designed a control experiment, using the CL of nanodiamonds as a standard. FNDs containing NV centers can be used as optical thermometers by tracking the spectral shape: the energy position of the zero phonon line (ZPL) or the FWHM of the ZPL [39]. We have done this for CL emission as a function of temperature in the range 160 K to about 240 K, and compared the tendencies with ensemble measurements of PL emission as a function of temperature found in the literature, measured in the range 5.6 K to 295 K from [57]. The results are shown in Fig. 3.18.

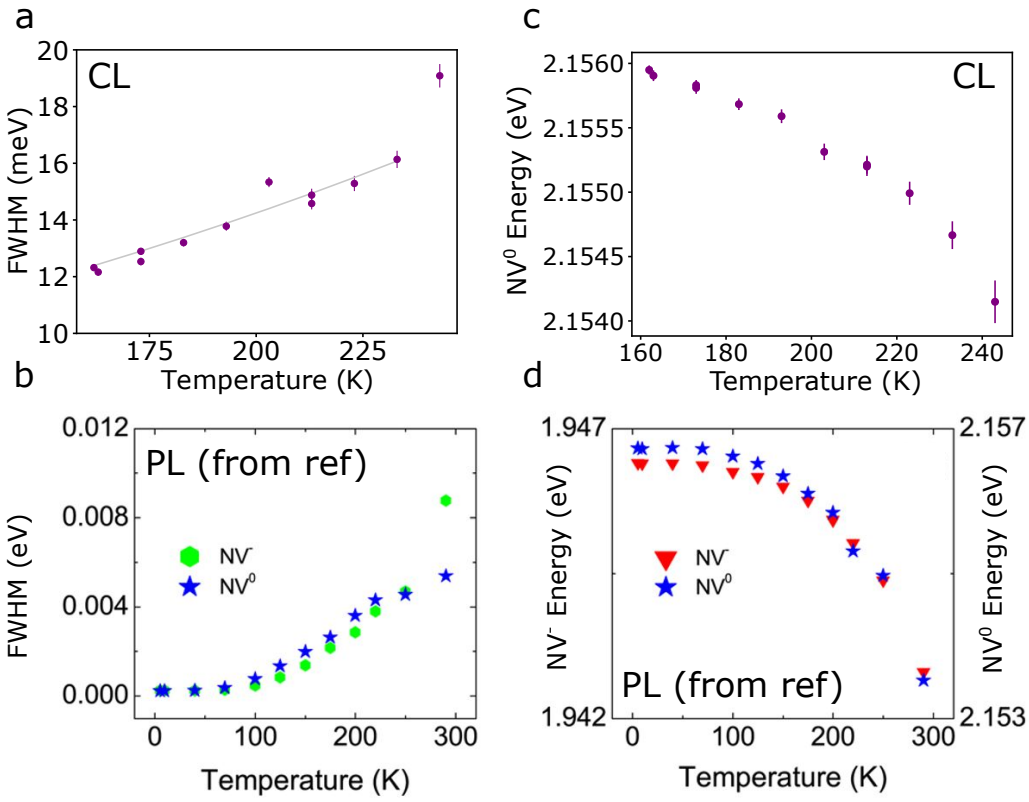

Figure 3.18: Comparison between temperature-controlled PL and CL experiments: (a) FWHM of the ZPL of NV^0 measured in CL on the D2 MEMS, **(b)** FWHM of the ZPL of NV^0 and NV^- measured in PL, reproduced from [57], the ZPL in both (a) and (b) are different due to sample quality difference, **(c)** energy change of the ZPL of NV^0 measured in CL, **(d)** energy change of the ZPL of NV^0 and NV^- measured in PL, reproduced from [57].

From the comparison between ensemble measurements on NV centers in CL and

PL, we can observe the same tendencies: a slow exponential increase of the FWHM with temperature, combined with a redshift of the ZPL.

These measurements can be used as temperature calibration measurements, since the MEMS measurement itself can be imprecise due to the imprecision on calibration. I have performed several measurements on two MEMS containing FNDs, and the results are presented in Fig. 3.19.

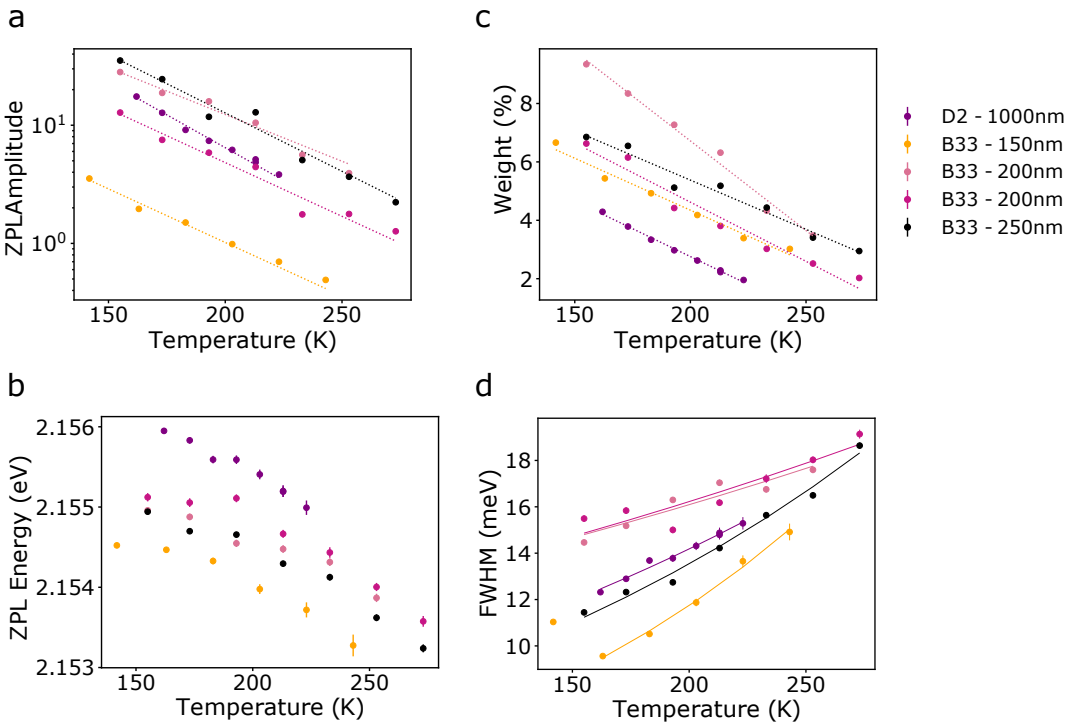

Figure 3.19: Comparison between the two MEMS (D2 and B33) used for the experiments: (a) amplitude of the zero phonon line (ZPL) of the NV centers for the 5 different area measured, labeled in the legend with the area sampled indicated, **(b)** ZPL energy, **(c)** weight of the ZPL in the CL spectra, **(d)** ZPL FWHM. The color code are labeled with the size of the area where the CL has been measured. For small areas, the use of CL emission can be unreliable due to the intrinsic differences between the FNDs.

Here, I compare the results obtained on the various temperature-controlled experiments performed. It has to be noted that the size of the areas measured vary from few hundreds of nanometers to about 1µm (labeled in the figure). The measurements from small areas contain only few FNDs, whereas a large area contains many FNDs. The spectral signature of each FND is unique (as shown in chapter 4), which produces discrepancies in the various measurements. The validity of using FNDs with NV centers as nanoscale thermometers is discussed in chapter 4.

3.5 Control experiments: PL under optical pumping

The goal of the optics experiments coupled in the electron microscope is to perform optical pumping of FND, such as described in chapter 4. In parallel to the setup next to the VG microscope, I have built an optical microscope to perform the purely optical laser pumping. The results have been compared to that in literature, and to that obtained in-situ.

This optical microscope has been made on a large optical table, with one to three laser sources in parallel (and the possibility to use lasers at 1064, 633, 543, 532 and 405 nm). The setup represented in Fig. 3.20 only shows the setup with 543 nm green laser and 1064 nm, which is the most important for chapter 4.

The FND sample is put on a smaller top table, 45 cm above the large optical table represented in Fig. 3.21. It can be illuminated from the bottom with a NA=1.2 oil immersion objective. Since thin lenses have chromatic aberrations, the optical path for IR and green laser is not exactly the same. Given that the IR spot is wider and does not trigger any luminescence, the limiting spot size is that of the green laser.

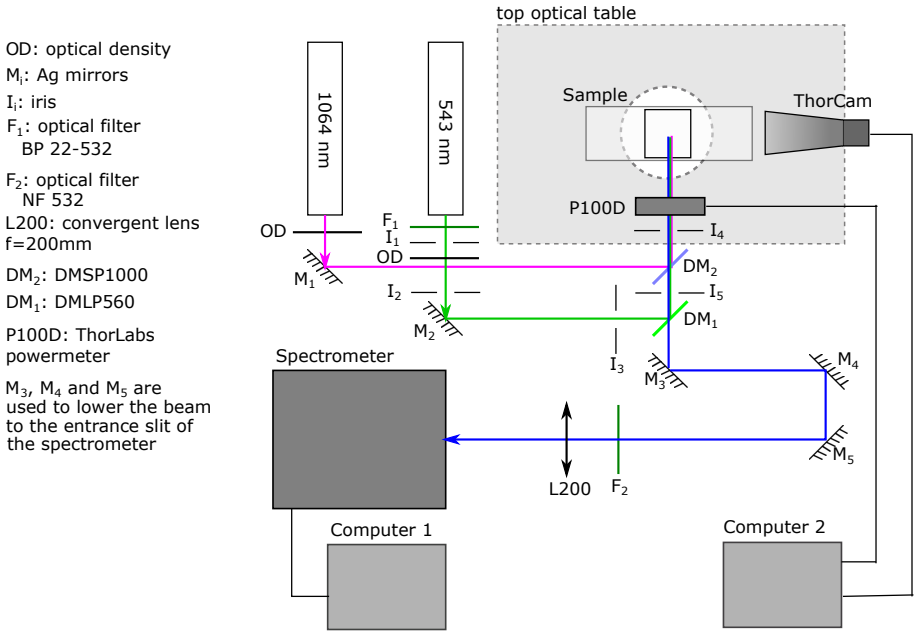

Figure 3.20: Optical table setup: the optical table contains two continuous lasers, a He-Ne at 543 nm and a 1064 nm solid-state laser. They are both directed independently to the objective though specific dichroic mirrors. The M_3 to M_5 mirrors are used to lower down the PL beam for the detection, since the spectrometer's entrance is lower than the others optics. A pinhole system can be added in the last part of the optical setup to enhance the spatial resolution, which is not represented here.

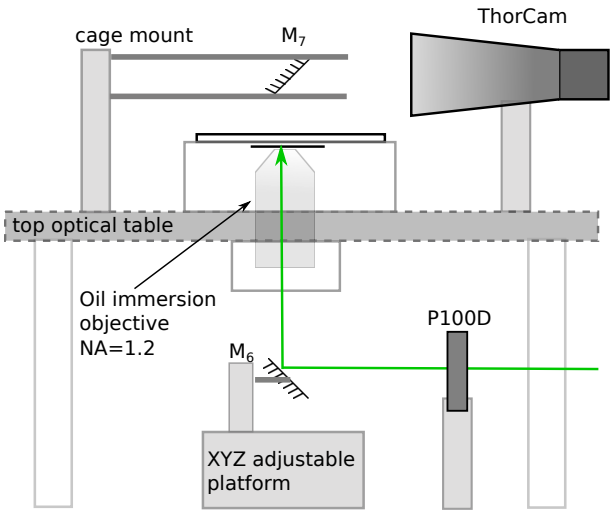

Figure 3.21: Top optical table setup: the top part of the optical table represented in grey in Fig. 3.20 is represented sideways. Only one light beam is represented for clarity since all optical paths are the same. The oil immersion objective is attached to the optical table with a home-made screw that allows for the fine focus of the objective on the sample. The superposition of the different laser beams is optimized with the ThorLabs camera.

The measurements performed on such setup were control experiments, to reproduce optical pumping from the literature, such as [9, 58]. The spatial resolution of the setup was not optimized since only ensemble measurements were targeted.

3.6 Summary

The technical details about the different µ-PL systems that have been created to perform optical pumping of NV centers, both inside and outside of the VG STEM microscope, have been presented in this chapter. A mechanical hyperspectral acquisition method has been developed for the µ-PL measurements with spatial resolution.

A compact PL system has been built for the ChromaTEM, that enable facile alignment and collection of the PL signal. The PL alignments are completely independent from the electron beam alignments, which allows for adding/removing the PL system during an experiment without realignment of the microscope.

The temperature-controlled CL experiments in a STEM have been performed in the ChromaTEM using a specific cryo single tilt holder that can be used with MEMS for heating and biasing. FNDs containing NV centers as optical nanothermometers have been used, that can be further taken as a reference for temperature measurements.

Chapter 4

Photoluminescence and cathodoluminescence of Nitrogen-Vacancy centers in nanodiamonds

Contents

Pure diamonds are naturally transparent (E_{gap}=5.54 eV [59]) with one of the highest natural refractive index, giving them their characteristic shine. What makes a diamond expensive, while it actually is a very common material, is its purity. Many natural diamonds are doped with nitrogen atoms, since it is one of the main components of the atmosphere. This doping changes the color of diamonds from transparent to yellow, because several nitrogen related defects absorb in the blue and red [60]. Other defects give various colors to diamonds, such as boron doping, which gives them a blue color. For this reason, these doping defects are known as color centers, since the doping itself gives a color to the diamond matrix. Indeed, the defects create new energy levels in the diamond bandgap, which can absorb and emit light in the visible range [60].

If a diamond is rich in substitutional nitrogen (N) and in vacancies (V), which are missing carbon atoms in the diamond lattice, both defects can combine, creating a new type of defect, the nitrogen-vacancy center (NV). NV centers absorb light in the green range of the spectrum, making diamonds pink. They also make diamonds fluorescent under green or blue excitation, and the light emitted is red, as detailed

in the later parts of the chapter. The NV centers have exciting physical properties: they are the brightest stable room-temperature single photon sources [61], have the highest temporal coherence (up to few ms [62]), and are two-level systems that can be used to produce solid-state qubits [5, 63, 64].

NV centers have been used in the previous chapter as bright light emitting sources for alignment. Here I specifically looked at the optical properties of these defects by measuring their emission in different situations. Indeed, even with the massive number of publications on NV centers, some phenomena remain unclear, such as the mechanism leading to the cathodoluminescence (CL) emission of only one out of three of the NV charge-states [8]. Moreover, NV centers can contain different number of electrons, leading to different charge-states, which are described in the first section of this chapter.

In PL, the excitation and de-excitation mechanisms have been characterized with photoluminescence excitation (PLE) experiments. In these experiments, the excitation energy is varied, and the emission amplitude at a specific energy is measured. By selecting the energy both in excitation and in emission, one can understand the full excitation and de-excitation mechanisms. In CL, this type of experiment is not yet possible, since the electron beam excitation is not monochromatic. Therefore, other methods are necessary to understand the processes, such as pump probe experiments [8]. Here, I have used continuous wave optical pumping by combining laser and electron beams. The optical pumping of the NV centers inside the electron microscope can lead to sample heating. I further characterized the sample heating induced by the laser by measuring the CL as a function of the temperature, with the MEMS system described in chapter 3.

The chapter is organized as follows: in section 4.1, I introduce the NV centers, the context of our work and the major applications. Then, in section 4.2, I present results on pure CL measurements, including the CL from the smallest fluorescent nanodiamond (FND) detected, the charge-state conversion and the irradiation damages induced by the electron beam. I present the temperature-controlled CL results in section 4.3. The PL charge-state conversion by IR, green and UV laser light is presented in section 4.4. Finally, the results on combined laser and electron beams are shown in section 4.5.

4.1 Generalities

Diamonds are made of carbon atoms in a face-centered cubic lattice structure that has 8 atoms per unit cell. The supplementary atoms added from the usual face-centered cubic lattice are placed at 1/4 of the diagonals of the cube, which makes it into two inter penetrating FCC lattices. Diamond belongs to the $Fd\bar{3}m$ space group. The lattice parameter is 2.527 Å and its bandgap energy value is 5.54 eV [9]. Its refractive index is 2.41 at 500 nm which makes it one of the highest for a natural material.

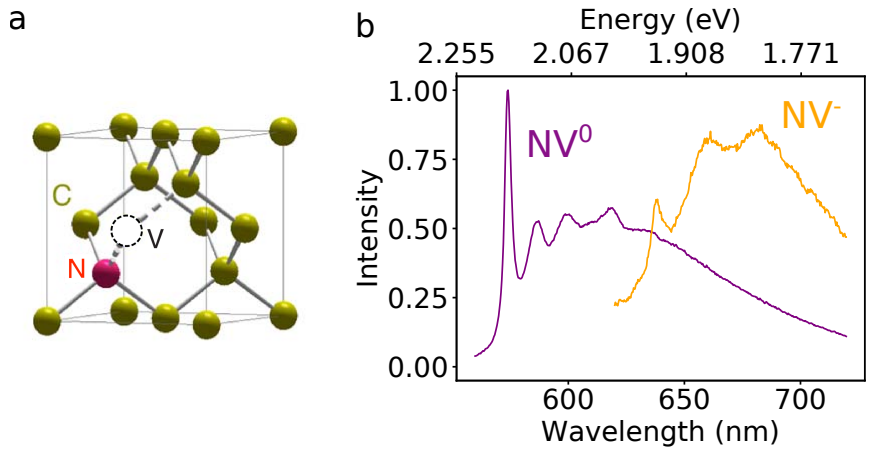

Figure 4.1: Structure and emission spectra of the NV center: (a) scheme of the diamond lattice with a nitrogen vacancy center, **(b)** emission spectra from the two charge-states NV^0 (CL, purple curve) and NV^- (PL, orange curve) described in section 4.1.1

Nanodiamonds are used instead of a bulk diamond to improve light collection. The FNDs are from H-C Chang (National Taiwan Normal University). With its high refractive index, the internal reflectivity of light prevents efficient collection of CL emission. Even with a thin plate the collection is not optimal. Indeed, a cavity mode can appear for a thickness of about 200 nm at 575 nm ($\lambda_m/2L = N$, where λ_m is the wavelength of light in the material, L the length of the cavity, and N the number of modes, here we used N=1), since the diamond refractive index is 2.41. Nanodiamonds have also the advantage of not charging under electron beam irradiation (since diamond is an insulating material) as much as a wide plate, which helps for the localized CL excitation.

FNDs containing a high density of NV centers can be produced by detonation, by laser irradiation of carbon black in water (under ambient conditions) [65], or by microwave plasma chemical vapor deposition [66]. The number of NV centers can be further increased by irradiation and annealing of the nanodiamonds [65].

The experiments described below are performed on various types of TEM grids:

- Lacey carbon copper grid, which is the one with the lowest surface area of membrane, preventing the fluorescence from the grid to conceal the PL of the FNDs,
- Holey carbon copper grid, which is similar to the lacey carbon, but allows for larger FNDs aggregates,
- Si grids with a continuous Si_3N_4 membrane, for CL only due to the membrane fluorescence under laser illumination.

The FNDs are deposited on the grid from deionized water solutions containing different sizes of FNDs, from about 40 nm to 100 nm. Two deposition protocols are used:

- for low concentration samples, the TEM grid is placed on a filter paper and diluted solution is drop cast on the grid,
- for high concentration samples, the TEM grid is suspended with tweezers, and the liquid drop cast on it is let completely to dry, so that all the FNDs stay on the grid.

The FNDs solutions can be diluted with deionized water, isopropanol (which forms small aggregates), or ethanol (which dries faster than water).

4.1.1 NV Charge-states

Isolated in the pure diamond matrix, NV centers are in the neutral form, which is labeled NV^0. There are four valence electrons in the center [67]. In the presence of electron donors, such as substitutional N atoms, the NV centers can capture a supplementary electron [58]. The center thus formed has five electrons, and is called negatively-charged NV center, and labeled NV^-. The two charge-states of NV centers, NV^0 and NV^-, can be distinguished by their emission spectra with peaks at: 575 nm (2.156 eV) for NV^0 and 637 nm (1.947 eV) for NV^- [60] (Fig. 4.1). Their energy structure also differ, making them suitable for distinct applications.

It has to be noted that a third charge-state exists, NV^+, which is not described here since it is electronic spinless and optically inactive [68].

Charge-states energy structure:

Fig. 4.2 represents the energy structure of NV^- and NV^0. NV^- centers have a triplet transitions and two singlet dark states [67]. Whereas NV^0 transitions are doublet, with no dark states. At zero magnetic and electric field, the energy states of the NV^- and NV^- centers are not strictly degenerate: local strain variations sligthly lifts the degeneracy [69].

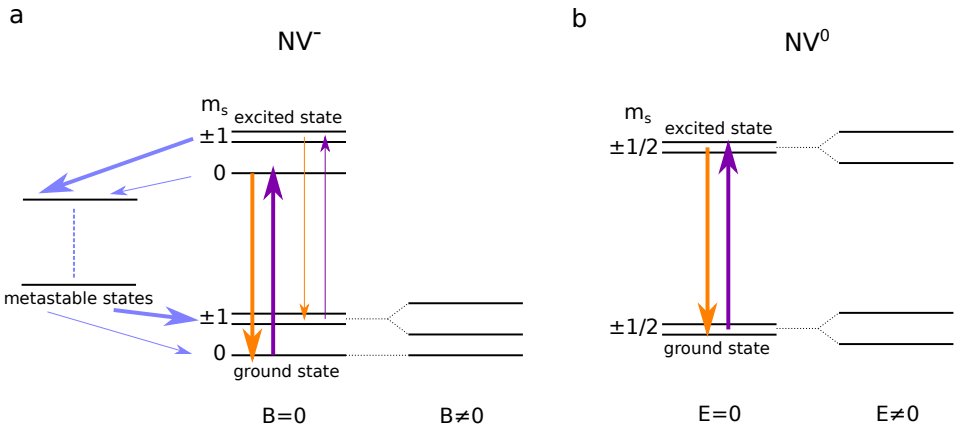

Figure 4.2: Energy structure of NV^0 and NV^-: (a) NV^- energy structure, the ground (^3A) and excited (^3E) triplet states degenerate, and the degeneracy of the m_s=±1 levels can be lifted by Zeeman effect by applying a magnetic field. The m_s=±1 levels are efficiently coupled to the singlet metastable states (top: ^1E and bottom ^1A), which are non-radiative. Therefore, the optical transition from m_s=0 level is brighter than that of m_s=± 1. **(b)** NV^0 energy structure. The ground (^2A) and excited (^2E) states are two times degenerate, and form dipole transitions perpendicular to each other. The degeneracy of the levels can be lifted by Stark effect by applying an electric field [70].

The lifting of degeneracy of the ground state of NV^- with a magnetic field by Zeeman effect makes it well suited for magnetic field sensing, which is described in section 4.1.2. The NV^0 energy levels' degeneracy can be lifted by application of an oriented electric field, which makes them well suited for state preparation and read out with polarized light.

The NV centers are efficient single photon sources. Their second order correlation function, $g^{(2)}(\tau)$ (its measurement and principle is described in chapter 2) are different for the two radiative charge-states. Since NV^- has metastable (singlet) dark states, its $g^{(2)}(\tau)$ function displays a shoulder at non-zero time delay, whereas

for NV^0 the curve is a usual exponential profile [34, 71]. With this method, the lifetime can be measured with an exponential fit, and for NV centers of nanodiamonds it is about 20 ns at 150 K [22]. The $g^{(2)}(\tau)$ measurement can be a way to distinguish NV^0 and NV^-.

NV photoluminescence:

Since the difference between NV^0 and NV^- is an electron, the charge-state of a single center can change over time. This is seen by measuring the emission from a single center, where both signatures of NV^- and NV^0 are present [51, 71]. This behavior is called photochromism.

As described in details in section 4.4, multi-laser excitation can favor one or the other charge-state, by means of photoionization of either the NV^- center, or ionization of the N substitutional atoms.

Another way of tuning the charge-state is by using charged liquid electrolytes. The gating of the electrolyte shifts the Fermi level at the diamond surface [72]. The type of surface state of the diamond is crucial (here it is H-terminated, which are acceptor states). In this case the NV centers are very close to the surface (7 and 10 nm).

Even if CL can be considered as a nanoscale counterpart of out-of-resonance PL [4], in some cases the measured spectra by the two techniques differ. This is the case for the emission of NV centers.

NV cathodoluminescence:

Indeed, in CL, only the NV^0 spectral signature is seen [60, 73]. This is due to a rapid ionization of the center by the electron beam [8], explained in more details in section 4.2. In CL, NV centers can be addressed individually [73] and the lifetime measured in nanodiamonds is about 18 ns, which matches that measured in PL. Due to the small carrier diffusion length (the spatial resolution of CL is discussed in chapter 2), individual NV centers can be addressed even if their are within the same nanodiamond.

In section 4.4, I have tried to optically convert the NV center charge-state to obtain CL emission from NV^-. The CL emission from NV^- was not observed, probably due to sample heating.

NV emission spectral shape:

Fig. 4.3 is a plot of the spectra of NV^- and NV^0 measured respectively in CL and PL (excitation at 543 nm).

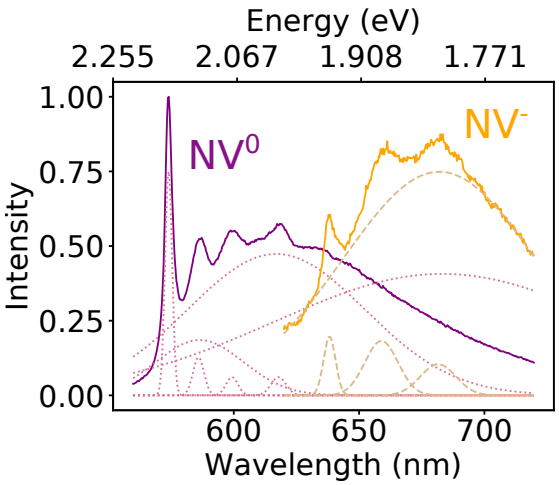

Figure 4.3: Spectral shape of NV^0 and NV^-: NV^0 spectrum (CL, purple curve) and NV^- spectrum (PL, orange curve). The zero phonon line for NV^0 is at 575 nm (2.157 eV) whereas that of NV^- is at 637 nm (1.947 eV). The Gaussian fit of ZPL and phonon replicas are represented in dotted (resp. dashed) lines for NV^0 (resp. NV^-). The measurements were performed at 150 K.

The spectral shape of NV^- includes a zero phonon line (ZPL) at 637 nm (1.945 eV). At the ZPL, the absorption and emission can occur at the same energy (the general spectral shape of absorption and emission are presented in chapter 2). At 8 K, the NV spectra also have four increasingly broad phonon replicas, with a phonon energy of about 63 meV. The weight of the ZPL is 2.4 % and the Huang-Rhys (HR) factor (coupling between the optical transition and the phonon emission) is S=3.73 [60]. The weight of the ZPL changes with temperature [56], whereas the HR factor is a constant [33].

NV photoluminescence excitation:

As shortly presented in the introduction of this chapter, PLE experiments give access to the excitation and de-excitation paths. For NV centers, they give insights about the mechanisms behind the charge-state transfers occurring when excited at different wavelengths (the PLE process is detailed in chapter 2). Two main behaviors are seen in PLE. They depend on the nitrogen concentration in the diamond matrix.

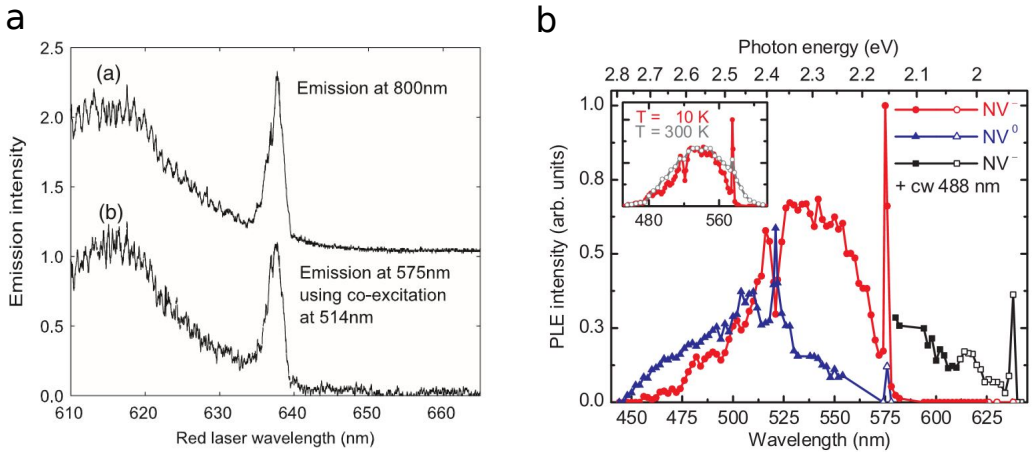

Figure 4.4: PLE measurements from references: (a) PLE measurement with high ($\approx$ 70 ppm) N doping, from reference [58] **(b)** PLE measurement with low (< 5 ppb) N doping, from reference [51].

For high N doping, in the order of 70 ppm, corresponding to 10^6 to 10^8 NV centers/cm^3, the PLE shows absorption from the NV^- center (from 600 to 637 nm) [58]. At these energies, the absorption from NV^0 is not seen, unless an additional green (514 nm) laser is used. This highlights the fact that for high N doping, the NV centers are in the NV^- charge-state. This is further seen with the PL spectrum of the FNDs that displays features only from NV^- at low laser power (λ_{exc} = 532 nm). This order of magnitude of N doping corresponds to that of our sample.

For low N doping (< 5 ppb), the opposite is observed: in the energy range 575 to 637 nm, no emission is measured, for both NV^0 and NV^-, unless a blue (488 nm) laser is added [51]. The NV absorption features (450 to 575 nm) for both NV^0 and NV^- emission are observed. This points out that for low N doping, the preferred charge-state is the NV^0.

These two situations are important to distinguish. Indeed, many PL experiments use sample with diluted NV centers to be able to address them individually. This greatly changes the charge-state conversion dynamics.

To summarize the charge-state conversion with out-of-resonance excitation, four different regimes can be separated, by comparing the energies of the excitation E_{exc}, that of the NV centers' optical transitions E_{NV}, and the bandgap of diamond E_{gap}:

$\mathbf{E}_{exc} < E_{NV} < E_{gap}$	$NV^0 \rightarrow NV^-$	no luminescence
$E_{NV} \leq \mathbf{E}_{exc} < E_{gap}$	$NV^- \rightarrow NV^0$	emission from both NV^0 and NV^-
$E_{NV} < E_{gap} < \mathbf{E}_{exc}$	$NV^- \rightarrow NV^0$	emission from both NV^0 and NV^-
$E_{NV} < E_{gap} \ll \mathbf{E}_{exc}$		emission from only NV^0

The four energy regimes have been investigated in this chapter, and are described in the following sections.

4.1.2 Major applications

Solid-state qubits:

In the NV^- ground state, electrons bound to the color centers have a net S=1 spin. The spin coherence is affected by magnetic interactions with surrounding electrons and nuclei spins. Interaction between the NV^- center and the ^{13}C nucleus allows to access to individual nuclear spins even at room temperature [74]. The ^{13}C center nuclear spin is I=1. The measurement consists of a correlation of the electron spin state with the nuclear spin state, and optical readout of the electron spin state. Logic operations between qubits can be achieved by selective excitation of transitions.

Cryptography:

This application uses mostly the fact that NV centers are bright and stable single photon sources. An electro-optical modulator (using a birefringent crystal with varying applied voltage) can polarize the emission on demand (linear horizontal/vertical, circular left/right) [34]. This polarization encrypts the message. It is then read by the receptor by using different projection bases (linear or circular). The intrinsic quantum properties of photons prevent the message to be read by a spy, since the reading of the message is a projection, and alters the photons themselves.

Thermometry (with electronic spin time coherence measurement):

The coherence time of the NV^- electronic spin is known to depend on temperature and can be exploited to measure it [55]. In the reference, they incorporate the FNDs containing many NV centers and gold nanoparticles to a human embryonic cell. They use a laser to excite the gold nanoparticles, which heat their local environment. Then the temperature variation with micrometric spatial resolution is probed by measuring the coherence time of the NV centers in various FND inside the cell [55]. Temperature variations in the range 200 - 600 K are detected.

Magnetometry:

NV centers can be used as nanosensors for local magnetic fields [7]. These measurements are non-invasive, since they use the lift of degeneracy between the two ms=$\pm$1 levels with Zeeman effect. Spatially resolved measurements are possible with a device made of a nanodiamond containing a unique NV center placed on an AFM tip. The tip is brought close to the magnetic surface to scan it. The separation between the two ms=$\pm$1 levels changes with the magnetic. This splitting can be measured in fluorescence since the m_s=$\pm$1 level is darker than the m_s=0 level. The transitions from m_s=$\pm$1 then appear as dips on the spectrum, which is measured by scanning a microwave field around the ground state energy level.

Biology:

Fluorescent nanodiamonds containing NV centers can be functionalized to bind to specific organelles in cells [75]. Correlative nanoscale imaging can then be used to measure the position and the emission of such nanoparticles inside the cell and understand the cell-nanoparticle interaction. In the reference, they have used a technique similar to CL, but instead of using electrons they use He^{2+} ions to excite the NV centers and map the cells.

4.2 Cathodoluminescence

CL of FND as small as 40 nm have previously been detected [76]. With the ChromaTEM CL setup, that result has been improved by measuring CL from FNDs as small as 15 nm, such as displayed in Fig. 4.6.

Various factors have helped to achieve this:

- the localization of the electron probe to an Å-sized beam, with the use of an aberration-corrected microscope, which leads to higher current density,
- the lower temperature of the cryo sample holder (about 110K),
- the high NA(=0.5) of the mirror, and its precise alignment.

The spatially-resolved measurement shown in Fig. 4.5 has a dwell time of 50 ms. At each position (pixel) a CL spectrum is measured. The intensity map is obtained by integrating the spectra over the range 570 to 590 nm (ZPL of NV^0), and normalized. A correlation between the intensity of the CL emission and the ADF image showing the positions of the FNDs can be retrieved. This measurement highlights the possibility for high spatial resolution CL acquisition.

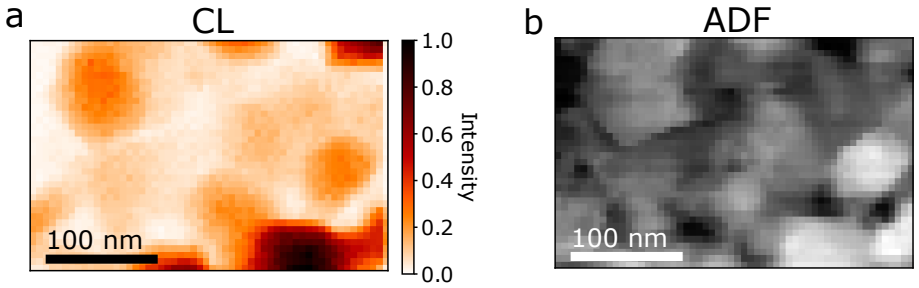

Figure 4.5: CL measurements of an aggregate of FNDs: (a) CL energy-filtered intensity of an aggregate (570-590 nm), **(b)** ADF image of the area.

Fig. 4.6 shows the smallest FNDs for which CL has been detected. The spectrum measured by exciting the FND during 75 s shows the NV^0 spectral features clearly (the ZPL and the phonon replicas) as well as a higher energy bump, from vacancy-related defects.

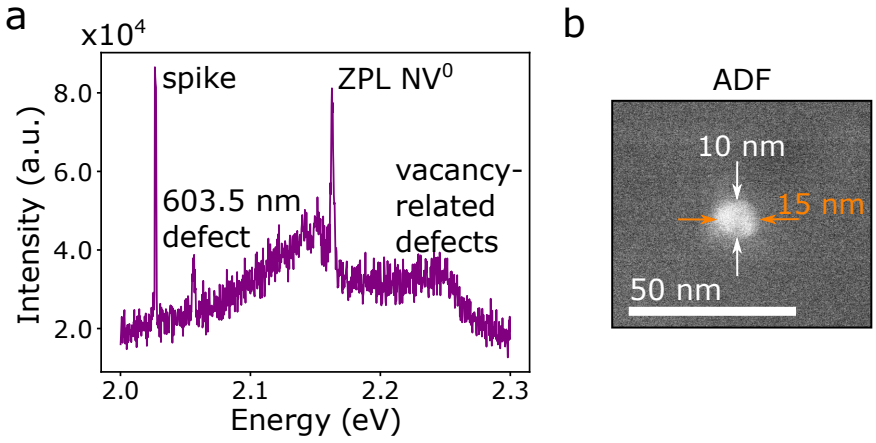

Figure 4.6: CL measurement of the smallest FND: (a) spectrum measured with the electron beam positioned on the FND, the defects emission contributions [60] are labeled on the spectrum, **(b)** ADF image of the FND.

4.2.1 Charge-state conversion by the electron beam

As shortly described in section 4.1.1, in CL, only NV^0 spectral features are observed. In this case, the excitation energy is much higher. The typical kinetic energy of the electron beam in CL, 60 keV, leading to the excitation of bulk plasmons of about 30 eV [22]. The CL excitation process is described in chapter 2. The energy of the bulk plasmon, which is the origin of the CL excitation, is much higher than that of the gap of diamond (E_{gap} = 5.5 eV). This illustrates the case $E_{exc} \gg E_{gap}$.

As seen in chapter 2, the interaction between the sample and the fast electron beam can create a bulk plasmon, whose energy is about three times the bandgap of the materials [24]. The bulk plasmon then decays into charge carriers that can form excitons that recombine radiatively in NV centers [22]. The dynamics of this process have been measured in time-resolved SEM [8], where a carrier diffusion of about 0.8 ns is estimated. The NV^0 decay is measured to be 20 ns and the NV^0 to NV^- back conversion, to be 500 ms. In the reference, the measurements have been performed in a SEM at 5 keV, where the interaction volume was estimated to be 0.4 μm^3. This large value is due to the SEM carrier diffusion, which creates more charge carriers in the sample than in a STEM. A 300 µm thick single-crystal with 1.2 ppb NV centers

and a coating with a charge dissipating layer was used. The NV^0 emission does not saturate when increasing the current. The authors estimated that each bulk plasmon creates about 2 e-h pairs [20].

4.2.2 Long electron irradiation

After a week of measurements on a thick nanodiamond aggregate that was used for the laser alignments and superposition of CL signal, I noticed an important increase of the signal to noise ratio (SNR) of the spectrum: at the beginning of the week, it was 12.5, and at the end of the week 1592. With a closer look at the spectrum, I saw the appearance of new high-energy peaks such as plotted in Fig. 4.7. Here, the experiment has only been made once, and was not reproduced (since the effect was already known). The irradiation experiment could be tried with and without the IR laser to compare the number of NV centers produced, and thus see if the IR heating is sufficient to enhance the NV center production.

The three new centers that appeared are [60]:
- 2.462 eV (503.4 nm): the NNV point defect, referred to as H3 center,
- 2.556 eV (483 nm): a vacancy-related defect,
- 3.188 eV (389 nm): a radiation damage product related to N^+ implantation. In diamond, substitutional nitrogen atoms are neutral, and can be ionized. In particular with IR excitation, the electron from N atoms can be transferred to NV centers.

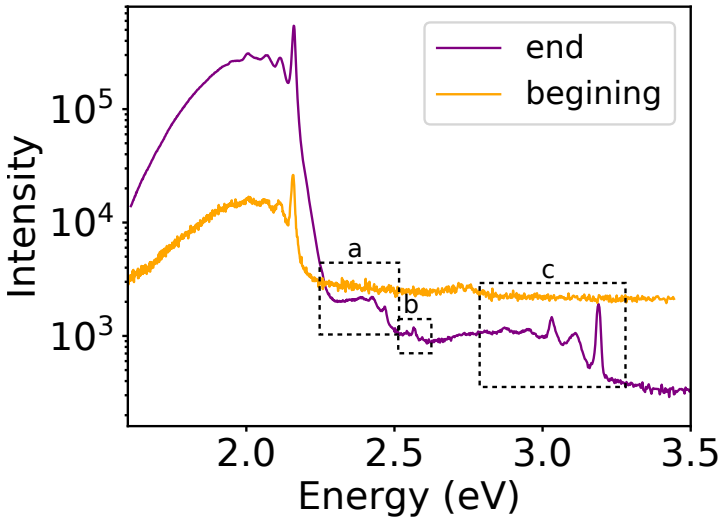

Figure 4.7: Effects of long electron irradiation: Measured spectra before (orange curve) and after (purple curve) a few days of experiments on the same nanodiamonds aggregate. The new peaks that appeared are highlighted in dashed boxes, **a** is the H3 center (NNV), **b** is the 2.556 eV center (related to vacancies), and **c** is the 3.188 eV defect (related to N^+).

The three new defects observed are all related to radiation damage. The increase in SNR from the NV emission can be explained by an increase of NV center number. This can be caused by the increase of vacancy number. Since the N doping is high in NV-rich FNDs (of the order of 100ppm), the chance of creating vacancies next to N atoms is non-zero. As the sample was illuminated with various laser beams, it may have heated the FNDs enough to make the vacancies mobile. The vacancies may

then have moved next to the substitutional N atoms to form new NV centers [65, 66].

The creation of vacancies in diamond to form more NV centers has been investigated previously in TEM [77]. The electron beam was used to irradiate a diamond sample to create vacancies, which can form the NV centers. The in-situ increase of NV center number is most efficient for thick diamond samples, and the vacancy creation is most efficient at about 200 nm of depth.

This effect is important to take into account, in particular in the framework of this thesis, which had an initial goal of creating qubits out of NV centers in the electron microscope. For example, if one created such a device, it could completely change over time if a new center was created with the electron beam excitation. Nevertheless, it also could create a new NV center next to an already existing one, and it could be interesting to look at the coupling between the two centers.

4.3 Temperature-controlled cathodoluminescence

Due to the increasing number nanoscale electronic devices, which generate heat, nanoscale temperature measurements are widely investigated [78]. Two main categories of nanoscale thermometers interest us here, the non-luminescent (e.g. nanoscale thermocouples, nanotubes with thermal expansion of liquids, Coulomb blockade nanothermometers, SIM tunnel junctions, MEMS based thermometers [40], plasmon energy in EELS [79] etc.) and luminescent thermometers (e.g. organic dyes, quantum dots, doped nanoparticles, blackbody radiation from metal nanoparticles, etc.) [39, 40].

Here, I have used two temperature measurements in tandem, the first from a MEMS and the second from the CL of FNDs containing NV centers. The question is to determine the validity of using spectral variations in individual NV centers for temperature measurements at the nanoscale. In this section, I present results on the CL spectral variation of NV centers in nanodiamonds using a STEM heating stage in the simple tilt cryo sample holder from HennyZ, described in more details in chapter 3. The nanodiamonds sit on a Si_3N_4 membrane that has been pierced with holes using a focused ion beam (FIB).

Light-emitting based nanothermometers can use various changing parameters such as the spectral position, the bandwidth, the bandshape, the intensity, the lifetime or the polarization (see section 2.4 in chapter 2). The spectral variations with temperature are detailed in chapter 2. The intensity variation with temperature T can be described by a Boltzmann distribution $I \propto gAE \exp\left(-\frac{E}{k_B T}\right)$, where g is degeneracy of states, A, the spontaneous emission rate, and E, the energy of the level.

Temperature is known to play an important role in the spectral shape of point defects emission [39]. To the best of our knowledge, the CL temperature dependence of the spectral shape has not yet been investigated in STEM. Some measurements of the nanoscale temperature have been performed in STEM EELS, by using the temperature dependence of the energy of plasmons [40]. SEM CL temperature measurements were performed by using the maximum of emission of semiconducting nanowires [80]. In the latter experiment, the authors have used the SEM electron beam both as the heat source and heat probe. Indeed, in SEM, most of the energy of the incoming electron beam is deposited into the sample. A large fraction of the energy is then dissipated through heat losses. For this reason, one has to precisely

know the current of the probe as well as the nature of the sample (composition, doping etc.) to retrieve the temperature.

The solution I propose here uses a transmitted fast electron beam, which induces negligible heating in the sample. Furthermore, the STEM spatial resolution is higher than that of SEM, allowing to access more localized phenomena. These experiments highlights how the CL emission of ensembles of NV centers can be used as a reference of temperature for further temperature-controlled CL experiments. Indeed, NV centers have been used as nanoscale temperature sensors, using various techniques including:

- the measurement of the spectral shape of NV centers [56],
- the measurement of the coherence time of NV centers [55].

Fig 4.8 shows an overview of the temperature-controlled CL measurement: the ADF and CL intensity images show FNDs about 100 nm wide. The FNDs have various number of NV centers, as well as different sizes and shapes. Thus, their emission intensity vary when excited by the electron beam. The spectral shape of the emission also depends on the FND excited, which is illustrated by the extracted spectra on Fig. 4.8 c-f.

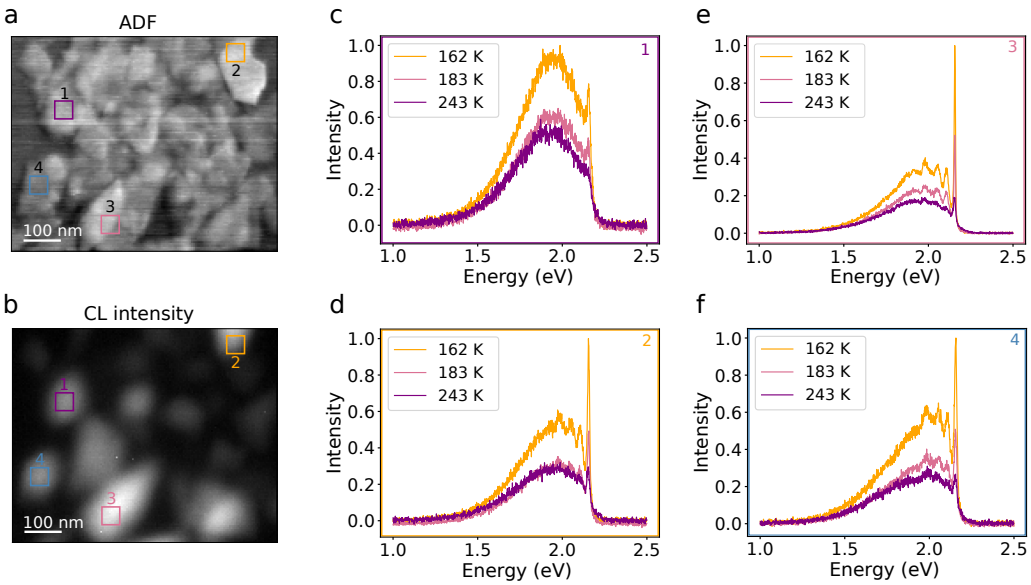

Figure 4.8: Temperature effect on CL spectra of individual nanodiamonds: **(a)** ADF image of the area with squares corresponding to the position of the (c-f) spectra, **(b)** corresponding CL intensity image, **(c-f)** spectra extracted from the indicated position, at three different temperatures, -111°C, -90°C and -30°C. For each nanodiamond, the emission spectrum has a specific shape, and the evolution with temperature is different.

Various parameters, such as the intensity, the energy position, the FWHM and the ZPL weight of the spectra can be used to characterize the temperature dependence of the spectra, such as illustrated in Fig. 4.9. The ZPL weight is extracted by integrating the ZPL peak from a Gaussian fit of the spectrum, and dividing the value by the integrated phonon side-band. These are extracted from the temperature-dependent CL data, for the summed spectra over the whole displayed area (Fig. 4.9), and for the four individual FNDs (Fig. 4.10).

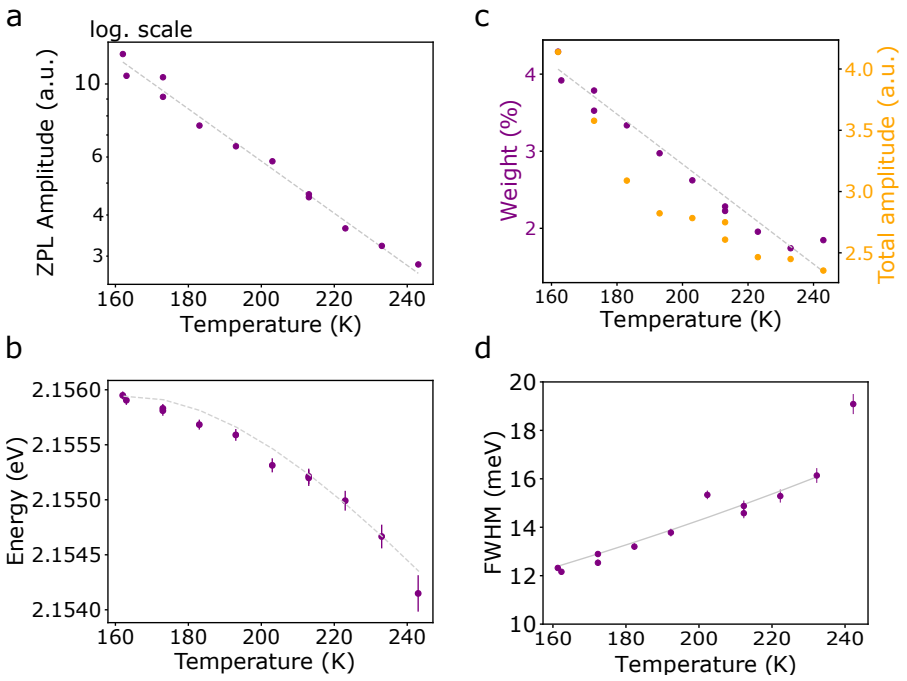

Figure 4.9: Spectral features evolution with temperature of the overall measurement: (a) mean ZPL peak amplitude as a function of temperature, the scale is semi logarithmic. **(b)** ZPL energy as a function of temperature, **(c)** ZPL weight as a function of temperature, with a linear evolution with temperature. **(d)** FWHM as a function of temperature.

The measured variation of the amplitude can be retrieved from the Boltzmann distribution, which is exponential, as displayed in Fig. 4.9.

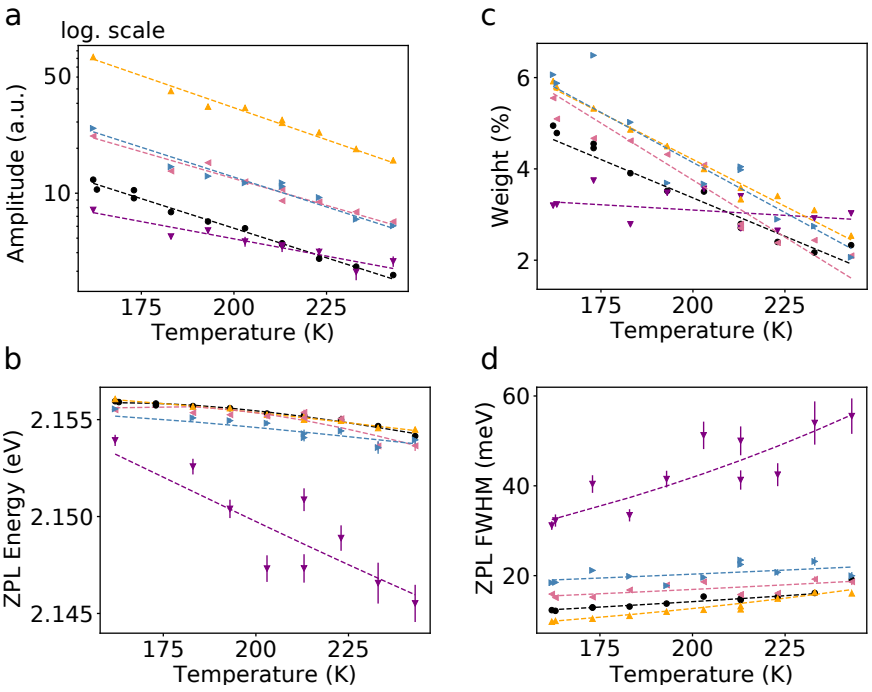

Figure 4.10: Spectral features evolution with temperature of individual nanodiamonds: (a) ZPL amplitude as a function of temperature, **(b)** ZPL energy as a function of temperature, **(c)** ZPL weight as a function of temperature, **(d)** FWHM as a function of temperature. In black the mean value, from Fig. 4.9, and in purple, pink, orange and blue, the individual FND from Fig. 4.8.

fitting parameter	mean value	standard deviation	R
Amplitude of the ZPL (α)	- 0.195	0.030	0.154
FHWM (β)	0.0458	0.0235	0.514
Weight (γ)	- 0.0359	0.0119	0.331

Table 4.1: Mean values extracted from the fitting parameters of the T-controlled CL data

With the individual nanodiamonds, the mean tendency measured for the average spectra can be roughly retrieved. The main difference is that for each nanodiamond, the CL measured spectra are different, such as highlighted in Fig. 4.8. This impacts the evolution of the intensity, energy position, FWHM and ZPL weight as a function of the temperature.

This can be attributed to variations in local strain and defects density in each nanodiamonds. One can now see the difficulty of using individual nanodiamonds to precisely measure the local temperature in a sample. By fitting the data with exponential functions for the amplitude of the ZPL and its FWHM, and with line functions for the weight, one can retrieve the temperature. For the amplitude, the function is fitted with $I(T) = A.\exp\left(-\frac{\alpha}{T}\right)$, for the FWHM, with $\Delta E(T) = B.\exp\left(\beta T\right)$, and for the weight, $W(T) = \gamma.T + \delta$. The histograms in Fig. 4.11 show the spread of the fitting values.

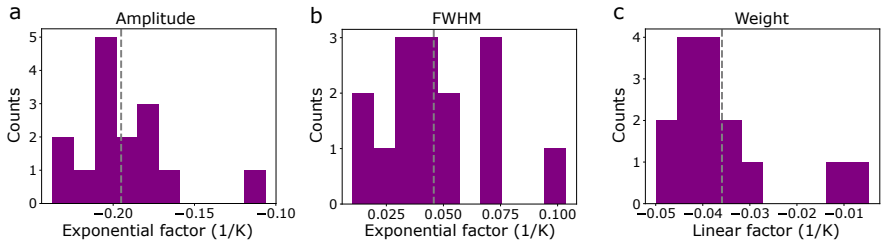

Figure 4.11: Histograms of the fitting parameters extracted from T-controlled CL data: (a) exponential fitting parameter α used for the amplitude of the ZPL peak, **(b)** exponential fitting parameter β used for the FWHM of the ZPL peak, **(c)** slope γ of the linear fit used for the weight of the ZPL. The mean values are highlighted with grey dashed lines.

I characterized the spread of the histograms by using the factor R defined by $R = \frac{standard\ deviation}{mean\ value}$.

From these results, the ZPL amplitude has the smallest R factor, which explains why it is commonly used as a marker for thermometry [56]. We emphasize that the behavior of the amplitude and energy of the ZPL is non-linear with temperature. The use of the weight instead of the amplitude or the FHWM of the ZPL can be interesting since it displays a linear variation with temperature.

Nevertheless, the measurements for the summed area correspond to that seen in temperature-controlled PL for ensemble of FNDs [57], the behavior of individual FNDs is less straightforward. For this reason, they can be unreliable and measurements with several FNDs are preferred.

4.4 Photoluminescence and optical pumping for charge-state conversion

A photoluminescence optical pumping is performed to reproduce results from [9], which uses a continuous 1064 nm laser to optical perform the charge-state conversion $NV^0 \rightarrow NV^-$. This is first done in an all-optical setup, to reproduce the results in the same conditions as in the reference, to then transfer the experiment inside the STEM microscope. The optical pumping, which is an all-optical setup with the sample placed on a glass coverslip, is described in this section.

Even if optical pumping in resonance with the ZPL of NV^- is often used for charge-conversion to NV^- [81], this method is not adapted for us since it would generate residual NV^- emission. For this reason, IR pumping is preferred. It does not trigger light emission from the sample, so that when in the electron microscope, the features seen in the spectra come from the CL only.

In all the following, the charge-conversion of NV centers is characterized by $\%NV^0$ or $\%NV^-$ plots. They respectively correspond to the ratio $A_{NV0}/(A_{NV0} + A_{NV-})$ and $A_{NV-}/(A_{NV0} + A_{NV-})$. The amplitude of the Gaussian fits have been directly used rather than the integrals over the ZPL of each charge state since the results is about the same (discrepancy about 10%), and the direct ratios of amplitude is more straightforward to calculate.

4.4.1 Optical charge-conversion of NV centers

I have reproduced the charge-conversion from the reference [9]. First, I have performed the optical pumping $NV^- \rightarrow NV^0$ which requires only one continuous laser (here at 543 nm). In this case, the regime is: $E_{exc} \gtrsim E_{NV}$. The charge-state transition NV^- to NV^0 is known to occur in this case since the energy of the laser is sufficient to ionize the center when in the excited state. The charge conversion percentage obtained is of the order of 20 %, as expected [58].

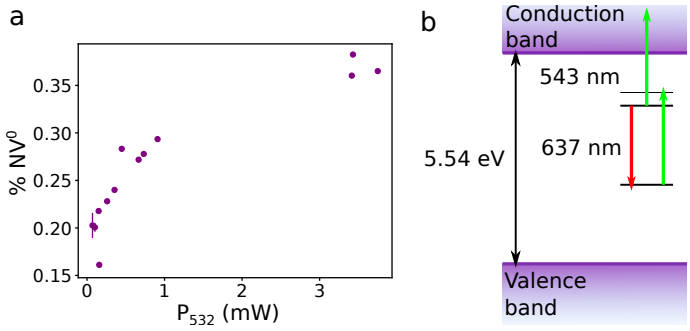

Figure 4.12: Ex-situ optical pumping with green laser: (a) fraction of NV^0 variation as a function of green laser (543 nm) power. The NV^0 fraction is seen to increase by about 20%. **(b)** Scheme of the optical charge-conversion performed.

Then, two continuous lasers have been used: a green laser (543 nm) at fixed power to excite PL, and an IR laser (1064 nm) to perform the optical pumping. The IR laser optical charge-state conversion corresponds to the regime $E_{exc} < E_{NV}$, and performs the charge conversion $NV^0 \rightarrow NV^-$ [9]. The results are shown in Fig. 4.13.

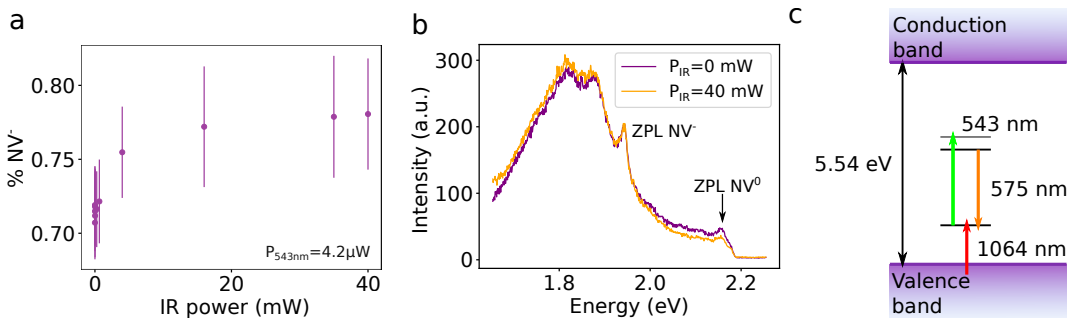

Figure 4.13: Ex-situ optical pumping with 1064 nm laser: (a) fraction of NV^- centers as a function of IR power, **(b)** spectra comparison with no IR and high IR power at the same green laser power. The change is small, but the decrease of NV^0 ZPL and increase of that of NV^- is visible, **(c)** scheme of the charge-conversion performed.

The process behind this charge-conversion is the ionization of the N substitutional atoms, that are then captured by the NV centers [9].

A conversion to NV^- of up to 7 % is measured, which is similar to the expectations [9]. Even if the error bars from the standard deviation of the Gaussian fitting of the ZPL peaks are large, this is not a new result, but only a reproduction of what has already been done. For this reason I have not accumulated more data to reduce the error bars.

4.4.2 UV photoluminescence of NV centers

As presented in section 4.2, the CL NV spectra display only NV^0 spectral features. One can wonder if this comes from the high energy of the charge carriers generated in STEM, which is much higher (about 30 eV, the energy of the diamond bulk plasmon) than the optical bandgap of diamond (5.54 eV [9]). Here, the case $E_{NV} < E_{exc} < E_{gap}$ is studied, where the energy of excitation is higher than that of the NV transition, but still within the gap energy of diamond. The goal is to compare the results with that of CL to understand the charge-state conversion in both cases.

Using UV light, the diamonds are excited below the energy bandgap, and observe similar features compared to CL of NV: the majority of emission come from NV^0 (90%) as displayed in Fig. 4.14. In this case, not all the NV^- centers are ionized, the 637 nm peak remains visible at all UV powers when exciting at 405 nm (Fig. 4.15).

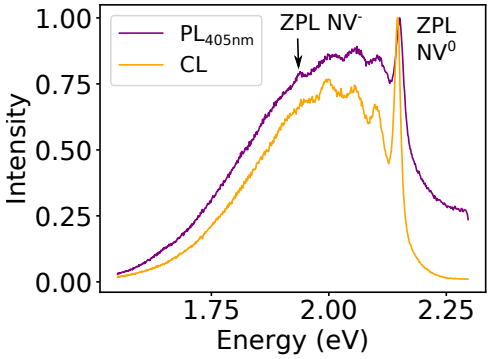

Figure 4.14: Comparison of spectral shape of UV PL and CL: CL (orange) and PL_{UV} (purple). The spectra shape are very similar, except that the PL_{UV} has a small peak at 1.94 eV from the NV^- emission that is not measured in CL. At high energy, a background is seen in PL_{UV} due to other centers emitting light.

When varying the UV power, one could expect to make the NV^- peak disappear, since the UV energy is sufficient to ionize the supplemental electron in NV (process used for the optical pumping with green light 4.4.1). Yet the peak remains visible, with some amplitude variations. The energy of both NV^0 and NV^- remain constant with increasing UV power.

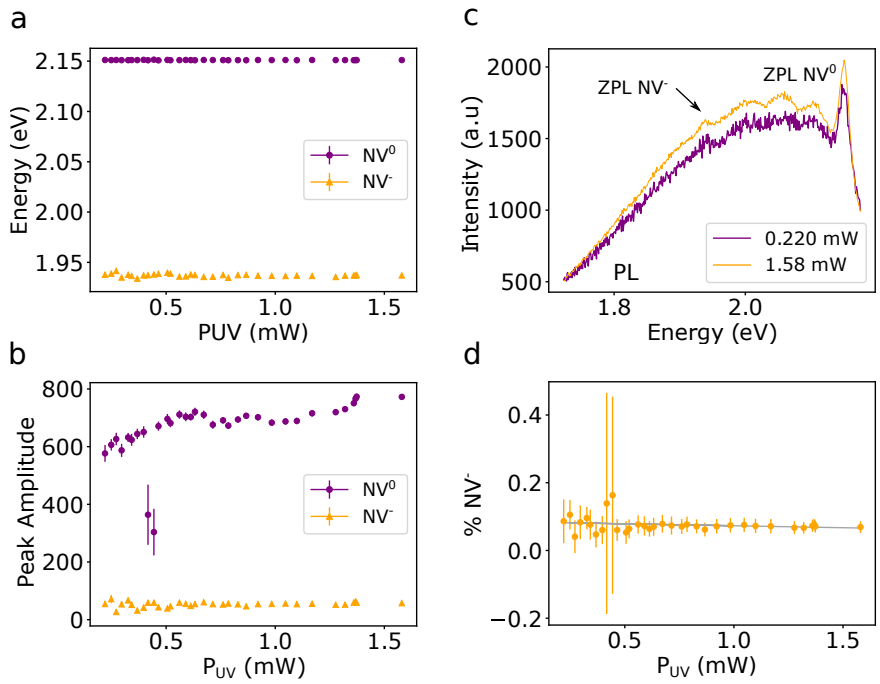

Figure 4.15: ex situ UV PL: (a) ZPL energy of NV^0 (purple) and NV^- (orange) as a function of UV laser power, **(b)** ZPL peak amplitude of NV^0 (purple) and NV^- (orange) as a function of UV laser power, **(c)** spectral change with increase of laser power. The spectra intensity are normalized by the respective laser power. **(d)** Fraction of NV^- centers evolution as a function of UV power. The charge-conversion between NV^- and NV^0 seems to be occurring at a slow rate.

I also have performed multi-laser excitation of the FNDs with green and UV lasers, to see if the optical pumping NV^- to NV^0 is enhanced by UV light. This is not the case, as displayed in Fig. 4.16, where the NV^0 fraction remains roughly constant for the various green laser power.

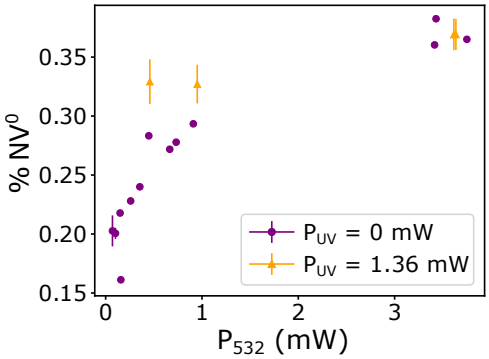

Figure 4.16: Comparison between pure green optical charge conversion and green and UV combined in PL: the NV^0 fraction remains at about 33 %.

UV PL and CL emission from NV centers seem to be similar. Even if the 405 nm laser wavelength is below the bandgap energy, similar features in the emission spectra are still seen, in particular the high NV^0 fraction. Moreover, as described in section 4.2, the CL emission is mediated by bulk plasmons. The 405 nm laser cannot excite these bulk plasmons, which energy is about 30 eV. The similarity between the UV PL and the CL is therefore unexpected.

4.5 Combined laser and electron beam excitation

Here, I have performed in-situ the optical pumping previously done ex-situ, inside the STEM microscope, using the same lasers.

4.5.1 Cathodoluminescence and optical pumping in the STEM

First, I have superimposed the IR laser with the electron beam to convert NV^0 into NV^- in CL. The use of IR laser is important since it does not excite any luminescence by itself, and therefore the light detected comes only from electron excitation. This experiment has failed and the NV^- ZLP was not measured in CL by optically pumping with IR laser. The probable reason for that is explained below.

In Fig. 4.17 the result of the experiment is plotted. The CL intensity decreases with increasing IR laser power. The spectra are corrected for the electron beam current variations and normalized. This intensity decrease is attributed to temperature effects, which are detailed in section 4.5.3.

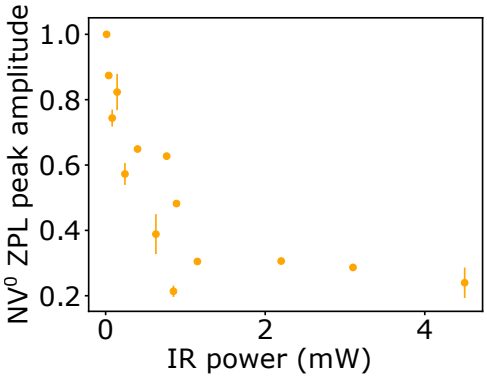

Figure 4.17: NV^0 ZPL Amplitude in CL with IR laser: the peak amplitude is divided by the current value to highlight the contribution of the IR power. The measurement is performed on a nanodiamond aggregate on a TEM lacey carbon grid kept at 150 K in the VG microscope. The NV^- CL peak is not seen.

The intensity decrease of the CL NV signal is further illustrated in Fig. 4.18, where the spectra at different IR power are plotted.

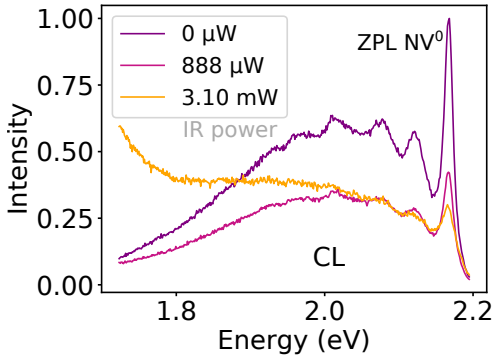

Figure 4.18: NV^0 CL emission at various IR laser power: the CL intensity decreases, and the ZPL of NV^0 becomes wider with increasing laser power.

The tail towards lower energies in Fig. 4.18 appears for high IR power. The tail is also slightly visible in Fig. 4.13, which corresponds to the ex-situ optical pumping. Its origin then has to be present in both experiments (it can be the lasers, the diamonds, residues etc.). The exact origin of this low-energy tail remains unknown, and requires more investigation.

4.5.2 Photoluminescence and optical pumping in the STEM

I have reproduced in-situ the IR all-optical pumping of section 4.4.1 for comparison, and the results are plotted in 4.19. In this plot, the first decrease of NV^0 population with increase of NV^- can be seen for low IR power (<0.25 mW), and for higher power the NV^0 ZPL peak increases again, which is a feature from the IR laser peak.

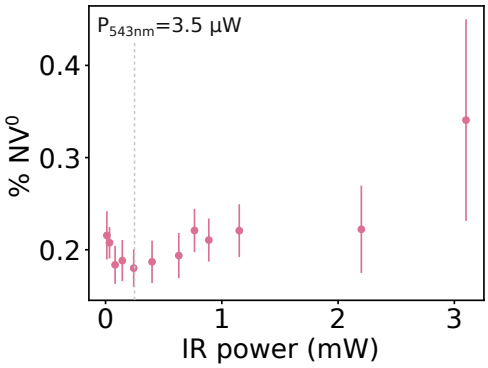

Figure 4.19: In situ optical pumping: same optical pumping as performed in Fig. 4.13. At low power, the charge-conversion occurs, converting NV^0 centers to NV^-, but this stops quickly. The increase of ZPL NV^0 is an artifact from the tail of the laser peak.

The results being different for the in-situ and ex-situ optical pumping, this raises questions about the origin of these discrepancy. The main differences between the two experiments are:

- the sample is in vacuum,
- the sample holder is cooled at 150 K,
- the FNDs are placed on a TEM grid with lacey carbon membrane.

The origin of the difference can be poor heat dissipation, which is not efficient with the TEM grid even with a cooled stage. This hypothesis is explored in the next section.

4.5.3 Sample heating with laser

The IR power that can be used inside the STEM is much lower than that used in the purely optical setup, due to the poor heat dissipation of the lacey carbon membrane of the TEM grid. Indeed, the measured NV^0 CL spectra rapidly disappears, as illustrated in Fig. 4.18. In the all-optical setup of section 4.4, even at the highest attainable power for the solid-state IR laser (about 40 mW), the NV centers PL spectra remain fully visible, whereas in CL, with only about 4 mW the NV spectral features disappear.

The weight of the ZPL changes with temperature due to the phonon side band increase (Fig. 4.20). The same phenomenon is seen in the CL spectra when illuminated by the IR laser. To link the increase of temperature with the laser power, I have plotted both the weight measured in temperature-controlled CL and in the CL and IR combined experiment (Fig. 4.20).

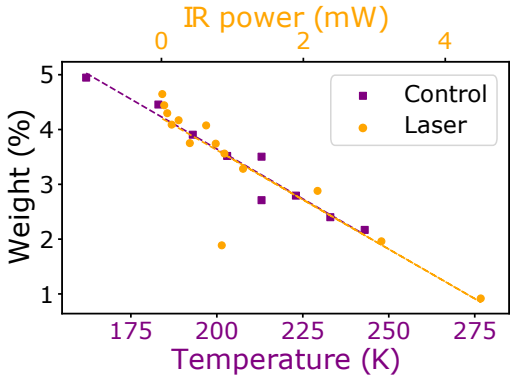

Figure 4.20: NV^0 ZPL weight decrease comparison: weight of the NV^0 ZPL in the temperature-controlled CL experiment (purple, 'Control'), weight of the ZPL as a function of the IR laser power (orange, 'Laser'). The two line fitted curves alignment is described in the text.

The two curves are matched by fitting the data with lines:

$$W(T) = a.T + b \tag{4.1}$$

$$W(P) = c.P + d \tag{4.2}$$

If the reason for the spectral change with the IR laser power is indeed the heat dissipation, the two curves should have the same slope. Therefore a and c should match, allowing for the estimation of the temperature with the IR laser illumination. An offset between the curves is seen, and the abscissas are realigned by changing the displayed range, so that the two fitted curves form a unique line. The offset between the two curves comes from the use of two different STEM microscopes for the experiments: the ChromaTEM samples (purple curve) can go to lower temperatures than the VG cold (orange curve), due to the design of the sample holders being improved for the ChromaTEM. This gives a conversion factor between the temperature and IR laser power in the experiment of $a/c = 21$ K/mW.

Even if the two lowest temperature for the control (purple) and IR heated (orange) experiments are different, the FNDs are from the same batch, therefore ensemble measurements as performed in the two experiments should be equivalent, which allows for the matching of the two curves.

This confirms that the optical charge-conversion from NV^0 to NV^- in CL is likely limited by heat dissipation, which I have tried to improve by using Ag-coated (which one of the bests heat conductors) TEM grid or graphite TEM grids. The issue with using such good conductors is that it quenches the light emission from FNDs by creating new non-radiative decay channels. Nevertheless, the Ag coating of a TEM grid with a continuous film, is to be kept in mind for optical measurements. This way the FNDs would not be in direct contact with the conductor, as opposed to the use of a graphite TEM grid, but few nanometers away from it. On top of being good heat dissipators, the Purcell effect from the Ag plasmon a few nanometers away from the emitter can improve the CL emission [82]. The light collection would also be increased due to the Ag thin film acting as a mirror.

4.6 Summary

In this chapter, I have presented results on PL and CL of FNDs containing a high density of NV centers. The detection of CL from small FNDs (about 15 nm) is reported. Long electron irradiation was shown to create new vacancies, leading to the increase of the CL signal of vacancy-related defects, such as NV or H3 centers.

Combined PL and CL measurements were have been performed to understand the charge-state photophysics of the combination of electron and photons. Various wavelengths have been used to perform the various charge-state conversions.

I compared the optical pumping performed in the all-optical setup and in the STEM microscope in Fig. 4.21. The NV^- CL emission was not detected, even if the optical conversion was reproduced ex-situ. The PL optical pumping performed inside the microscope has the same behavior as the control experiment for low IR power (below 4 mW),and behaves differently at higher powers. We attributed this difference to sample heating, due to poor dissipation. This hypothesis has been confirmed by comparing the results with that of temperature-controlled CL. These experiments also have allowed to characterize the limit of using individual FNDs as nanothermometers.

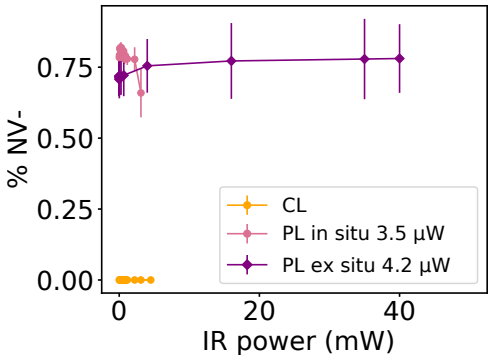

Figure 4.21: In situ and ex situ optical pumping with green and IR lasers: due to heating, the IR range accessible for optical pumping in situ is much lower than that ex-situ.

With their many applications in various domains, in particular in quantum optics, NV centers have attracted tremendous attention. Another emerging material with potential capabilities in quantum optics is the transition metal dichalcogenide monolayer. Due to the 2D nature of the material, the Coulomb screening is much lower and the transitions can be more easily manipulated. They are presented in the next chapter.

Chapter 5

Influence of nanoscale structure and chemistry on the neutral and charged excitons in 2D TMD semiconductors

Contents

NV centers are stable room-temperature light emitting point defects, which makes them suitable for quantum manipulation. Other optical quantum emitters are widely studied, and possible new candidates are single photon emitters in transition metal dichalcogenides (TMD) monolayers [83]. These materials are semiconductors with exciting novel properties, which are shortly described in section 5.1. TMDs have the chemical formula MX_2 where M is a transition metal, such as tungsten (W) or molybdenum (Mo), and chalcogen atoms such as sulfur (S), selenium (Se) or tellurium (Te). In this chapter, I focused particularly on samples made up of tungsten disulfide, noted WS_2. One particular aspect of the unusual properties of TMDs is that they display bright luminescence when exfoliated to atomically thin monolayers, which have a direct bandgap, whereas when they are multi-layers or bulk, the

bandgap is indirect and the luminescence is less efficient [13, 84].

All-optical microscopy and spectroscopy techniques are usually limited to few hundreds of nanometers due to diffraction [85]. Near-field techniques, usually tip-enhanced experiments, can reach better resolutions, down to few nanometers scale [86]. Nevertheless the tip being nanometers away from the sample, the dielectric environment can be greatly perturbed. Moreover, tip-based experiments do not allow for the characterization of embedded materials, such as the layers of heterostructures.

For these reasons, there is a lack of understanding of the origins of variations of the optical spectrum of TMDs at the few nanometers scale, which corresponds to the length scale of the quasi-particles involved in the optical processes (the Bohr radius of the excitons is of the order of a few nanometers). This lack of understanding comes also from the fact that spectral changes are measured separately from the structural and chemical changes, since they are usually not available in the same setup.

Here, I used STEM microscopy to measure the structure with atomically-resolved images and µ-diffraction for strain, low-loss EELS spectroscopy for exciton absorption, CL spectroscopy for light emission, and core-loss EELS for chemical environment characterization. All the experiments were performed in similar conditions in two STEM microscopes: the Nion UltraSTEM 200 and the modified Nion Hermes 200 (ChromaTEM).

This chapter presents the results obtained on a WS_2 monolayer encapsulated with hexagonal boron-nitride (h-BN). I have measured local variations, down to tens of nanometers, of both absorption and emission that I have directly linked to various phenomena, including chemical environment or strain. The objective of this chapter is to understand the origins of variations of the excitons and trions at a scale matching that of the size of these quasi-particles.

The general properties of TMDs and research topics linked to them are presented in section 5.1, including the state of the art in photoluminescence and cathodoluminescence. The neutral and charged-excitons are introduced in subsection 5.1.2 and 5.1.3 respectively. The design used for the samples studied is presented in section 5.2 and the excitation process and sample preparation are detailed in subsection 5.2.1. The variations of the optical properties of the TMD monolayer are discussed in section 5.3. The last section, 5.4, concerns the charged-excitons local variations at the tens of nanometer scale and their origins.

5.1 Generalities on TMDs

5.1.1 Crystallography and band structure

The most common TMDs used for their optoelectronic properties are $MoSe_2$, MoS_2, WSe_2 and WS_2. The information given in the following is valid for them with only slight differences.

TMDs are layered materials made up of monolayers held together by van der Waals forces, that can be grown either in bulk or directly in monolayers [87]. The monolayer CVD growth has been shown to be less homogeneous than the bulk

crystal that can be then exfoliated (mechanically [88] or chemically [89]) to extract monolayers of the material. The crystal structure of the TMDs monolayers studied here is illustrated in 5.1a and b. It is trigonal prismatic, with alternate metal (M) and chalcogen atoms (X) displaying an hexagonal arrangement in the [001] direction. They are semiconducting in the 2H (trigonal prismatic) phase, displayed in Fig. 5.1, and metallic in the metastable 1T (octahedral) phase.

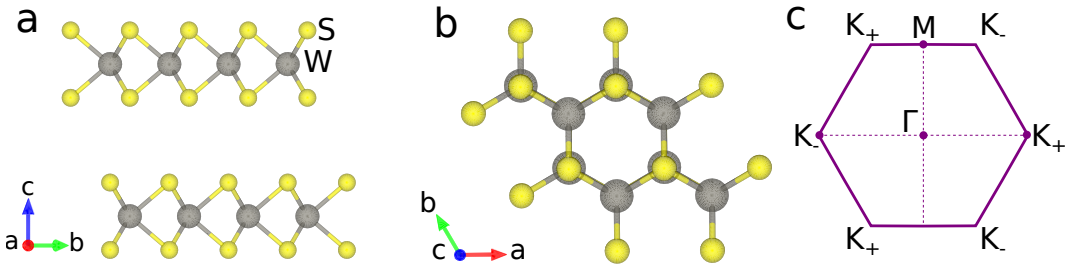

Figure 5.1: Sketch of the WS_2 lattice in the 2H phase: (a) side view of a monolayer, along the *a* axis, **(b)** top view of a bilayer, along the *c* axis, **(c)** first Brillouin zone, labeled with the characteristic points K (K_+ and K_- for the two non-equivalent valleys), Γ and M. The symmetry breaking is highlighted by the two schemes of (a).

Their bandgap energy and lattice parameters are listed in the table below [59].

	$MoSe_2$	MoS_2	WSe_2	WS_2
Bandgap energy (eV)	1.874	2.160	1.890	2.238
Lattice parameter *a* (Å)	3.327	3.190	3.327	3.191
Lattice parameter *c* (Å)	15.451	14.879	15.069	14.202

Table 5.1: Summary of the bandgap energy (E_g) and lattice parameters in TMDs, from [59, 90]. E_g is measured from the TMD monolayers encaspulated in hBN.

Such monolayers can then be stacked, to form more complex structures, starting from TMD bilayers, which display interesting effects such as interlayer excitons [91], to multi-layer stacks with TMDs and other materials, commonly graphene or h-BN [92]. The TMDs lattice might be changed when the material is encapsulated in other crystals with a different lattice parameter, such as h-BN (2.512 Å [59]) or graphene (2.468 Å [59]). The mechanical properties and band structure changes of such encapsulated monolayers are described in section 5.3.

As shortly described in the introduction of the chapter, TMDs display a large change in band structure when their dimensions are reduced from bulk to monolayer. In particular, the bandgap becomes direct at the K point of the first Brillouin zone (FBZ), for TMD monolayers, which allows for the emergence of bright luminescence [13]. The calculated change in bandgap for a monolayer, bilayer and bulk TMDs (specifically of MoS_2) is shown in Fig. 5.2.

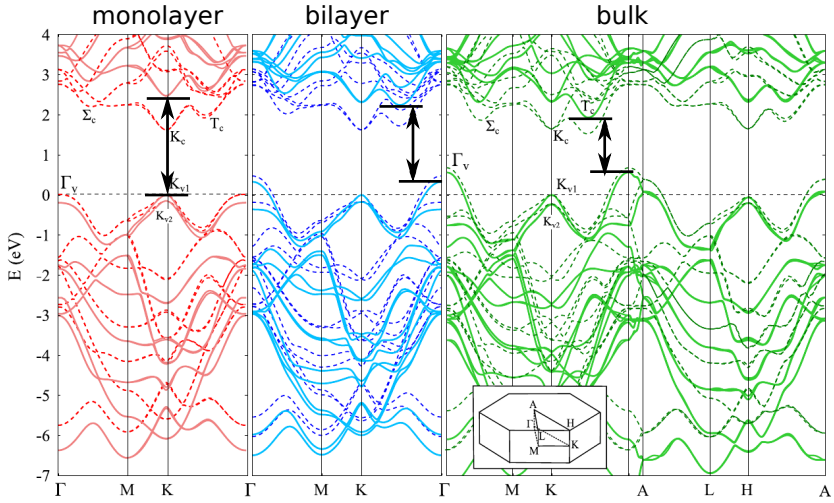

Figure 5.2: Band structure calculations for MoS_2: for a monolayer (red), bilayer (blue) and bulk (green). Reproduced from [93].

The direct bandgap transition of the monolayer, at the K point, is also called valley optical transition. There are six K valleys at the edge of the FBZ which belong to two different groups (K_+ and K_-). The separation in two groups comes from the spin orbit splitting of the two levels. These levels are spin polarized, and the spin polarization is inverted for K_+ and K_-.

The choice of the WS_2 among other TMD materials comes first from the availability of TEM samples made from our collaborators at the MIT (see sample fabrication section 5.2.1). Indeed, only few studies in CL have been conducted previously, partly due to the challenge of producing heterostructures laying on thin TEM grids. Moreover, the WS_2 has the largest dipole transition of the TMDs cited in table 5.1. This leads to an overall more efficient photon emission. WS_2 is a "dark" TMD, which means that the lowest-lying exciton transition at the K point of the FBZ is spin-forbidden [36]. However, this can be an issue only at low temperature, since the conduction bands splitting is of few meV. In our experimental conditions (about 120 to 300 K), both conduction bands can be populated, and the emission from WS_2 remains sufficient [38].

5.1.2 Neutral excitons

From the bandgap structure, different excitons with specific properties can be seen (Fig. 5.3b). The three lowest-energy excitons are labelled X_A, X_B and X_C. X_A and X_B both originate from the K point in the Brillouin zone, whereas X_C comes from band nesting (conduction and valence bands being parallel) between Γ and K (Fig. 5.3a). In optical absorption and in low-loss EELS, the three exciton peaks are seen and have the same shape, illustrating that low-loss EELS can be a nanoscale counterpart of optical absorption for TMD monolayers (see chapter 2).

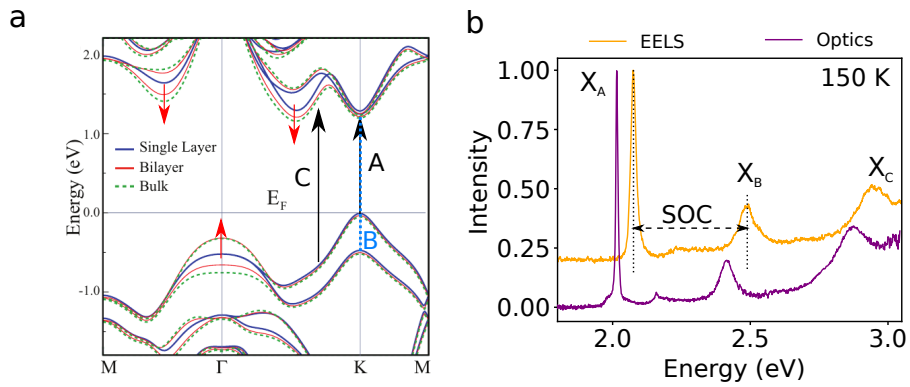

Figure 5.3: Excitons in TMDs: (a) calculated band structure of WSe_2 highlighting the locations of the different excitons optical transitions of the various excitons: X_A, X_B and X_C. Reproduced from [94]. The red arrows highlight the large changes when going from monolayer to bulk. **(b)** Measurement of the exciton peaks in low-loss EELS (orange) and optical absorption (purple). The exciton peaks corresponding to the transitions seen in (a) are labeled. The measurement were performed on a WS_2 encaspulated monolayer, at 150 K. The optical measurement curve was reproduced from [38].

At the K point of the FBZ, X_A and X_B are separated in energy due to the lift of degeneracy of the two levels in the valence and in the conduction band. This energy separation, originating from spin-orbit coupling (SOC), is of the order of 400 meV for WS_2. The binding energy of the excitons in TMDs is exceptionally high, of the order of few hundreds of meV [95], and their Bohr radii as small as a few nm [96]. X_A is the only exciton peak seen in emission with a non-resonant excitation, such as PL and CL, as shown in Fig. 5.4.

Two processes are usually seen for the exciton formation in semiconducting materials: (i) the direct exciton generation, called "geminate" process, and (ii) the bimolecular exciton formation, corresponding to the random binding of free electrons and holes under Coulomb interaction [36]. A signature of the first is the presence of exciton absorption in the vicinity of the bandgap of the material, which is seen for TMD materials. As explained in section 5.2, this might not be the dominant process for CL excitation.

Due to the high Coulomb interaction in 2D seminconductors thanks to charge confinement and low screening, excitons can interact to form biexcitons. They are only observed at low temperature, and are not detected in our experiments at 150 K [38]. They are preferably formed at grain boundaries or edges [97]. The signature of biexcitons has been identified with varying the laser power, and measuring the intensity dependence with laser power: the biexciton has a quadratic dependency, whereas the exciton only a linear dependency [97, 98, 99].

5.1.3 Charged excitons: trions

The light emission spectra at 150 K of TMDs almost always show an additional peak at a lower energy than that of the X_A (Fig. 5.4). At room temperature, this peak is less visible and appears as a low-energy shoulder of X_A (as displayed in Fig. 5.21 in section 5.3). This lower-energy peak has been attributed to the emission of the charged-excitons, called trions. These are three-particle complexes, made up of an A exciton and a supplemental charge, that can be either an electron (negative trion, noted X^-) or a hole (positive trion, noted X^+). The binding energy of trions (positive

and negative) is of the order of 20-30 meV [95, 100], which means that they can be stable even at room temperature.

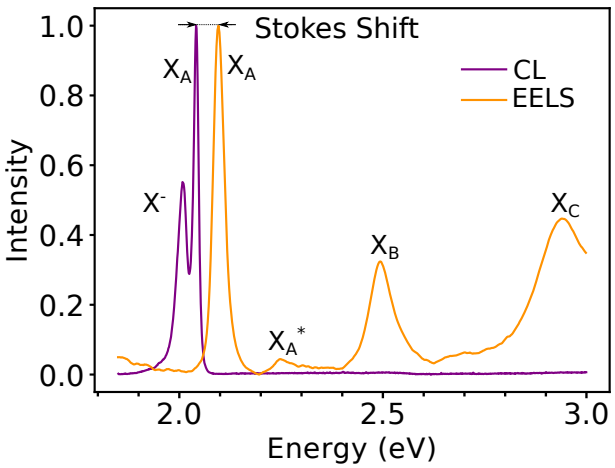

Figure 5.4: EELS and CL spectra: the only exciton seen in CL is the X_A (purple curve). The lower energy peak seen in CL is the trion, X^-. In EELS (orange curve), The X_A, X_B and X_C are visible. X_A^* is the first excited state of X_A. The energy separation between the CL and EELS X_A peaks is called Stokes shift.

Trions are usually identified in the literature through gated experiments, where the TMD monolayer sample is excited with a non-resonant laser (PL) and the charge carriers in the TMD are controlled by the electric gating, which injects holes or electrons selectively [101]. For p-doping, holes are injected in the monolayer and X^+ intensity peak increases. For n-doping, electrons are injected in the monolayer and X^- intensity peak increases. On top of increasing the ratio $X^\pm$ to X_A, the energy of the trion and exciton shift with the gating potential. The trion energy slightly redshifts with the electron doping increase [101, 102] and when the laser excitation power increases [103].

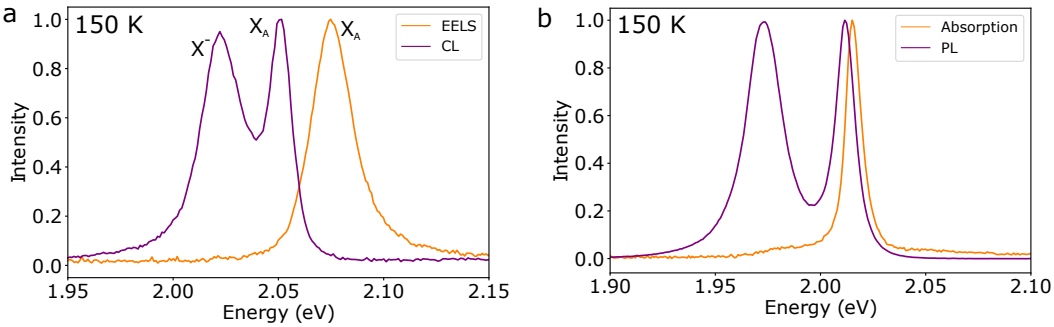

Figure 5.5: Comparison between spectra: (a) from electron excitation **(b)** from pure optical excitation. The measurements are done on encapsulated WS_2 monolayers at 150 K, performed on two different samples. The optical measurements curves (PL and absorption) were reproduced from [38] with permission.

For CL experiments, gating has not yet been performed, but the peak identification to X^- rather than X^+ can be justified by the energy separation value between X_A and the trion peak, which is 35 meV at 150 K (see Fig. 5.5 for a comparison between PL and CL emission at 150 K), corresponding to that of X^- in the literature [38]. Additionally, it is known that non intentionally doped TMDs are n-type [104],

which supports the hypothesis that the trions are negative.

The X^- peak is actually composed of two peaks, which are not resolved at 150 K. The two contributions come from intra- and inter-valley trions [105], which means that the charges are either all in the same valley (intra) or the supplemental electron is in the neighboring valley (inter). Additional non-radiative trions exist and are called "dark" trions, whose structure and energy are predicted by calculations [38, 106], but are not discussed here due to their optical inactivity.

5.1.4 Exciton and trion dynamics

Time resolved measurements are usually performed at low temperature (< 20 K). For WS_2, the behavior at low temperature differs greatly from that between 120 to 300 K, due to the spin-forbidden lowest optical transition (WS_2 is a "dark" TMD). At low temperatures, below 40 K, the exciton lifetime (τ^0_{rad}) is seen to be independent of the temperature, and of about 2 ps for $MoSe_2$ and WSe_2 [35]. Above 40 K, τ^0_{rad} decreases with the temperature increase, due to the increase of non-radiative decay channels (such as the coupling with phonons). This is supported by the decrease of PL intensity. In this regime, the decay time decreases to values lower than the setup temporal resolution (which is 0.8 ps in ref [35]). At these temperatures, the exciton decay profile is composed of two parts: an initial drop, corresponding to the fast τ^0_{rad} decay, and a longer time scale, corresponding to the effective PL lifetime (a large number of exciton escapes from the light cone, lowering the efficiency of radiative recombination). The behavior cited above has been measured for $MoSe_2$, which might be different at low temperature, from that of WS_2.

The trion formation time has been measured in $MoSe_2$ at low temperature (13 K), and is about 1.6 to 2.3 ps [107]. The recombination time of X_A in $MoSe_2$ is of the same order of magnitude at these temperatures [35, 108], which indicates a competition between the formation of trions and the decay of X_A. At room temperature, the trion binding energy is of about 20 meV, which is the order of k_BT at 300 K, and the trion emission can disappear.

There is a lack of data for WS_2, likely due to its "dark" nature, making the dynamics interpretation more complicated than for Mo-based "bright" TMDs. Furthermore, our measurements are done at about 150 K, which corresponds to an intermediate temperature. In optics, many experiments are performed either at room temperature or at low temperatures (< 20 K), and information on the exciton dynamics at 150 K is lacking.

The exciton lifetime can also be tuned by changing the dielectric environment. The weak coupling between the exciton in the TMD monolayer and its surrounding environment can be characterized by the Purcell effect. For example the tuning of the encapsulating h-BN thickness leads to change in lifetime from about 1 to 10 ps in $MoSe_2$ at 7 K [37]. The lifetime tuning does not affect the trion lifetime in the same manner.

5.1.5 Applications and interesting features

TMDs have been studied extensively in the past years thanks to their physical properties, which are listed below with a short description of the interesting phenomena:

Light-emitting nanoscale devices:

The bright luminescence of TMD monolayers enables the creation of nanoscale opto-electronic devices. Using the knowledge on heterostructure fabrication and lithography for electrical contacts, stable and efficient light-emitting components can be produced [109, 110].

Quantum emitters:

Some quantum emitters occurrences in TMDs have been attributed to strain. These can be created in a deterministic way by straining the TMD with a patterned surface on which the monolayer is placed [111, 112]. The various types of quantum emitters in TMDs monolayers are described in more details in the chapter 6.

Spin-polarized valley physics:

As described in more details in section 5.1.1, at the optical transition the band structure is degenerate, and the lack of inversion symmetry of TMD monolayers in the semiconducting (2H) phase (illustrated in Fig. 5.1) lifts the degeneracy in the valence and conduction bands. In particular, at the lowest point of the Brillouin zone (K, called the valley) where the optical emission occurs, the lifting of degeneracy enables two distinct optical transitions (corresponding respectively to exciton A and to exciton B, which are described in more details in section 5.1.2). With associated selection rules, this means that the optical transitions at the two different valleys are spin-polarized [113]. This can be addressed optically, by exciting selectively one valley or the other by using circularly-polarized light [114, 115]. These valley-selective properties give rise to a new class of electronics, called "Valley-tronics".

Moiré patterns:

Layered 2D materials with a misalignment creates a new periodic arrangement, referred to as moiré patterns. This can be realized with stacked TMD monolayers, and the supercells created have new electronic properties due to the resulting potential [116, 117, 118]. The properties of such twisted layers can be tuned with the angle, giving rise to another new class of electronics called "Twistronics".

5.1.6 State of the art

The light-emitting quasi particles in TMDs, described in parts 5.1.2 and 5.1.3, have a wavefunction of only few nanometers (size of the Bohr radius of excitons [96]) due to the low screening in the TMD monolayer and the high binding energy of these particles [95]. To understand the physics of these quasi-particles, one has to probe them at their length scale, which is difficult to perform with purely optical methods due to diffraction.

Several ways of performing optical measurements below the visible light diffraction limit exist. They can use the light confinement between a sample and a metal tip [119], or an etched optical fiber brought close to the sample [120]. The spatial resolution achieved with these methods (called scanning near-field optical microscopy, SNOM) can go down to few nm [52], and allow for measuring several quantities in the same experiment, usually the PL or tip-enhanced Raman spectroscopy (TERS), and the topography [119]. Nevertheless, the presence of a tip close to the sample

influences its dielectric environment, which has an important influence on the optical response of TMDs [121, 122]. Optical absorption is not available at such high spatial resolution with these methods. Moreover, such measurements are performed directly on the TMD monolayers surface and do not allow the probing of embedded material such as TMDs encapsulated in h-BN.

Atomically-resolved TEM imaging coupled with µ-PL, which is PL spatially resolved down to the µm scale, measurements have been performed to understand the light-emission origin at the edges of the TMDs, which have been identified to come from contaminants [54]. Even if the method enables some understanding of the photophysics of the TMD monolayers, the direct relationship between the atomically-resolved images and the µ-PL measurements are not performed at the same lengths scales, which can make the correlation between the two quantities unclear.

S(T)EM CL and EELS experiments:

A solution for correlating the high spatial resolution of TEM and the light emission is the use of CL. However, measurements of CL emission of TMD monolayers were performed for the first time only in 2017 [14] and only two other reports have been published on the subjects so far [123, 124]. Few other results have been published on TMDs CL emission on thick crystals or powders [125, 126].

The main reason for this lack of results in CL comes from the fact that encapsulation of the TMD monolayer is necessary to obtain detectable CL (see section 5.2 of this chapter), and such samples are particularly difficult to produce on a fragile TEM grid. A good surface contact between the components of the produced heterostructure is crucial to ensure the brightness of the CL signal.

The first success in sample fabrication allowed measurements of CL in a SEM, from WSe_2 and $MoSe_2$ monolayers encapsulated in h-BN [14]. The spatial resolution obtained was about 0.5 µm. From the comparison with PL, the energy shift measured was of 16.8 meV (at room temperature), which the authors explained by sample heating with the electron beam. Moreover, a correlation between the CL intensity and h-BN encapsulation thickness has been measured, and the CL intensity has been found to be proportional to the h-BN thickness [14].

The second SEM CL experiment was done on WS_2, at 5 K [124]. Even with the low temperature, damage was observed on the sample, which highlights the importance of the high-quality of the heterostructure.

The third paper is the first STEM CL measurement of a TMD monolayer emission [123]. It was performed on h-BN encapsulated WS_2, and the spatial resolution measured was 100 nm at 80 keV. The measurements were done at room temperature and damage was observed, which lead to quenching of CL.

On top of enabling CL detection, the h-BN encapsulation has shown to also narrow the WS_2 exciton peaks in EELS. Previous measurements [30, 127] on freestanding TMD monolayers exhibited larger EELS peaks than our measurements (Fig. 5.4).

So far, the CL measurements were limited essentially by damage on the sample, that can originate from the heterostructure quality (good contact between the layers, quality of the h-BN, cleanness of the surfaces), the vacuum of the microscope and

the temperature at which the measurements are done. Here, I carried the CL experiments on few h-BN encapsulated WS_2 monolayers. The samples were kept at 150 K in the high vacuum quality of Nion microscopes (of the order of 10^{-9} Torr). These experimental conditions enable the precise measurement of CL. The experiments were conducted in an aberration-corrected STEM microscope, which allows for high spatial resolution measurements together with spectroscopic measurements. In particular, the microscope used is equipped with a monochromator, giving access to the low-loss energy range in EELS with high spectral resolution, and a CL mirror, enabling the correlated CL and EELS experiments.

Correlated CL and μ-diffraction (diffraction measurements with a convergent electron beam) measurements in STEM have been performed before on thick h-BN [128], but the correlation between EELS, CL and strain has never been done on a 2D material. All these quantities measured for the same areas give information about the origin of the local variations of the excitonic effects.

Two microscopes were used for the measurements: the CL and low-loss EELS were measured in the ChromaTEM, the atomically-resolved imaging and core-loss EELS in the UltraSTEM. The μ-diffraction has been measured in both microscopes, and they are indicated in the corresponding figures.

5.2 h-BN/WS_2/h-BN sample design for CL, TEM and EELS

For bare 2D semiconductors, no CL detection has been reported in S(T)EM. As mentioned in the state of the art, this likely has to do with the low charge-carriers density produced by the nanometer-sized electron beam on the thin sample, exciting insufficient electrons and holes in the thin material to produce detectable CL. A way of producing sufficient charge-carriers, used first by Zheng et al. [14] is the h-BN encapsulation of the TMD monolayer. The interaction volume between the electron beam and the sample is then increased, leading to a higher free charge carriers number in the sample, which can recombine radiatively in the WS_2 monolayer (Fig. 5.6).

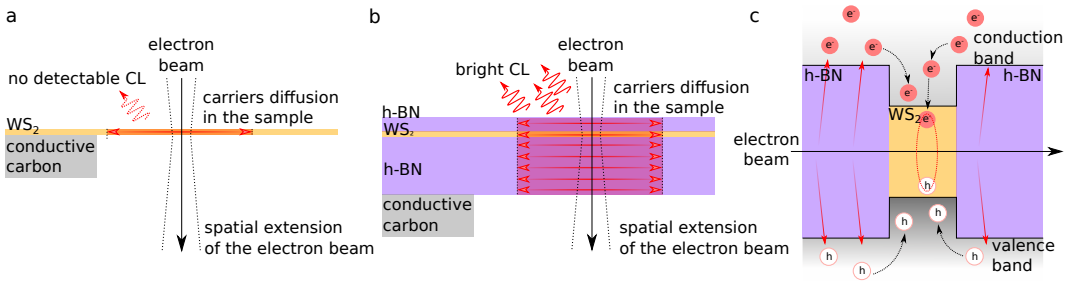

Figure 5.6: Scheme of the interaction volume of the beam with the sample: **(a)** scheme of the interaction with the freestanding WS_2 monolayer, the width of the electron beam is indicated with dotted lines, and the carriers diffusion length in the sample is highlighted. **(b)** Scheme of the interaction with the encaspulated monolayer. The h-BN is represented in purple, and the WS_2 monolayer in orange. This time, the interaction volume being larger, more charge carriers are excited, leading to brighter CL than in the freestanding monolayer case. **(c)** Scheme of the CL excitation leading to carrier recombination in the WS_2 monolayer [124]. The process is described in the text.

When crossing the sample, the fast electron beam transfers energy to electrons of the sample. Since the primary beam arrives with an energy between 60 and 100 keV,

and the electrons of the sample only need few eV to get promoted in the conduction band, many electrons are excited, leaving hot holes behind. Those hot carriers can relax through collision or other non-radiative processes. After losing some energy, they can interact to form excitons or trions, preferably in the TMD monolayer. These quasi-particles can then relax radiatively to produce CL emission.

In Fig. 5.7, an EELS spectrum of the heterostructure, measured in the range 0 to 8 eV, shows the absorption features from both WS_2 and h-BN in the low-loss range. This measurement highlights the fact that most of the energy is absorbed in the h-BN (purple part of the spectrum), and only a small fraction goes directly to the WS_2 (red and orange parts). The X_A peak is particularly highlighted (in red) since the absorption in this specific energy range would potentially lead to coherent CL emission. Since the direct absorption from the X_A is small compared to the absorption of the other excitons and of the h-BN, one can suppose that only a small fraction of the exciton formation is geminate, contrary to what is observed in PL [36].

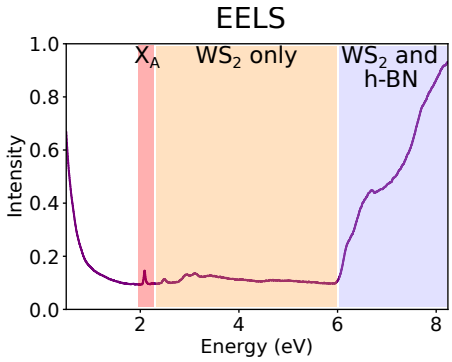

Figure 5.7: Low-loss EELS of the heterostructure: the spectrum shows the specific features from WS_2, including its excitonic peaks (contribution highlighted in orange). X_A is particularly highlighted in red since the absoprtion in energy this range leads to coherent CL. The absorption contribution from h-BN starts around 6 eV and is highlighted in purple. The spectrum shows that the most absorption in the low-loss range occurs in the h-BN.

Why using h-BN as the encapsulation material? As opposed to epitaxial crystalline growth of layered materials, the heterostructure construction does not depend on the lattice parameter. At first sight, any layered material whose thickness can be controlled can be a good candidate for the encapsulation. The aim of the encapsulation is to increase the CL signal, i.e. to increase the number of radiative de-excitation of excitons in the WS_2 semiconductor. For this reason, the use of a conductive material, such as graphene, is rejected as the presence of a conductive material in contact with a semiconductor would quench the luminescence by creating new non-radiative decay channels. The use of an insulating material, with a bandgap superior than that of the TMD, thus, is favorable for the recombination in the TMD monolayer. This way, even if most charge carriers are produced in the insulating material, which thickness is higher (about 25 nm), they will recombine in the TMD (thickness < 1 nm), increasing the measured CL (Fig. 5.6). Then, naturally, the choice was directed to h-BN, which is the most well-controlled insulator used for heterostructures, and exists in very high quality.

On top of making the sample thicker to produce more charge-carriers for detectable CL, the h-BN encapsulation have other advantages described below. The first observation is that when encapsulated, the TMD excitonic peaks become narrower [30, 127]. The general origin of peak widening can be both homogeneous

(directly from the lifetime of the exciton) and heterogeneous (from the peak position varying around a center due to small heterogeneity in the direct environment of the exciton). We estimate that the narrowing of the X_A peak comes from the heterogeneous width reduction (the homogeneous width is of about 9 µeV for a lifetime of 75 ps). The reduction of heterogeneous widening can come from several phenomena, such as the TMD being more flat when in between layers of h-BN, or the local dielectric environment being more controlled.

Furthermore, the encapsulation prevents the chemical reactions on the surface of the sample, since the surface of the TMD is not accessible. This allows, for example, for long electron beam irradiation without knock-on damage, or imaging free edges of the TMD monolayer. Indeed, I have experimented on one particular heterostructure for more than one hundred hours over a year, without observing major changes. The few changes I have seen were on cracks or on bubbles, such as displayed in Fig. 5.8. The bubbles can be trapped during sample preparation, and in here, they contain contaminants including carbon and silicon, likely from the sample preparation (the bubbles are further characterized in chapter 6). As mentioned previously, these feature behave differently from the typical parts of the sample: no CL emission is measured, and the free edges can be damaged easily.

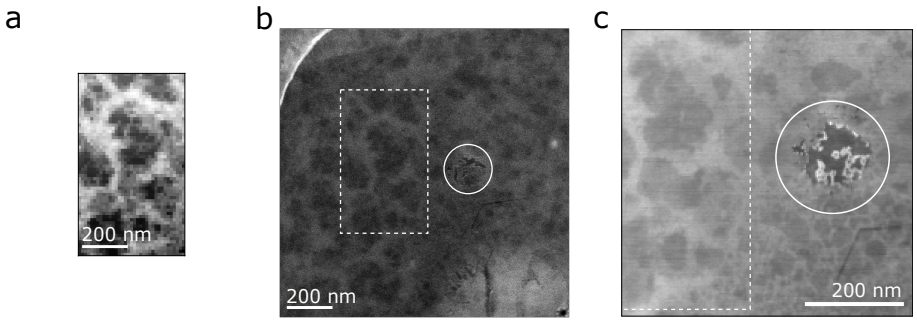

Figure 5.8: Damage from the electron beam irradiation: (a) HAADF image from a CL acquisition (ChromaTEM, 60 keV, 150 K), **(b)** same area measured later on the same day in the same conditions. **(c)** HAADF of the same area measured few months later (USTEM, 100 keV, 300 K), after few EELS spectra measurements. The imaging conditions differ from (a,b) and (c), in particular since the sample is asymetrical and upside down between the two days. Two areas are highlighted, and in the bubble (circle) the edges have changed under irradiation.

This measurement highlights the importance of the good encapsulation between the h-BN layers and the TMD, whose fabrication process is described in the following. Moreover, the h-BN flattens the TMD monolayer, and is an homogeneous dielectric environment, which can further reduce the inhomogeneous broadening.

5.2.1 Sample preparation

The samples were prepared by Hae Yeon Lee from the Massachusetts Instistute of Technology (MIT). The different steps for sample preparation are described below, and available in more details in [15].

The WS_2 was purchased from 2DSemiconductors, and the high-quality h-BN was synthetized by the high-pressure high-temperature method [129]. The h-BN quality is crucial to obtain good homogeneity and bright CL signal [14].

Each material constituting the heterostructure was exfoliated using the scotch-tape method and put onto SiO_2/Si substrate. A polymer stamp made of PDMS (polydimethylsiloxane) and PPC (polypropylene carbonate) was used to perform dry-transfer. The stamp was placed on a micromanipulator to pick up each component of the heterostructure:

- First, the top h-BN layer was picked up by contacting for 1 minute the exfoliated flake at 50°C, and the WS_2 monolayer and bottom h-BN were picked up in the same way.
- Then, the stack was put on a new SiO_2/Si substrate, and cleaned in acetone and isopropanol (IPA).
- The sample was then annealed for 6 hours at 250°C in an argon environment.
- Finally, to perform the transfer to the TEM grid, the heterostructure was spin-coated with PMMA (polymethylmethacrylate), lifted-off in a KOH solution, and picked up with the TEM grid. It was then cleaned with acetone and IPA to remove the remains of PMMA.

An optical microscope image of one of the heterostructures produced with this protocol is displayed in Fig. 5.9, with the WS_2 monolayer surrounded in blue. The mean area of encapsulated TMD is about 150 μm^2. The bottom h-BN layer is of about 5 nm thick whereas the top h-BN layer is of about 20 nm thick. Since the bottom layer does not cover the whole WS_2 flake area, the TMD monolayer is in contact with the conductive carbon layer.

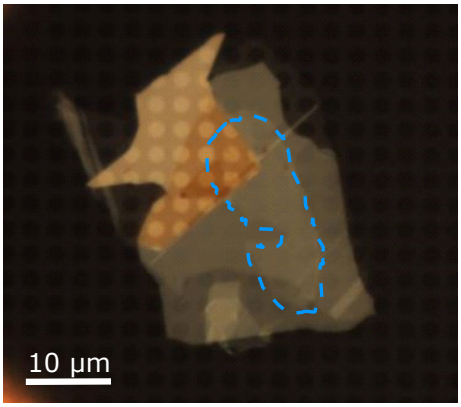

Figure 5.9: Optical microscope image of the sample: the heterostructure is imaged with a white light illumination, and contrast from the h-BN and TMD monolayer can be seen. In particular, the WS_2 monolayer is surrounded with a blue dashed line. The heterostructure lies on a quantifoil copper TEM grid with holes of 2 µm.

5.2.2 Specific TEM sample fabrication leading to high strain

The encapsulation deeply modifies the mechanical properties of the sample. I have measured the diffraction to recover the mean lattice parameters over micrometer-sized areas of the TMD monolayer at two specific temperatures: 150 K and room temperature (300 K). The results are shown in Fig. 5.10, where the lattice parameter of h-BN is plotted as a function of that of WS_2. This gives information on how the h-BN and WS_2 lattice parameters changes with respect to one another as the temperature changes. The measurement has been performed in five areas of about 1 µm of diameter. For each area, a diffraction pattern is measured, from which the lattice

parameters are extracted.

In this section, the data processing is different than that usually performed for µ-diffraction: instead of scanning the area with a convergent beam of 1 to 5 nm, the electron beam was positioned at the center of a TEM grid hole (beam size of the order of 100 nm). The diffraction spots are then smaller than with a more convergent beam (see chapter 2), and their position have been measured by Gaussian fit.

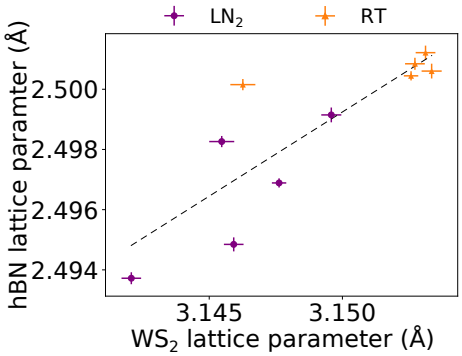

Figure 5.10: Lattice parameter change of WS_2 and h-BN: each diffraction measurement is performed on a region of about 1 µm^2, at 150 K (LN_2, purple dots) and then at room temperature (RT, orange triangles). For each of the 5 regions at the two temperatures, the lattice parameter of the WS_2 monolayer is plotted as a function of the h-BN lattice parameter. The error bars come from the Gaussian fit of the corresponding diffraction peaks.

At room temperature, the measurements are mostly confined to one value (mean values: 2.501 Å for h-BN, 3.152 Å for WS_2), whereas at 150 K, the values are widely separated from one another (mean values: 2.497 Å for h-BN, 3.146 Å for WS_2). The lattice parameters, even at room temperature, are smaller than expected, for both h-BN and WS_2 (respectively 2.512 Å and 3.191 Å [59]). This can come from the sample preparation being designed for having good contact between the h-BN and the WS_2 which allows for the charge-carriers to move more easily to the TMD to recombine.

5.2.3 Atomically-resolved imaging of encapsulated monolayer

The encapsulation is crucial to obtain a bright CL signal, nevertheless, the measurement of atomically-resolved images is still required since the primary goal of the sample is to identify nanoscale emitters and their emission origin. h-BN is composed of light elements, since the atomic number of boron is Z_B=5 and that of nitrogen is Z_N=7. The WS_2 is composed of heavier elements, in particular the tungsten has Z_W=74. Since the contrast in HAADF is proportional to the projected atomic number Z, this leads to higher contrast from the WS_2 in HAADF imaging.

To illustrate this, I measured two types of atomically-resolved images of the heterostructure at 100 kV in the Nion UltraSTEM 200: BF images, and HAADF images of the same areas. The results are shown in Fig. 5.11. The imaging is performed slightly off-axis to limit scattering from h-BN [130].

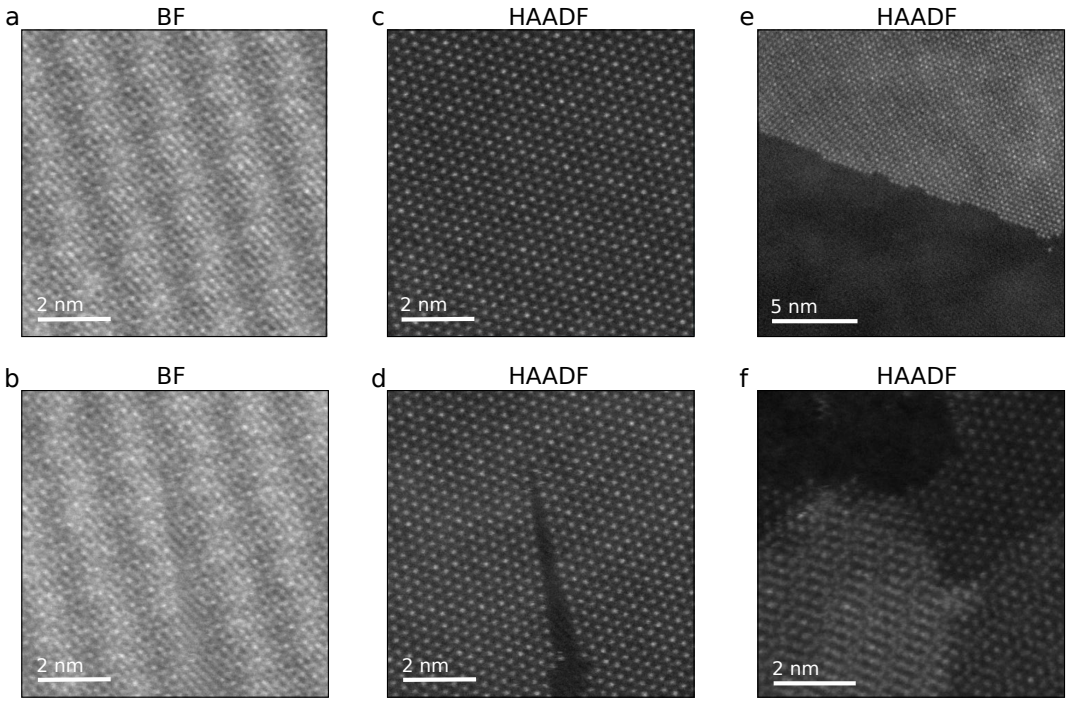

Figure 5.11: High resolution imaging of the WS_2 encapsulated monolayer: **(a)** Bright-field (BF) image of a pristine area of the WS_2 encapsulated monolayer crystal, corresponding to the area in (c), **(b)** BF image of an area containing a crack of the WS_2 monolayer in the center, barely visible in this imaging mode, corresponding to the area in (d). **(c)** HAADF image of the same area as (a). The bright dots are atoms of tungsten. **(d)** HAADF image of the same area as (b), this time, the crack in the WS_2 monolayer is obvious. **(e)** HAADF image of an edge of the membrane, with the whole area encapsulated in h-BN, **(f)** HAADF image of an encapsulated fold in the WS_2 layer, creating various moiré patterns.

On this figure, the contrast in BF comes from both h-BN and WS_2, and features from the WS_2 monolayer itself, such as the crack visible in 5.11d, are hidden by the h-BN signal, as shown in Fig. 5.11b. On the contrary, in HAADF imaging, most of the contrast comes from the tungsten atoms, making it very clear for features such as cracks (Fig. 5.11d), edges (Fig. 5.11e) or even moiré patterns (Fig. 5.11f).

With these atomically-resolved images, one can measure the deformation of the lattice using geometrical phase analysis (GPA) algorithms, as shown at the end of the next section.

5.3 Energy variations of the excitons and trions

Variations of the excitons X_A and X^-, are seen across different areas of a sample, and among several samples. What is the origin of such variations? The first one that comes to mind is the TMD's intrinsic properties: if it is exfoliated from a bulk crystal or a CVD-grown monolayer, the chemical composition, or the doping (the change in intrinsic local charge-carrier density). These parameters are intrinsic parameters of the sample that can influence the excitons properties. The properties can also be influenced by external parameters, such as the substrate and encapsulation [122], the dielectric environment [121], or the strain. In the latter case, the change of lattice parameters modifies the electron wavefunctions overlapping of the atoms, and thus, the band structure [131, 132]. The CL emission variations within a single sample are

illustrated in Fig. 5.12.

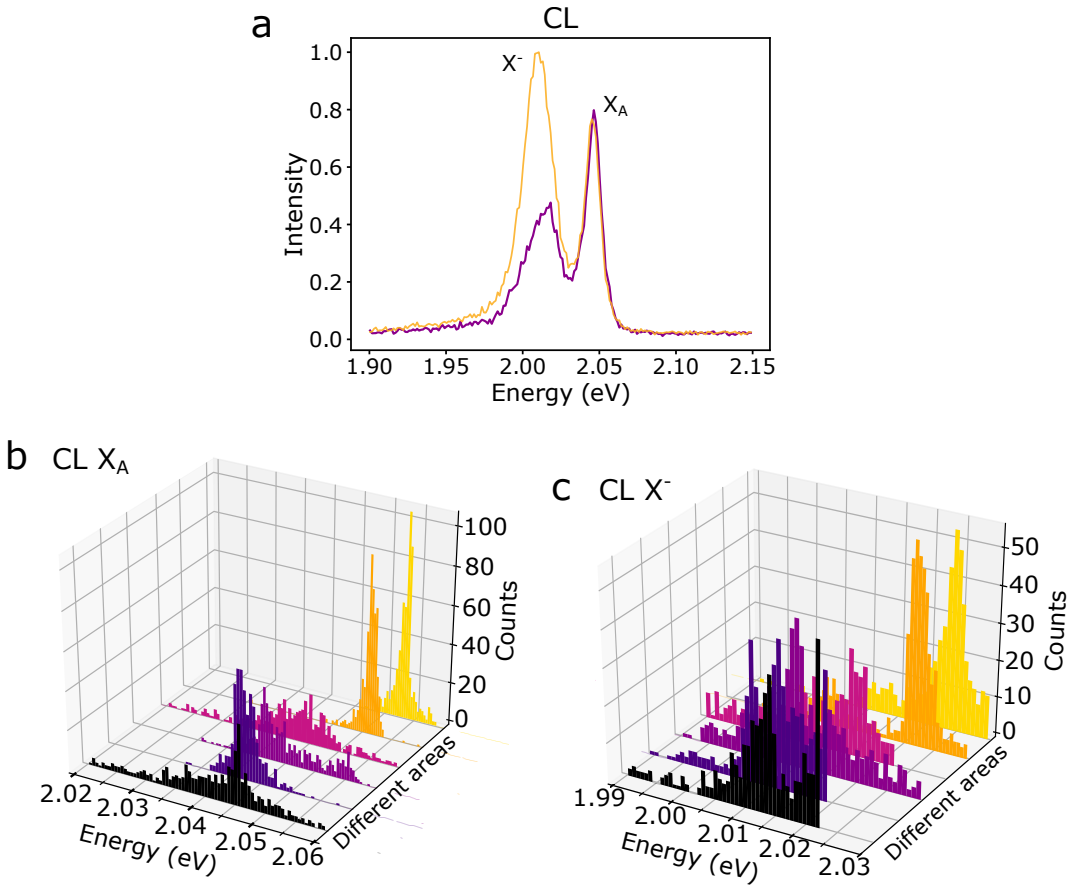

Figure 5.12: Variation of the CL signal in the sample: (a) example of spectra extracted from the CL data at two different positions. The intensity of the trion is seen to change. **(b)** Histograms of the X_A energy in CL from six different areas, of about 1 µm wide, **c** histograms of the X^- energy in CL from the same areas, each color corresponds to a specific area. The energy value of X_A and X^- are spread on few tens of meV.

mean X_A energy (eV)	std (meV)	mean X^- energy (eV)	std (meV)
2.054	2	2.023	7
2.052	3	2.018	11
2.047	14	1.993	28
2.046	7	2.011	11
2.045	8	2.010	7
2.041	10	2.009	14

Figure 5.13: Center (energy) and standard deviation (std) of the histograms in Fig. 5.12: the order corresponds to that of the figure, with at the top of the table the parameters of the yellow histogram, and at the bottom of the table, the parameters of the black histogram.

The understanding of the influence of internal and external parameters on the emission is crucial for the development of devices [122]. A way to characterize the origin of the variations of the excitons is to search for the correlations between the emission and absorption of the X_A energy peak, whose variations depend on whether the doping, the strain or local disorder [17]. The energy difference between the absorption and emission peaks is commonly called Stokes shift.

Insights on the origin of exciton variations can be obtained by plotting 2D histograms of the energy, FWHM of X_A, X^- in CL, and X_A, X_B in EELS [17]. However, at our measurements temperature, the FWHM is limited by the temperature widening (about 13 meV at 150 K). For this reason, the FWHM variations do not carry much relevant information, and the 2D histogram plotted are that of energy variation of the peaks (such as in Fig. 5.16).

5.3.1 Stokes shift

The Stokes shift is the energy difference between the absorption and emission spectra of a material, defect or molecule. Its origin is detailed in chapter 2. In summary, the Stokes shift can originate from various phenomena, such as the phonons, the doping of a material, the strain etc.

To understand the origin of the Stokes shift variations, I have performed a study similar to the reference [17], using the nanoscale counterparts of PL and differential reflectance (for absorption), respectively CL and EELS in the low-loss range [15]. In this study, the authors have plotted 2D histograms of the Stokes shift with the X_A energy in absorption, in emission, and the FHWM.

Fig. 5.14 illustrates what the Stokes shift looks like on the h-BN/WS_2/h-BN heterostructure measured in CL and EELS. The area on which the measurements are done is of the order of 1 μm^2, and contains a suspended part (left-hand side, inside the large white circle) where a crack and a bubble can be seen, and a supported part (right-hand part, outside of the large white circle), where the heterostructure is on top of the conductive carbon membrane. The CL and EELS spectra display both the X_A peak, which are separated by 48.5$\pm$0.2 meV. This value is quite high for encapsulated WS_2 and the reason for the large Stokes shift is explored throughout the chapter.

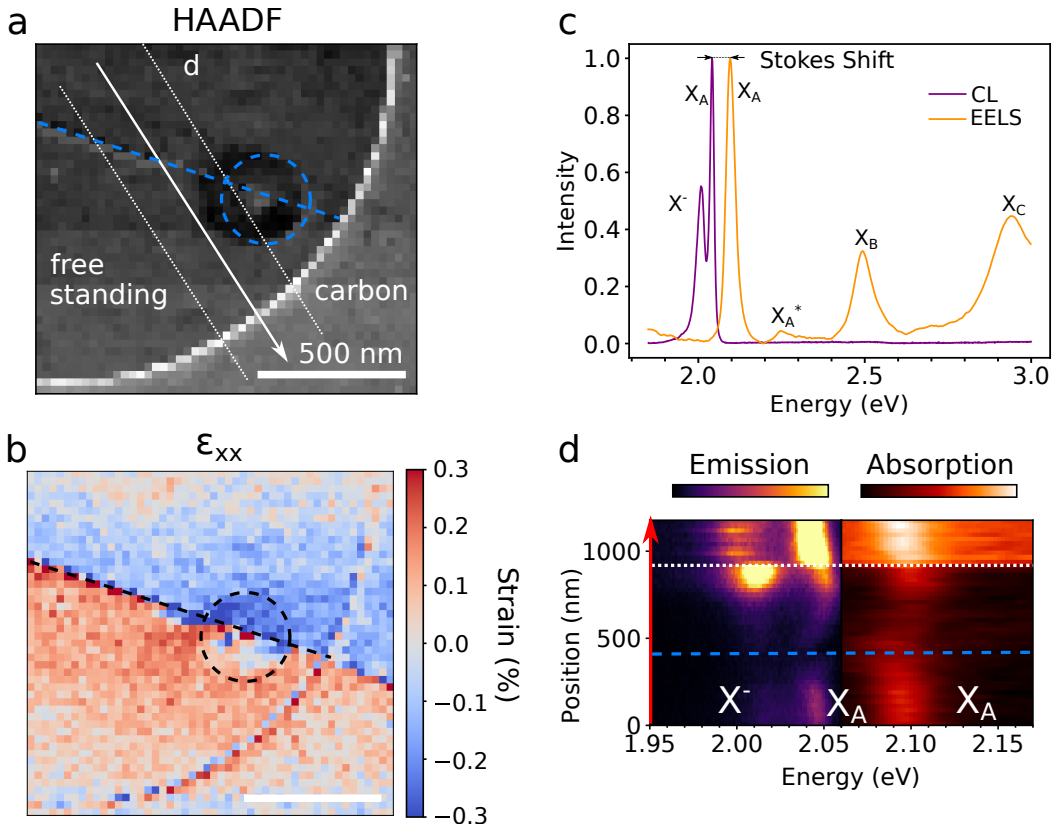

Figure 5.14: Variation of the energy of X_A in emission and absorption: (a) HAADF image of the area, the white arrow shows the path where the data from which (d) is extracted, with the width of integration. **(b)** ϵ_{xx} component of the strain tensor, showing a sign inversion across the crack. The other components of the strain tensor do not show a sign inversion. **(c)** Typical spectra measured in EELS (orange curve) and CL (purple curve), with the excitons and trion peaks labeled, and the Stokes shift SS = $E_{X_{A,EELS}}$ - $E_{X_{A,CL}}$ indicated. **(d)** Spectra along the arrow in (a) in both CL (emission) and EELS (absorption). A lowering in intensity is seen on the crack (highlighted by the dashed lines) for CL, and an energy shift of both CL and EELS spectra is seen on each side of the crack.

During sample preparation, bubbles (such as highlighted in the dashed circle in Fig. 5.14) can form on the monolayer or on the h-BN [119]. Here, they contain contaminants, such as carbon and silicon, which are trapped between the TMD and the h-BN (the bubbles are studied in more details in chapter 6). This can lead to a lack of contact between the TMD and the h-BN, thus quenching the CL emission. These area are also under high strain, which can lower the bandgap energy and create potential wells where localized excitons can recombine (see chapter 6).

Quenching of CL emission is also observed few tens of nanometers away from edges or cracks. The exact reason for this is unknown for now, but we can formulate the hypothesis that new non-radiative recombination paths are created. These could be due to the increasing number of defects, such as vacancies, in these areas. Moreover, in CL, the excitation is indirect and comes from the bulk plasmon, which has spatial extension. For this reason, when when approaching the crack, the electron beam excitation might decrease due to the limitation of the charge-carrier diffusion through the crack.

In Fig. 5.15, a measurement of the local Stokes shift is shown: the area studied is the same as in Fig. 5.14. Fitted maps of X_A in both CL and EELS are plotted in Fig. 5.15. They display respectively the energy of X_A in emission (CL) and in absorption

(EELS). For each pixel, the Stokes shift is obtained by subtracting these energies as SS = $E_{X_{A,EELS}}$ - $E_{X_{A,CL}}$, and the obtained map is shown in Fig. 5.15d. This measurement shows that the Stokes shift changes when the heterostructure is suspended and when it is supported by the carbon membrane. More precisely, the Stokes shift is smaller in the suspended area, and larger in the supported area.

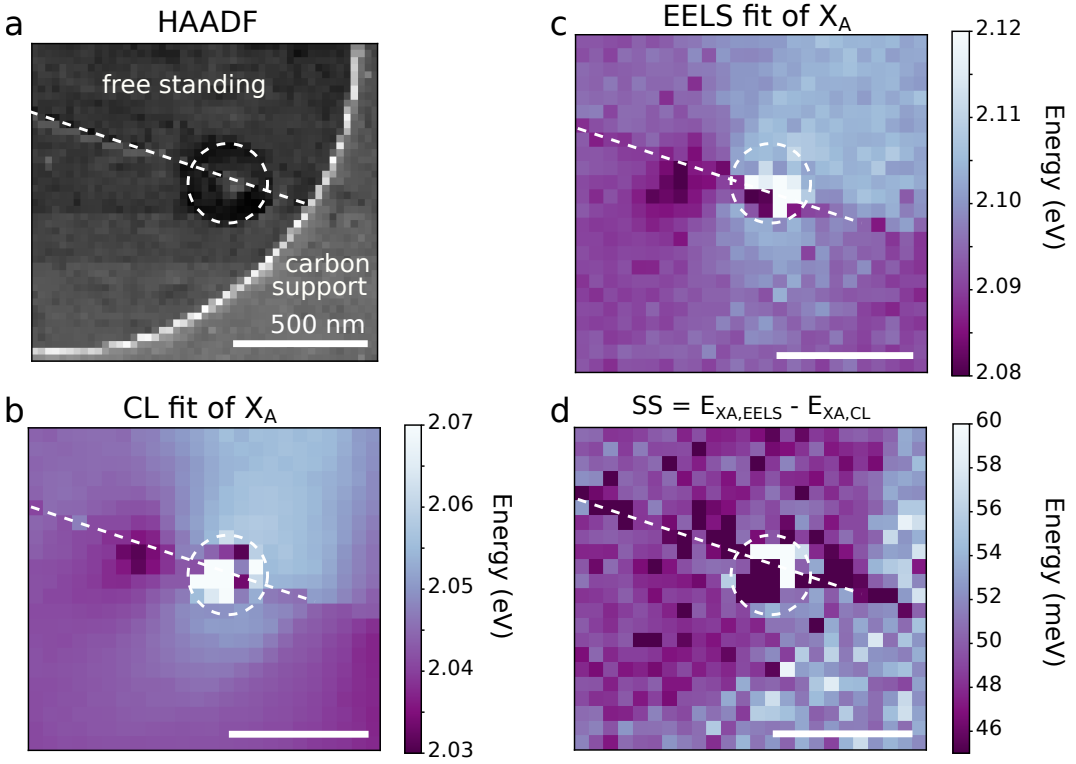

Figure 5.15: Map fitting and local Stokes shift measurement: (a) HAADF image of the area, **(b)** X_A energy from Gaussian fit of CL data, **(c)** X_A energy from Gaussian fit of EELS data, **(d)** Stokes shift showing a variation between the suspended area and the area supported by the conductive carbon membrane, showing that on the suspended area, both CL and EELS shift of the same amount. The bubble is clearly visible in all panels (highlighted with the dashed circle), in particular due to the lack of X_A absorption and emission. This makes the spectra difficult to fit, leading to imprecise values inside the dashed circles.

From the X_A energy in EELS, CL and the Stokes shift, one can plot their 2D histograms (Fig. 5.16) to have insights about the origin of the Stokes shift [17].

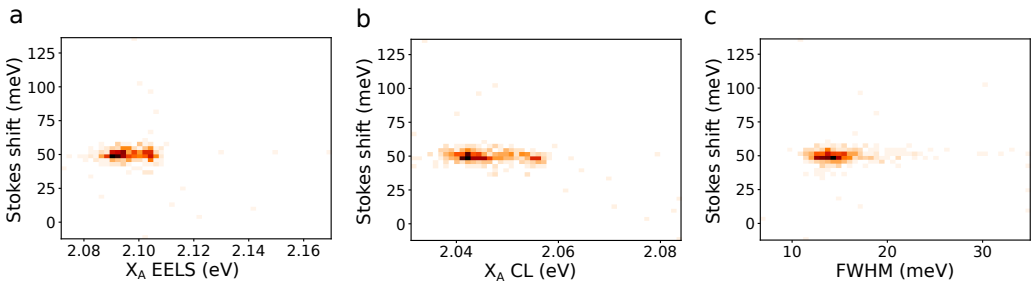

Figure 5.16: 2D histograms of the Stokes shift: (a) with the X_A energy in EELS, **(b)** the X_A energy in CL, **(c)** the FWHM of X_A in CL.

These data do not display slopes with inflection points such as seen in [17]. The

reason for this might be the reduced size of the area probed or the small discrepancies between the data values, which indicates that the area measures is quite homogeneous.

5.3.2 Influence of strain on the optical properties

The previous section exhibited that the energy of X_A can be influenced by various parameters such as the dielectric environment, the doping or the strain [17]. The latter comes from the deformation of a material, which here is crystalline and composed of two sub-parts: h-BN and WS_2 which have two different lattice constants, respectively 2.512 Å and 3.191 Å [59]. The basic principles for its measurements have been presented in chapter 2. As a reminder, the 2D strain tensor we extract from µ-diffraction data is:

$$\epsilon_{pyxem} = \begin{pmatrix} \epsilon_{xx} & \epsilon_{yy} \\ \epsilon_{xy} & \theta \end{pmatrix} \tag{5.1}$$

Another manner of measuring the strain uses the geometrical phase analysis (GPA) of atomically-resolved images such as presented at the end of this part.

From the way the sample is prepared (presented in section 5.2), both materials are under important strain to favor the adhesion between the TMD monolayer and the h-BN. The correct contact between the two materials ensures the circulation of the free charge-carriers from the h-BN to the WS_2 to enhance the CL emission. Additionally, the carbon support of the TEM grid is pierced with holes, where the heterostructure is suspended, which can be a supplementary source of strain. The sample preparation (exfoliation, transfer) can also tear the monolayer apart, creating cracks, such as illustrated in this part. It can also trap bubbles, which are studied in more details in chapter 6.

The strain originates from lattice parameter and rotation change, how does it affect the A exciton energy? Theoretical calculations on how biaxial [133, 134, 135] (expansion/contraction in the two directions of the plane) and uniaxial [135, 136] (expansion/contraction in one direction of the plane) strain affect the band structure have been performed. What is noticeable in these band structures is the decrease of bandgap energy at the K points in both cases (uniaxial and biaxial) of tensile strain, which leads to a redshift of the X_A energy in both absorption and emission. The binding energy of the excitons can also be affected. Several methods to measure the X_A emission energy as a function of strain have been used:

- by straining the TMD monolayer with an AFM tip [137],
- by measuring the AFM profile of bubbles and retrieving the strain, and correlating it with the emission [85, 119],
- by using the biaxial deformation of the substrate under thermal expansion [131],
- by bending the substrate of a sample without slippage [136, 138, 139].

For WS_2 monolayers, this leads to gauge factors (energy shift per percent of strain) measurements of - 62 meV/% [139] and - 46 meV/% [138] for uniaxial strain experiments.

Here, I performed the direct measurements of the strain with µ-diffraction on a crack in the TMD monolayer, where the h-BN is continuous. The strain was then correlated to CL and EELS measurements of the X_A. The energy profiles in emission

and absorption across the crack are plotted in Fig. 5.17.

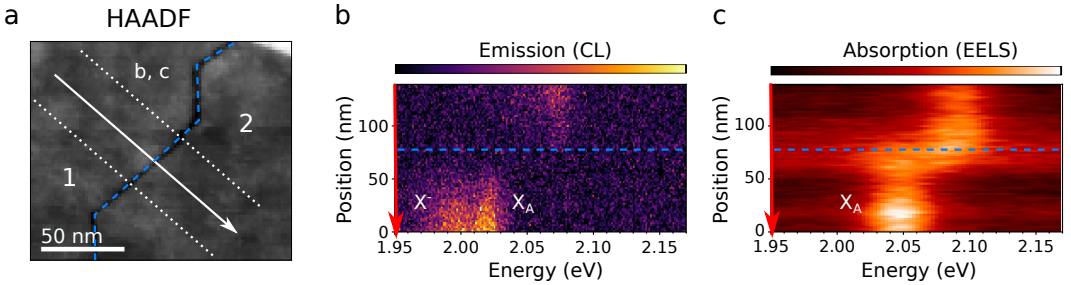

Figure 5.17: Emission and absorption measurements across a crack: (a) HAADF of the area, the arrow shows the path of measurement used for (b) and (c), **(b)** spectral change in CL emission along the arrow in (a), **(c)** spectral change in EELS absorption along the arrow in (a). It can be seen that the CL intensity strongly decreases close to the crack, while the EELS peaks remain visible. A rapid redshift in energy can be seen at the position of the crack.

If we look at the emission and absorption of the monolayer across this crack, we can see two separate regions: the left-hand side, where the emission and absorption are both redshifted, and the right-hand side, where the emission and absorption are both blueshifted. It also has to be noticed that the CL emission is quenched close to the crack, probably due to the presence of new non-radiative decay channels (since the absorption does not exhibit the same intensity decrease).

To understand why the left-hand side has a lower energy than the right-hand side, we measured the strain of the same area, using two methods: diffraction (Fig. 5.18 and 5.19) and GPA, with a series of atomically-resolved images (Fig. 5.20). As described in details in chapter 2, the strain measurements are imprecise due to the difficulty of finding the center of the diffraction spots in µ-diffraction experiments, and one should be careful when looking at these data.

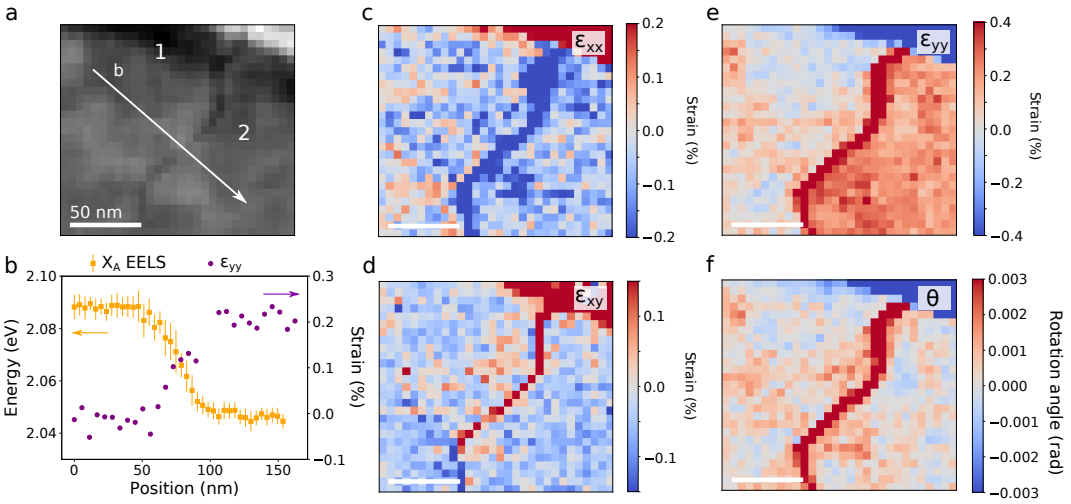

Figure 5.18: Components of the 2D strain tensor on the crack area: (a) HAADF image of the area, **(b)** strain profile (purple, ϵ_{xx}) and X_A energy in EELS (orange) as a function of position along the arrow in (a). The X_A energy is highest where ϵ_{xx} is low. **(c)** ϵ_{xx}, **(d)** ϵ_{xy}, **(e)** ϵ_{yy} and **(f)** θ.

From the summed spectra over region 1 (right-hand side) and 2 (left-hand side) as displayed in Fig. 5.19e,f, we can measure the mean energy shift across the crack

in CL $\Delta E_{XA,CL}$=39±2 meV, in EELS $\Delta E_{XA,EELS}$= 34.7±0.4 meV and in Stokes shift Δ SS=4.6±0.6 meV. This corresponds to about -200 meV/ %, whereas about -50 meV/ % was measured in uniaxial strain [138, 139]. The origin of the difference is explained in the following.

In most realistic cases, the strain is not uniaxial nor biaxial, it is a combination of the two, with additional shear strain and rotation components. For this reason, if we want to attribute the X_A energy shifts origin to the strain, we first have to ensure that the measured strain corresponds more or less to the uniaxial or biaxial case. Here, for the crack, we can see that ϵ_{xx} and ϵ_{xy} have around the same values on the left-hand and on the right-hand sides of the crack, whereas ϵ_{yy} varies from about 0 to +0.2 % (the limitations in μ-diffraction measurements are discussed in chapter 2). The rotation angle also is negligible. In this case, the expansion along one direction is dominant, which makes the situation somewhat similar to that of uniaxial strain. If the strain is far from this situation, for example if there is a dominant shear strain (ϵ_{xy}) or rotation angle component, we cannot interpret it.

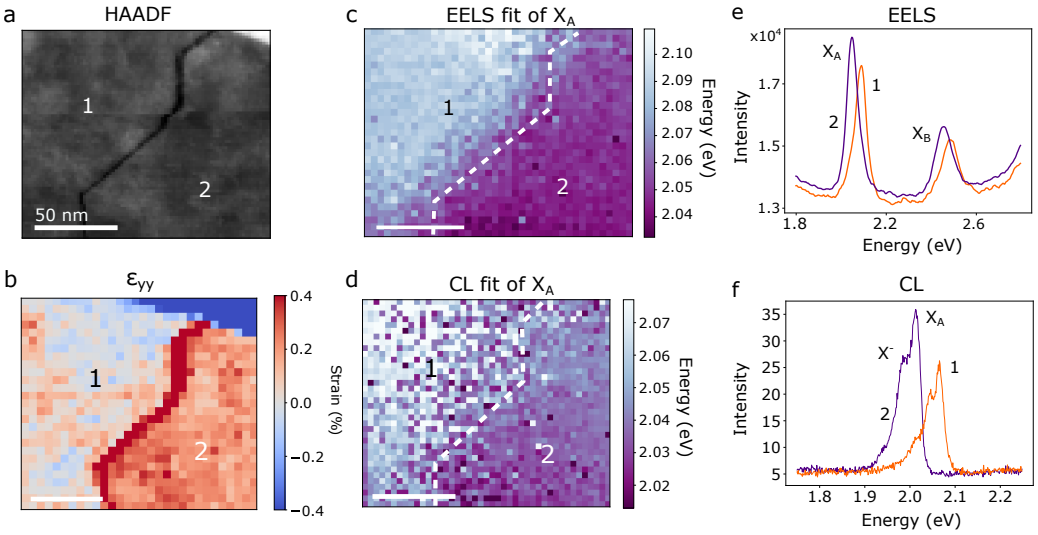

Figure 5.19: X_A energy shift and strain measurement: (a) HAADF image of the area, with number 1 (left-hand side) and 2 (righ-hand side) labeling the two sides of the crack, **(b)** ϵ_{yy} component of the strain tensor, showing an expansion on the right-hand side of the crack. The other strain components do not show a change of sign between the two sides. **(c)** X_A energy from Gaussian fit of EELS measurement, **(d)** X_A energy from Gaussian fit of CL measurement (the pixelated effect comes from the low intensity of emission close to the crack), **(e)** EELS spectra summed over area 1 and 2, highlighting the energy shift between the two regions, **(f)** CL spectra summed over area 1 and 2, showing the same tendency as (e), which is a blueshift in 1, where the monolayer is contracted, and a redshift in 2, where the monolayer is expanded.

The μ-diffraction method is limited mostly due to the extension of the diffraction spots, which illumination is not perfectly homogeneous. For strain values below 1%, the variations might be due to changes in illumination of the diffraction spot rather than actual lattice deformation. Therefore, here, the interpretations of the strain measurements can be debatable.

Another approach for strain measurement is the geometrical phase analysis, that uses the Fourier transform of atomically-resolved images to retrieve the strain components [43], described in more details in chapter 2.

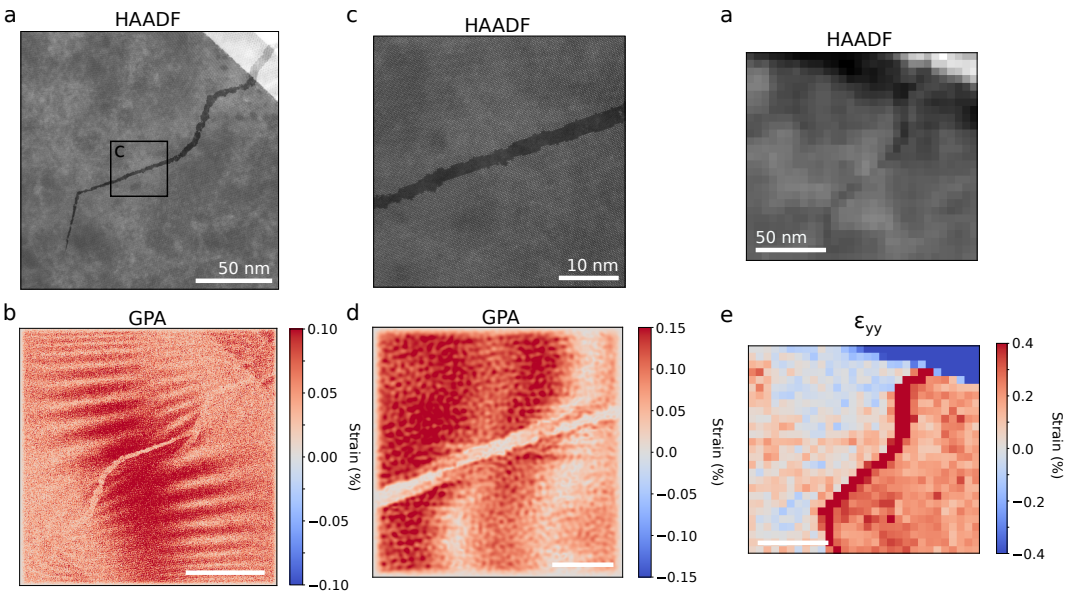

Figure 5.20: Comparison of strain measurements with GPA: (a) atomically-resolved HAADF measurement of the whole crack, **(b)** corresponding a* parameter from GPA, **(c)** atomically-resolved HAADF image of a part of the crack, **(d)** corresponding a* parameter from GPA, **(e)** HAADF image of the crack from the µ-diffraction measurement, **(e)** µ-diffraction ϵ_{yy} component.

Even if the µ-diffraction measurements are not perfectly reliable below 1%, we can extract the same tendency as with GPA: on the right-hand side, the lattice expansion is greater than on the left-hand side.

Strain is an extrinsic parameter that can be controlled to tune the optical bandgap of TMD monolayers. Nevertheless, the sample preparation of monolayers creates strain by itself, which is not simply uniaxial or biaxial. More theoretical studies, in particular on the shear strain influence on the energy structure, are necessary to fully understand the influence of strain on the bandgap energy.

5.3.3 Influence of the temperature on the optical properties

As briefly described before, the Stokes shift measured is high compared to the literature [17, 38, 138, 139], even when taking into account the imprecision of the EELS calibration of the drift tube (about 1 %, which corresponds to about 20 meV at 2 eV).

A reason for this might be the high strain necessary for the preparation of the heterostructure on the TEM grid. I studied this by varying the temperature of the sample from LN_2 to RT, and see if the lattice parameter change matches the expectations for WS_2, which are about 0.5 % between 150 and 300 K [140].

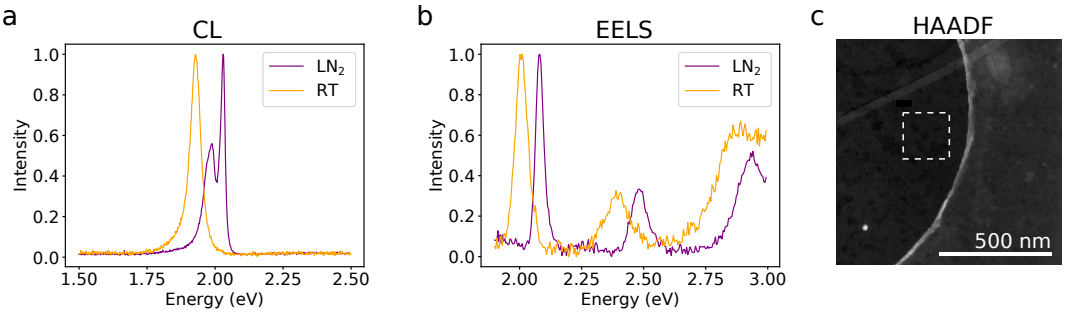

Figure 5.21: Effect of temperature on the EELS low-loss measurement: (a) CL Spectra obtained for two different temperatures: room-temperature (RT, orange), about 300 K, and liquid nitrogen (LN_2, purple), about 150 K. A redshift in energy, a broadening of the exciton peaks and a lowering in intensity can be seen when the temperature is increased. For CL, the redshift of X_A is of about 90 meV. **(b)** Corresponding EELS measurements. For EELS, the redshift of X_A is of about 50 meV. **(c)** HAADF image of the area, the CL and EELS measurements were performed in the dotted square.

Additionally to the redshift of the X_A with heating the sample to RT ($\Delta E_{XA,CL}$=87±7 meV and $\Delta E_{XA,EELS}$= 45±10 meV), the Stokes shift change is around 40±12 meV. The X^- peak also changes in intensity which is expected since trions binding energy are of the same order of the k_BT value at room temperature. X^- varies when changing T, nevertheless other parameters have been shown to change the X^- emission, such as described in the next section.

When changing the temperature of the sample from LN_2 to RT, one can observe a redshift of the excitonic peaks of the WS_2 in absorption and emission. This energy shift is known to be about 40 meV for encapsulated WS_2 in PL and optical differential reflectance [38], and is primarily due to the sample contraction when the temperature decreases. Whereas, in our sample, the shift in emission (CL) about 90 meV, and about 50 meV in absorption (EELS). A similar difference between the shift in PL emission and that in differential reflectance is also seen [139], and corresponds to a reduction of the Stokes shift due to the change in exciton-phonon coupling under strain [139].

I measured the lattice parameter at the center of five holes in µ-diffraction. One diffraction pattern is measured per hole, with a large beam size of a few hundred nm. The lattice deformation was correlated with the CL and EELS spectra. The results are shown in Fig. 5.22.

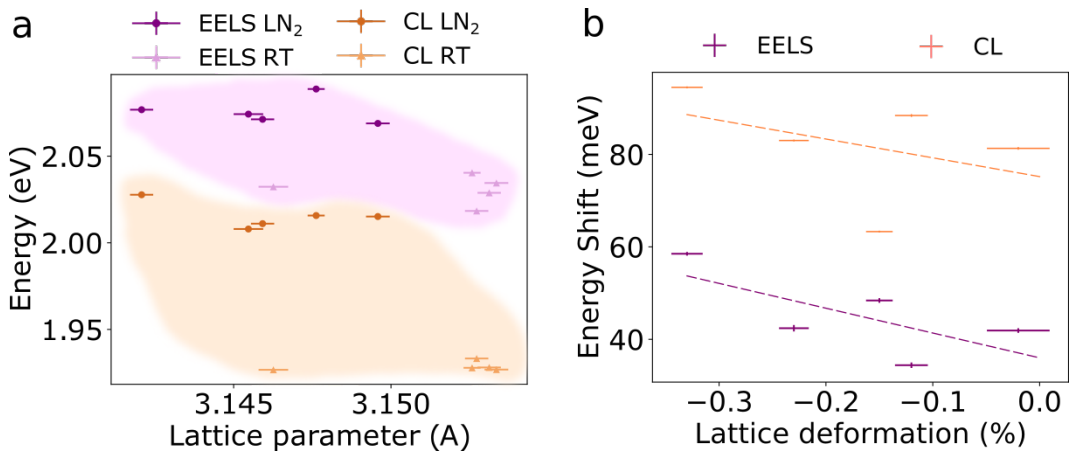

Figure 5.22: X_A energy in EELS and CL at two temperatures: (a) X_A energy as a function of WS_2 lattice parameter. **(b)** Energy shift ΔE_{XA} = $E_{X_{A,LN2}}$ - $E_{X_{A,RT}}$ as a function of relative lattice deformation Δa = $a_{X_{A,RT}}$ - $a_{X_{A,LN2}}$

At room temperature, the lattice parameters are quite similar to one another, whereas at 150 K they are spread among more values, as displayed previously in Fig. 5.10. This means that at low temperature, the TMD monolayer's lattice is not contracted in the same way everywhere. Moreover, the value of the lattice contraction expected for this temperature difference is about 0.4% [140], and our mean value is about 0.2%. The thermal expansion coefficent of few-layer h-BN is known to be negative [141], which means that as the temperature is lowered, the h-BN expands. Here, we measured a contraction of the h-BN lattice for a temperature decrease, of about 0.2 %, which is unexpected. The presence of h-BN explains the reduction of the contraction of the WS_2 monolayer, whose thermal expansion coefficients are measured for the bare monolayers.

5.4 Origin of X^- variations

Trions play a large role in the TMD monolayer emission [38]. Since they are made from X_A and a supplementary charge (here an electron). Parameters influencing the X_A and the free charge-carriers density can impact them.

Here, I present measurements of X^- intensity and energy variations at the few tens of nanometers scale. These measurements combine, on top of spatially-resolved CL, absorption measurements from EELS low-loss, chemical mapping from EELS core-loss, strain measurements (µ-diffraction) and atomically-resolved images.

The combination of all these measurements allow for some understanding of the X^- variations' origin. The same type of measurements are used in the next chapter for understanding the causes of localized exciton emissions.

In this section, three particular phenomena are described:

1. The X^- enhancement and energy shifts when approaching the conducting carbon support is described in section 5.4.1. This X^- enhancement can originate from charge accumulation due to the conductive carbon membrane forming a metal-insulator-semiconductor junction with the h-BN and TMD.

2. The X_A enhancement due to Purcell effect on top of the conductive carbon support is characterized in section 5.4.2.

3. The X^- enhancement on small patches due to dielectric environment changes is described in section 5.4.3.

5.4.1 Metal-insulator-semiconductor capacitor

An effect often observed on the CL emission is the sudden increase of intensity of the X^- peak when approaching the carbon support membrane, as displayed in Fig. 5.23. This rapid increase in intensity of the trion is accompanied by a characteristic energy redshift. At first, at the center of the carbon support membrane hole, the trion has an energy of $E^0_{X^-}$. When approaching the carbon membrane support (at about 200 nm), the trion peak starts increasing in intensity, together with a small but reproducible redshift in energy. This redshift is of the order of 10 meV. Then the X^- peak shifts back to $E^0_{X^-}$ when getting closer to the edge of the carbon membrane, at about 50 nm. This typical behavior is illustrated in Fig. 5.23d.

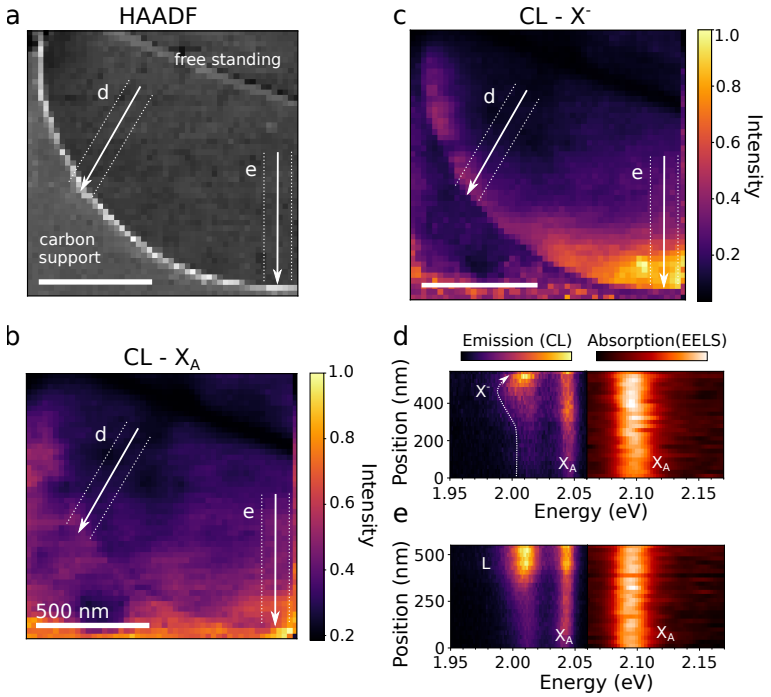

Figure 5.23: X^- enhancement next to the carbon support membrane: (a) HAADF image of the area, the arrows correspond respectively to the profiles shown in (d) and (e), **(b)** CL X_A intensity map, **(c)** CL X^- intensity map, **(d)** combined spectral profiles in both emission (CL) and absorption (EELS). A redshift followed by a shift back to $E^0_{X^-}$ can be seen on the X^- peak profile when approaching the carbon membrane, this energy shift is highlighted by the dotted arrow. **(e)** Combined profile of both emission (CL) and absorption (EELS), the lower-energy peak profile does not shift in the same way that X^- does, maybe indicating that the emission origin is different.

The first effect, the increase in X^- intensity accompanied with the peak redshift, is attributed to the increase of the free charge-carrier density. This free charge-carrier density increase can be due to band bending of the WS_2 monolayer due to the presence of a meta-insulator-semiconductor (MIS) capacitor. Indeed, the vertical stacking h-BN/WS_2/h-BN/conductive carbon make a MIS capacitor, where M is the conductive carbon, I is the 5 nm h-BN layer and S is the TMD monoayer. Thus, the free-electrons in the center of the carbon support hole and those close to the support edge have a different potential. This leads to charge-accumulation close to the carbon support edge. The high free-electron density increases the X^- density, whose

emission intensity increase and redshifts. The redshift is known to occur when the charge density is increased with gating [104, 114]. In the reference, the authors measured a redshift of 40 meV with a 40 V gating that leads to charge density of about $3.2\times10^{12}\ cm^{-2}$. A capacitance created by 5 nm of h-BN (considering its bulk dielectric function) can induce charge densities of the order of $2.5\times10^{12}\ cm^{-2}$. The magnitude of the energy shift we observe (around 10 meV) is in the same order of magnitude as that for gated experiments. Therefore, we interpret the redshift in energy and higher emission rate as an increase in the X^- population due to higher free electron density.

The second effect, the shift back to $E^0_{X^-}$ when approaching the edge of the carbon membrane, cannot be interpreted by the MIS capacitor hypothesis. Indeed, it would only induce the increase in intensity of X^- and the redshift, whereas we observe an increase in intensity with a blueshift. A reduction of the free electrons density would explain the blueshift, but should be accompanied by a decrease in the X^- intensity. For these reasons, we interpret the blueshift in energy with an increase of X^- to a local increase of optical mode density, which increases the X^- recombination rate, quickly decreasing the X^- population. The decrease in X^- population would then be the reason for the redshift. Another possibility, rather than the increase of optical mode density, is the increase of non-radiative decay channels, which would also reduce the radiative lifetime, but would decrease the CL intensity. The general increase of optical modes density due to Purcell effect of the carbon membrane is explained in details in the next part.

The two effects explained above cannot be caused by a change in optical bandgap, since the X_A energy would be affected. The intensity decrease when the beam moves towards the hole center for X_A and X^- in Fig. 5.23 is due to the presence of a bubble and a fold, which reduce the radiative recombination of X_A and X^- by creating new non-radiative decay paths. This X^- enhancement with energy shift next to the carbon support is observed in most holes, so that we estimate that it does not come from intrinsic doping of the monolayer.

From the other extracted profile similar to that in Fig. 5.23, the X_A and X^- peaks can be fitted with Gaussian functions and their intensity and their energy can be plotted as a function of position (Fig. 5.24).

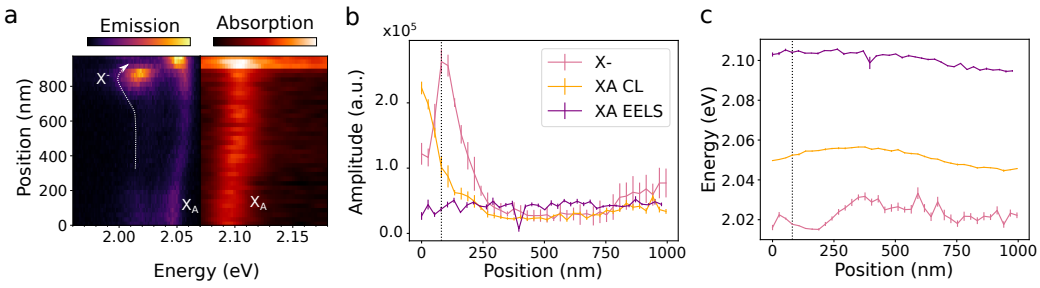

Figure 5.24: Intensity an energy profiles close to the carbon membrane: (a) CL (emission) and EELS (absorption) of the X_A and X^- peaks, **(b)** intensity profiles from the Gaussian fitted data in (a), the 8.4 fold increase of X^- close to the carbon membrane is visible. **(c)** energy shifts along the profile, the 10 meV characteristic redshift is visible for X^-, whereas X_A shifts continuously in energy both in emission and absorption. The position of the edge of the carbon membrane is highlighted by the dotted line.

The mean X^- to X_A intensity enhancement is of 8.4-fold close to the carbon membrane. The X_A enhancement occurs at shorter distances from the carbon support, and is due to Purcell effect, which is detailed in the next part. The characteristic energy shift is visible in Fig. 5.24c, where the 10 meV redshift show up together with a slow energy shift, that is followed by the X_A both in emission and absorption.

The hypothesis on the MIS capacitor cannot be verified by solely these experiments, but the other possibility often invoked, which is strain [137], can be eliminated. The µ-diffraction across the same area as Fig. 5.23 has been measured to see if the strain component changes match that of X^-.

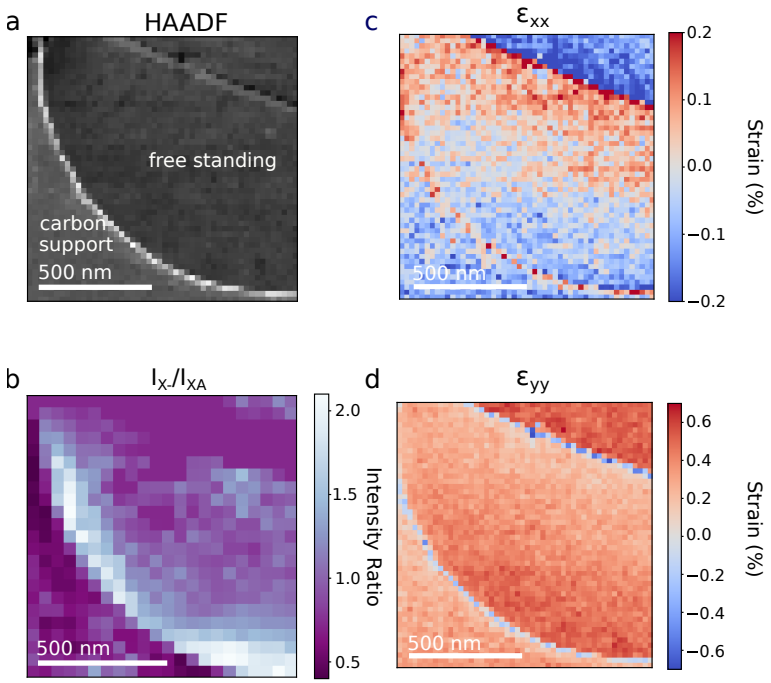

Figure 5.25: Origin of X^- enhancement: (a) HAADF of the area. The "carbon support" label indicates where the carbon support is, and it is delimited by the circular white contrast in the image. The square corresponds to the area mapped in (e). **(b)** Intensity ratio of X^- and X_A, showing trion enhancement when approaching the carbon support membrane. **(c)** ϵ_{xx} and **(d)** ϵ_{yy} components of the strain tensor, showing some variations that do not spatially correspond to the X^- enhancement seen in (b).

Some variations are measured, particularly on ϵ_{xx} and ϵ_{yy}, but they do not match the intensity pattern seen for X^- enhancement in Fig. 5.25b. Moreover, the strain values are quite small, within the error of µ-diffraction measurements (see chapter 2).

On Fig. 5.23e, another line profile was plotted, since it shows the behavior in energy of the highest intensity spot of the area. Nevertheless, the characteristic energy shift close to the carbon membrane is not seen. This peak (L) will be treated in chapter 6 since it has a slightly higher energy separation than that of X^- with X_A, and does not behave the same as the X^- peak.

5.4.2 Purcell effect on the carbon membrane

On the carbon support membrane, the X_A is seen to increase in intensity, by about a factor 2, whereas the X^- peak decreases, by about a factor 4 (Fig. 5.26). The presence of the carbon support membrane seems to be the cause of this intensity modulation. Indeed, the carbon membrane changes the electromagnetic local density

of states (EMLDOS), which in returns modifies the recombination rate of emitters [142, 143]. The recombination rate increase would increase the emitted intensity. The emission enhancement can still occur hundreds of nanometers away from the conductor, even with encapsulated TMDs [37].

The X_A emission enhancement is accompanied by a strong decrease in X^- intensity. It is highlighted in Fig. 5.26c, where X_A intensity increases suddenly when the edge of the carbon support membrane is crossed. What is more striking is that while the CL peak increases, the EELS absorption peak barely changes, and is even slightly reduced (one has to keep in mind that direct absorption of the X_A is not the principal excitation path). This change in intensity emission for X_A can be explained by the change in radiative recombination rate of the exciton an trion due to Purcell effect [142].

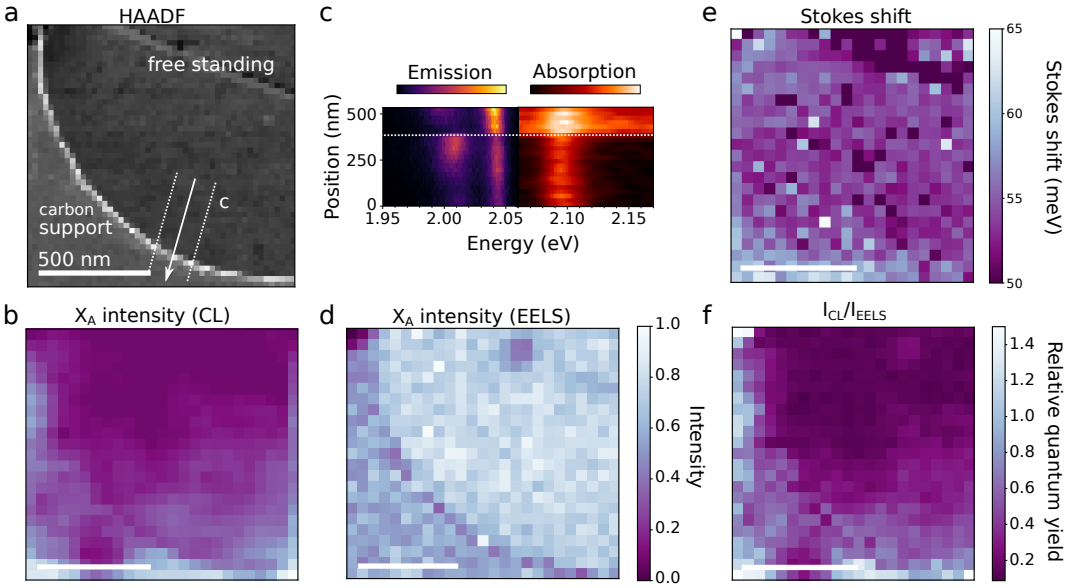

Figure 5.26: X_A enhancement on the carbon support membrane: (a) HAADF image of the area, the "carbon support" label indicates where the carbon membrane is, and it is delimited by the circular white contrast in the image. The white arrow indicates the path where (c) profiles were extracted. **(b)** X_A emission (CL) Gaussian fitted map, **(c)** Spectral profiles along the arrow in (a), **(d)** X_A absorption (EELS) Gaussian fitted map, **(e)** map of the Stokes shift SS = ($E_{X_{A,EELS}}$) - ($E_{X_{A,CL}}$) from Gaussian fitted measures of X_A in (b) and (d), **(f)** relative quantum yield $I_{X_{A,CL}}/I_{X_{A,EELS}}$ showing X_A emission enhancement on the carbon membrane.

If we look at the intensity ratio $I_{X_{A,CL}}/I_{X_{A,EELS}}$, which is the relative quantum yield (ratio between emission intensity and absorption intensity), the values are higher on the carbon membrane, and lower everywhere on the free standing part. Together with this enhancement of the relative quantum yield, a slight increase in Stokes shift is seen, due to the redshift of the X_A.

This intensity inversion between the X_A and X^- peaks at the edge of the carbon support highlights how much the dielectric environment impacts the energy of the excitons and trions in the monolayer, even if this one is encapsulated in h-BN [122].

Both variations, the X_A intensity increase and the X^- intensity decrease, can be attributed to the Purcell effect: the lifetime τ of both X_A (τ_{X_A}) and X^- (τ_{X^-}) are reduced. For X_A, the lifetime reduction directly increases the intensity emitted on top

of the carbon membrane. For X^-, the process is not that straightforward: the lifetime reduction of X_A could be such that the excitons do not exist long enough to capture a free electron, meaning that even if there is a charge density increase due to the presence of the carbon membrane and the formed MIS junction, the excitons do not have time to form trions. This would also explain the redshift of the X^- peak on top of the carbon membrane, while there is a decrease of X^- intensity.
The trion formation time is about of 2 ps and recombination time of X_A is a few ps at low temperature [107]. The X_A decay time is known to be longer at higher temperature, up to tens of ps [144].

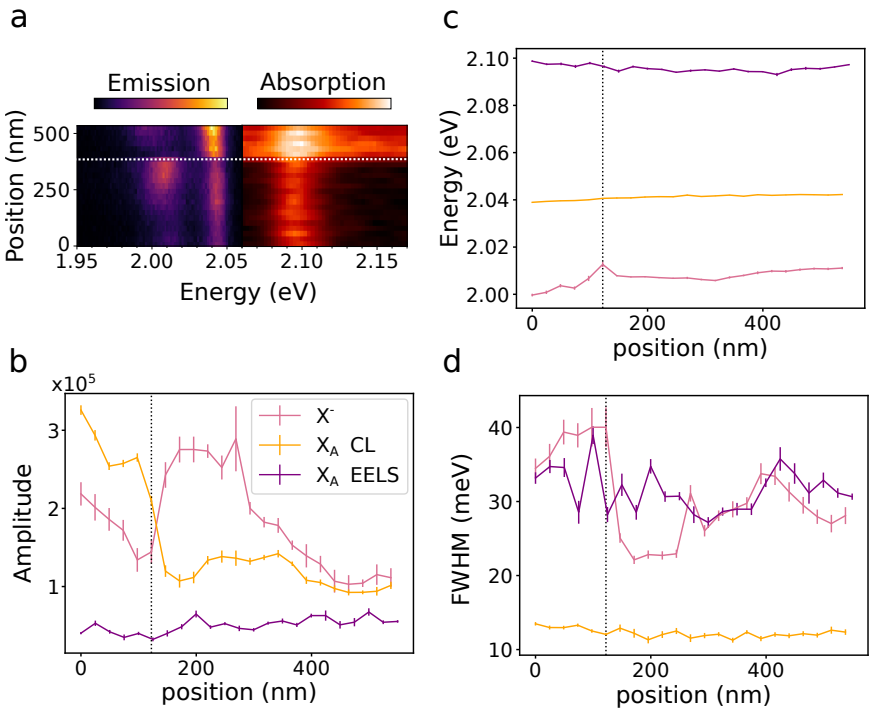

Figure 5.27: Gaussian fitted profile parameters: (a) energy profile on which the fit is performed, **(b)** peak amplitude $X_{A,EELS}$ (purple), $X_{A,CL}$(orange) and X^-_{CL} (pink). The membrane edge position is marked with the dotted line. **(c)** peak energy and **(d)** FWHM.

A way to confirm that a lifetime reduction is indeed responsible for the X_A enhancement and quenching of the X^- would be to directly measure it in CL, in HBT [22], or in time-resolved CL (detection synchronized with a pulsed electron beam). Our HBT setup time resolution is limited to about 0.1 ns [20]. It prevents us from measuring excitons and trions lifetimes, which are of the order few ps to a hundred of ps [145]. To be the reason for X^- quenching the lifetime would have to be reduced to the formation time of the trions, which is of about 2 ps at 13 K for $MoSe_2$ [107].

Another method would be to look at the broadening of the FWHM. The intrinsic FWHM of the exciton peak is directly linked to its lifetime, and at 300 K, the lifetime of TMDs monolayers of about 75 ps [144], which leads to an intrinsic peak width is of about 9 µeV. At low temperature, the lifetime of the exciton drastically decreases, and is about 2 ps (at 14 K) [108], which leads to a peak width of 330 µeV. Either way, the peak width measured in our experiments are of a few tens of meV, which indicates supplementary temperature broadening (at 150 K, k_BT is about 13 meV), and prevents the measurement of the intrinsic linewidth.

For now, the origin of the X_A intensity increase on the carbon membrane still remains a question.

5.4.3 Nanometer-scale X^- enhancement due to dielectric patches

The last effect described in this chapter is the X^- intensity enhancement at the tens of nanometers scale, in suspended areas. In this part, I present results on one area of a couple hundreds of nanometers, where the X^- localized emission is clearly visible.

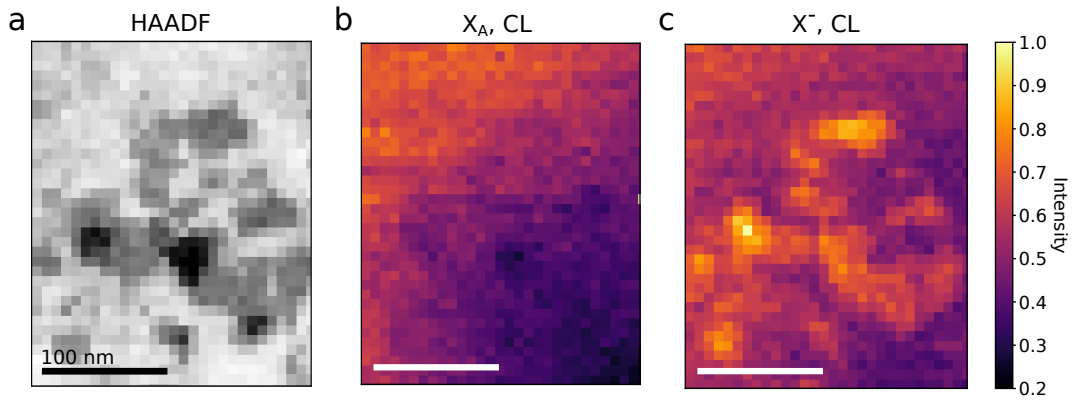

Figure 5.28: Local change in X^- intensity: (a) HAADF image of the area, **(b)** corresponding energy filtered X_A intensity map, **(c)** energy filtered X^- intensity map from the same area.

X_A is seen to gradually increase across the area, in a smooth way, while X^- shows some high intensity spots, with areas as small as few tens of nanometers. A corresponding pattern in the HAADF image is seen.

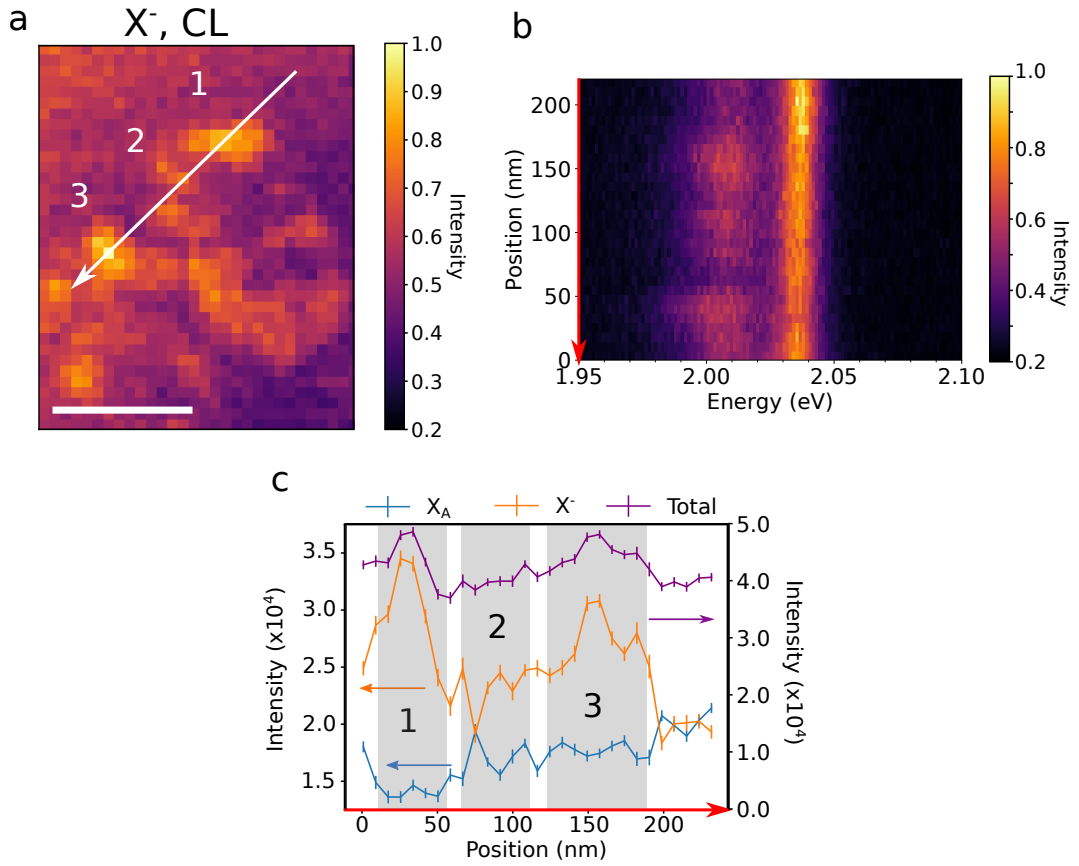

Figure 5.29: Local change in X^- intensity: (a) energy filtered X^- map. The arrow shows the position where the spectral profile in (b) and (c) are extracted. The high intensity spots are numbered from 1 to 3, corresponding to the intensity increase in (c). **(b)** spectral profile extracted from (a), **(c)** Gaussian fitted intensity parameter extracted (b).

The spectral profiles show a compensation between X_A and X^- intensities: where X^- is highest, X_A decreases. The compensation is not perfect since the total intensity is not constant.

Why does the X^- intensity pattern match the HAADF contrast? What is the origin of the HAADF image contrast? To find the origin of this variation, I explored two hypotheses: first the chemical environment change [121], that is likely to cause the contrast in HAADF imaging, and then the strain [137], that is a candidate for localization of CL emission.

To characterize the chemical environment, I measured the EELS core-loss spectra of the area, and performed a BSS decomposition (see chapter 2). The results are shown in Fig. 5.30. This experiment, contrary to the previous, have been performed in the UltraSTEM.

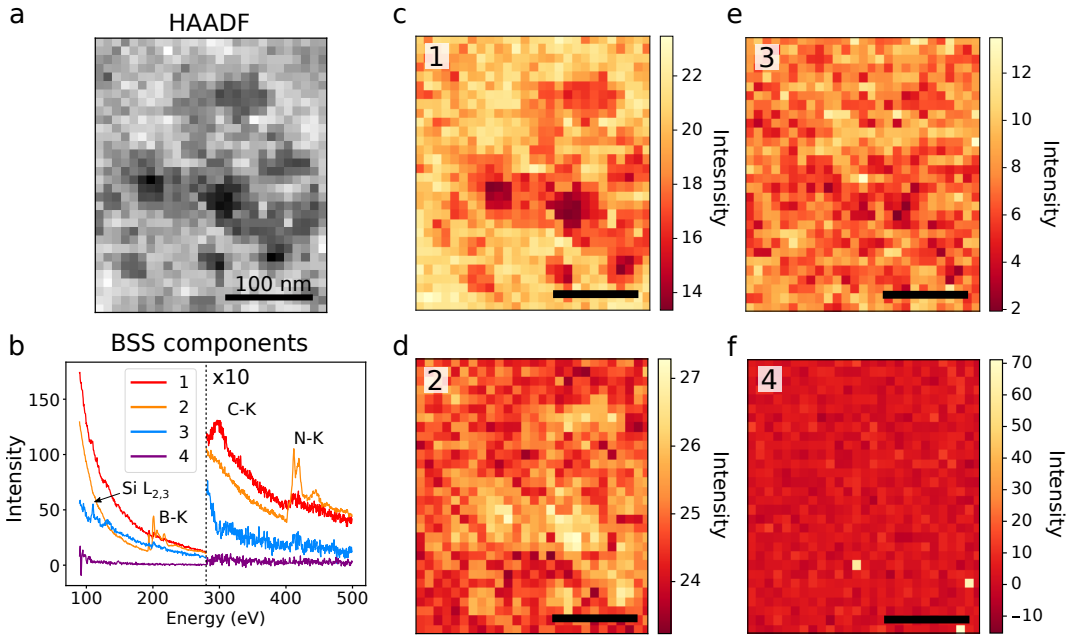

Figure 5.30: Local change in chemical environment: (a) HAADF image of the area studied, which is the same as in Fig. 5.28. **(b)** BSS spectral components from EELS core-loss measurement. **(c)** map of the first component of the BSS decomposition, containing mainly background and carbon, **(d)** map of the second component, containing mainly background and h-BN, **(e)** map of the third component, containing some silicon, **(f)** map of the fourth component, containing noise probably from X-rays.

For a decomposition with four components, the results show a pattern matching that of the ADF for components number 1 and 2. These spectral components contain mainly background, which is linked to thickness [24], and carbon, which is an expected contaminant from the sample preparation. The darker areas, where X^- is most intense, correspond to a decrease in carbon.

A strain measurement was also performed, since it is known to change the bandgap energy of the TMD monolayer [139], and I found variations of the 2D strain tensor, displayed in Fig. 5.31. In particular, a sign inversion of ϵ_{xx} is measured. Nevertheless, its pattern does not match that of X^- intensity, and therefore, is excluded as a candidate for X^- localization in this case. Another feature seen in the strain measurement is the increase in ϵ_{yy} at the bottom right, where the intensity of X_A is lowered. This could mean that the strain is creating non-radiative decay paths for X_A recombination.

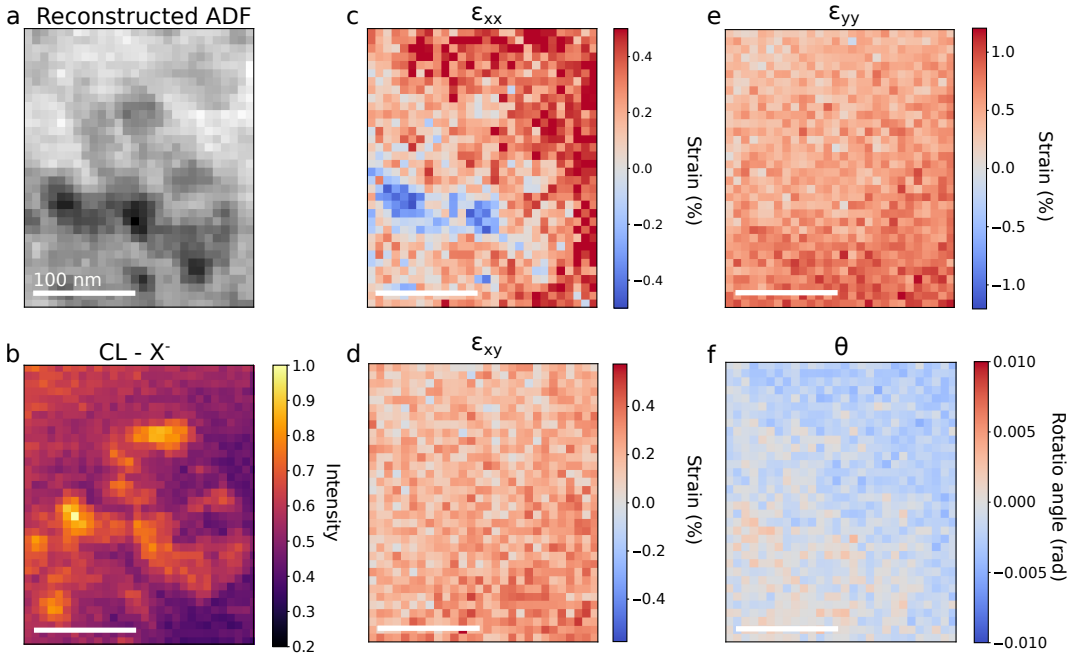

Figure 5.31: Local change in strain: (a) HAADF image of the area, which is the same as in Fig. 5.28 and Fig. 5.30, **(b)** X^- intensity from Fig. 5.28, where the enhanced patches are visible, **(c)** ϵ_{xx} component, **(d)** ϵ_{xy} component of the strain measurement,**(e)** ϵ_{yy} component, **(f)** θ rotation angle.

In Fig. 5.31, the reconstructed ADF has a slightly different geometry, due to the calibration of the scan in the UltraSTEM. Indeed, this measurement was performed on a larger area, and has been cropped to shown the zone corresponding to the CL measurement. For wide fields of view, the UltraSTEM calibration can be slightly off, which deforms the image (indeed, the scan calibration at the atomic scale is calibrated more carefully in aberration-corrected electron microscopes, and the scan calibration for few hundreds of nanometer scale was slightly off in this experiment).

In this part, I studied the origin for X^- intensity variations at the tens of nanometer scale on a suspended area of the TMD monolayer. A summary of the results is shown in Fig. 5.32. I found that the presence of carbon-rich contaminants was best correlated to the decrease of X^- intensity. Strain was measured but the role it plays for X^- localized emission is inconclusive.

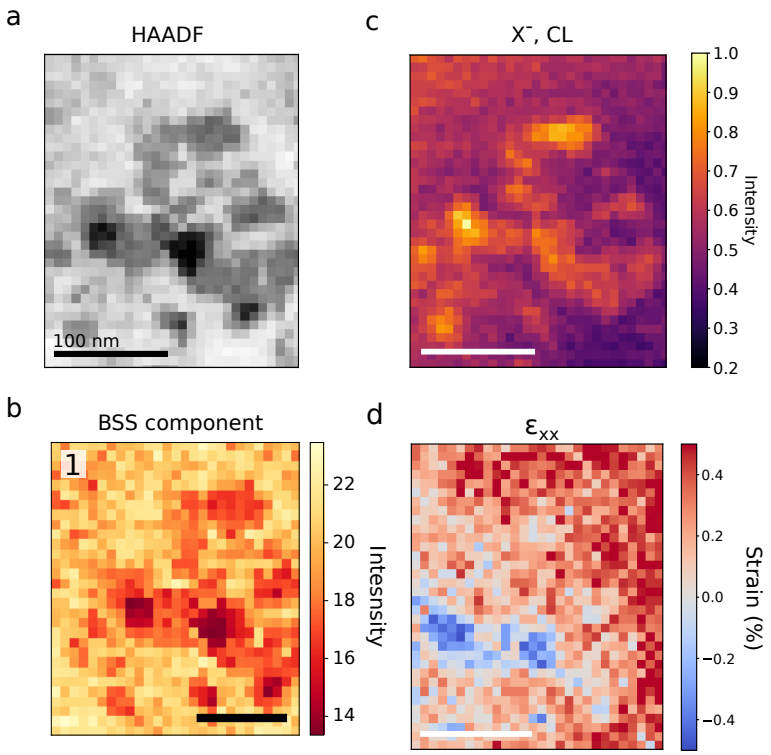

Figure 5.32: Summary of the localized X^- intensity enhancement: (a) HAADF image of the area, **(b)** BSS component (1) from Fig. 5.30, **(c)** energy filtered X^- intensity map, **(d)** ϵ_{xx} strain component. The scales are 100 nm.

5.5 Summary

In this chapter, I studied the origin of excitonic effects at the nanoscale in WS_2 monolayers encaspulated in h-BN. I correlated measurements of CL, low-loss EELS, µ-diffraction, core-loss EELS and atomically-resolved images to have access to the emission and absorption of the X_A, the strain and the chemical environment. The two latter were also correlated to the X^- measurements.

First, I showed that atomically-resolved imaging of the WS_2 encapsulated monolayer was possible. These images can give information on strain (GPA) and could be used to find the origin of SPE emission if it is linked to point defects.

The sample design is crucial to obtain sufficient CL signal from the monolayer. Indeed, the h-BN encapsulation, on top of protecting the TMD monolayer from damage and contamination, allows for the enhancement of CL signal. The heterostructure fabrication, specifically for TEM grids, puts the TMD monolayer under important strain, which modifies the optical properties of the TMD. The X_A emission and absorption energies, as well as the Stokes shift, are higher than what is usually measured for encapsulated WS_2.

Variations of the X_A and X^- intensity and energy related to the presence of the TEM grid carbon support have been measured. They take place on length scales of few hundreds of nanometers. There are two main behaviors: i) the X^- intensity enhancement and energy redshift when approaching the edge of the carbon support, and ii) the X_A intensity enhancement (coupled to a decrease of X^- emission) on top of the carbon support.

The X^- intensity increases when approaching the carbon support, with the subsequent redshift (i) could be explained by an increase in free-electron density close to the carbon support. The free electron density could be increased with the MIS capacitor formed with the carbon support/h-BN/WS_2 layers. The increase of X^- intensity is known to induce a redshift in energy, which is about 10 meV in our case. The intensity increase with redshift of the X^- is followed by an intensity increase with a blueshift (or shift back to the X^- initial energy, at the center of the hole), which is explained by the decrease of X^- population due to the Purcell effect few tens of nanometers away from the carbon support.
The X_A intensity increase on top of the carbon membrane (ii) can be due to the Purcell effect, which increases the local optical density of states. It increases the recombination rate of X_A, which increases the emission intensity. The X^- intensity is strongly decreased on the carbon membrane, which could be from the formation time of trions being longer than the lifetime of X_A.

Finally, I measured variations of the X^- emission at the tens of nanometers scale, on suspended areas. This length scale in CL, EELS and µ-diffraction is not accessible with others methods. I attributed these changes to the charge trapping due to the dielectric environment change, which I characterized with EELS core-loss measurements.

With the combined measurements of CL, EELS and µ-diffraction, I have investigated in the next chapter the lower energy emission lines.

Chapter 6

Localized emission from TMD monolayers

Contents

As seen in the introduction of chapter 4, single photon emitters (SPE) have drawn tremendous attention, due to their applications in quantum computing and quantum networks. To deterministically produce single photon sources (SPS) in a system, the origin of the quantum emission has to be known. SPE have been detected in TMD monolayers for the first time in 2015 [146], but the origin of most localized emission is not well understood yet. Indeed, correspondence between the diffraction-limited PL measurements and the nanometer-scale structure measurements is difficult to obtain.

In this chapter, I study the properties of localized low-energy ($< X_A$ and X^- energy, i.e. < 2.00 eV) CL emission in h-BN encapsulated WS_2 monolayers. The low-energy emission is suspected to originate from excitons localized in energy potentials, which is attributed to strain [137]. We want to link the emission energy to a defect, strain pattern, dielectric environment change etc. The origin of the emission is explored by means of HAADF imaging, for the morphology of the areas, EELS core-loss spectroscopy, for the chemical environment, and µ-diffraction, to have information about the strain.

In chapter 5, I have measured the nanometer scale variations of X_A and X^- emission in CL. In this chapter, I use the same type of data to look at the low-energy emission from the TMD monolayer. Even if the monolayer is encapsulated in h-BN, the emission comes from the WS_2 monolayer, as described in chapter 5. Indeed, the exciton emission from h-BN is in the UV range (about 5.7 eV [147]), which is above the X_A (about 2.05 eV), and is not measured with our samples. Nevertheless, lower energy emission from defects in h-BN could be involved in the low emission

presented in this chapter. Yet, the low-energy emission signatures in h-BN are well-known, and the origin of low energy emission displayed here comes most probably from WS_2.

Examples of low-energy emission CL spectra are plotted in Fig. 6.2.

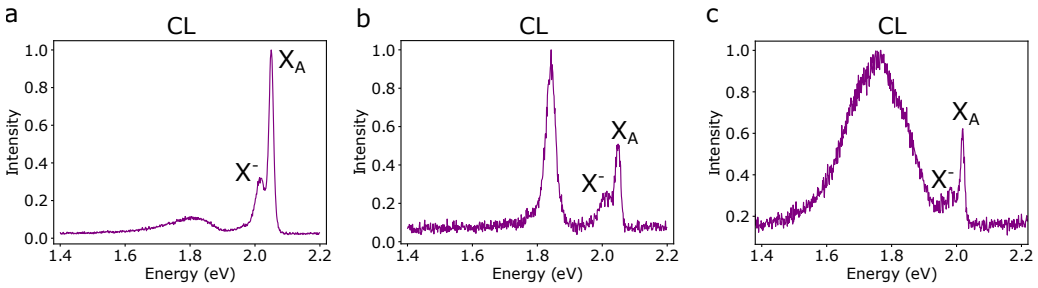

Figure 6.1: Examples of low-emission spectra in CL in the WS_2/h-BN heterostructure: spectra extracted from three different areas of a sample, displaying various spectral features at lower energy than X_A and X^-. The measurements are performed at 150 K.

The energy of X_A, X^- and lower-energy peaks measured in CL are reported in the histogram in Fig. 6.2. Both the X_A and X^- peaks are clearly visible, and the X^- low-energy tail measured is what I referred to as L emission. Individual values extracted from the CL data produce a low-energy band centered at 1.8 eV.

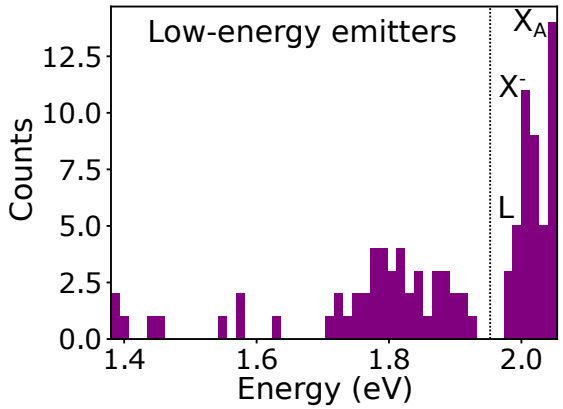

Figure 6.2: Histogram of the energy of the localized emitters in h-BN encapsulated WS_2 monolayer at 150 K in CL: the histogram is built from 124 values extracted from 24 different areas on two different samples. The two peaks above 2 eV correspond to X^- and X_A, whereas all the other values are from low-energy emission.

From the data I measured, several categories of emitters can be identified, and are described in the following order throughout the chapter:

- the L emitter, with a characteristic mean energy of 45 meV below the X_A energy, is described in section 6.2,
- localized emission from the edge of a bubble, in section 6.3.1,
- peak emission forming lines in the CL intensity maps, which energy shift over time, in section 6.4,
- long decay lines, in section 6.4.1,

- thin peak (about 30 meV of FHWM) on dielectric patches, in section 6.4.2.

The chapter mostly displays raw CL data with the corresponding HAADF images, data (EELS core-loss and CL) processed with a blind source separation algorithm (BSS, described in chapter 2 for CL and EELS core-loss), and strain measurements. The results presented are preliminary, and insufficient to conclude about the origin of the localized emission or the nature of the emitters. For each emitter, the number of times the detection of emission from the specific spectral feature is displayed. Each area has been measured several times, so that this number can include the multiple measurement of the same feature. For all measurements, I made sure to have at least five different areas displaying the same behavior to mention it in the chapter.

The measurements have been performed in two microscopes: the CL and HAADF in ChromaTEM, and the core-loss EELS and µ-diffraction in the UltraSTEM. It has to be noted that the two microscopes are operated at different voltages (60 kV for the ChromaTEM, and 100 keV for the UltraSTEM), and have different temperatures (150 K for the sample in the ChromaTEM, and 300 K in the UltraSTEM).

6.1 Generalities and state-of-the-art

Low-energy emission from single photon sources in monolayer TMDs have been detected for the first time in 2015 [146]. In addition to measuring PL emission from defects, the defects were created deterministically by scratching the edges of the WSe_2 monolayer with an AFM tip. The origin of the emission is suspected to be linked to the presence of vacancies, but it was not directly measured [146].

In this section, I summarize the literature on SPE detection in WS_2 and WSe_2 using PL and electroluminescence (EL) techniques. The low-energy emission data extracted from graphs in the references is summarized in table 6.1. In the literature, the lower-energy emission are referred to with many different names. In this chapter, I label "L" for the lower-energy emission that is close to that of X^- (above 1.95 eV), and "lower-energy emission" for the others. This notation is used only because the L emission has a specific energy, at about 45 meV below that of X_A.

The PL from quantum emitters in TDM monolayers is often measured at low temperature (see Fig. 6.3), below 10 K [112, 146]. Nevertheless, single-photon emission can still be visible up to room temperature [85]. Some single photon emission can be linked to features on the monolayer, such as bubbles [85], holes [112], or tips [111]. From the understanding of the origin of the single photon emission, centers can be created deterministically [85, 111, 148].

The production of quantum emitting devices being attractive, the electroluminescence (EL), which is the light-emission from the excitation with electrical injection of charges, has been studied. Devices with contacts, such as graphene sheets, are necessary to produce for such an experiment. The EL emission is often measured on TMD monolayers encapsulated with h-BN. Emission from individual defects can be observed at low temperature (< 5 K) [109, 149]. The EL excitation is non-local and does not give information about the local environment, or the position of the localized emission.

Tip-based experiments have access to the localized light-emission and the topography of the sample, such as described in chapter 5. In reference [86], the emission

from a single defect, which is a sulfur vacancy, has been measured in STM-lum. This method is powerful, but does not allow for the measurement of emission of embedded materials, such as encapsulated TMD monolayers.

Reference	Material	X_A (eV)	X^- (eV)	(eV)	(eV)	(eV)
[38] PL	WS_2 5K sapphire substrate	2.034	1.998 2.004	1.985	1.972	1.961
	WSe_2 5K sapphire substrate	1.727	1.691	1.698	1.677	1.651
[101] PL	WSe_2 4 K SiO_2	1.753	1.716 1.721	1.700 1.665	1.687	1.682
[150] PL	WS_2 7 K SiO_2/Si	2.095	2.054	2.035	2.010	1.986
	WSe_2 7 K SiO_2/Si	1.747	1.717	1.694 1.661	1.683 1.638	1.671
[109] EL	WS_2 5 K encapsulated in h-BN on top of Au and graphene	2.075	2.043 2.038	2.005	1.976	
	WSe_2 5 K encapsulated in h-BN on top of Au and graphene	1.732	1.701 1.693	1.661 1.617	1.652 1.594	1.631
[105] PL	WS_2 4 K SIO_2/Si	2.092	2.070 2.059	2.037	2.005	
[146] PL	WSe_2 10 K SiO_2/Si	1.747	1.718	1.697 1.639	1.682 1.622	1.661
	WSe_2 10 K	1.751	1.722	1.704 1.668	1.693 1.662	1.683 1.589
	SiO_2/Si WSe_2 10 K h-BN/SiO_2/Si		1.693	1.681 1.614	1.666 1.594	1.650 1.576

Table 6.1: Table summarizing the localized emission in WS_2 and WSe_2 from literature.

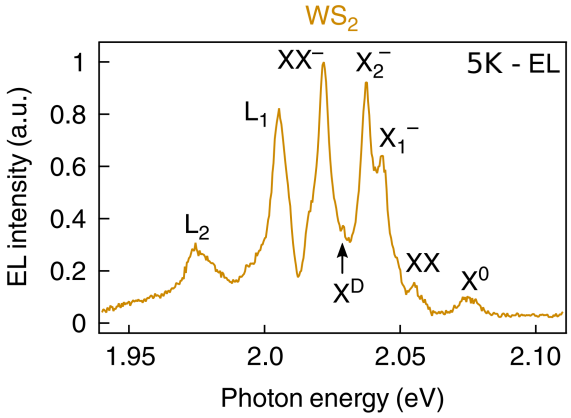

Figure 6.3: Spectrum of the low-energy emission in PL: measured on WS_2 encapsulated in h-BN, contacted with graphene and Au/Pt to obtain electroluminescence (EL). X^0 is the neutral exciton (noted X_A in the thesis), XX is the biexciton emission, X_1^- and X_2^- are the two trion peaks, unresolved at 150 K and noted X^- in this thesis, X_D is the dark exciton, XX^- is the charged biexciton, and L_1 and L_2 are two unknown lower emission lines. The measurement was performed at 5 K. Reproduced from [109].

6.2 L emitter

I refer to as L emission a peak at about 45 meV below the X_A emission. This peak differs from the X^-, first because of the mean energy difference with X_A, which is 35 meV, and because of the spatial and spectral behavior of the emission. In this section, three cases of L emission are described:

1. spatially extended emission next to the edge of the carbon support membrane,
2. localized on the edge of the carbon support membrane,
3. localized on dielectric patches.

An illustration of the L peak spectrum is displayed in Fig. 6.4, where the L and X^- peaks are resolved.

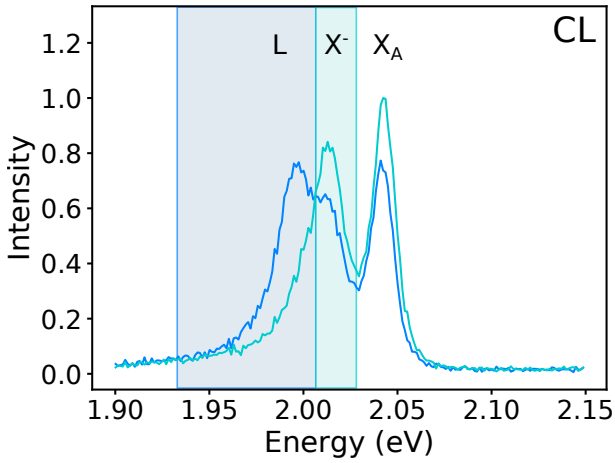

Figure 6.4: Comparison between the X^- and L peaks in CL at 150 K: two spectra, measured few tens of nanometers apart, are displayed. The L emission peak is visible below 2.00 eV and is highlighted in blue (1.997 eV), whereas X^- is above 2.00 eV and highlighted in turquoise (2.013 eV). X_A is at 2.043 eV.

The X^- peak contains the emission from two types of trions, the intra- and inter-valley trions, as explained in chapter 5. At 150 K, the temperature of the CL measurements, the trion peaks are unresolved [38], whereas the L peak is clearly visible in our measurements, indicating a possible different origin for the L emission. The origin of the L emission is explored in the following sections.

6.2.1 Spatially extended emission next to the edge of a membrane

The intense emission next to a carbon support membrane edge is seen at the tens to few hundreds of nanometers scale. The emission hotspot is more intense than that of the X^- and it does not shift when approaching the membrane, as displayed in Fig. 6.5. I have measured this type of emission 8 times.

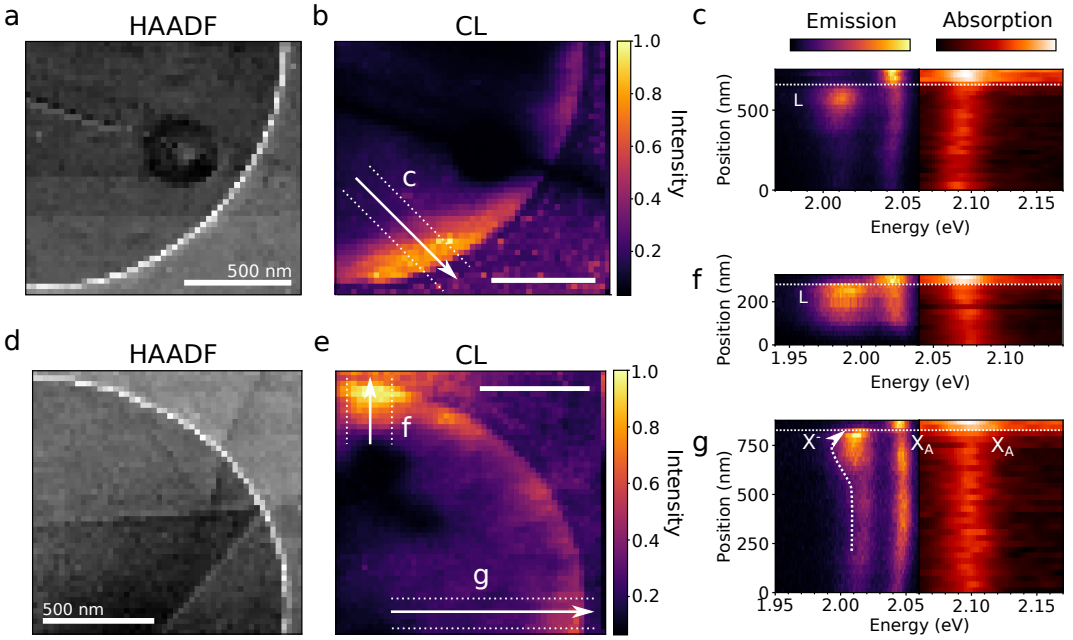

Figure 6.5: Difference between the localized L peak and X^- when approaching the carbon membrane: (a) HAADF image of the area. A crack crosses the heterostructure, as well as a bubble. **(b)** Energy-filtered (2.00 to 2.02 eV) CL intensity map, with an arrow indicating the positions of the extracted profile (c), **(c)** extracted profile from (b), left-hand side CL emission, right-hand side EELS, **(d)** HAADF image of the area, **(e)** energy-filtered (1.89 to 2.03 eV) CL intensity map, **(f,g)** extracted profiles from (e). The (c) and (f) profiles do not display the energy shift as in (g), and the energy is slightly lower. The measurements are performed at 150 K.

As seen in Fig. 6.5b and e, the hotspots are most intense on the c and f profiles, whereas the g profile displays a typical X^- behavior. The intensity, energy and FHWM from the profiles in Fig. 6.5 are plotted in Fig. 6.6.

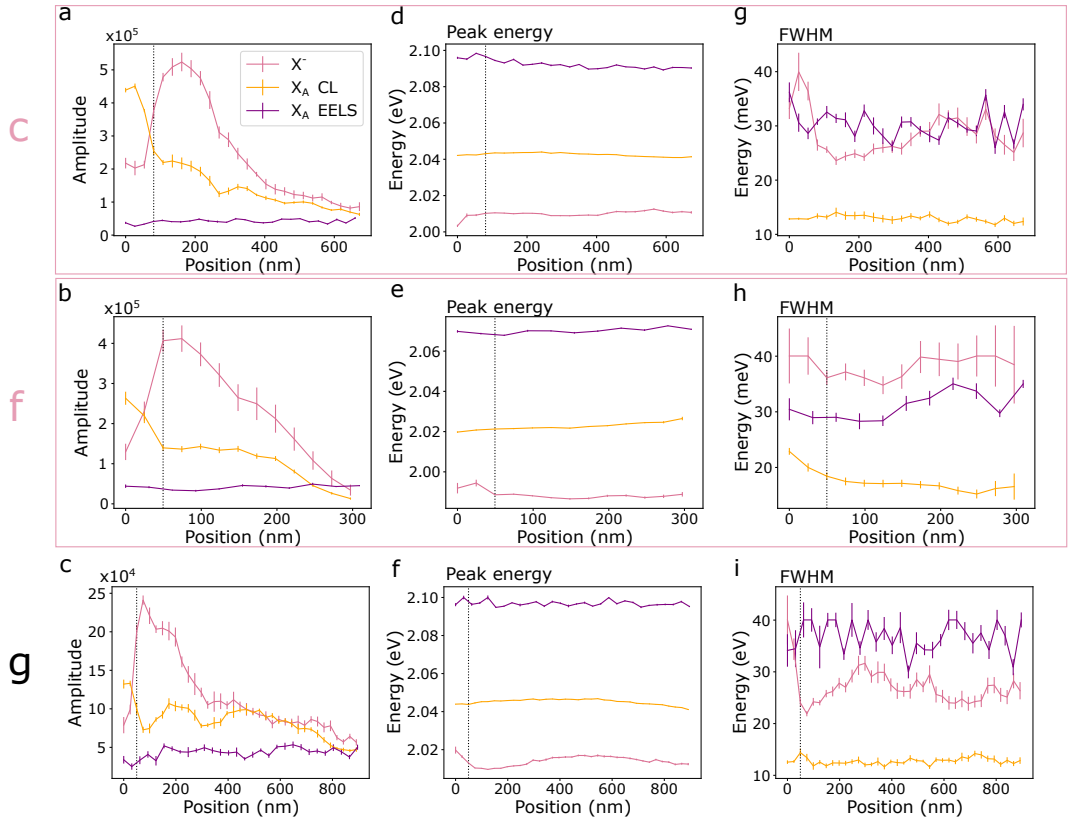

Figure 6.6: Amplitude, energy and FWHM of the X^- and L peaks along the profiles in Fig. 6.5: (a) amplitude of the profile in Fig. 6.5c, **(b)** amplitude of the profile in Fig. 6.5d, **(c)** amplitude of the profile in Fig. Fig. 6.5g, **(d,e,f)** corresponding peak energy, and **(g,h,i)** corresponding FWHM. The (a,d,g) profiles correspond to the behavior of the X^-, whereas the other profiles show that of the L line.

	Profile c	Profile f	Profile g
ℓ_t	220 nm	175 nm	338 nm
ΔE	1 meV	1 meV	10 ± 2 meV
$\Delta FWHM$	10 ± 2 meV	1 meV	18 ± 5 meV
I/I_0	6.4	12	3.1
$< X_A - L >$	32 meV	33 meV	28 meV

Table 6.2: Table summarizing the values extracted from the profiles in Fig. 6.6: ℓ_t is the typical length of the peak increase, ΔE is its energy variation, $\Delta FWHM$ is its FHWM variation, I/I_0, the intensity increase, and $< X_A - L >$, the mean energy separation with X_A.

Here, the L emission looks mostly like a X^- emission with higher yield. It behaves as if the area was more negatively doped.

6.2.2 Small sized emission on top of the edge of a membrane

Spatially localized emissions have been detected on top of the edge of the carbon support membrane. Two examples of measurements are displayed in Fig. 6.7. I have measured this type of emission 18 times.

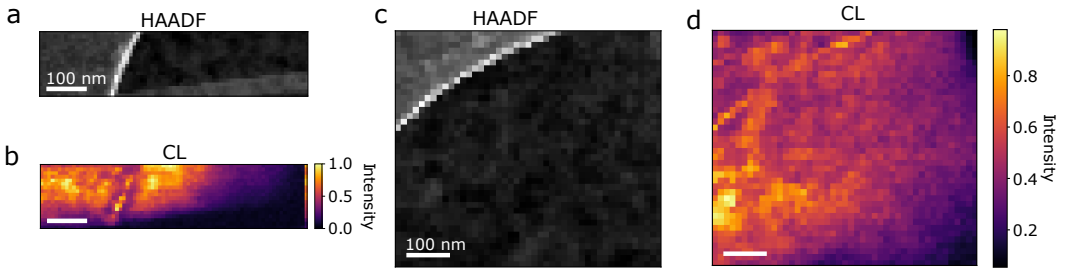

Figure 6.7: L emission on the carbon membrane edge: (a) HAADF image of the area, **(b)** corresponding CL intensity map (at 150 K), **(c)** HAADF image of the area, **(d)** corresponding CL intensity map. A high emission intensity is seen on the edge of the carbon support membrane, which is the bright pixels in (a) and (c). The CL emission maps is on the 1.00 to 2.25 eV range (unfiltered).

As shown in the figure, the emission is precisely on the edge of the carbon support membrane. In this case, the membrane edge appears clear in the HAADF image, indicating that it contains heavier elements than carbon, or that it is thicker than the surrounding carbon support membrane. The BSS from core-loss EELS is close to that displayed in Fig. 6.21, in section 6.4.1. The position of the measurements do not exactly correspond, so that they are plotted in the more adapted section.

The localized emission can be spectrally separated from the background by means of BSS, such as displayed in Fig. 6.8 and 6.9.

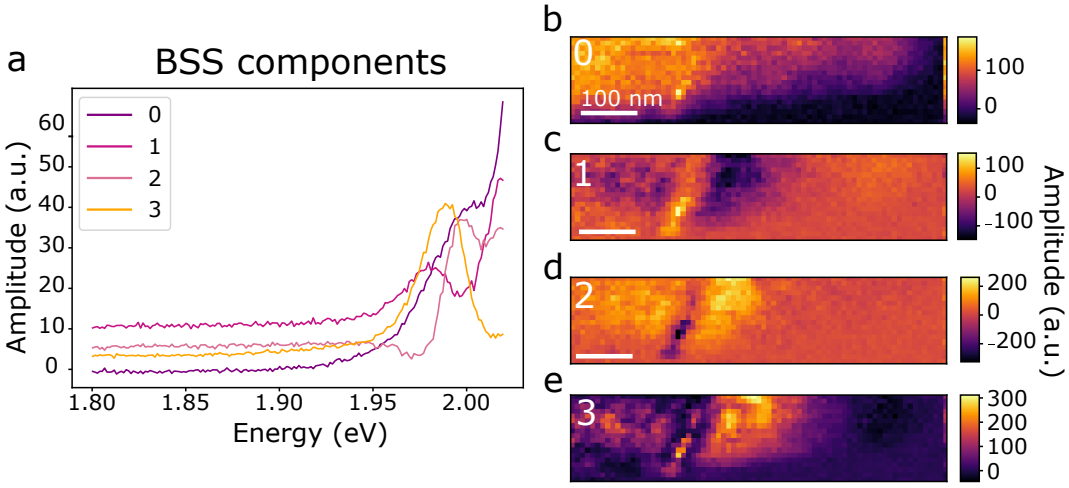

Figure 6.8: BSS components from Fig. 6.7a,b: (a) spectral components from the BSS decomposition with 4 components, **(b,c,d,e)** intensity map of the components from the BSS decomposition. The 1 and 3 components show emission localized on the edge of the membrane, with a corresponding emission peak at a lower emission than X^-.

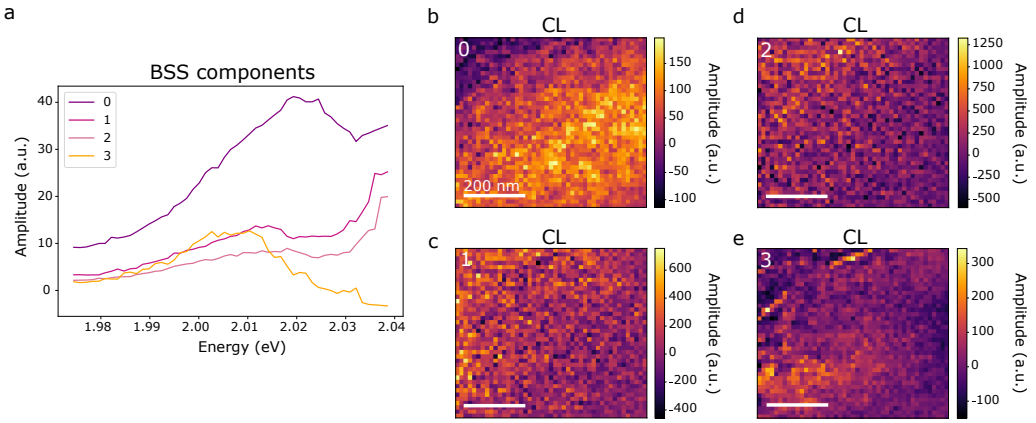

Figure 6.9: BSS components from Fig. 6.7c,d: (a) spectral components from the BSS decomposition with 4 components, **(b,c,d,e)** CL intensity map of the components from the BSS decomposition. The 3 component show emission localized on the edge of the membrane, with a corresponding emission peak at a lower emission than X^-.

The components separated with BSS show a bright emission precisely on top of the edge. Strain has also been measured in an area close to the region, and is displayed in Fig. 6.22, in section 6.4.1.

The high carbon and silicon content at the edges, as well as their thickness increase, might be the reason for the localized L emission. This emission can be from a potential trap, such as observed with strain variations. The strain could be modified by the thick edged of the carbon membrane edge.

6.2.3 Localized emission on patches

L emission has been measured on dielectric patches, such as displayed in Fig. 6.10. The dielectric patches also localize the X^- emission to few tens of nanometers, and has been investigated in chapter 5. I have measured this type of emission 27 times.

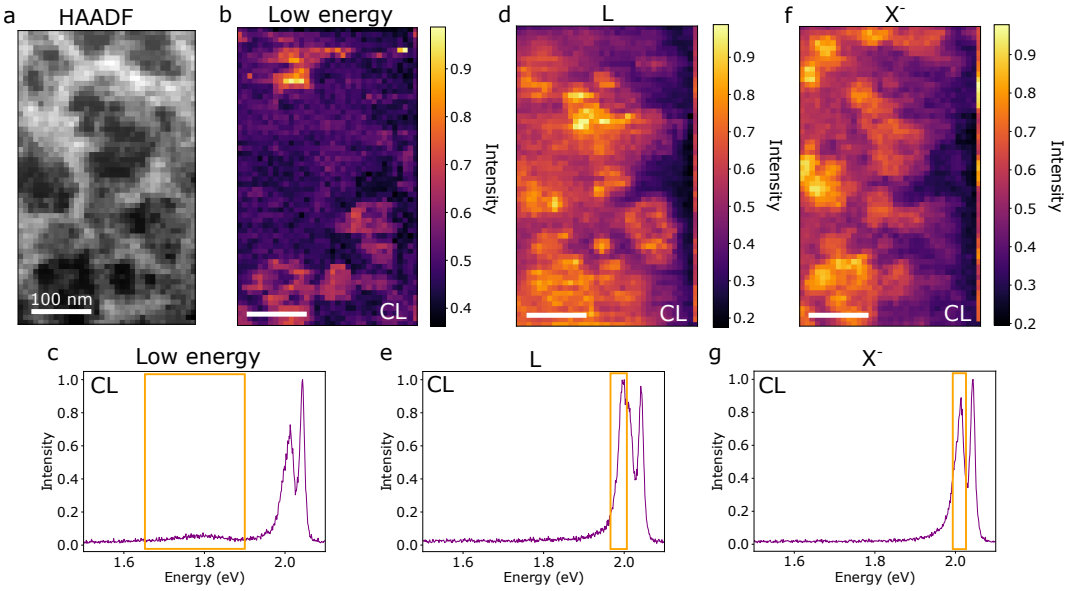

Figure 6.10: Localized L emission on patches: (a) HAADF image of the area, **(b)** energy-filtered CL intensity map (at 150 K), from the energy range indicated in (c), **(c)** corresponding spectrum, **(d)** energy-filtered CL intensity map (at 150 K), from the energy range indicated in (e), **(e)** corresponding spectrum, **(f)** energy-filtered CL intensity map, from the energy range of the X^- indicated in (g), **(g)** corresponding spectrum. The area is the same as in reference [15].

In the areas where this sort of emission is observed, high contrast patches are seen in HAADF. The emission intensity usually is higher for the L and X^- peaks where the HAADF image is darker.

A competition between the emitters is often seen: where the L emission in intense, the X^- is low, and reciprocally. The X_A generally has a smooth intensity variation and do not follow the patches patterns, contrary to X^- and L. In this measurement (Fig. 6.10), a low-energy emission on the dark part of the patches is also seen, and is discussed in section 6.4.2. From the images only, it is difficult to pinpoint the origin of each emission.

To understand the source of the localization of the emission, I have measured the core-loss EELS (Fig. 6.11) and the strain of the area (Fig. 6.12).

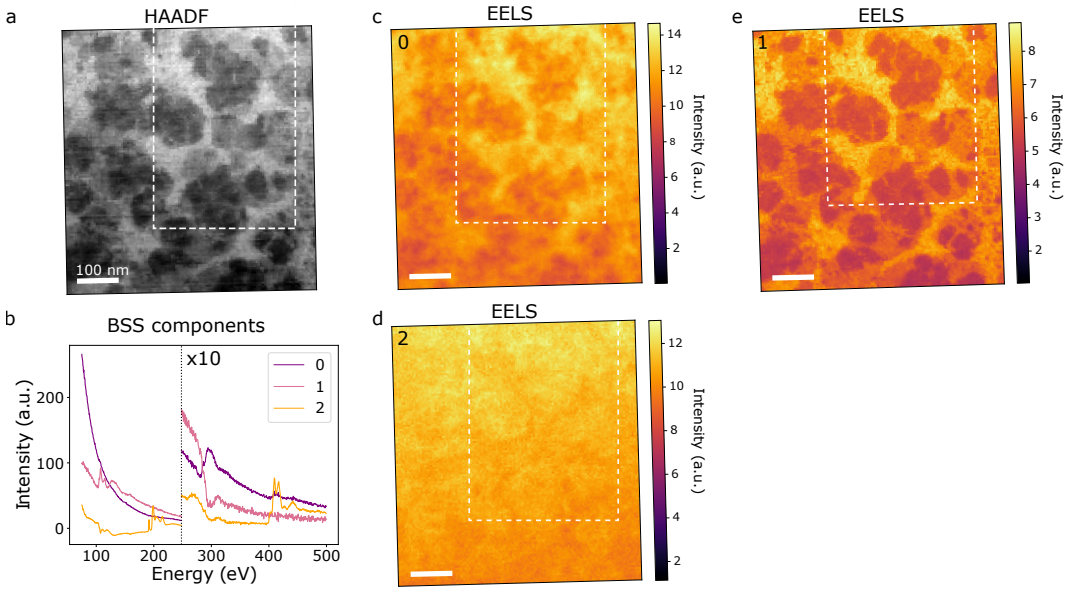

Figure 6.11: BSS components from core-loss EELS on the same area in Fig. 6.10: (a) HAADF image of the area, the position of the CL measurement is highlighted in the dashed rectangle, **(b)** BSS components spectra, **(c,d,e)** BSS components intensity maps. The pattern of the HAADF correspond to the 0 and 1 components, which contain respectively carbon and silicon. The measurements are done at room temperature.

From the BSS data in EELS, the patches containing Si and C seem to form several layers. If the layers are on each side of the TMD monolayer or on top of the h-BN, this might change the dielectric environment of the emitters, and some trapping potentials might be formed.

Since the strain could also be in cause, and it can create trapping potentials, I measured the the μ-diffraction of the same area, which is displayed in Fig. 6.12.

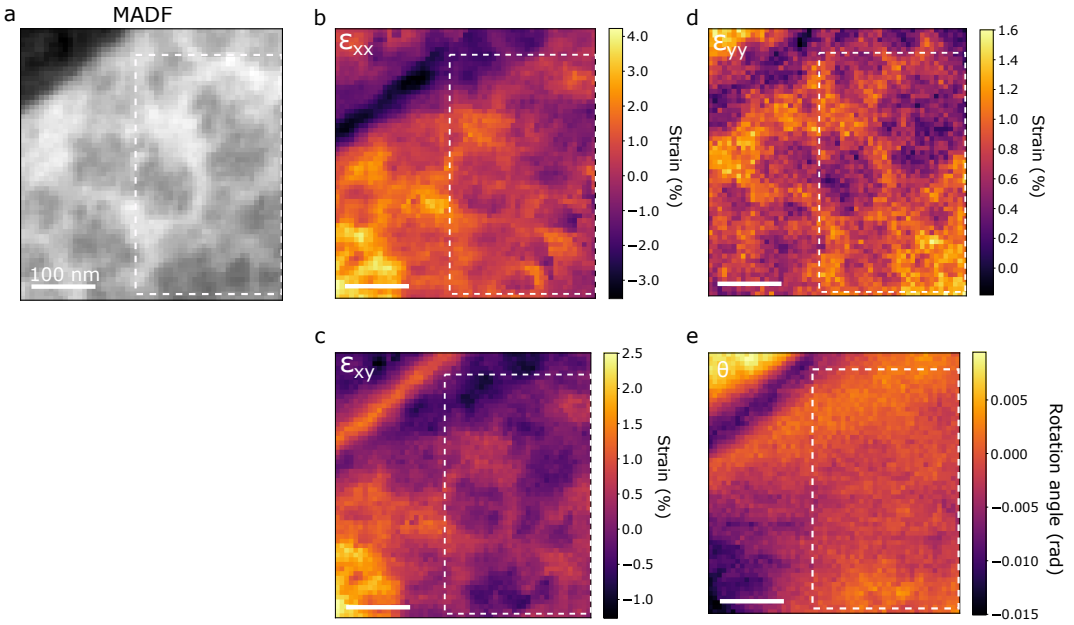

Figure 6.12: Strain components from the same area as in Fig. 6.10: (a) MADF image of the area, the position of the CL measurement is highlighted in the dashed rectangle, **(b,c,d,e)** strain tensor components maps. The measurements are done at room temperature.

The strain measurements also show some variations that might be correlated to substrate thickness and orientation changes (due to the presence of patches). This could also localize the emission.

From these experiments, the L emission can be correlated to the morphology of the sample, such as the emission being on the edge of the carbon membrane next to it, or in between dielectric patches. Yet, the origin of the L emission remains unknown. We lack the information about the precise nature of the emitters, e.g. if they are from excitons or trions. Further experiments, such as time-resolved CL (HBT), to have information about the lifetime of the emitters, or PLE, to have information about the excitation and de-excitation paths, would be required.

6.3 Other low-energy emission peaks

I also have measured lower-energy emissions. In the following sections, I describe four types of emission that occur at lower energy than the L emission:

1. emission on the edge of bubbles,
2. peak emission forming lines in the CL intensity maps, which energy shift over time,
3. emission on a line displaying an intensity decay,
4. emission from thin (FHWM of about 30 meV) peaks.

6.3.1 Emission from the edge of bubbles

During the preparation of the heterostructure, bubbles can be trapped. As seen in the literature, localized PL emission is often seen on these bubbles, and they can be SPS [119]. The suspected origin is the strain creating trapping potential where the exciton recombination is favored. In this section, I look at the emission from a micrometer-sized bubble. In particular, the low-energy CL emission is seen to occur at the edges of the bubble, as displayed in Fig. 6.13. On top of the bubble, no emission is seen, probably due to the lack of physical contact between the WS_2 and the h-BN. I have measured this type of emission 11 times.

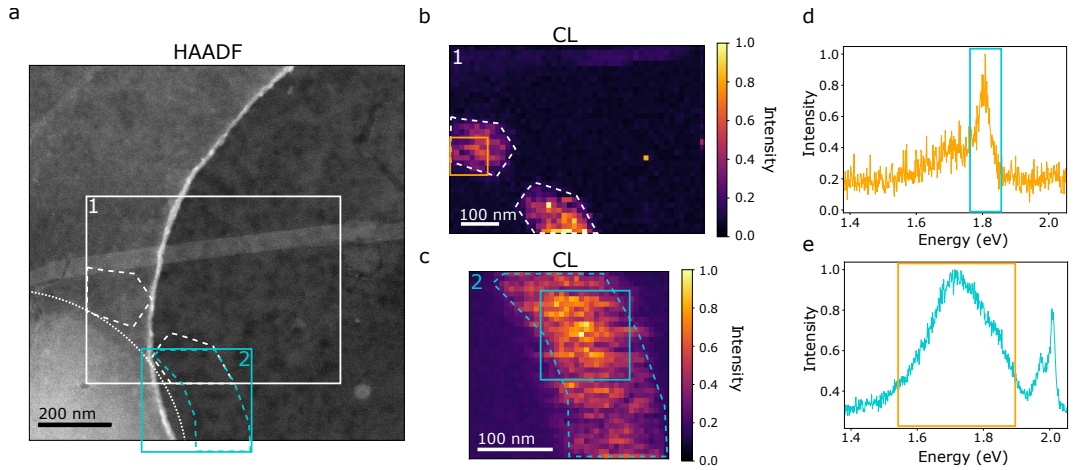

Figure 6.13: Localized emission from the edge of a bubble: (a) HAADF image of the area. The bubble is highlighted by the dotted line at the bottom left of the image. **(b)** CL energy-filtered map (energy range indicated in (d)) from the white rectangle in (a), **(c)** CL energy-filtered map (energy range indicated in (e)) from the blue square in (a), **(d)** extracted spectrum from the orange square in (b), **(e)** extracted spectrum from the blue square in (c). The CL emission is most intense at the edges of the bubble. Some peaks (such as in (d)) are visible within the energy band highlighted in (e). The CL emission is contained within the dashed areas in white and blue. The measurements are done at 150 K.

The CL emission is located on a 200-nm band at the edge of the bubble. It contains two parts: one that is above the carbon support membrane, and the other is on top of the hole. The two parts are separated by the membrane edge on which no CL is detected, probably due to the lack of contact between the TMD monolayer and the h-BN, which prevents the good migration of charge-carriers between the layers. No emission from X_A and X^- is measured outside of the low-energy CL region.

Spectrally, the emission is inhomogeneous. Indeed, the emission band seems to be composed of many contributions, such as the peak at 1.8 eV seen in Fig. 6.15d. The different contributions are unresolved, and BSS separation of CL does not give further information.

Even if strain is the hypothesis for the localization of emission next to the bubble, I have measured core-loss EELS to have information about the content of the bubble. The results are displayed in Fig. 6.14.

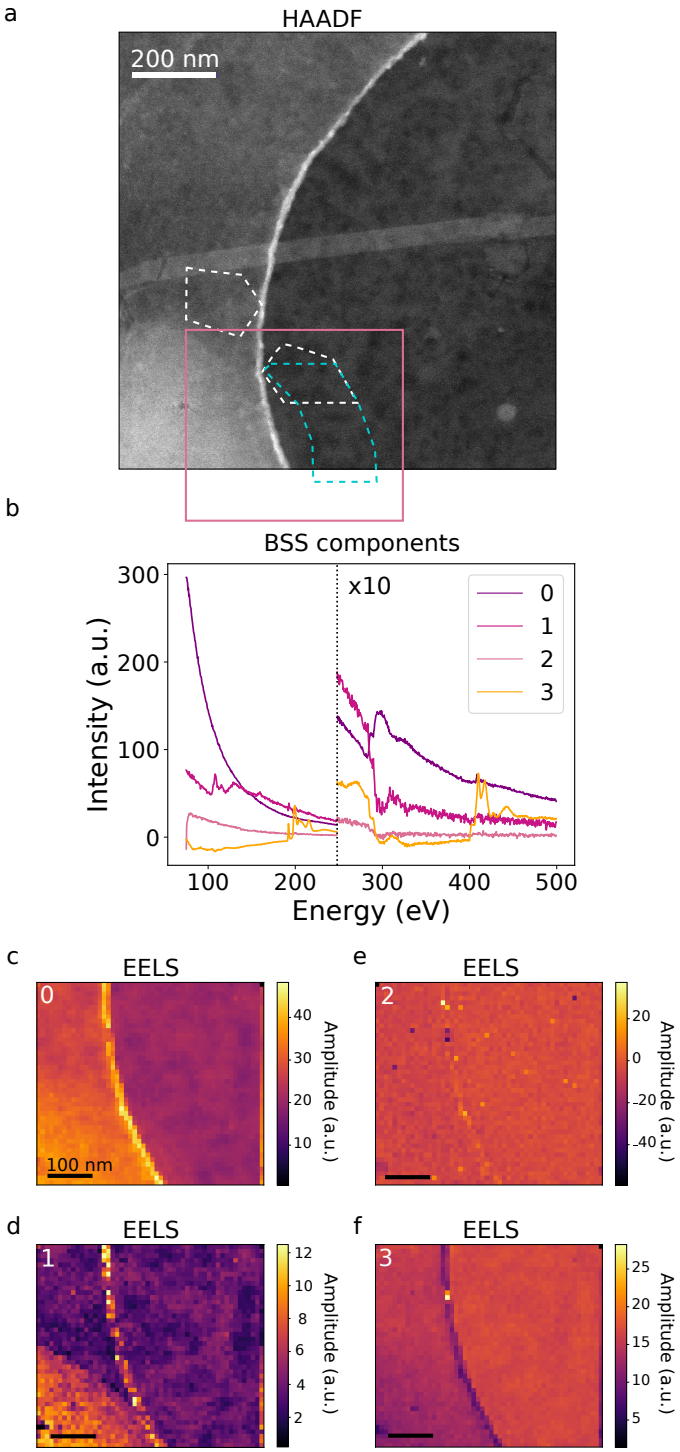

Figure 6.14: BSS components from the core-loss EELS measured in the same area as in Fig. 6.13: (a) HAADF image of the area, the BSS is measured in the area highlighted in orange, **(b)** BSS components spectra, **(c,d,e,f)** BSS components intensity maps. The bubble is visible in components 0 and 1, indicating that it might contain carbon and silicon. The measurements are done at room temperature.

On the HAADF, the contrast displays a slightly higher contrast at the position of the bubble. This could indicate the presence matter inside. The core loss EELS indeed shows a change in chemical composition: the bubble seems to contain carbon and silicon, such as the dielectric patches measured in section 6.2 and in chapter 5. The chemical content of the bubble, however, should not impact the CL emission. Indeed, the CL emission appears at the edges of the bubble, and not on top of it.

µ-diffraction of the area has been measured and the strain tensor components are displayed in Fig. 6.15.

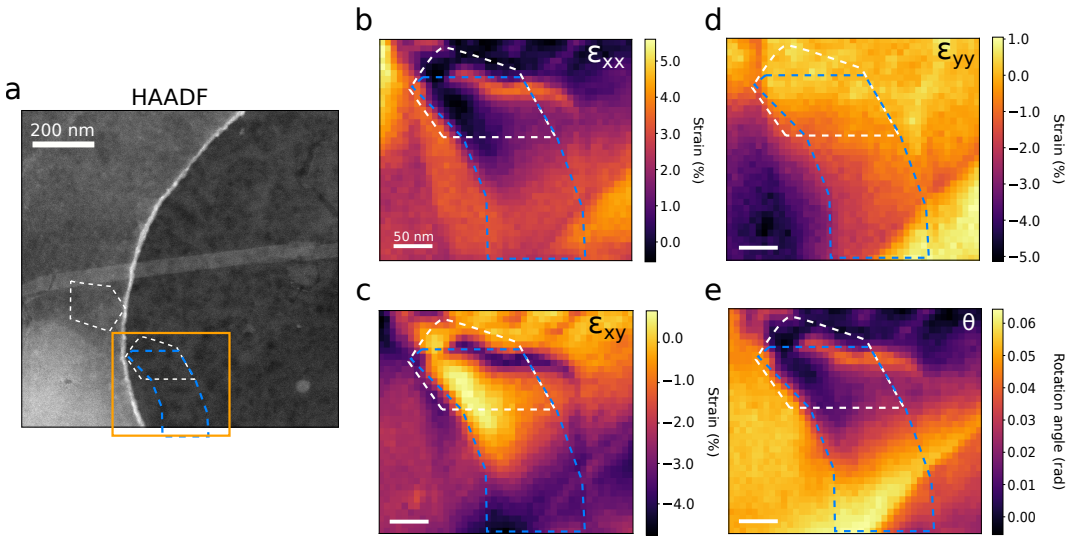

Figure 6.15: Strain components from the same area in Fig. 6.13 and 6.14: (a) HAADF image of the area, the position of the strain measurement is indicated in the orange square, **(b,c,d,e)** strain tensor component maps. The position of the high CL emission correspond to the edge of the bubble visible in (d), as well as a fold, visible in (b,c,e). The measurements are done at room temperature.

The µ-diffraction data show that the monolayer is under tremendous strain, of few % at the edge of the bubble (this value is approximate due to the limitations of the strain measurements in µ-diffraction). The shape of the CL intensity emission at low energy matches that of the strain pattern on the left-hand side of the emission. On the right-hand side, the reason for the lack of CL emission is not visible in the strain measurement.

Inside the CL pattern, the strain profiles are inhomogeneous, which could be explained by the variation of strain in the CL emission area. The chemical environment changes inside the bubble, but not on the emission area.

6.4 Emission from scanning lines with energy shifts

The most commonly observed low-energy CL emission appears as short emission lines, of few pixels long. They suddenly appear and disappear along with the scanning. Spectrally, the emission are low-intensity peaks of energy between 1.75 and 1.95 eV, which energy changes along the lines, thus the reference as "shifting lines". I have measured this type of emission 43 times.

A typical CL signature of the shifting lines emission is displayed in Fig. 6.16.

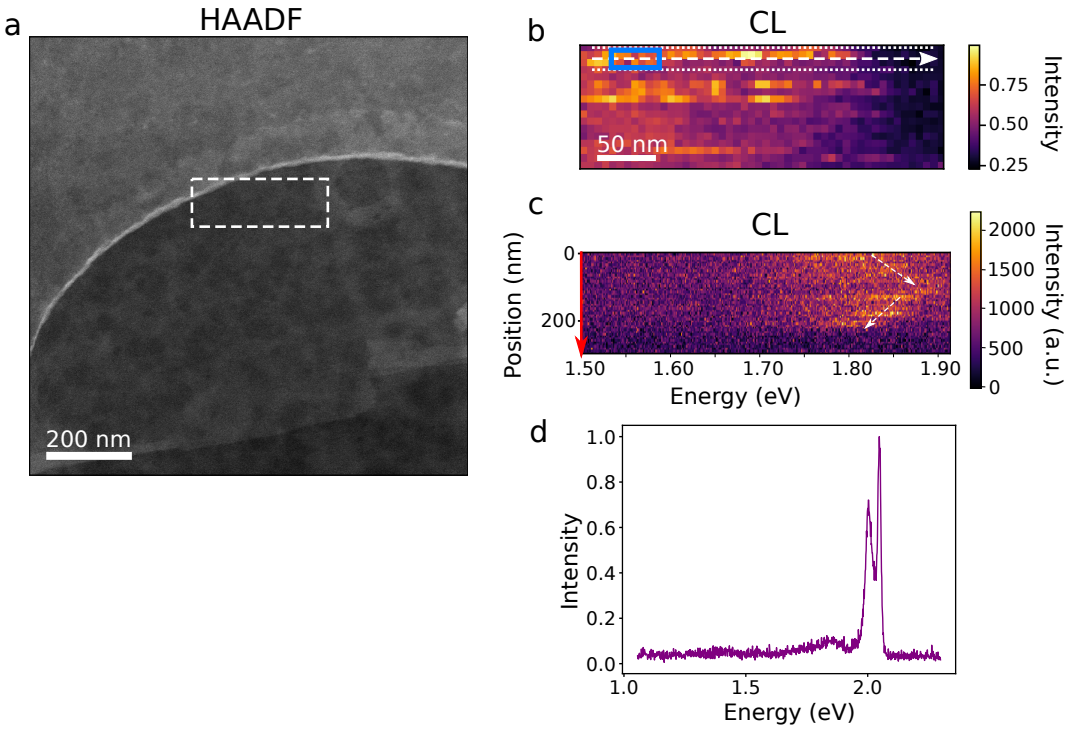

Figure 6.16: CL emission from shifting lines: (a) HAADF image of the area, the position of the CL measurement is in the dashed rectangle, **(b)** energy-filtered CL map (1.75 to 1.90 eV), **(c)** energy profile along the arrow in (a), the energy shifts are highlighted with dashed arrows. **(d)** spectrum extracted from the blue rectangle in (b). The low-energy peak is at about 1.85 eV. The measurements are performed at 150 K.

In the HAADF, no clear origin of emission is visible. I measured the core-loss EELS to have more information about the chemical environment (Fig. 6.17).

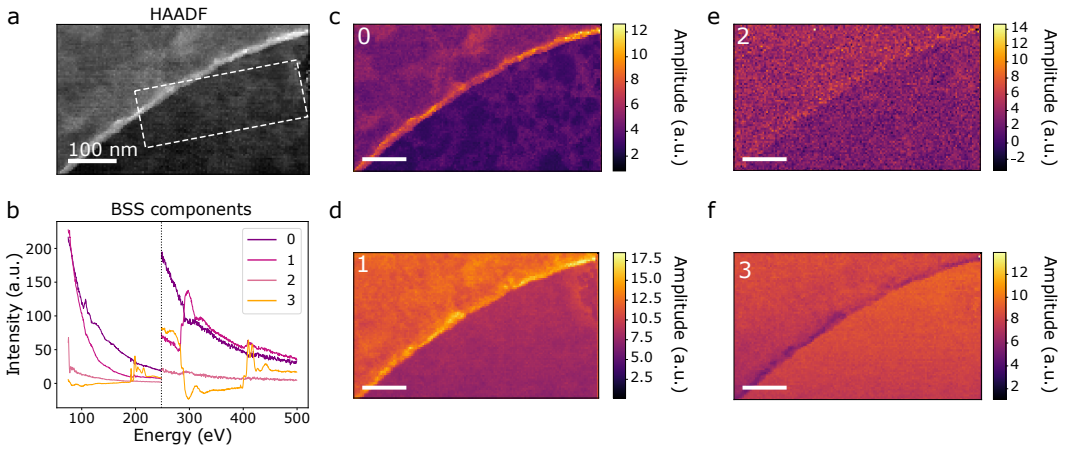

Figure 6.17: BSS components from EELS core-loss of the same area of Fig. 6.16: (a) HAADF image of the area, the position of the CL measurement is highlighted in the dashed rectangle, **(b)** BSS components spectra, **(c,d,e,f)** BSS components maps. The measurements are done at room temperature.

The EELS measurement do not give more information about the origin of the emission, I also measured the strain of the area, which is displayed in Fig. 6.18.

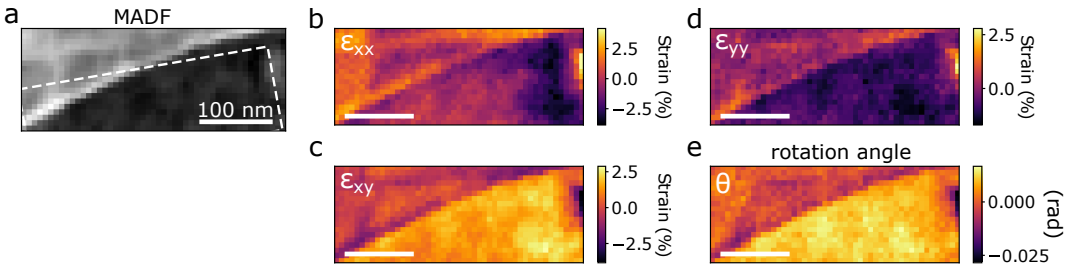

Figure 6.18: Strain components from the same area in Fig. 6.16: (a) MADF image of the area, **(b,c,d,e)** strain components maps. The measurements are done at room temperature.

From the strain measurement, no further information about the origin of the emission is seen. Since the origin of the emission lines do not seem to be from chemical environment change, nor strain, it could be from point defects which are not visible at the measurement scale.

The origin of the CL intensity shape, which are lines, can originate from various phenomena. They can be from the excitation of long-lived species, that can emit for a long time after the excitation has moved away. However, this type of emitters also tend to emit few photons, due to their long lifetime, which makes them difficult to detect unless a large number of emitters is present. Another possibility is the blinking, or bleaching of the center with illumination. Indeed, many light emitting centers are unstable over time, due to charging effects or the change of the emitting center over time (e.g. if the emission is from an adatom, it can be knocked-off by the electron beam).

6.4.1 Emission from scanning line displaying an intensity decay

As described in the previous part, emission lines have been observed during CL measurements. Here, I study the emission along scan lines, which display a specific behavior: an intensity decay along the scan. Such signature can originate from large objects which emission blinks or bleaches over time, or can originate from long-lived (phosphorescent) defects. The carrier-diffusion has to be taken into account. Indeed, at several positions of the electron beam, a point defect position away from the position of the beam can be excited if the carriers migrate to it. I have measured this type of emission 5 times.

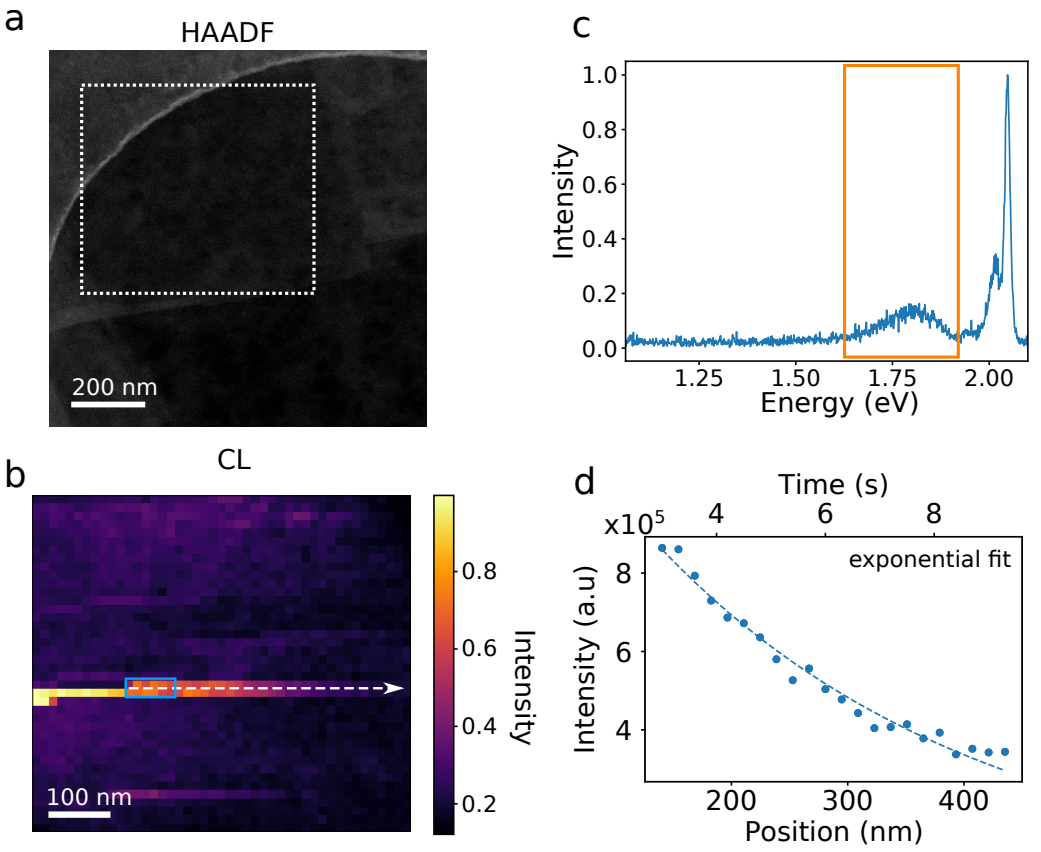

Figure 6.19: Long decay emitter: (a) HAADF of the area, the dotted rectangle correspond to the position of the CL measurement, **(b)** energy-filtered CL intensity map (energy range indicated in (c)), **(c)** spectrum extracted from the blue rectangle in (b), **(d)** exponential fit of the intensity along the dashed arrow in (b). The horizontal scales correspond to the distance along the arrow, and a corresponding time scale has been built (pixel dwell time 300 ms). The measurements are performed at 150 K.

The emission source is not visible in the HAADF image. Since it starts at a line in the raster scan, and then suddenly disappears, it seems to be prone to blinking.

The decay characteristic length is measured to be 277 nm, which corresponds to a characteristic time of 5.9 s (dwell time 300 ms). The presence of many long-lived defects on the left-hand side of the intensity decay could explain this behavior.

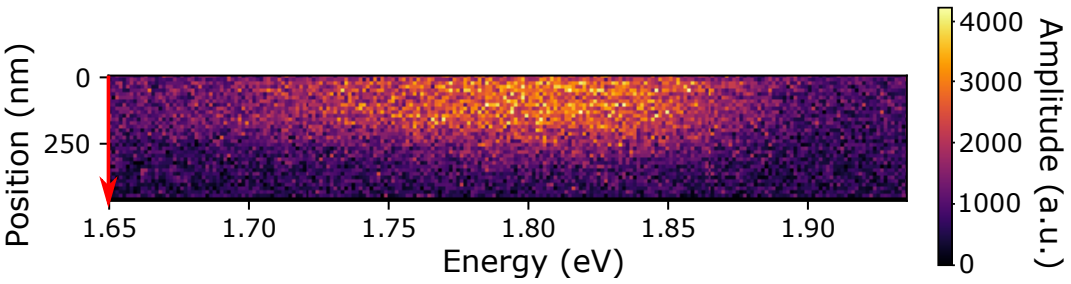

Figure 6.20: Energy profile along the exponential decay emission in Fig. 6.19: the intensity decreases but the energy of the emitter remains constant.

From the HAADF image alone, the origin of such emission remains unknown. Core-loss EELS and strain have been measured on the area, and are displayed in Fig. 6.21 and Fig. 6.22.

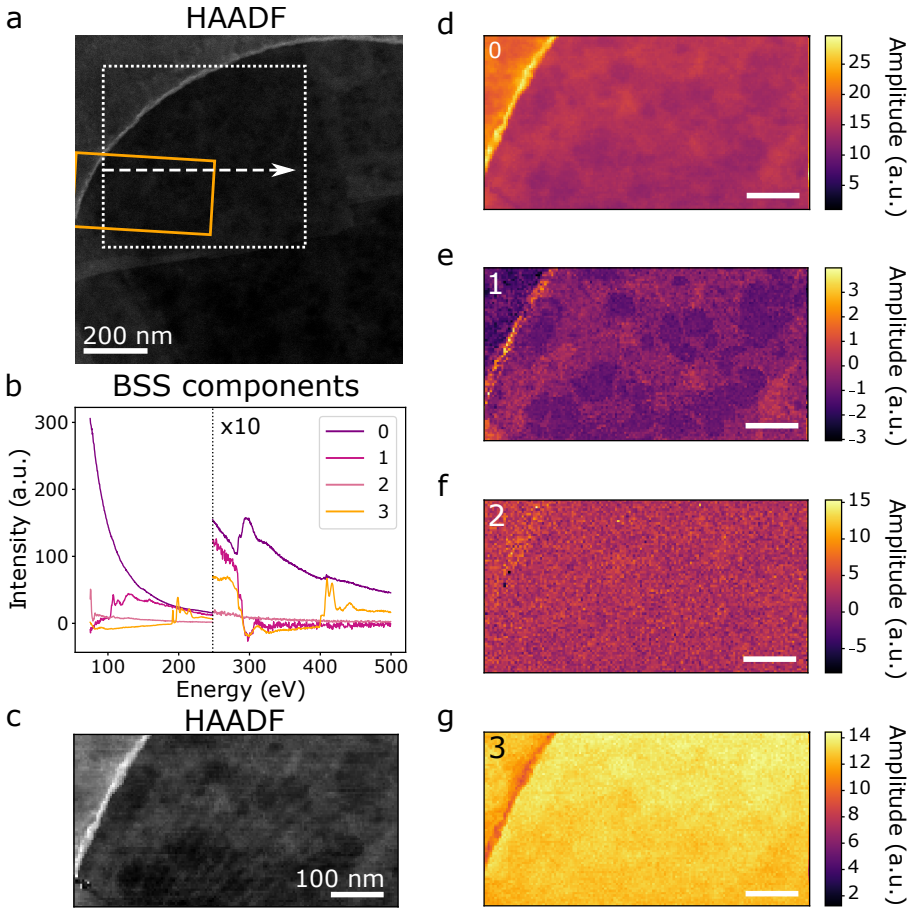

Figure 6.21: BSS components in core-loss EELS from the same area as Fig. 6.19 and Fig. 6.9: (a) HAADF of the area, the position of the CL measurement is highlighted in the dotted rectangle, and the position where the core-loss EELS is measured is highlighted with an orange rectangle. The position of the emission decay is along the dashed arrow. **(b)** BSS components, **(c)** HAADF image of corresponding to the EELS area, **(d,e,f,g)** BSS component maps. The measurements are done at room temperature.

The EELS data do not give further information about the origin of the emission. The area looks like other areas containing dielectric patches.

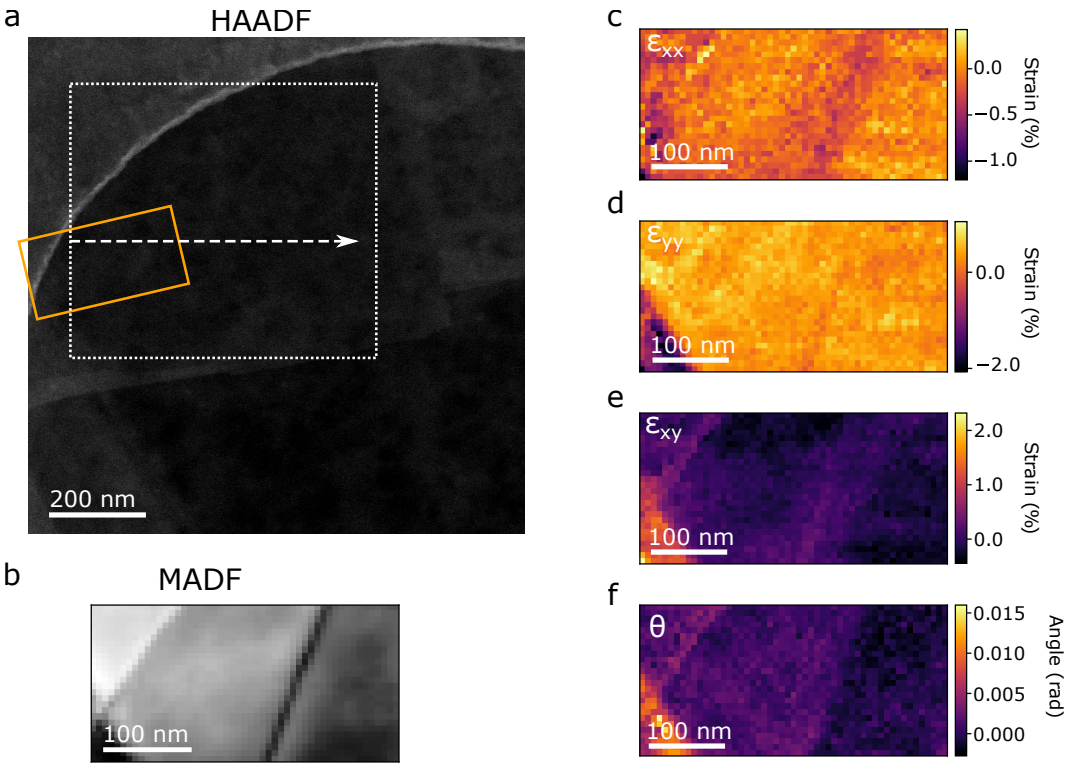

Figure 6.22: Strain components corresponding to the area in Fig. 6.19 and Fig. 6.9: (a) HAADF of the area, the position of the CL measurement is highlighted with the dotted rectangle, and the position of the strain measurements is highlighted with the orange rectangle. The emission decay is marked with the dashed arrow. **(b)** MADF image of the area, **(c,d,e,f)** strain tensor components. The measurements are done at room temperature.

The strain data do not give further information about the CL emission origin.

As for the shifting lines, the origin of the emission could be from point defects, such as sulfur or tungsten vacancies. Indeed, the long-decay lines appears as a particular case of low-energy lines.

6.4.2 Emission from localized thin lines

On areas with dielectric patches, thin (about 36 meV), low-energy (about 1.84 eV) peaks are observed, such as displayed in Fig. 6.23. I have measured this type of emission 13 times.

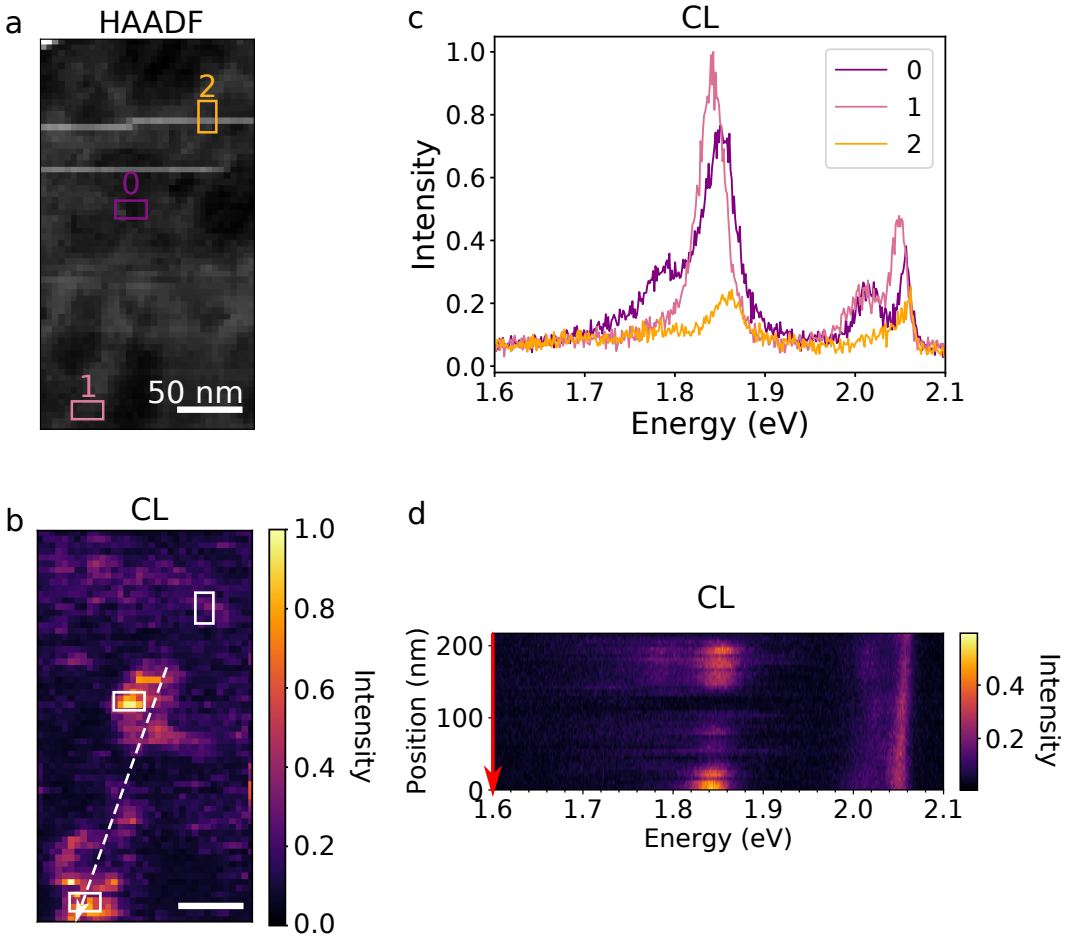

Figure 6.23: CL measurement of thin lines: (a) HAADF image of the area, the brighter lines are due to fluctuations of the electron source during the measurement. **(b)** CL energy-filtered map (1.7 to 1.95 eV), **(c)** CL spectra extracted from the rectangles in (a,b), **(d)** energy profile along the dashed line in (b). The energy shift of X_A and X^- is followed by the thin line emission. The measurements are performed at 150 K.

The intensity patterns form patches of few tens to few hundreds of nanometers. The correlation between the emission pattern and the contrast in HAADF is not straightforward.

As illustrated on the figure, this sort of emission is quite intense, often more than that of X_A and X^- emission. It can be a single peak, or a peak accompanied by a lower-energy shoulder (about 50 meV energy separation with the most intense peak). The spectral components from the peaks and its shoulder can be separated from the background with BSS, as displayed in Fig. 6.24.

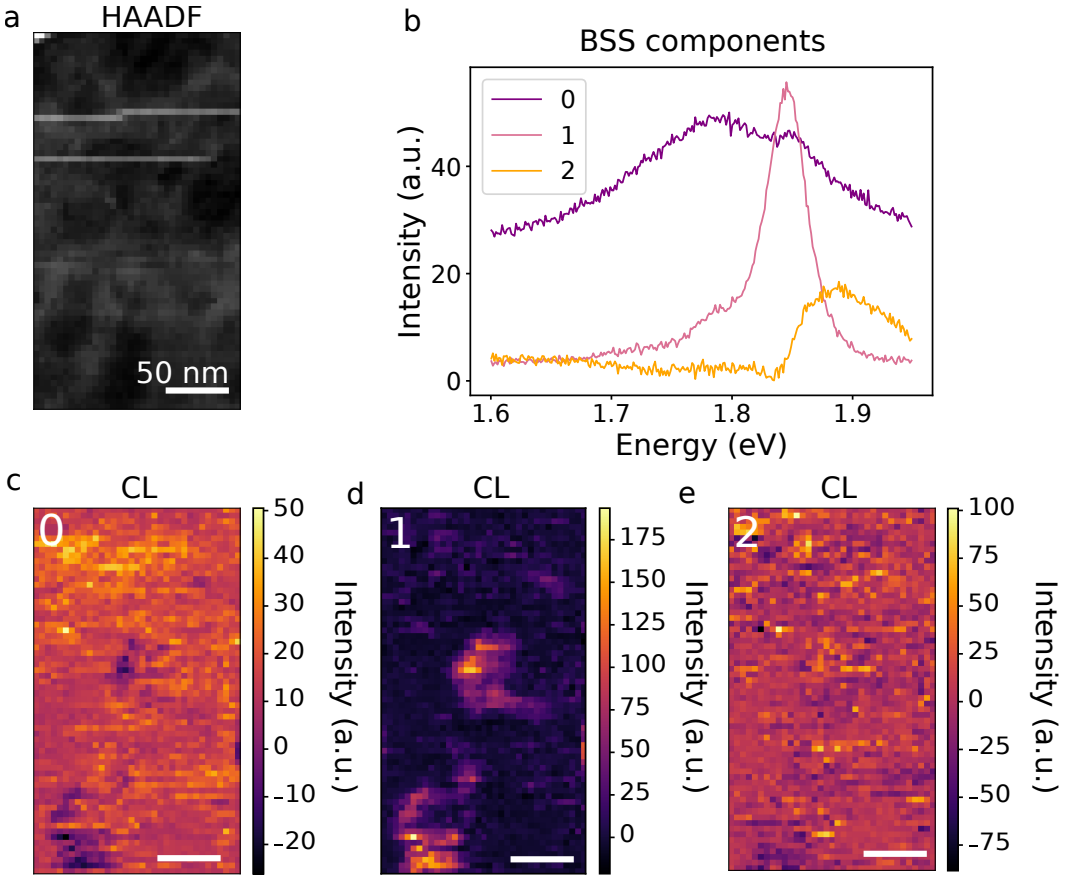

Figure 6.24: BSS components from the CL measurement: (a) HAADF image of the area, **(b)** BSS spectra components, **(c,d,e)** BSS components maps. The thin line emission is visible in (d).

From the BSS sources extracted from the CL data, the localized low-energy emission is better isolated than in Fig. 6.24. Still, the emission pattern do not seem to mach that of HAADF. I measured the EELS core-loss to have more information about the patches.

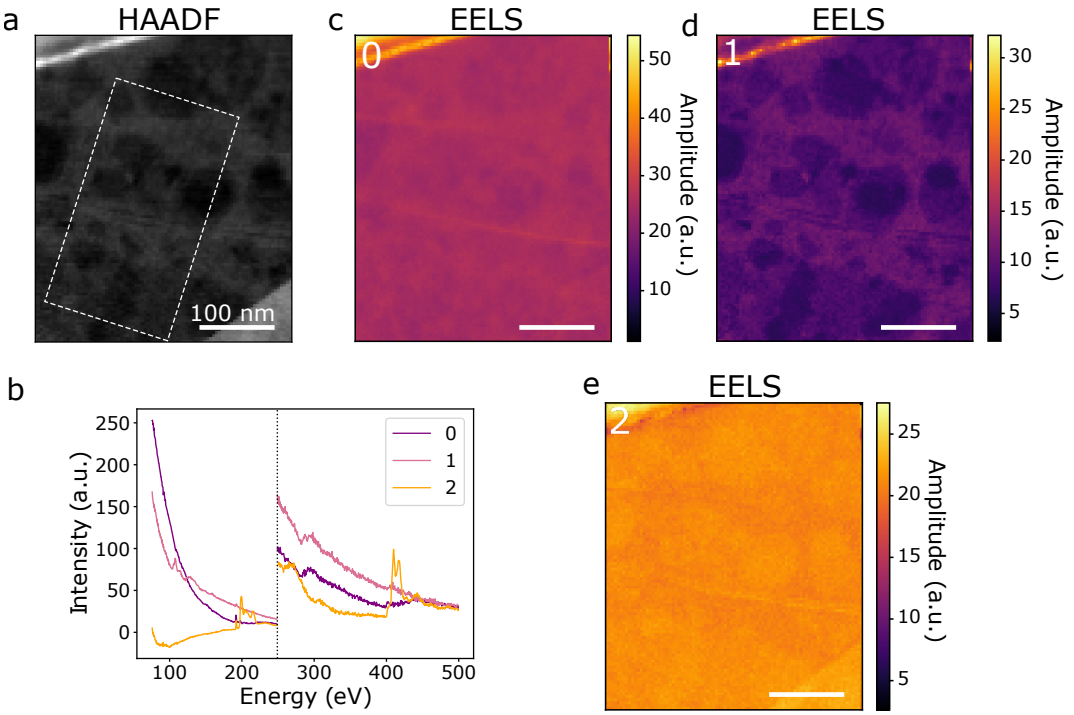

Figure 6.25: BSS components from EELS core-loss of the same area in Fig. 6.23: (a) HAADF image of the area, the position of the CL measurement is highlighted in the dashed rectangle, **(b)** BSS spectra components, **(c,d,e)** BSS components maps. The measurements are done at room temperature.

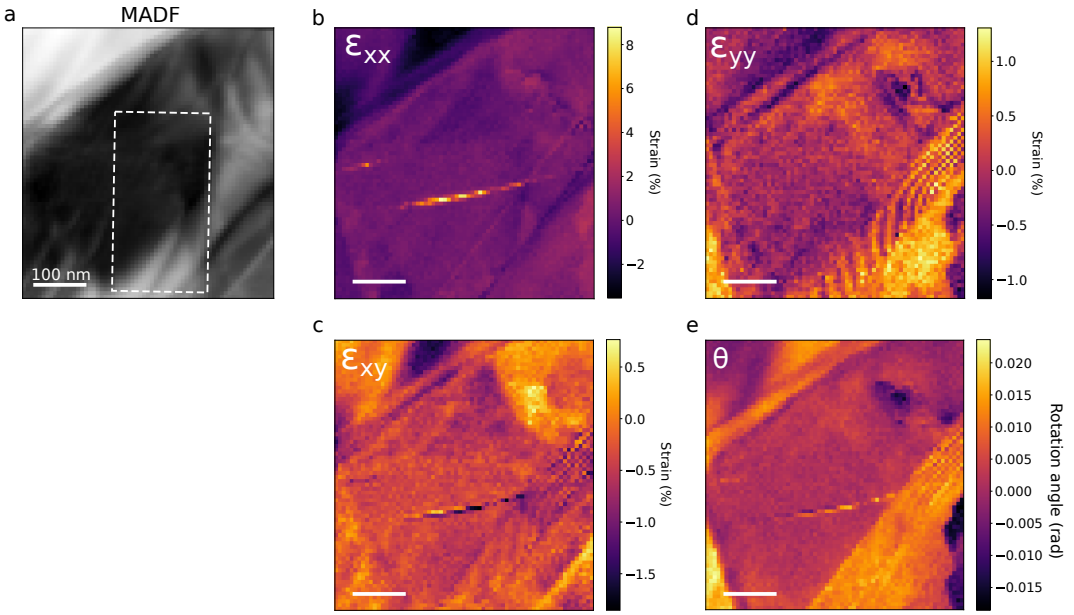

Figure 6.26: Strain components from the same area as Fig. 6.23: (a) MADF image of the area, the position of the CL measurement is highlighted in the dashed rectangle, **(b,c,d,e)** strain tensor components maps. The measurements are done at room temperature.

This emission line appears in areas with patches, but the emission does not match the HAADF and core-loss EELS. This might have different origins, whether the emission has an origin at a smaller scale, such as point defects, or is from the layers of dielectric patches, which configuration might lead to different emission energy.

6.5 Summary

In this chapter, I have seen that many low-energy emitters exist in WS_2, forming a low-energy band. The origin of the individual emission has been investigated using CL, core-loss EELS and µ-diffraction. The CL measurements have been performed on h-BN encapsulated WS_2 monolayers at 150 K, and the corresponding core-loss EELS and µ-diffraction measurements have been measured at room temperature in the same areas.

I have identified several types of emitters:

- L emission:
  - the spatially extended L emission next to the carbon support membrane,
  - the L emission on the edge of the carbon support membrane, when the edge is strongly contrasted,
  - the L emission in between dielectric patches,
- other lower energy emission:
  - next to bubbles (which contain contaminants from the sample preparation), probably from strain,
  - peak emission in the shape of lines, along the CL scan, possibly from point defects,
  - long decay emission, a special case of the CL lines along the scan,
  - thin peak, measured in areas with dielectric patches.

6.6 Conclusion

An attempt of identification has been done by correlating the nanometer-scale spectral information from CL with the morphology (HAADF and MADF images, strain), and core-loss EELS. In some cases (e.g. for the shifting lines), the emission origin could not clearly be identified. The reason might be that the origin of emission is point defects, and have to be measured with atomically-resolved images. Nevertheless, only tungsten vacancies would be detectable, due to the sulfur being too light to stand out of the background (due to the h-BN encapsulation).

The numerical methods used, in particular µ-diffraction has limitations, as explained in chapter 2 for the strain measurements. For the BSS, there are two sources of limitations: in CL, some emission peaks shift over the scan, and this might be treated as separate sources by the BSS algorithm, whereas it only is spectral diffusion. Moreover, the ICA algorithm is supposed to only produce additive components, but sometimes a chemical element still appears as negative (cf the carbon edge in Fig. 6.21).

Additionally, charge-carrier diffusion has to be taken into account: the excitation position is known, but the exact position of the recombination might be further away. The exact origin for localization can then be hidden because the recombination does not occur at the excitation position.

To further identify the origin of localized emission, more experiments have to be performed, such as time resolved spectroscopy (to have information about the

energy structure of the emitters) and high-resolution imaging on the precise positions of the emitters. The latter could have been performed, nevertheless, the high-resolution measurements are not done in the same microscope as the CL measurements. The areas being nanometer-sized, it can be difficult to find the exact same spot in the two experiments. On the contrary, in some areas the emission is quite large, which can make it difficult to perform atomically-resolved images.

Chapter 7

Conclusion

In this thesis, I have explored the nanoscale optical properties of two types of materials: point-defects in nanodiamonds, and TMD monolayers. The STEM microscope has shown to be a powerful tool for the study of the optical properties of materials at the nanometer scale, in particular thanks to the possibility of measuring CL emission, the nanoscale counterpart of PL, and low-loss EELS, that of absorption. This was enabled by the ChromaTEM, which is an aberration-corrected STEM microscope. It is equipped with an electron monochromator, which allows for the measurement of low-loss EELS, and an Attolight CL mirror, which allows for light collection with high efficiency.

Light-injection has been demonstrated in the STEM microscope, leading to in-situ PL measurements of NV centers in FNDs, as well as optical pumping for charge-state conversion of the centers. The latter has shown to be difficult to perform in the STEM, due to the use of TEM grid. Indeed, the TEM grids are designed to be electron transparent, and not to perform optical measurements. For this reason, the membranes often are fluorescent upon laser excitation, which produces an intense background that can conceals the PL signal. To prevent this, I used lacey carbon TEM membranes, which have a small surface. The fluorecence background was then negligible, but the heat dissipation was reduced, leading to sample heating with the lasers. This effect is indesirable for PL measurements, but the sample heating with lasers can be used for in-situ sample cleaning.

To characterize the sample heating with the laser beams, I have performed temperature -controlled CL experiments with NV centers. This was enabled by the specific design of the nitrogen-cooled sample holder from HennyZ, which is compatible with the CL mirror in ChromaTEM. This sample holder has the capability of carrying MEMS (micro electro mechanical systems) which can heat a TEM membrane by means of Joule's effect, with a micrometer sized circuit. The combination of the nitrogen-cooling and the heating with MEMS is a unique capability, that enables temperature control of samples in the 110 - 1000 K range. The sample holder is also designed for high-resolution imaging and has thermal stabilization capabilities.

The STEM microscope enables the measurement of multiple signals, including EELS (core-loss for chemical environment analysis, low-loss, for inter- and intra-band absorption), CL, μ-diffraction (which is the diffraction measured with a convergent electron beam) and high-resolution imaging. By combining these signals, the information about the origin of localization of charged excitons (X^-), present in WS_2, was recovered. The measurements were performed on h-BN encapsulated monolayers, which enable sufficient CL emission to be detected. Contaminants from sample preparation have been shown to play a large role in the trion and localized exciton emission. Other origins for localized emission have been identified, such as strain. Point-defects are also suspected to play a role in some type of localized emission, but further experiments need to be done.

The encapsulation of TMD monolayers, additionally to enabling the CL measurements, protects the sample from radiation damage. Indeed, the samples have been irradiated for tens of hours, and did not show visible damage, except in areas where cracks or bubbles were already present. These areas might be in less good contact with the h-BN, or contain contaminants (C, Si, O), from sample preparation and transfer, which enables irradiation damage.

The combined emission and absorption measurements allow for the understanding of many optical properties of materials. With the possibility of measuring CL and low-loss EELS of the same features, such as the excitons in TMD monolayers, this enables the optical characterization of semiconductors or point-defects at the nanoscale in the ChromaTEM. The EELS-CL measurements have been performed before [16], on plasmons rather than excitons. The monochromation opens new possibilities for specimen characterization, in the visible to near-IR energy range.

The temperature-controlled CL experiments highlighted the possibility of using FNDs with NV centers as optical thermometers in the STEM microscope. The temperature of samples can be tuned in situ by means of MEMS systems, or with lasers. Temperature is known to play a large role in light emission processes, which emphasizes the importance of precisely knowing the temperature of optical measurements.

The built light-injection setups can be used for characterization of many types of samples. Indeed, PL and TEM imaging are already among the most common manners of testing sample quality. In a setup where both can be combined, the sample testing time could be decreased. Moreover, some specimen respond differently to electron beam and laser beam excitation, such as exhibited with NV centers (which exist in several charge-states). In this case, the PL measurement can be crucial to identify emitters. Additionally, some samples do not emit CL light, such as bare TMD monolayers. For the identification of single photon emitters, one could measure the emission in PL, and look for the emission origin with high-resolution imaging directly of the monolayer. The HAADF contrast would then be better than with TMD encapsulated in h-BN.

This work has opened many perspectives, both for 2D materials and point-defects. These are described in the next chapter.

Chapter 8

Perspectives

Contents

In this chapter, few experiments that can follow the ones performed during my PhD are presented.

8.1 HBT measurement of the low-energy emission in WS_2 monolayer encapsulated in h-BN

The identification of the localized emission origin in TMD monolayers is crucial for applications. To better understand the emitters, information about their energy structure has to be gathered. A way of getting this information is to perform time-resolved spectroscopy. This could be done at the nanoscale, to isolate the emission from a specific emitter (since the samples have shown to have many localized emitters in the same regions), by using an HBT setup in CL.

The HBT measurement in CL (described in chapter 2) gives the autocorrelation function, which curve is directly linked to the lifetime of the emitter, either it is an SPE or not [22]. The information of lifetime can give insights about the nature of the emitter. An expected difficulty for this measurement is the low number of photons (compared to the noise) emitted by the localized emitters, and the blinking of some emitters.

8.2 PL system implementation in ChromaTEM with the high power laser source

The compact photoluminescence setup, described in chapter 3, has been tested on the ChromaTEM, but no PL was measured so far. The reason for this is the low power of the source used (continuous 543 nm He-Ne laser coupled with a monomode

fiber). The theoretical output power of this laser is only of 5 mW (in practice, at the time of the test, it was lower than 1 mW). The coupling of the laser beam to the monomode optical fiber (that is necessary to keep a gaussian laser beam) creates losses, about 2/3 of the incoming laser power. The laser power is further decreased by the use of the 50/50 beamsplitter, that was used to image the mirror, as described in chapter 3. The excitation power was then too low for aligning the PL emission of NV centers.

An optical fiber bringing a ns-pulsed laser has been installed in the laboratory. The laser source only has to be replaced with the pulsed laser in the light injection setup, and PL should be straightforward to detect with NV centers. A specific mechanical hyperspectral image acquisition code has been developed in NionSwift, which should be more precise than that of the VG, due to the better reproducibility of the mechanical steps of the sample holder.

8.3 Polarized detection

The experiments on the polarized detection of NV^0 CL emission have not been performed yet. In this part is a short description on how it could be done with the ChromaTEM setup.

The NV^0 centers being point defects, and having two orthogonal dipole transitions (E_x and E_y for the two m_s=$\pm$1/2), their energy can be tuned by applying an electric field parallel to one of the dipoles. The parameters for the electrical tuning of the NV^0 optical transitions have been calculated in the reference [70]. The calculations were performed to propose a protocol for the creation of quantum memory using exclusively NV^0 centers. This would be exciting to produce in the electron microscope since the CL excitation exclusively produces NV^0 light emission.

The important parameters calculated there are: the static electric field required (for an electric field parallel to the NV center axis) which is 10 V/µm for a lift of degeneracy with Stark effect of 120 GHz ($\approx$ 0.5 meV, or $\approx$ 1 nm at the energy of the NV^0 ZPL) [70]. The MEMS we use (cf chapter 3) have a 5 µm separation between the two electrodes for biasing. This means that a 50 V voltage has to be used to achieve the 120 GHz separation between the two optical transitions.

For NV^-, similar processes have been performed to control electrically the energy splitting between the levels [151].

A scheme of the hypothetical setup based on the compact PL setup for ChromaTEM, is shown in Fig. 8.1. To perform a CL polarization-selective detection, one has to use a specific setup using a slit in the detection path (of about 3 mm) to enhance the polarization contrast of dipole emission [152]. The polarization then has to be filtered to select one or the other dipole, and the spectrum of the ZPL of NV^0 emission of the FND has to be recorded. The expectations are an energy shift of 0.1 nm for 50 V in the MEMS. Nevertheless, one has to be careful, since these estimations are for an electric field parallel to the NV center, which may not be straightforward to get since the nanodiamonds orientation is not controlled.

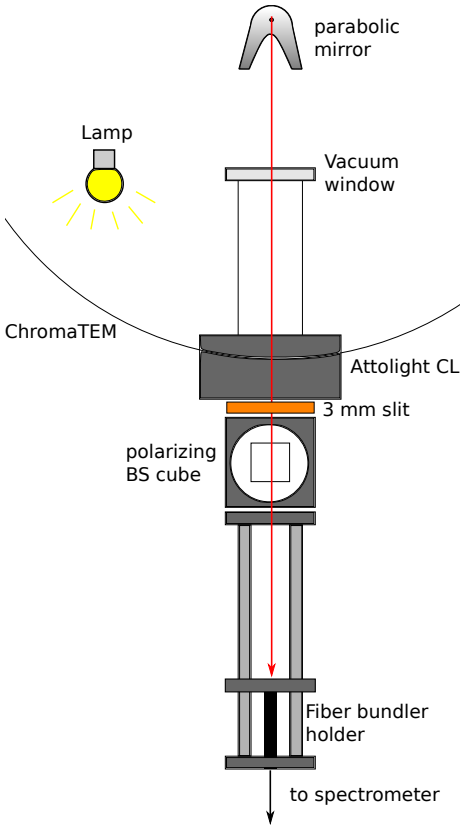

Figure 8.1: Scheme of the polarized detection setup for ChromaTEM: the FNDs would have to be put in a MEMS in the cryo simple tilt holder. A 3 mm vertical slit would be positioned in the optical detection part, followed by a polarizing beamsplitter cube to filter the different contributions.

8.4 Determination of the spatial resolution in CL in FND

In chapter 4, we have measured the CL coming from small nanodiamonds, down to 15×10 nm. Nevertheless, this measurement has been performed with the electron beam position fixed on top of the nanodiamond, and an integration time of 75 s, to obtain a SNR of about 4. The objective now would be to determine what is the spatial resolution of this type of measurement, which can give information about the CL process involved.

Indeed, if the CL is triggered only when the electron beam is on the nanodiamond, we can assume that it corresponds to the process described in chapter 2. If the signal is visible away from the nanodiamond, it could have been triggered by the generation of secondary electrons, which would greatly limit the spatial resolution.

8.5 IR optical pumping of NV centers with thermal contacts

As described in chapter 4, a reason for the failure of the IR optical charge conversion of NV centers in CL is the poor heat dissipation of TEM grids, especially the lacey carbon grid that we used, due to its small contact surface with the cold finger linked with the liquid nitrogen tank.

A possibility to prevent the heating of the sample would be to make better thermal contacts, such as Ag contacts, and use TEM grid with a continuous membrane.

The issue with continuous membranes for the PL experiment is that they emit light. In the frame of the IR optical pumping of NV centers in CL, no light is emitted unless excited in CL. Since the TEM membranes are thin, no CL is detectable from them. Moreover, no PL is emitted when exciting with the IR laser.

Additional advantages of using an Ag layer as a thermal contact, is that it is reflective, and the light collection should be greatly improved. Moreover, a metallic surface few nanometers away from an emitter has been shown to increase the rate of emission of defects, such as NV centers [82, 153].

The main drawback is the difficulty of performing the optical pumping in situ for the control experiment. Indeed, since the membrane emits light, it produces a large background, at the energy of the NV centers emission. So that the PL spectra are impacted by the presence of the membrane.

The experiment could be done in the ChromaTEM directly, by injecting the light from the IR laser to the setup with a compatible optical fiber. Since the PL cannot be performed due to the TEM membrane luminesence, the overlapping of two laser beams does not have to be performed.

Moreover, we can try to generate NV centers with higher precision than what is done so far, since the focused electron beam is smaller in size than ion beams.

8.6 Atomically-resolved images of localized emission in TMD monolayers

The high-resolution images that I measured were acquired in the UltraSTEM, whereas the CL measurements are performed in the ChromaTEM. The first issue is the difficulty of recovering precisely the same areas in the sample with the two microscopes, especially for small areas.

A solution would be to optimize the ChromaTEM alignements, and to use WSe_2 rather than WS_2 to enhance the contrast in HAADF. Preliminary measurements have been performed, and exhibited promising images. Now the CL from TMD crystal defects have to be measured, together with the images.

8.7 Random scan CL measurement on long-decay emitters

The emitters shaped as CL intensity lines presented in chapter 6 could display this type of emission along the scan of the electron beam for several reason:

- they are long-lived,
- they blink, which means that they can be reactivated,
- they bleach, which means that they do not emit light anymore.

For these reasons, it would be interesting to perform a random-scan. If the emitters blink, they would have some time to recharge and re-emit light (the time scale of blinking can vary, and in this type of scans it would be on the scale of seconds). It the emitters are long-lived, remanence would be seen on the scan. If they bleach, the signal from a specific position would disappear at some point and never reappear.

8.8 Irradiation damage and evolution of h-BN/TMDs heterostructures

Some localized emitters presented in chapter 6 seem to have appeared in the later measurements and were not measured from the beginning of the experiments. Irradiation by the electron beam could explain the evolution of the emission, even if no clear damage or contamination is observed in most regions.

Electron beam irradiation as shown to be at the origin of SPE emission, combined with strain [154].

The experiment would consist in creating defects with the electron beam and imaging them in high resolution. The luminescence can be measured in PL, or in CL but with an encapsulated monolayer.

Bibliography

[1] Rachel A Oliver. Advances in AFM for the electrical characterization of semiconductors. *Reports on Progress in Physics*, 71(7):076501, July 2008. ISSN 0034-4885, 1361-6633. doi: 10.1088/0034-4885/71/7/076501. URL https://iopscience.iop.org/article/10.1088/0034-4885/71/7/076501.

[2] R. Marty, C. Girard, A. Arbouet, and G. Colas des Francs. Near-field coupling of a point-like dipolar source with a thin metallic film: Implication for STM plasmon excitations. *Chemical Physics Letters*, 532:100–105, April 2012. ISSN 00092614. doi: 10.1016/j.cplett.2012.02.058. URL https://linkinghub.elsevier.com/retrieve/pii/S0009261412002631.

[3] Eva Rittweger, Kyu Young Han, Scott E. Irvine, Christian Eggeling, and Stefan W. Hell. STED microscopy reveals crystal colour centres with nanometric resolution. *Nature Photonics*, 3(3):144–147, March 2009. ISSN 1749-4885, 1749-4893. doi: 10.1038/nphoton.2009.2. URL http://www.nature.com/articles/nphoton.2009.2.

[4] M. Kociak and L.F. Zagonel. Cathodoluminescence in the scanning transmission electron microscope. *Ultramicroscopy*, 176:112–131, May 2017. ISSN 03043991. doi: 10.1016/j.ultramic.2017.03.014. URL https://linkinghub.elsevier.com/retrieve/pii/S0304399117301134.

[5] Wolfgang Pfaff, Tim H. Taminiau, Lucio Robledo, Hannes Bernien, Matthew Markham, Daniel J. Twitchen, and Ronald Hanson. Demonstration of entanglement-by-measurement of solid-state qubits. *Nature Physics*, 9(1):29–33, January 2013. ISSN 1745-2473, 1745-2481. doi: 10.1038/nphys2444. URL http://www.nature.com/articles/nphys2444.

[6] Hannes Bernien, Lilian Childress, Lucio Robledo, Matthew Markham, Daniel Twitchen, and Ronald Hanson. Two-Photon Quantum Interference from Separate Nitrogen Vacancy Centers in Diamond. *Physical Review Letters*, page 5, 2012.

[7] Loïc Rondin. Realisation d'un magnetometre a centre colore NV du diamant.

[8] Magdalena Sola-Garcia, Sophie Meuret, Toon Coenen, and Albert Polman. Electron-Induced State Conversion in Diamond NV Centers Measured with Pump–Probe Cathodoluminescence Spectroscopy. *ACS Photonics*, 7:232–240, January 2020. ISSN 2330-4022, 2330-4022. doi: 10.1021/acsphotonics.9b01463. URL https://pubs.acs.org/doi/10.1021/acsphotonics.9b01463.

[9] Peng Ji and M. V. Gurudev Dutt. Charge state dynamics of the nitrogen vacancy center in diamond under 1064 nm laser excitation. *Physical Review B*, 94 (2):024101, July 2016. ISSN 2469-9950, 2469-9969. doi: 10.1103/PhysRevB.94.024101. URL http://arxiv.org/abs/1603.08066. arXiv: 1603.08066.

[10] N. Bonnet, *et al.* Luminescence of nitrogen-vacancy centers under electron and laser light excitation at different temperatures. *in preparation*, .

[11] Noemie Bonnet, François Treussart, Huan Chang, Mathieu Kociak, and Luiz H. G. Tizei. Combining in situ micro-photoluminescence and cathodoluminescence to understand defects photophysics in nanodiamonds. *Microscopy and Microanalysis*, 27:2104–2106, August 2021. doi: 10.1017/S1431927621007601.

[12] N. Bonnet, *et al.* Free space laser injection and detection in the scanning transmission electron microscope. *in preparation*, .

[13] Kin Fai Mak, Changgu Lee, James Hone, Jie Shan, and Tony F. Heinz. Atomically Thin MoS_2 : A New Direct-Gap Semiconductor. *Physical Review Letters*, 105(13):136805, September 2010. ISSN 0031-9007, 1079-7114. doi: 10.1103/PhysRevLett.105.136805. URL https://link.aps.org/doi/10.1103/PhysRevLett.105.136805.

[14] Shoujun Zheng, Jin-Kyu So, Fucai Liu, Zheng Liu, Nikolay Zheludev, and Hong Jin Fan. Giant Enhancement of Cathodoluminescence of Monolayer Transitional Metal Dichalcogenides Semiconductors. *Nano Letters*, 17(10): 6475–6480, October 2017. ISSN 1530-6984, 1530-6992. doi: 10.1021/acs.nanolett.7b03585. URL https://pubs.acs.org/doi/10.1021/acs.nanolett.7b03585.

[15] Noémie Bonnet, Hae Yeon Lee, Fuhui Shao, Steffi Y. Woo, Jean-Denis Blazit, Kenji Watanabe, Takashi Taniguchi, Alberto Zobelli, Odile Stéphan, Mathieu Kociak, Silvija Gradečak, and Luiz H. G. Tizei. Nanoscale Modification of WS_2 Trion Emission by Its Local Electromagnetic Environment. *Nano Letters*, 21(24): 10178–10185, December 2021. ISSN 1530-6984, 1530-6992. doi: 10.1021/acs.nanolett.1c02600. URL https://pubs.acs.org/doi/10.1021/acs.nanolett.1c02600.

[16] Arnaud Arbouet, Adnen Mlayah, Christian Girard, and Gérard Colas des Francs. Electron energy losses and cathodoluminescence from complex plasmonic nanostructures: spectra, maps and radiation patterns from a generalized field propagator. *New Journal of Physics*, 16(11):113012, November 2014. ISSN 1367-2630. doi: 10.1088/1367-2630/16/11/113012. URL https://iopscience.iop.org/article/10.1088/1367-2630/16/11/113012.

[17] Pavel V Kolesnichenko, Qianhui Zhang, Tinghe Yun, Changxi Zheng, Michael S Fuhrer, and Jeffrey A Davis. Disentangling the effects of doping, strain and disorder in monolayer WS_2 by optical spectroscopy. page 11, 2020.

[18] G. Naresh-Kumar, J. Bruckbauer, A. Winkelmann, X. Yu, B. Hourahine, P. R. Edwards, T. Wang, C. Trager-Cowan, and R. W. Martin. Determining GaN Nanowire Polarity and its Influence on Light Emission in the Scanning Electron Microscope. *Nano Letters*, 19(6):3863–3870, June 2019. ISSN 1530-6984, 1530-6992. doi: 10.1021/acs.nanolett.9b01054. URL https://pubs.acs.org/doi/10.1021/acs.nanolett.9b01054.

[19] N. Bonnet *et al.* *Charaterization of lower energy emission lines in WS_2 monolayers using combined cathodoluminescence, electron energy loss spectroscopy and diffraction*.

[20] L H G Tizei and M Kociak. Spectrally and spatially resolved cathodoluminescence of nanodiamonds: local variations of the NV^0 emission properties. *Nanotechnology*, 23(17):175702, May 2012. ISSN 0957-4484, 1361-6528. doi: 10.1088/0957-4484/23/17/175702. URL https://iopscience.iop.org/article/10.1088/0957-4484/23/17/175702.

[21] Romain Bourrellier, Sophie Meuret, Anna Tararan, Odile Stéphan, Mathieu Kociak, Luiz H. G. Tizei, and Alberto Zobelli. Bright UV Single Photon Emission at Point Defects in *h* -BN. *Nano Letters*, 16(7):4317–4321, July 2016. ISSN 1530-6984, 1530-6992. doi: 10.1021/acs.nanolett.6b01368. URL https://pubs.acs.org/doi/10.1021/acs.nanolett.6b01368.

[22] S. Meuret, L.H.G. Tizei, T. Cazimajou, R. Bourrellier, H.C. Chang, F. Treussart, and M. Kociak. Photon Bunching in Cathodoluminescence. *Physical Review Letters*, 114(19):197401, May 2015. ISSN 0031-9007, 1079-7114. doi: 10.1103/PhysRevLett.114.197401. URL https://link.aps.org/doi/10.1103/PhysRevLett.114.197401.

[23] Helmut Kohl Ludwig Reimer. *Transmission Electron Microscopy*. Springer, fifth edition edition, 2008.

[24] R. F. Egerton. *Electron Energy-Loss Spectroscopy in the Electron Microscope*. Plenum Publishing Corporation, second edition edition, 1996.

[25] Mark Fox. *Optical Properties of Solids*. OUP Oxford, 2010. URL https://books.google.fr/books/about/Optical_Properties_of_Solids.html?id=K9YJ950kBDsC&redir_esc=y.

[26] Ondrej L. Krivanek, Tracy C. Lovejoy, Niklas Dellby, Toshihiro Aoki, R. W. Carpenter, Peter Rez, Emmanuel Soignard, Jiangtao Zhu, Philip E. Batson, Maureen J. Lagos, Ray F. Egerton, and Peter A. Crozier. Vibrational spectroscopy in the electron microscope. *Nature*, 514(7521):209–212, October 2014. ISSN 0028-0836, 1476-4687. doi: 10.1038/nature13870. URL http://www.nature.com/articles/nature13870.

[27] Ralf Hambach. Theory and ab-initio calculations of collective excitations in nanostructures: towards spatially-resolved EELS. page 217.

[28] O.L. Krivanek, G.J. Corbin, N. Dellby, B.F. Elston, R.J. Keyse, M.F. Murfitt, C.S. Own, Z.S. Szilagyi, and J.W. Woodruff. An electron microscope for the aberration-corrected era. *Ultramicroscopy*, 108(3):179–195, February 2008. ISSN 03043991. doi: 10.1016/j.ultramic.2007.07.010. URL https://linkinghub.elsevier.com/retrieve/pii/S0304399107002331.

[29] F. J. García de Abajo. Optical excitations in electron microscopy. *Reviews of Modern Physics*, 82(1):209–275, February 2010. ISSN 0034-6861, 1539-0756. doi: 10.1103/RevModPhys.82.209. URL https://link.aps.org/doi/10.1103/RevModPhys.82.209.

[30] Luiz H.G. Tizei, Yung-Chang Lin, Masaki Mukai, Hidetaka Sawada, Ang-Yu Lu, Lain-Jong Li, Koji Kimoto, and Kazu Suenaga. Exciton Mapping at Subwavelength Scales in Two-Dimensional Materials. *Physical Review Letters*, 114(10):107601, March 2015. ISSN 0031-9007, 1079-7114. doi: 10.1103/PhysRevLett.114.107601. URL https://link.aps.org/doi/10.1103/PhysRevLett.114.107601.

[31] Luiz Fernando Zagonel, Stefano Mazzucco, Marcel Tenc, Benoît Laslier, Rudeesun Songmuang, and Mathieu Kociak. Nanometer Scale Spectral Imaging of Quantum Emitters in Nanowires and Its Correlation to Their Atomically Resolved Structure. *Nano Letters*, page 6, 2011.

[32] Mark Fox. *Quantum Optics*. OXFORD MASTER SERIES IN PHYSICS. 2006.

[33] G Davies. The Jahn-Teller effect and vibronic coupling at deep levels in diamond. *Reports on Progress in Physics*, 44(7):787–830, July 1981. ISSN 0034-4885, 1361-6633. doi: 10.1088/0034-4885/44/7/003. URL https://iopscience.iop.org/article/10.1088/0034-4885/44/7/003.

[34] Alexios Beveratos. Réalisation expérimentale d'une source de photons uniques par fluorescence de centres colorés individuels dans le diamant ; application à la cryptographie quantique. page 151.

[35] C. Robert, D. Lagarde, F. Cadiz, G. Wang, B. Lassagne, T. Amand, A. Balocchi, P. Renucci, S. Tongay, B. Urbaszek, and X. Marie. Exciton radiative lifetime in transition metal dichalcogenide monolayers. *Physical Review B*, 93(20):205423, May 2016. ISSN 2469-9950, 2469-9969. doi: 10.1103/PhysRevB.93.205423. URL https://link.aps.org/doi/10.1103/PhysRevB.93.205423.

[36] Gang Wang, Alexey Chernikov, Mikhail M. Glazov, Tony F. Heinz, Xavier Marie, Thierry Amand, and Bernhard Urbaszek. *Colloquium* : Excitons in atomically thin transition metal dichalcogenides. *Reviews of Modern Physics*, 90(2):021001, April 2018. ISSN 0034-6861, 1539-0756. doi: 10.1103/RevModPhys.90.021001. URL https://link.aps.org/doi/10.1103/RevModPhys.90.021001.

[37] H.H. Fang, B. Han, C. Robert, M.A. Semina, D. Lagarde, E. Courtade, T. Taniguchi, K. Watanabe, T. Amand, B. Urbaszek, M.M. Glazov, and X. Marie. Control of the Exciton Radiative Lifetime in van der Waals Heterostructures. *Physical Review Letters*, 123(6):067401, August 2019. ISSN 0031-9007, 1079-7114. doi: 10.1103/PhysRevLett.123.067401. URL https://link.aps.org/doi/10.1103/PhysRevLett.123.067401.

[38] Ashish Arora, Nils Kolja Wessling, Thorsten Deilmann, Till Reichenauer, Paul Steeger, Piotr Kossacki, Marek Potemski, Steffen Michaelis de Vasconcellos, Michael Rohlfing, and Rudolf Bratschitsch. Dark trions govern the temperature-dependent optical absorption and emission of doped atomically thin semiconductors. *Physical Review B*, 101(24):241413, June 2020. ISSN 2469-9950, 2469-9969. doi: 10.1103/PhysRevB.101.241413. URL https://link.aps.org/doi/10.1103/PhysRevB.101.241413.

[39] Daniel Jaque and Fiorenzo Vetrone. Luminescence nanothermometry. *Nanoscale*, 4(15):4301, 2012. ISSN 2040-3364, 2040-3372. doi: 10.1039/c2nr30764b. URL http://xlink.rsc.org/?DOI=c2nr30764b.

[40] Carlos D. S. Brites, Patricia P. Lima, Nuno J. O. Silva, Angel Millán, Vitor S. Amaral, Fernando Palacio, and Luís D. Carlos. Thermometry at the nanoscale. *Nanoscale*, 4(16):4799, 2012. ISSN 2040-3364, 2040-3372. doi: 10.1039/c2nr30663h. URL http://xlink.rsc.org/?DOI=c2nr30663h.

[41] Pyxem, . URL https://pyxem.github.io/pyxem-website/.

[42] Steven E Zeltmann, Alexander Müller, Karen C Bustillo, Benjamin Savitzky, Lauren Hughes, Andrew M Minor, and Colin Ophus. Patterned probes for high precision 4D-STEM bragg measurements. *Ultramicroscopy*, 209:112890, February 2020. ISSN 03043991. doi: 10.1016/j.ultramic.2019.112890. URL https://linkinghub.elsevier.com/retrieve/pii/S0304399119302451.

[43] M.J. Hÿtch, E. Snoeck, and R. Kilaas. Quantitative measurement of displacement and strain fields from HREM micrographs. *Ultramicroscopy*, 74(3):131–146, August 1998. ISSN 03043991. doi: 10.1016/S0304-3991(98)00035-7. URL https://linkinghub.elsevier.com/retrieve/pii/S0304399198000357.

[44] Raymond James Lamb. Exploring methods for imaging dynamics in transmission electron microscopy. page 228.

[45] Ondrej L. Krivanek, Tracy C. Lovejoy, Niklas Dellby, and R.W. Carpenter. Monochromated STEM with a 30 meV-wide, atom-sized electron probe. *Microscopy*, 62(1):3–21, February 2013. ISSN 2050-5698, 2050-5701. doi: 10.1093/jmicro/dfs089. URL https://academic.oup.com/jmicro/article-lookup/doi/10.1093/jmicro/dfs089.

[46] Ondrej L. Krivanek, Jonathan P. Ursin, Neil J. Bacon, George J. Corbin, Niklas Dellby, Petr Hrncirik, Matthew F. Murfitt, Christopher S. Own, and Zoltan S. Szilagyi. High-energy-resolution monochromator for aberration-corrected scanning transmission electron microscopy/electron energy-loss spectroscopy. *Philosophical Transactions of the Royal Society A: Mathematical, Physical and Engineering Sciences*, 367(1903):3683–3697, September 2009. ISSN 1364-503X, 1471-2962. doi: 10.1098/rsta.2009.0087. URL https://royalsocietypublishing.org/doi/10.1098/rsta.2009.0087.

[47] T.C. Lovejoy, N.J. Bacon, A.L. Bleloch, N. Dellby, M.V. Hoffman, and O.L. Krivanek. Ultra-High Energy Resolution EELS. *Microscopy and Microanalysis*, 23(S1):1552–1553, July 2017. ISSN 1431-9276, 1435-8115. doi: 10.1017/S143192761700842X. URL https://www.cambridge.org/core/product/identifier/S143192761700842X/type/journal_article.

[48] Adrien Teurtrie. Towards a magnetic semiconductor using Ca and Y co-substituted bismuth iron garnet thin films.

[49] Rik Brydson. *Aberration-Corrected Analytical Transmission Electron Microscopy*. Wiley, 2011. URL https://www.wiley.com/en-us/Aberration+Corrected+Analytical+Transmission+Electron+Microscopy-p-9781119979906.

[50] Hyperspy, . URL https://hyperspy.org/.

[51] K. Beha, A. Batalov, N. B. Manson, R. Bratschitsch, and A. Leitenstorfer. Optimum Photoluminescence Excitation and Recharging Cycle of Single Nitrogen-Vacancy Centers in Ultrapure Diamond. *Physical Review Letters*, 109(9):097404, August 2012. ISSN 0031-9007, 1079-7114. doi: 10.1103/PhysRevLett.109.097404. URL https://link.aps.org/doi/10.1103/PhysRevLett.109.097404.

[52] Teng-Xiang Huang, Xin Cong, Si-Si Wu, Kai-Qiang Lin, Xu Yao, Yu-Han He, Jiang-Bin Wu, Yi-Fan Bao, Sheng-Chao Huang, Xiang Wang, Ping-Heng Tan, and Bin Ren. Probing the edge-related properties of atomically thin MoS_2 at nanoscale. *Nature Communications*, 10(1):5544, December 2019. ISSN 2041-1723. doi: 10.1038/s41467-019-13486-7. URL http://www.nature.com/articles/s41467-019-13486-7.

[53] Hans Blom and Jerker Widengren. Stimulated Emission Depletion Microscopy. *Chemical Reviews*, 117(11):7377–7427, June 2017. ISSN 0009-2665, 1520-6890. doi: 10.1021/acs.chemrev.6b00653. URL https://pubs.acs.org/doi/10.1021/acs.chemrev.6b00653.

[54] Pawan Kumar, Dipanwita Chatterjee, Takuya Maeda, Ahin Roy, Kenji Kaneko, and Viswanath Balakrishnan. Scalable faceted voids with luminescent enhanced edges in WS_2 monolayers. *Nanoscale*, 10(34):16321–16331, 2018. ISSN 2040-3364, 2040-3372. doi: 10.1039/C8NR02246A. URL http://xlink.rsc.org/?DOI=C8NR02246A.

[55] G. Kucsko, P. C. Maurer, N. Y. Yao, M. Kubo, H. J. Noh, P. K. Lo, H. Park, and M. D. Lukin. Nanometre-scale thermometry in a living cell. *Nature*, 500(7460): 54–58, August 2013. ISSN 0028-0836, 1476-4687. doi: 10.1038/nature12373. URL http://www.nature.com/articles/nature12373.

[56] Yuen Yung Hui, Oliver Y Chen, Terumitsu Azuma, Be-Ming Chang, Feng-Jen Hsieh, and Huan-Cheng Chang. All-Optical Thermometry with Nitrogen-Vacancy Centers in Nanodiamond-Embedded Polymer Films. *J. Phys. Chem. C*, page 9, 2019.

[57] X.-D. Chen, C.-H. Dong, F.-W. Sun, C.-L. Zou, J.-M. Cui, Z.-F. Han, and G.-C. Guo. Temperature dependent energy level shifts of nitrogen-vacancy centers in diamond. *Applied Physics Letters*, 99(16):161903, October 2011. ISSN 0003-6951, 1077-3118. doi: 10.1063/1.3652910. URL http://aip.scitation.org/doi/10.1063/1.3652910.

[58] N.B. Manson and J.P. Harrison. Photo-ionization of the nitrogen-vacancy center in diamond. *Diamond and Related Materials*, 14(10):1705–1710, October 2005. ISSN 09259635. doi: 10.1016/j.diamond.2005.06.027. URL https://linkinghub.elsevier.com/retrieve/pii/S0925963505002402.

[59] Anubhav Jain, Shyue Ping Ong, Geoffroy Hautier, Wei Chen, William Davidson Richards, Stephen Dacek, Shreyas Cholia, Dan Gunter, David Skinner, Gerbrand Ceder, and Kristin A. Persson. Commentary: The Materials Project: A materials genome approach to accelerating materials innovation. *APL Materials*, 1(1):011002, July 2013. ISSN 2166-532X. doi: 10.1063/1.4812323. URL http://aip.scitation.org/doi/10.1063/1.4812323.

[60] Alexander M. Zaitsev. *Optical Properties of Diamond - A data Handbook*. Springer, 2001. URL https://www.springer.com/gp/book/9783540665823.

[61] A. Gruber. Scanning Confocal Optical Microscopy and Magnetic Resonance on Single Defect Centers. *Science*, 276(5321):2012–2014, June 1997. ISSN 00368075, 10959203. doi: 10.1126/science.276.5321.2012. URL https://www.sciencemag.org/lookup/doi/10.1126/science.276.5321.2012.

[62] E. D. Herbschleb, H. Kato, Y. Maruyama, T. Danjo, T. Makino, S. Yamasaki, I. Ohki, K. Hayashi, H. Morishita, M. Fujiwara, and N. Mizuochi. Ultra-long coherence times amongst room-temperature solid-state spins. *Nature Communications*, 10(1):3766, December 2019. ISSN 2041-1723. doi: 10.1038/s41467-019-11776-8. URL http://www.nature.com/articles/s41467-019-11776-8.

[63] Lucio Robledo, Lilian Childress, Hannes Bernien, Bas Hensen, Paul F. A. Alkemade, and Ronald Hanson. High-fidelity projective read-out of a solid-state spin quantum register. *Nature*, 477(7366):574–578, September 2011. ISSN 0028-0836, 1476-4687. doi: 10.1038/nature10401. URL http://www.nature.com/articles/nature10401.

[64] W. Pfaff, B. J. Hensen, H. Bernien, S. B. van Dam, M. S. Blok, T. H. Taminiau, M. J. Tiggelman, R. N. Schouten, M. Markham, D. J. Twitchen, and R. Hanson. Unconditional quantum teleportation between distant solid-state quantum bits. *Science*, 345(6196):532–535, August 2014. ISSN 0036-8075, 1095-9203. doi: 10.1126/science.1253512. URL https://www.sciencemag.org/lookup/doi/10.1126/science.1253512.

[65] Jean-Paul Boudou, Patrick A Curmi, Fedor Jelezko, Joerg Wrachtrup, Pascal Aubert, Mohamed Sennour, Gopalakrischnan Balasubramanian, Rolf Reuter, Alain Thorel, and Eric Gaffet. High yield fabrication of fluorescent nanodiamonds. *Nanotechnology*, 20(23):235602, June 2009. ISSN 0957-4484, 1361-6528. doi: 10.1088/0957-4484/20/23/235602. URL https://iopscience.iop.org/article/10.1088/0957-4484/20/23/235602.

[66] Alastair Stacey, Igor Aharonovich, Steven Prawer, and James E. Butler. Controlled synthesis of high quality micro/nano-diamonds by microwave plasma chemical vapor deposition. *Diamond and Related Materials*, 18(1):51–55, January 2009. ISSN 09259635. doi: 10.1016/j.diamond.2008.09.020. URL https://linkinghub.elsevier.com/retrieve/pii/S0925963508004597.

[67] Audrius Alkauskas. First-principles theory of the luminescence lineshape for the triplet transition in diamond NV centres. *New J. Phys.*, page 24, 2014.

[68] Matthias Pfender, Nabeel Aslam, Patrick Simon, Denis Antonov, Gergő Thiering, Sina Burk, Felipe Fávaro de Oliveira, Andrej Denisenko, Helmut Fedder, Jan Meijer, Jose A. Garrido, Adam Gali, Tokuyuki Teraji, Junichi Isoya, Marcus William Doherty, Audrius Alkauskas, Alejandro Gallo, Andreas Grüneis, Philipp Neumann, and Jörg Wrachtrup. Protecting a Diamond Quantum Memory by Charge State Control. *Nano Letters*, 17(10):5931–5937, October 2017. ISSN 1530-6984, 1530-6992. doi: 10.1021/acs.nanolett.7b01796. URL https://pubs.acs.org/doi/10.1021/acs.nanolett.7b01796.

[69] Adam Gali. Ab initio calculation of spin-orbit coupling for an NV center in diamond exhibiting dynamic Jahn-Teller effect. *Physical Review B*, page 6, 2017.

[70] E. Poem, C. Weinzetl, J. Klatzow, K. T. Kaczmarek, J. H. D. Munns, T. F. M. Champion, D. J. Saunders, J. Nunn, and I. A. Walmsley. Broadband noise-free optical quantum memory with neutral nitrogen-vacancy centers in diamond. *Physical Review B*, 91(20):205108, May 2015. ISSN 1098-0121, 1550-235X. doi: 10.1103/PhysRevB.91.205108. URL https://link.aps.org/doi/10.1103/PhysRevB.91.205108.

[71] Martin Berthel, Oriane Mollet, Geraldine Dantelle, Thierry Gacoin, Serge Huant, and Aurelien Drezet. Photophysics of single nitrogen-vacancy centers in diamond nanocrystals. *Physical Review B*, page 13, 2015.

[72] Bernhard Grotz, Moritz V. Hauf, Markus Dankerl, Boris Naydenov, Sébastien Pezzagna, Jan Meijer, Fedor Jelezko, Jörg Wrachtrup, Martin Stutzmann, Friedemann Reinhard, and Jose A. Garrido. Charge state manipulation of qubits in diamond. *Nature Communications*, 3(1):729, January 2012. ISSN 2041-1723. doi: 10.1038/ncomms1729. URL http://www.nature.com/articles/ncomms1729.

[73] L. H. G. Tizei and M. Kociak. Spatially Resolved Quantum Nano-Optics of Single Photons Using an Electron Microscope. *Physical Review Letters*, 110(15):153604, April 2013. ISSN 0031-9007, 1079-7114. doi: 10.1103/PhysRevLett.110.153604. URL https://link.aps.org/doi/10.1103/PhysRevLett.110.153604.

[74] Philipp Neumann, Johannes Beck, Matthias Steiner, Florian Rempp, Helmut Fedder, Philip R Hemmer, Jörg Wrachtrup, and Fedor Jelezko. Single-Shot Readout of a Single Nuclear Spin. 329:4, 2010.

[75] Zhaohong Mi, Hong Qi Tan, Ce-Belle Chen, Yanxin Dou, Chengyuan Yang, Shuvan Prashant Turaga, Frank Watt, and Andrew Bettiol. Quantifying nanodiamonds biodistribution in whole cells with correlative iono-nanoscopy. *Nature Communications*, 12:4657, 2021. URL https://www.nature.com/articles/s41467-021-25004-9. https://doi.org/10.1038/s41467-021-25004-9.

[76] Huiliang Zhang, David R. Glenn, Richard Schalek, Jeff W. Lichtman, and Ronald L. Walsworth. Efficiency of Cathodoluminescence Emission by Nitrogen-Vacancy Color Centers in Nanodiamonds. *Small*, 13(22):1700543, June 2017. ISSN 16136810. doi: 10.1002/smll.201700543. URL http://doi.wiley.com/10.1002/smll.201700543.

[77] D. Farfurnik, N. Alfasi, S. Masis, Y. Kauffmann, E. Farchi, Y. Romach, Y. Hovav, E. Buks, and N. Bar-Gill. Enhanced concentrations of nitrogen-vacancy centers in diamond through TEM irradiation. *Applied Physics Letters*, 111(12):123101, September 2017. ISSN 0003-6951, 1077-3118. doi: 10.1063/1.4993257. URL http://aip.scitation.org/doi/10.1063/1.4993257.

[78] E. Pop, S. Sinha, and K.E. Goodson. Heat Generation and Transport in Nanometer-Scale Transistors. *Proceedings of the IEEE*, 94(8):1587–1601, August 2006. ISSN 0018-9219, 1558-2256. doi: 10.1109/JPROC.2006.879794. URL http://ieeexplore.ieee.org/document/1705144/.

[79] Matthew Mecklenburg, William A. Hubbard, E. R. White, Rohan Dhall, Stephen B. Cronin, Shaul Aloni, and B. C. Regan. Nanoscale temperature mapping in operating microelectronic devices. *Science*, 347(6222):629–632, February 2015. ISSN 0036-8075, 1095-9203. doi: 10.1126/science.aaa2433. URL https://www.science.org/doi/10.1126/science.aaa2433.

[80] Kelly W. Mauser, Magdalena Solà-Garcia, Matthias Liebtrau, Benjamin Damilano, Pierre-Marie Coulon, Stéphane Vézian, Philip A. Shields, Sophie Meuret, and Albert Polman. Employing Cathodoluminescence for Nanothermometry and Thermal Transport Measurements in Semiconductor Nanowires. *ACS Nano*, 15(7):11385–11395, July 2021. ISSN 1936-0851, 1936-086X. doi: 10.1021/acsnano.1c00850. URL https://pubs.acs.org/doi/10.1021/acsnano.1c00850.

[81] P. Siyushev, H. Pinto, M. Vörös, A. Gali, F. Jelezko, and J. Wrachtrup. Optically Controlled Switching of the Charge State of a Single Nitrogen-Vacancy Center in Diamond at Cryogenic Temperatures. *Physical Review Letters*, 110(16):167402, April 2013. ISSN 0031-9007, 1079-7114. doi: 10.1103/PhysRevLett.110.167402. URL https://link.aps.org/doi/10.1103/PhysRevLett.110.167402.

[82] Sotatsu Yanagimoto, Naoki Yamamoto, Takumi Sannomiya, and Keiichirou Akiba. Purcell effect of nitrogen-vacancy centers in nanodiamond coupled to propagating and localized surface plasmons revealed by photon-correlation cathodoluminescence. *Physical Review B*, 103(20):205418, May 2021. ISSN 2469-9950, 2469-9969. doi: 10.1103/PhysRevB.103.205418. URL https://link.aps.org/doi/10.1103/PhysRevB.103.205418.

[83] Philipp Tonndorf, Robert Schmidt, Robert Schneider, Johannes Kern, Michele Buscema, Gary A Steele, Andres Castellanos-Gomez, Steffen Michaelis De Vasconcellos, and Rudolf Bratschitsch. Single-photon emission from localized excitons in an atomically thin semiconductor. page 6.

[84] Andrea Splendiani, Liang Sun, Yuanbo Zhang, Tianshu Li, Jonghwan Kim, Chi-Yung Chim, Giulia Galli, and Feng Wang. Emerging Photoluminescence in Monolayer MoS2. *Nano Lett.*, page 5, 2010.

[85] Thomas P. Darlington, Christian Carmesin, Matthias Florian, Emanuil Yanev, Obafunso Ajayi, Jenny Ardelean, Daniel A. Rhodes, Augusto Ghiotto, Andrey Krayev, Kenji Watanabe, Takashi Taniguchi, Jeffrey W. Kysar, Abhay N. Pasupathy, James C. Hone, Frank Jahnke, Nicholas J. Borys, and P. James Schuck. Imaging strain-localized excitons in nanoscale bubbles of monolayer WSe_2 at room temperature. *Nature Nanotechnology*, 15(10):854–860, October 2020. ISSN 1748-3387, 1748-3395. doi: 10.1038/s41565-020-0730-5. URL http://www.nature.com/articles/s41565-020-0730-5.

[86] Bruno Schuler, Katherine A. Cochrane, Christoph Kastl, Edward S. Barnard, Edward Wong, Nicholas J. Borys, Adam M. Schwartzberg, D. Frank Ogletree, F. Javier García de Abajo, and Alexander Weber-Bargioni. Electrically driven photon emission from individual atomic defects in monolayer WS_2. *Science Advances*, 6(38):eabb5988, September 2020. ISSN 2375-2548. doi: 10.1126/sciadv.abb5988. URL https://advances.sciencemag.org/lookup/doi/10.1126/sciadv.abb5988.

[87] Matteo Bosi. Growth and synthesis of mono and few-layers transition metal dichalcogenides by vapour techniques: a review. *RSC Advances*, 5(92):75500–75518, 2015. ISSN 2046-2069. doi: 10.1039/C5RA09356B. URL http://xlink.rsc.org/?DOI=C5RA09356B.

[88] Andres Castellanos-Gomez, Michele Buscema, Rianda Molenaar, Vibhor Singh, Laurens Janssen, Herre S J van der Zant, and Gary A Steele. Deterministic transfer of two-dimensional materials by all-dry viscoelastic stamping. *2D Materials*, 1(1):011002, April 2014. ISSN 2053-1583. doi: 10.1088/2053-1583/1/1/011002. URL https://iopscience.iop.org/article/10.1088/2053-1583/1/1/011002.

[89] Manish Chhowalla, Hyeon Suk Shin, Goki Eda, Lain-Jong Li, Kian Ping Loh, and Hua Zhang. The chemistry of two-dimensional layered transition metal dichalcogenide nanosheets. *Nature Chemistry*, 5(4):263–275, April 2013. ISSN 1755-4330, 1755-4349. doi: 10.1038/nchem.1589. URL http://www.nature.com/articles/nchem.1589.

[90] M. Goryca, J. Li, A. V. Stier, T. Taniguchi, K. Watanabe, E. Courtade, S. Shree, C. Robert, B. Urbaszek, X. Marie, and S. A. Crooker. Revealing exciton masses and dielectric properties of monolayer semiconductors with high magnetic fields. *Nature Communications*, 10(1):4172, December 2019. ISSN 2041-1723. doi: 10.1038/s41467-019-12180-y. URL http://www.nature.com/articles/s41467-019-12180-y.

[91] Maurizia Palummo, Marco Bernardi, and Jeffrey C. Grossman. Exciton Radiative Lifetimes in Two-Dimensional Transition Metal Dichalcogenides. *Nano Letters*, 15(5):2794–2800, May 2015. ISSN 1530-6984, 1530-6992. doi: 10.1021/nl503799t. URL https://pubs.acs.org/doi/10.1021/nl503799t.

[92] Kristian Sommer Thygesen. Calculating excitons, plasmons, and quasiparticles in 2D materials and van der Waals heterostructures. *2D Materials*, 4(2):022004, June 2017. ISSN 2053-1583. doi: 10.1088/2053-1583/aa6432. URL https://iopscience.iop.org/article/10.1088/2053-1583/aa6432.

[93] Alejandro Molina-Sánchez, Kerstin Hummer, and Ludger Wirtz. Vibrational and optical properties of MoS_2 : From monolayer to bulk. *Surface Science Reports*, 70(4):554–586, December 2015. ISSN 01675729. doi: 10.1016/j.surfrep.2015.10.001. URL https://linkinghub.elsevier.com/retrieve/pii/S016757291500028X.

[94] H. Sahin, S. Tongay, S. Horzum, W. Fan, J. Zhou, J. Li, J. Wu, and F. M. Peeters. Anomalous Raman spectra and thickness-dependent electronic properties of WSe 2. *Physical Review B*, 87(16):165409, April 2013. ISSN 1098-0121, 1550-235X. doi: 10.1103/PhysRevB.87.165409. URL https://link.aps.org/doi/10.1103/PhysRevB.87.165409.

[95] M V Durnev and M M Glazov. Excitons and trions in two-dimensional semiconductors based on transition metal dichalcogenides. page 22.

[96] Alejandro Molina-Sánchez, Davide Sangalli, Kerstin Hummer, Andrea Marini, and Ludger Wirtz. Effect of spin-orbit interaction on the optical spectra of single-layer, double-layer, and bulk MoS 2. *Physical Review B*, 88(4):045412, July 2013. ISSN 1098-0121, 1550-235X. doi: 10.1103/PhysRevB.88.045412. URL https://link.aps.org/doi/10.1103/PhysRevB.88.045412.

[97] Min Su Kim, Seok Joon Yun, Yongjun Lee, Changwon Seo, Gang Hee Han, Ki Kang Kim, Young Hee Lee, and Jeongyong Kim. Biexciton Emission from Edges and Grain Boundaries of Triangular WS_2 Monolayers. *ACS Nano*, 10(2):2399–2405, February 2016. ISSN 1936-0851, 1936-086X. doi: 10.1021/acsnano.5b07214. URL https://pubs.acs.org/doi/10.1021/acsnano.5b07214.

[98] Gerd Plechinger, Philipp Nagler, Julia Kraus, Nicola Paradiso, Christoph Strunk, Christian Schüller, and Tobias Korn. Identification of excitons, trions and biexcitons in single-layer WS_2: Identification of excitons, trions and biexcitons in single-layer WS_2. *physica status solidi (RRL) - Rapid Research Letters*, 9(8):457–461, August 2015. ISSN 18626254. doi: 10.1002/pssr.201510224. URL http://doi.wiley.com/10.1002/pssr.201510224.

[99] Yumeng You, Xiao-Xiao Zhang, Timothy C. Berkelbach, Mark S. Hybertsen, David R. Reichman, and Tony F. Heinz. Observation of biexcitons in monolayer WSe_2. *Nature Physics*, 11(6):477–481, June 2015. ISSN 1745-2473, 1745-2481. doi: 10.1038/nphys3324. URL http://www.nature.com/articles/nphys3324.

[100] Bogdan Ganchev, Neil Drummond, Igor Aleiner, and Vladimir Fal'ko. Three-Particle Complexes in Two-Dimensional Semiconductors. *Physical Review Letters*, 114(10):107401, March 2015. ISSN 0031-9007, 1079-7114. doi: 10.1103/PhysRevLett.114.107401. URL https://link.aps.org/doi/10.1103/PhysRevLett.114.107401.

[101] E. Courtade, M. Semina, M. Manca, M. M. Glazov, C. Robert, F. Cadiz, G. Wang, T. Taniguchi, K. Watanabe, M. Pierre, W. Escoffier, E. L. Ivchenko, P. Renucci, X. Marie, T. Amand, and B. Urbaszek. Charged excitons in monolayer WSe_2: experiment and theory. *Physical Review B*, 96(8):085302, August 2017. ISSN 2469-9950, 2469-9969. doi: 10.1103/PhysRevB.96.085302. URL http://arxiv.org/abs/1705.02110. arXiv: 1705.02110.

[102] Kin Fai Mak, Keliang He, Changgu Lee, Gwan Hyoung Lee, James Hone, Tony F. Heinz, and Jie Shan. Tightly bound trions in monolayer MoS_2. *Nature Materials*, 12(3):207–211, March 2013. ISSN 1476-1122, 1476-4660. doi: 10.1038/nmat3505. URL http://www.nature.com/articles/nmat3505.

[103] Yongjae Kwon, Kangwon Kim, Wontaek Kim, Sunmin Ryu, and Hyeonsik Cheong. Variation of photoluminescence spectral line shape of monolayer WS_2. *Current Applied Physics*, 18(8):941–945, August 2018. ISSN 15671739. doi: 10.1016/j.cap.2018.05.007. URL https://linkinghub.elsevier.com/retrieve/pii/S1567173918301317.

[104] Alexey Chernikov, Arend M. van der Zande, Heather M. Hill, Albert F. Rigosi, Ajanth Velauthapillai, James Hone, and Tony F. Heinz. Electrical Tuning of Exciton Binding Energies in Monolayer WS_2. *Physical Review Letters*, 115(12):126802, September 2015. ISSN 0031-9007, 1079-7114. doi: 10.1103/PhysRevLett.115.126802. URL https://link.aps.org/doi/10.1103/PhysRevLett.115.126802.

[105] Gerd Plechinger, Philipp Nagler, Ashish Arora, Robert Schmidt, Alexey Chernikov, Andrés Granados del Águila, Peter C.M. Christianen, Rudolf Bratschitsch, Christian Schüller, and Tobias Korn. Trion fine structure and coupled spin–valley dynamics in monolayer tungsten disulfide. *Nature Communications*, 7(1):12715, November 2016. ISSN 2041-1723. doi: 10.1038/ncomms12715. URL http://www.nature.com/articles/ncomms12715.

[106] Thorsten Deilmann and Kristian Sommer Thygesen. Dark excitations in monolayer transition metal dichalcogenides. *Physical Review B*, 96(20):201113, November 2017. ISSN 2469-9950, 2469-9969. doi: 10.1103/PhysRevB.96.201113. URL https://link.aps.org/doi/10.1103/PhysRevB.96.201113.

[107] Akshay Singh, Galan Moody, Kha Tran, Marie E. Scott, Vincent Overbeck, Gunnar Berghäuser, John Schaibley, Edward J. Seifert, Dennis Pleskot, Nathaniel M. Gabor, Jiaqiang Yan, David G. Mandrus, Marten Richter, Ermin Malic, Xiaodong Xu, and Xiaoqin Li. Trion formation dynamics in monolayer transition metal dichalcogenides. *Physical Review B*, 93(4):041401, January 2016. ISSN 2469-9950, 2469-9969. doi: 10.1103/PhysRevB.93.041401. URL https://link.aps.org/doi/10.1103/PhysRevB.93.041401.

[108] Etienne Lorchat, Luis E. Parra Lopez, Cédric Robert, Delphine Lagarde, Guillaume Froehlicher, Takashi Taniguchi, Kenji Watanabe, Xavier Marie, and Stéphane Berciaud. *Nature Nanotechnology*, 15:283–288, 2020. doi: https://doi-org.ezproxy.universite-paris-saclay.fr/10.1038/s41565-020-0644-2.

[109] Matthias Paur, Aday J. Molina-Mendoza, Rudolf Bratschitsch, Kenji Watanabe, Takashi Taniguchi, and Thomas Mueller. Electroluminescence from multi-particle exciton complexes in transition metal dichalcogenide semiconductors. *Nature Communications*, 10(1):1709, December 2019. ISSN 2041-1723. doi: 10.1038/s41467-019-09781-y. URL http://www.nature.com/articles/s41467-019-09781-y.

[110] Battulga Munkhbat, Denis G. Baranov, Ankit Bisht, Md Anamul Hoque, Bogdan Karpiak, Saroj P. Dash, and Timur Shegai. Electrical Control of Hybrid Monolayer Tungsten Disulfide–Plasmonic Nanoantenna Light–Matter States at Cryogenic and Room Temperatures. *ACS Nano*, 14(1):1196–1206, January 2020. ISSN 1936-0851, 1936-086X. doi: 10.1021/acsnano.9b09684. URL https://pubs.acs.org/doi/10.1021/acsnano.9b09684.

[111] Carmen Palacios-Berraquero, Dhiren M. Kara, Alejandro R.-P. Montblanch, Matteo Barbone, Pawel Latawiec, Duhee Yoon, Anna K. Ott, Marko Loncar, Andrea C. Ferrari, and Mete Atatüre. Large-scale quantum-emitter arrays in atomically thin semiconductors. *Nature Communications*, 8(1):15093,

August 2017. ISSN 2041-1723. doi: 10.1038/ncomms15093. URL http://www.nature.com/articles/ncomms15093.

[112] Leo Yu, Minda Deng, Jingyuan Linda Zhang, Sven Borghardt, Beata Kardynal, Jelena Vučković, and Tony F. Heinz. Site-Controlled Quantum Emitters in Monolayer $MoSe_2$. *Nano Letters*, 21(6):2376–2381, March 2021. ISSN 1530-6984, 1530-6992. doi: 10.1021/acs.nanolett.0c04282. URL https://pubs.acs.org/doi/10.1021/acs.nanolett.0c04282.

[113] Di Xiao, Gui-Bin Liu, Wanxiang Feng, Xiaodong Xu, and Wang Yao. Coupled Spin and Valley Physics in Monolayers of MoS_2 and Other Group-VI Dichalcogenides. *Physical Review Letters*, 108(19):196802, May 2012. ISSN 0031-9007, 1079-7114. doi: 10.1103/PhysRevLett.108.196802. URL https://link.aps.org/doi/10.1103/PhysRevLett.108.196802.

[114] Keliang He Kin Fai Mak and Tony F. Heinz Jie Shan. Control of valley polarization in monolayer MoS_2 by optical helicity. 7:494–498, 2012. URL https://www.nature.com/articles/nnano.2012.96.

[115] Ting Cao, Gang Wang, Wenpeng Han, Huiqi Ye, Chuanrui Zhu, Junren Shi, Qian Niu, Pingheng Tan, Enge Wang, Baoli Liu, and Ji Feng. Valley-selective circular dichroism of monolayer molybdenum disulphide. *Nature Communications*, 3(1):887, January 2012. ISSN 2041-1723. doi: 10.1038/ncomms1882. URL http://www.nature.com/articles/ncomms1882.

[116] Yang Xu, Connor Horn, Jiacheng Zhu, Yanhao Tang, Liguo Ma, Lizhong Li, Song Liu, Kenji Watanabe, Takashi Taniguchi, James C. Hone, Jie Shan, and Kin Fai Mak. Creation of moiré bands in a monolayer semiconductor by spatially periodic dielectric screening. *Nature Materials*, January 2021. ISSN 1476-1122, 1476-4660. doi: 10.1038/s41563-020-00888-y. URL http://www.nature.com/articles/s41563-020-00888-y.

[117] Dante M. Kennes, Martin Claassen, Lede Xian, Antoine Georges, Andrew J. Millis, James Hone, Cory R. Dean, D. N. Basov, Abhay N. Pasupathy, and Angel Rubio. Moiré heterostructures as a condensed-matter quantum simulator. *Nature Physics*, 17(2):155–163, February 2021. ISSN 1745-2473, 1745-2481. doi: 10.1038/s41567-020-01154-3. URL http://www.nature.com/articles/s41567-020-01154-3.

[118] Sandhya Susarla, Lucas M. Sassi, Alberto Zobelli, Steffi Y. Woo, Luiz H. G. Tizei, Odile Stéphan, and Pulickel M. Ajayan. Mapping Modified Electronic Levels in the Moiré Patterns in MoS_2 /WSe_2 Using Low-Loss EELS. *Nano Letters*, 21(9):4071–4077, May 2021. ISSN 1530-6984, 1530-6992. doi: 10.1021/acs.nanolett.1c00984. URL https://pubs.acs.org/doi/10.1021/acs.nanolett.1c00984.

[119] Thomas P. Darlington, Andrey Krayev, Vishal Venkatesh, Ravindra Saxena, Jeffrey W. Kysar, Nicholas J. Borys, Deep Jariwala, and P. James Schuck. Facile and quantitative estimation of strain in nanobubbles with arbitrary symmetry in 2D semiconductors verified using hyperspectral nano-optical imaging. *The Journal of Chemical Physics*, 153(2):024702, July 2020. ISSN 0021-9606, 1089-7690. doi: 10.1063/5.0012817. URL http://aip.scitation.org/doi/10.1063/5.0012817.

[120] Wei Bao, Nicholas J. Borys, Changhyun Ko, Joonki Suh, Wen Fan, Andrew Thron, Yingjie Zhang, Alexander Buyanin, Jie Zhang, Stefano Cabrini, Paul D. Ashby, Alexander Weber-Bargioni, Sefaattin Tongay, Shaul Aloni, D. Frank

Ogletree, Junqiao Wu, Miquel B. Salmeron, and P. James Schuck. Visualizing nanoscale excitonic relaxation properties of disordered edges and grain boundaries in monolayer molybdenum disulfide. *Nature Communications*, 6 (1):7993, November 2015. ISSN 2041-1723. doi: 10.1038/ncomms8993. URL http://www.nature.com/articles/ncomms8993.

[121] Archana Raja. Dielectric disorder in two-dimensional materials. *Nature Nanotechnology*, 14:7, 2019.

[122] M. Iqbal Bakti Utama, Hans Kleemann, Wenyu Zhao, Chin Shen Ong, Felipe H. da Jornada, Diana Y. Qiu, Hui Cai, Han Li, Rai Kou, Sihan Zhao, Sheng Wang, Kenji Watanabe, Takashi Taniguchi, Sefaattin Tongay, Alex Zettl, Steven G. Louie, and Feng Wang. A dielectric-defined lateral heterojunction in a monolayer semiconductor. *Nature Electronics*, 2(2):60–65, February 2019. ISSN 2520-1131. doi: 10.1038/s41928-019-0207-4. URL http://www.nature.com/articles/s41928-019-0207-4.

[123] Akshay Singh, Hae Yeon Lee, and Silvija Gradečak. Direct optical-structure correlation in atomically thin dichalcogenides and heterostructures. *Nano Research*, 13(5):1363–1368, May 2020. ISSN 1998-0124, 1998-0000. doi: 10.1007/s12274-019-2601-7. URL http://link.springer.com/10.1007/s12274-019-2601-7.

[124] G. Nayak, S. Lisi, W. L. Liu, T. Jakubczyk, P. Stepanov, F. Donatini, K. Watanabe, T. Taniguchi, A. Bid, J. Kasprzak, M. Richard, V. Bouchiat, J. Coraux, L. Marty, N. Bendiab, and J. Renard. Cathodoluminescence enhancement and quenching in type-I van der Waals heterostructures: Cleanliness of the interfaces and defect creation. *Physical Review Materials*, 3(11):114001, November 2019. ISSN 2475-9953. doi: 10.1103/PhysRevMaterials.3.114001. URL https://link.aps.org/doi/10.1103/PhysRevMaterials.3.114001.

[125] Farabi Bozheyev, Damir Valiev, and Renata Nemkayeva. Pulsed cathodoluminescence and Raman spectra of MoS_2 and WS_2 nanocrystals and their combination MoS_2 /WS_2 produced by self-propagating high-temperature synthesis. *Applied Physics Letters*, 108(9):093111, February 2016. ISSN 0003-6951, 1077-3118. doi: 10.1063/1.4943144. URL http://aip.scitation.org/doi/10.1063/1.4943144.

[126] F. Fabbri, E. Rotunno, E. Cinquanta, D. Campi, E. Bonnini, D. Kaplan, L. Lazzarini, M. Bernasconi, C. Ferrari, M. Longo, G. Nicotra, A. Molle, V. Swaminathan, and G. Salviati. Novel near-infrared emission from crystal defects in MoS_2 multilayer flakes. *Nature Communications*, 7(1):13044, December 2016. ISSN 2041-1723. doi: 10.1038/ncomms13044. URL http://www.nature.com/articles/ncomms13044.

[127] Luiz H. G. Tizei, Yung-Chang Lin, Ang-Yu Lu, Lain-Jong Li, and Kazu Suenaga. Electron energy loss spectroscopy of excitons in two-dimensional-semiconductors as a function of temperature. *Applied Physics Letters*, 108(16): 163107, April 2016. ISSN 0003-6951, 1077-3118. doi: 10.1063/1.4947058. URL http://aip.scitation.org/doi/10.1063/1.4947058.

[128] Fariah Hayee, Leo Yu, Jingyuan Linda Zhang, Christopher J. Ciccarino, Minh Nguyen, Ann F. Marshall, Igor Aharonovich, Jelena Vučković, Prineha Narang, Tony F. Heinz, and Jennifer A. Dionne. Revealing multiple classes of stable quantum emitters in hexagonal boron nitride with correlated optical and electron microscopy. *Nature Materials*, 19(5):534–539, May 2020.

ISSN 1476-1122, 1476-4660. doi: 10.1038/s41563-020-0616-9. URL http://www.nature.com/articles/s41563-020-0616-9.

[129] T. Taniguchi and K. Watanabe. Synthesis of high-purity boron nitride single crystals under high pressure by using Ba–BN solvent. *Journal of Crystal Growth*, 303(2):525–529, May 2007. ISSN 00220248. doi: 10.1016/j.jcrysgro.2006.12.061. URL https://linkinghub.elsevier.com/retrieve/pii/S0022024807000486.

[130] Martin Couillard, Guillaume Radtke, Andrew P. Knights, and Gianluigi A. Botton. Three-Dimensional Atomic Structure of Metastable Nanoclusters in Doped Semiconductors. *Physical Review Letters*, 107(18):186104, October 2011. ISSN 0031-9007, 1079-7114. doi: 10.1103/PhysRevLett.107.186104. URL https://link.aps.org/doi/10.1103/PhysRevLett.107.186104.

[131] Riccardo Frisenda. Biaxial strain tuning of the optical properties of single-layer transition metal dichalcogenides. page 7, 2017.

[132] Felix Carrascoso, Der-Yuh Lin, Riccardo Frisenda, and Andres Castellanos-Gomez. Biaxial strain tuning of interlayer excitons in bilayer MoS_2. *Journal of Physics: Materials*, 3(1):015003, October 2019. ISSN 2515-7639. doi: 10.1088/2515-7639/ab4432. URL https://iopscience.iop.org/article/10.1088/2515-7639/ab4432.

[133] Do Muoi, Nguyen N. Hieu, Huong T.T. Phung, Huynh V. Phuc, B. Amin, Bui D. Hoi, Nguyen V. Hieu, Le C. Nhan, Chuong V. Nguyen, and P.T.T. Le. Electronic properties of WS_2 and WSe_2 monolayers with biaxial strain: A first-principles study. *Chemical Physics*, 519:69–73, March 2019. ISSN 03010104. doi: 10.1016/j.chemphys.2018.12.004. URL https://linkinghub.elsevier.com/retrieve/pii/S0301010418312904.

[134] Xiangying Su, Weiwei Ju, Ruizhi Zhang, Chongfeng Guo, Jiming Zheng, Yongliang Yong, and Xiaohong Li. Bandgap engineering of MoS_2/MX_2 (MX_2 = WS_2 , $MoSe_2$ and WSe_2) heterobilayers subjected to biaxial strain and normal compressive strain. *RSC Advances*, 6(22):18319–18325, 2016. ISSN 2046-2069. doi: 10.1039/C5RA27871F. URL http://xlink.rsc.org/?DOI=C5RA27871F.

[135] Maja Feierabend, Alexandre Morlet, Gunnar Berghäuser, and Ermin Malic. Impact of strain on the optical fingerprint of monolayer transition-metal dichalcogenides. *Physical Review B*, 96(4):045425, July 2017. ISSN 2469-9950, 2469-9969. doi: 10.1103/PhysRevB.96.045425. URL http://link.aps.org/doi/10.1103/PhysRevB.96.045425.

[136] Joshua O. Island, Agnieszka Kuc, Erik H. Diependaal, Rudolf Bratschitsch, Herre S. J. van der Zant, Thomas Heine, and Andres Castellanos-Gomez. Precise and reversible band gap tuning in single-layer $MoSe_2$ by uniaxial strain. *Nanoscale*, 8(5):2589–2593, 2016. ISSN 2040-3364, 2040-3372. doi: 10.1039/C5NR08219F. URL http://xlink.rsc.org/?DOI=C5NR08219F.

[137] Moshe G Harats. Dynamics and efficient conversion of excitons to trions in non-uniformly strained monolayer WS_2. *Nature Photonics*, 14:7, 2020.

[138] Xin He, Hai Li, Zhiyong Zhu, Zhenyu Dai, Yang Yang, Peng Yang, Qiang Zhang, Peng Li, Udo Schwingenschlogl, and Xixiang Zhang. Strain engineering in monolayer WS_2 , MoS_2 , and the WS_2 /MoS_2 heterostructure. *Applied Physics Letters*, 109(17):173105, October 2016. ISSN 0003-6951, 1077-3118. doi: 10.1063/1.4966218. URL http://aip.scitation.org/doi/10.1063/1.4966218.

[139] Iris Niehues, Robert Schmidt, Matthias Drüppel, Philipp Marauhn, Dominik Christiansen, Malte Selig, Gunnar Berghäuser, Daniel Wigger, Robert Schneider, Lisa Braasch, Rouven Koch, Andres Castellanos-Gomez, Tilmann Kuhn, Andreas Knorr, Ermin Malic, Michael Rohlfing, Steffen Michaelis de Vasconcellos, and Rudolf Bratschitsch. Strain Control of Exciton–Phonon Coupling in Atomically Thin Semiconductors. *Nano Letters*, 18(3):1751–1757, March 2018. ISSN 1530-6984, 1530-6992. doi: 10.1021/acs.nanolett.7b04868. URL https://pubs.acs.org/doi/10.1021/acs.nanolett.7b04868.

[140] Yingchun Ding and Bing Xiao. Thermal expansion tensors, Grüneisen parameters and phonon velocities of bulk MT_2 (M = W and Mo; T = S and Se) from first principles calculations. *RSC Advances*, 5(24):18391–18400, 2015. ISSN 2046-2069. doi: 10.1039/C4RA16966B. URL http://xlink.rsc.org/?DOI=C4RA16966B.

[141] Qiran Cai, Declan Scullion, Wei Gan, Alexey Falin, Shunying Zhang, Kenji Watanabe, Takashi Taniguchi, Ying Chen, Elton J. G. Santos, and Lu Hua Li. High thermal conductivity of high-quality monolayer boron nitride and its thermal expansion. *Science Advances*, 5(6):eaav0129, June 2019. ISSN 2375-2548. doi: 10.1126/sciadv.aav0129. URL https://www.science.org/doi/10.1126/sciadv.aav0129.

[142] Pascal Anger, Palash Bharadwaj, and Lukas Novotny. Enhancement and Quenching of Single-Molecule Fluorescence. *Physical Review Letters*, 96(11):113002, March 2006. ISSN 0031-9007, 1079-7114. doi: 10.1103/PhysRevLett.96.113002. URL https://link.aps.org/doi/10.1103/PhysRevLett.96.113002.

[143] Sina Najmaei, Adnen Mlayah, Arnaud Arbouet, Christian Girard, Jean Léotin, and Jun Lou. Plasmonic Pumping of Excitonic Photoluminescence in Hybrid MoS_2 –Au Nanostructures. *ACS Nano*, 8(12):12682–12689, December 2014. ISSN 1936-0851, 1936-086X. doi: 10.1021/nn5056942. URL https://pubs.acs.org/doi/10.1021/nn5056942.

[144] Hongyan Shi, Rusen Yan, Simone Bertolazzi, Jacopo Brivio, Bo Gao, Andras Kis, Debdeep Jena, Huili Grace Xing, and Libai Huang. Exciton Dynamics in Suspended Monolayer and Few-Layer MoS_2 2D Crystals. *ACS Nano*, 7(2):1072–1080, February 2013. ISSN 1936-0851, 1936-086X. doi: 10.1021/nn303973r. URL https://pubs.acs.org/doi/10.1021/nn303973r.

[145] Yuanshuang Liu, Xiangmin Hu, Ting Wang, and Dameng Liu. Reduced Binding Energy and Layer-Dependent Exciton Dynamics in Monolayer and Multilayer WS_2. *ACS Nano*, 13(12):14416–14425, December 2019. ISSN 1936-0851, 1936-086X. doi: 10.1021/acsnano.9b08004. URL https://pubs.acs.org/doi/10.1021/acsnano.9b08004.

[146] Philipp Tonndorf, Robert Schmidt, Robert Schneider, Johannes Kern, Michele Buscema, Gary A. Steele, Andres Castellanos-Gomez, Herre S. J. van der Zant, Steffen Michaelis de Vasconcellos, and Rudolf Bratschitsch. Single-photon emission from localized excitons in an atomically thin semiconductor. *Optica*, 2(4):347, April 2015. ISSN 2334-2536. doi: 10.1364/OPTICA.2.000347. URL https://www.osapublishing.org/abstract.cfm?URI=optica-2-4-347.

[147] T. C. Doan, J. Li, J. Y. Lin, and H. X. Jiang. Bandgap and exciton binding energies of hexagonal boron nitride probed by photocurrent excitation spectroscopy. *Applied Physics Letters*, 109(12):122101, September 2016. ISSN 0003-6951, 1077-3118. doi: 10.1063/1.4963128. URL http://aip.scitation.org/doi/10.1063/1.4963128.

[148] Kamyar Parto, Shaimaa I. Azzam, Kaustav Banerjee, and Galan Moody. Defect and strain engineering of monolayer WSe2 enables site-controlled single-photon emission up to 150 K. *Nature Communications*, 12(1):3585, December 2021. ISSN 2041-1723. doi: 10.1038/s41467-021-23709-5. URL http://www.nature.com/articles/s41467-021-23709-5.

[149] S Schwarz, A Kozikov, F Withers, J K Maguire, A P Foster, S Dufferwiel, L Hague, M N Makhonin, L R Wilson, A K Geim, K S Novoselov, and A I Tartakovskii. Electrically pumped single-defect light emitters in WSe_2. *2D Materials*, 3(2):025038, June 2016. ISSN 2053-1583. doi: 10.1088/2053-1583/3/2/025038. URL https://iopscience.iop.org/article/10.1088/2053-1583/3/2/025038.

[150] J Jadczak, J Kutrowska-Girzycka, P Kapuściński, Y S Huang, A Wójs, and L Bryja. Probing of free and localized excitons and trions in atomically thin WSe_2 , WS_2 , $MoSe_2$ and MoS_2 in photoluminescence and reflectivity experiments. *Nanotechnology*, 28(39):395702, September 2017. ISSN 0957-4484, 1361-6528. doi: 10.1088/1361-6528/aa87d0. URL https://iopscience.iop.org/article/10.1088/1361-6528/aa87d0.

[151] V. M. Acosta, C. Santori, A. Faraon, Z. Huang, K.-M. C. Fu, A. Stacey, D. A. Simpson, K. Ganesan, S. Tomljenovic-Hanic, A. D. Greentree, S. Prawer, and R. G. Beausoleil. Dynamic Stabilization of the Optical Resonances of Single Nitrogen-Vacancy Centers in Diamond. *Physical Review Letters*, 108(20):206401, May 2012. ISSN 0031-9007, 1079-7114. doi: 10.1103/PhysRevLett.108.206401. URL https://link.aps.org/doi/10.1103/PhysRevLett.108.206401.

[152] Toon Coenen and Albert Polman. Polarization-sensitive cathodoluminescence Fourier microscopy. *Optics Express*, 20(17):18679, August 2012. ISSN 1094-4087. doi: 10.1364/OE.20.018679. URL https://www.osapublishing.org/oe/abstract.cfm?uri=oe-20-17-18679.

[153] Hugo Lourenço-Martins, Mathieu Kociak, Sophie Meuret, François Treussart, Yih Hong Lee, Xing Yi Ling, Huan-Cheng Chang, and Luiz Henrique Galvao Tizei. Probing Plasmon-NV^0 Coupling at the Nanometer Scale with Photons and Fast Electrons. *ACS Photonics*, 5(2):324–328, February 2018. ISSN 2330-4022, 2330-4022. doi: 10.1021/acsphotonics.7b01093. URL https://pubs.acs.org/doi/10.1021/acsphotonics.7b01093.

[154] Kamyar Parto, Kaustav Banerjee, and Galan Moody. Irradiation of Nanostrained Monolayer WSe_2 for Site-Controlled Single-Photon Emission up to 150K. In *Frontiers in Optics / Laser Science*, page FW1C.3, Washington, DC, 2020. OSA. ISBN 978-1-943580-80-4. doi: 10.1364/FIO.2020.FW1C.3. URL https://www.osapublishing.org/abstract.cfm?URI=FiO-2020-FW1C.3.

université PARIS-SACLAY | ÉCOLE DOCTORALE Ondes et matière (EDOM)

Titre : Spectroscopie optique et électronique de semiconducteurs 2D et de défauts dans le microscope électronique

Mots clés : nano-optique, spectroscopie électronique, optique quantique

Résumé : La compréhension de l'interaction lumière-matière est essentielle pour développer de nouveaux composants opto-électroniques. Ce type d'interaction est souvent gouverné par la physique des excitons, qui n'est pas entièrement comprise à l'échelle de ces quasi-particules. De ce fait, des mesures à haute résolution spatiale de la lumière absorbée et émise est cruciale pour la compréhension de la physique des excitons à l'échelle nanométrique, ce qui est un challenge particulier du fait de la limite fondamentale de la diffraction en optique. Des techniques purement optiques ont été développées ces dernières décennies pour surpasser cette limite, et sont appelées microscopie à super-résolution (SRM). Elles permettent la mesure optique de différents échantillons, en particulier de nano-objets, en dessous de la limite de la diffraction.

Il y a deux catégories de SRM : les techniques de champ proche et les techniques de champ lointain. Les techniques de champ proche comprennent souvent une pointe située à proximité de l'échantillon, ce qui modifie grandement l'environnement diélectrique de celui-ci, et les techniques de champ lointain sont généralement basées sur des teintures ou des centres colorés particuliers, ce qui peut limiter l'utilisation de celles-ci pour l'étude de nouveaux matériaux.

Durant ma thèse, j'ai utilisé une approche différente de mesure optique en champ lointain, qui permet d'accéder à des résolutions spatiales bien en-dessous de la limite de la diffraction. Cette technique, la cathodoluminescence (CL) est non-sélective, et est mesurée avec des électrons rapides dans un microscope électronique à balayage en transmission (STEM). J'ai principalement étudié deux sortes de nano-objets : les centres azote-lacune (NV) dans des nanodiamants, que j'ai illuminé avec des lasers et des faisceaux électroniques, et des monocouches de métaux de transition dichalcogénures (TMD) encapsulées dans du nitrure de bore hexagonal (h-BN). J'ai étudié les monocouches en combinant la cathodoluminescence (émission), la spectroscopie de perte d'énergie des électrons (EELS, absorption) et la µ-diffraction (cartographie de déformation).

La combinaison de ces techniques dans un microscope électronique permet de caractériser les excitons des TMD encapsulés (ici WS_2) à l'échelle nanométrique. Le faible écrantage des charges dans la monocouche semiconductrice permet à différents types d'excitons d'être stables à température ambiante, en particulier, les excitons chargés, appelés trions (négatif, X^-, et positif, X^+) sont visibles en émission. Les variations de la CL des excitons et des trions ont été étudiées à l'aide de la cartographie d'éléments chimiques en core-loss EELS (à l'échelle de la centaine d'eV), et les cartes de déformations avec la µ-diffraction, à l'échelle nanométrique. De plus, la combinaison entre l'émission en CL et l'absorption à petite échelle d'énergie en EELS de la même quasi-particule (ici l'exciton A du TMD) à l'échelle nanométrique, donne des informations sur l'origine de ces variations.

L'étude de la photophyique des centres NV a été faite avec deux techniques : la CL (émission à partir d'excitation par des électrons) et la photoluminescence (PL, émission à partir d'excitation par des photons). L'excitation laser a été ajoutée au STEM de façon à pouvoir effectuer la CL et la PL dans la même expérience. En effet, certains échantillons sont fragiles, ou n'émettent pas de CL. De ce fait, la possibilité de faire la PL dans le STEM, pour corréler la mesure de structure et celle de la luminescence est attractive. L'illumination par des faisceaux lasers chauffe l'échantillon localement, ce qui peut être utilisé pour nettoyer celui-ci in-situ. L'échauffement de l'échantillon a été étudié plus en détails par des mesures de CL en température, avec des porte-échantillon chauffant dans le STEM.

université PARIS-SACLAY

ÉCOLE DOCTORALE
Ondes et matière (EDOM)

Title : Electron and optical spectroscopy of 2D semiconductors and defects in the electron microscope
Keywords : nano-optics, electron spectroscopy, quantum optics

Abstract : Understanding the interactions between light and matter is essential to develop new nanoscale opto-electronic devices. These interactions are often governed by exciton physics that is still not well understood at the scale of these quasiparticles. High spatial resolution measurements of the light absorption and emission is therefore crucial for understanding the exciton physics at the nanoscale, which is particularly challenging due to the optical diffraction fundamental limit. Many purely optical techniques have been developed in the past decades to overcome this limit, and are called super-resolution microscopy (SRM). They allow for the sub-diffraction optical measurements of various specimens, including nano-objects.

There are two main categories of SRM : the near-field and the far-field techniques. The near-field techniques often rely on the proximity of a tip on the sample, which highly modifies its dielectric environment, and the far-field techniques are commonly based on specific dyes or light-emitting centers, which may prevent the study of new materials.

In this thesis, I used a different far-field approach that enables resolutions far below the diffraction limit and non-selective excitation of samples : cathodoluminescence (CL) with fast electrons in a scanning transmission electron microscope (STEM). I mainly studied two sorts of nano-objects : nitrogen-vacancy (NV) color centers in nanodiamonds, excited both by the fast electron beam and various lasers, to understand the defects photophysics. The other objects studied were transition metal dichalcogenide (TMD) monolayers encapsulated in h-BN, using combined CL (emission), electron energy-loss spectroscopy (EELS, absorption) and µ-diffraction (strain mapping).

The combination of these techniques in the electron microscope enabled the nanoscale characterization of exciton emission in TMD monolayers (WS_2) encapsulated in hexagonal boron nitride (h-BN). The low screening in these semiconducting monolayers allows for several types of excitons to be stable at room temperature, including charged-excitons, called trions (negative trion, X^-, and positive trion, X^+). The CL emission variations of the excitons and trions was studied using nanoscale chemical environment characterization in core-loss EELS (in the hundreds of eV range), and strain mapping with µ-diffraction. Moreover, the combination of CL emission and absorption in low-loss EELS (here, in the few eV range) of the same quasiparticle (here, the A exciton) at the nanoscale gives information about the origin of its variations.

The study of NV centers photophysics was performed using two techniques, the CL (light emission with electron excitation) and the photoluminescence (PL, light emission with photon excitation). The laser excitation was implemented to the STEM microscope in free space, without optical fibers, to perform PL and CL in the same setup. Indeed, some specimen are fragile and get damaged upon electron irradiation, or do not emit light in CL. For these reasons, the possibility of performing PL experiments inside the electron microscope, to correlate luminescence and structure, is attractive. The illumination by laser beams led to sample heating which can be used for in-situ cleaning of sample. The heating of the NV centers has further been investigated using temperature-controlled CL experiments, with sample heating stages in the STEM microscope.